

CR-137913

**STATIC AND WIND TUNNEL NEAR-FIELD/FAR-FIELD  
JET NOISE MEASUREMENTS FROM MODEL  
SCALE SINGLE-FLOW BASELINE AND  
SUPPRESSOR NOZZLES**

**Volume 1: Noise Source Locations and Extrapolation  
of Static Free-Field Jet Noise Data**

**C. L. Jaeck**

**September 1976**

**(NASA-CR-137913) STATIC AND WIND TUNNEL  
NEAR-FIELD/FAR-FIELD JET NOISE MEASUREMENTS  
FROM MODEL SCALE SINGLE-FLOW BASELINE AND  
SUPPRESSOR NOZZLES. VOLUME 1: NOISE SOURCE  
LOCATIONS AND (Boeing Commercial Airplane**

**N76-32972  
HC 47.50**

**Unclas  
03450**



**Prepared under contract NAS2-8213 by**

**Boeing Commercial Airplane Company  
P.O. Box 3707  
Seattle, Washington 98124**

**for**

**Ames Research Center  
NATIONAL AERONAUTICS AND SPACE ADMINISTRATION**

1. Report No. <b>CR-137913</b>	2. Government Accession No.	3. Recipient's Catalog No.	
4. Title and Subtitle <b>Static and Wind Tunnel Near-Field/Far-Field Jet Noise Measurements From Model Scale Single-Flow Baseline and Suppressor Nozzles. Volume 1: Noise Source Locations and Extrapolation of Static Free-Field Jet Noise Data</b>		5. Report Date <b>September 1976</b>	6. Performing Organization Code <b>D6-44121-1</b>
		8. Performing Organization Report No.	
7. Author(s) <b>Carl L. Jaeck</b>		10. Work Unit No.	
9. Performing Organization Name and Address <b>Boeing Commercial Airplane Company P.O. Box 3707 Seattle, Washington 98124</b>		11. Contract or Grant No. <b>NAS2-8213</b>	
		13. Type of Report and Period Covered <b>Contract Report</b>	
12. Sponsoring Agency Name and Address <b>National Aeronautics and Space Administration Ames Research Center Moffett Field, California 94035</b>		14. Sponsoring Agency Code	
		15. Supplementary Notes  <b>NASA Project Manager, Adolph Atencio, Jr.</b>	
16. Abstract  <b>A test was conducted in the Boeing Large Anechoic Chamber to (1) determine static jet noise source locations of six baseline and suppressor nozzle models, and (2) establish a technique for extrapolating near-field data into the far field. The test covered nozzle pressure ratios from 1.44 to 2.25 and jet velocities from 412 to 594 m/s at a total temperature of 844 K.</b>			
17. Key Words (Suggested by Author(s)) <b>Jet noise Model scale Suppressor nozzles Noise source locations</b>		18. Distribution Statement  <b>Unclassified-unlimited</b>	
19. Security Classif. (of this report) <b>Unclassified</b>	20. Security Classif. (of this page) <b>Unclassified</b>	21. No. of Pages <b>177</b>	22. Price*

## PREFACE

The work presented in this report has been accomplished by The Boeing Company under a jointly funded contract number NAS2-8213 with NASA Ames Research Center, Moffett Field, California. F. Strout was the Boeing Program Manager and A. Atencio, Jr. was NASA Project Manager. The final report consists of two volumes:

Volume 1-Noise Source Locations and Extrapolations of Static Free-Field Jet Noise  
Data

Volume 2-Forward Speed Effects

## CONTENTS

	Page
SUMMARY .....	1
INTRODUCTION .....	1
ABBREVIATIONS AND SYMBOLS .....	3
TEST DESCRIPTION .....	5
Boeing Large Anechoic Chamber .....	5
Test Hardware .....	5
Instrumentation .....	7
Acoustic Data Reduction .....	8
Test Conditions .....	9
DATA ANALYSIS .....	10
Near-Field Jet Noise Problem .....	10
Proposed Model and Method of Analysis .....	10
15.24-cm RC Nozzle Results .....	12
Annular Nozzle Results .....	14
20-Lobe Nozzle Results .....	15
Annular and 20-Lobe Nozzles With Lined Ejector .....	16
57-Tube Nozzle With Lined Ejector .....	17
CONCLUDING REMARKS .....	19
REFERENCES .....	19

PRECEDING PAGE BLANK NOT FILMED

## TABLES

No.		Page
1	Annular Nozzle Dimensions .....	21
2	Dimensions for 20-Lobe Nozzle .....	21
3	Dimensions for 57-Tube Nozzle .....	22
4	Summary of Microphone Locations .....	23
5	Model Conditions for Static Near-/Far-Field Test .....	24

## FIGURES

No.		Page
1	15.24-cm RC Nozzle .....	27
2	20-Lobe and Annular Nozzles .....	28
3	Lined Ejector for 20-Lobe and Annular Nozzles .....	29
4	57-Tube Composite Nozzle .....	30
5	Lined Ejector for 57-Tube Nozzle .....	31
6	Near-Field Microphone Array .....	32
7	0.6-, 1.5-, and 3-M Sideline Microphone Arrays .....	33
8	Anechoic Chamber With 0.6-, 1.5-, and 5.33-m Sideline Arrays .....	34
9	Multiple Sideline Source Location Technique .....	35
10	Coordinate System .....	36
11	Determination of Apparent Noise Source Locations and Noise Radiation Angles .....	37
12	Deviation of Jet Noise Measurements From the Spherical Divergence/Point Source Assumption .....	38
13	One-Third-Octave-Band SPL Directivities for a 15.24-cm RC Nozzle—NPR = 1.75, $T_T = 884$ K .....	39
14	Peak Noise Source Locations for an RC Nozzle at 900 K Using the Wall Isolation Technique .....	43
15	Comparison of Peak Axial Noise Source Location for a 15.24-cm RC Nozzle Using the Wall Isolation and Multiple Side Techniques .....	44
16	Analytical Prediction of Noise Source Locations for a 15.24-cm RC Nozzle Using the Lu/Berman Flow/Noise Analysis .....	45
17	Correlation of Peak Noise Source Radiation Angle for a 15.24-cm RC Nozzle .....	46
18	Distributed Noise Source Location for a Jet From a 15.24-cm RC Nozzle .....	47
19	OASPL and One-Third Octave-Band SPL Directivity Data for a 15.24-cm RC Nozzle Extrapolated to a 5.33-m Sideline—NPR = 1.44, $T_T = 844$ K .....	51
20	OASPL and One-Third-Octave-Band SPL Directivity Data for a 15.24-cm RC Nozzle Extrapolated to a 5.33-m Sideline—NPR = 1.75, $T_T = 844$ K .....	54

## FIGURES (Continued)

21	OASPL and One-Third-Octave-Band SPL Directivity Data for a 15.24-cm RC Nozzle Extrapolated to a 5.33-m Sideline-NPR = 2.25, $T_T = 844$ K .....	57
22	Measured One-Third-Octave-Band Spectra for a 15.24-cm RC Nozzle Extrapolated to a 15-m Sideline .....	60
23	Comparison of 15-m Sideline Extrapolated Data for the 15.24-cm RC Nozzle and Empirical, Clean, Far-Field Jet Noise Predictions .....	64
24	One-Third Octave Band SPL Directivities for the Annular Nozzle-NPR = 1.44, $T_T = 844$ K .....	68
25	Peak Noise Source Locations for an Annular Nozzle .....	72
26	Peak Noise Source Radiation Angles for the Annular Nozzle .....	74
27	Distributed Noise Source Locations for a Jet From an Annular Nozzle .....	74
28	OASPL and One-Third-Octave-Band SPL Directivity Data for the Annular Nozzle Extrapolated to a 3.0-M Sideline-NPR = 1.44, $T_T = 844$ K .....	77
29	OASPL and One-Third-Octave-Band SPL Directivity Data for the Annular Nozzle Extrapolated to a 3.0-m Sideline-NPR = 1.75, $T_T = 844$ K .....	80
30	OASPL and One-Third-Octave-Band SPL Directivity Data for the Annular Nozzle Extrapolated to a 3.0-m Sideline-NPR = 2.25, $T_T = 844$ K .....	83
31	Comparison of 15-m Sideline Extrapolated Data for the Annular Nozzle and Clean, Far-Field Jet Noise Predictions .....	86
32	One-Third-Octave-Band SPL Directivities for the 20-Lobe Nozzle-NPR = 2.25, $T_T = 844$ K .....	90
33	Peak Noise Source Locations and Radiation Angles for the 20-Lobe Nozzle ..	94
34	Distributed Noise Source Locations for the 20-Lobe Nozzle .....	96
35	OASPL and One-Third-Octave-Band Directivity Data for the 20-Lobe Nozzle Extrapolated to a 3.0-m Sideline-NPR = 1.44, $T_T = 844$ K .....	99
36	OASPL and One-Third-Octave-Band SPL Directivity Data for the 20-Lobe Nozzle Extrapolated to a 3.0-m Sideline-NPR = 1.75, $T_T = 844$ K .....	102
37	OASPL and One-Third-Octave-Band SPL Directivity Data for the 20-Lobe Nozzle Extrapolated to a 3.0-m Sideline-NPR = 2.25, $T_T = 844$ K .....	105
38	Comparison of 15-m Sideline Extrapolation Data for the 20-Lobe Nozzle and Clean, Far-Field Jet Noise Predictions .....	108
39	Ejector Performance With Annular and 20-Lobe Nozzles .....	112
40	One-Third-Octave-Band SPL Directivities for the Annular Nozzle With Lined Ejector-NPR = 1.44, $T_T = 844$ K .....	114
41	Peak Noise Source Locations for the Annular Nozzle With Lined Ejector ....	119
42	Peak Noise Source Radiation Angles for the Annular Nozzle With Lined Ejector .....	119
43	Distributed Noise Source Locations for the Annular Nozzle With Lined Ejector .....	120
44	OASPL and One-Third-Octave-Band SPL Directivity Data for the Annular Nozzle With Lined Ejector Extrapolated to a 3.0-m Sideline-NPR = 1.44, $T_T = 844$ K .....	123
45	OASPL and One-Third-Octave-Band SPL Directivity Data for the Annular Nozzle With Lined Ejector Extrapolated to a 3.0-m Sideline-NPR = 1.75, $T_T = 844$ K .....	126

## FIGURES (Concluded)

46	OASPL and One-Third-Octave-Band SPL Directivity Data for the Annular Nozzle With Lined Ejector Extrapolated to a 3.0-m Sideline-NPR = 2.25, $T_T = 844$ K .....	129
47	One-Third-Octave-Band SPL Directivities for the 20-Lobe Nozzle With Lined Ejector-NPR = 2.25, $T_T = 844$ K .....	132
48	Peak Noise Source Locations for the 20-Lobe Nozzle With Lined Ejector .....	136
49	Peak Noise Source Radiation Angles for the 20-Lobe Nozzle With Lined Ejector .....	139
50	Distributed Noise Source Locations for the 20-Lobe Nozzle With Lined Ejector .....	138
51	OASPL and One-Third-Octave-Band SPL Directivity Data for the 20-Lobe Nozzle With Lined Ejector Extrapolated to a 3.0-m Sideline-NPR = 1.44, $T_T = 844$ K .....	141
52	OASPL and One-Third-Octave-Band SPL Directivity Data for the 20-Lobe Nozzle With Lined Ejector Extrapolated to a 3.0-m Sideline-NPR = 1.75, $T_T = 844$ K .....	144
53	OASPL and One-Third-Octave-Band SPL Directivity Data for the 20-Lobe Nozzle With Lined Ejector Extrapolated to a 3.0-m Sideline-NPR = 2.25, $T_T = 844$ K .....	147
54	Ejector Performance With 57-Tube Nozzle .....	150
55	One-Third-Octave-Band SPL Directivities for the 57-Tube Nozzle With Lined Ejector-NPR = 2.6, $T_T = 844$ K .....	152
56	Peak Noise Source Locations for the 57-Tube Nozzle With Lined Ejector .....	156
57	Peak Noise Source Radiation Angles for the 57-Tube Nozzle With Lined Ejector .....	157
58	Distributed Noise Source Locations for the 57-Tube Nozzle With Lined Ejector .....	159
59	OASPL and One-Third-Octave-Band SPL Data for the 57-Tube Nozzle With Lined Ejector Extrapolated to a 3.0-m Sideline-NPR = 1.44, $T_T = 844$ K ...	161
60	OASPL and One-Third-Octave-Band SPL Data for the 57-Tube Nozzle With Lined Ejector Extrapolated to a 3.0-m Sideline-NPR = 1.75, $T_T = 844$ K ...	164
61	OASPL and One-Third-Octave-Band SPL Data for the 57-Tube Nozzle With Lined Ejector Extrapolated to a 3.0-m Sideline-NPR = 2.25, $T_T = 844$ K ...	167
62	OASPL and One-Third-Octave-Band SPL Data for the 57-Tube Nozzle With Lined Ejector Extrapolated to a 3.0-m Sideline-NPR = $T_T = 844$ K .....	170
63	Comparison of Data Extrapolated to a 15-m Sideline for the 57-Tube Nozzle and Lined Ejector with Clean, Far-Field Jet Noise Predictions .....	173

STATIC AND WIND TUNNEL NEAR-FIELD/FAR-FIELD  
JET NOISE MEASUREMENTS FROM MODEL SCALE  
SINGLE-FLOW BASELINE AND SUPPRESSOR NOZZLES

Volume 1: Noise of Source Locations and Extrapolation  
of Static Free-Field Jet Noise Data

by C. L. Jaeck  
Boeing Commercial Airplane Company

### SUMMARY

A test was conducted in the Boeing large anechoic test chamber (LTC) to study the near-far/field jet noise characteristics of six baseline and suppressor nozzle models. The objectives of the study were to (1) determine the static noise source locations, and (2) establish a technique for extrapolating near-field jet noise measurements into the far field. Test models included a 15.24-cm round convergent nozzle, an annular nozzle with and without a lined ejector, a 20-lobe nozzle with and without a lined ejector, and a 57-tube nozzle with a lined ejector.

The noise source locations were derived from acoustic measurements along multiple sideline locations. The noise source locations were determined to be a function of Strouhal number and a noise source radiation or propagation angle. In the case of the 20-lobe and 57-tube nozzles, the noise source locations were a function of jet Mach number or pressure ratio. The test covered nozzle pressure ratios from 1.44 to 2.25, and jet velocities from 412 to 594 m/s at a total temperature of 844 K.

Analysis techniques were developed to interpret near-field noise data and extrapolate noise measurements from relatively close to the sources to the far field. An empirical correlation was defined that accounts for the deviation from spherical spreading loss in the near field caused by distributed noise sources, nonpoint sources, and pseudosound effects.

### INTRODUCTION

There is presently a worldwide effort to understand and predict the influence of flight on aircraft noise. Since flight testing is very costly, alternate methods to simulate flight effects are being developed by industry and Government. These include wind tunnels, free jets, rotary rigs, and ground vehicles. Agreement and differences between flight data and data from ground facilities have been presented by numerous investigations (refs. 1-4).

Flight effects on engine noise determined from aircraft flyovers are affected by differences in static and flight measurement technique, engine/airframe effects,

propagation path variations, integration times, and contamination by the many engine noise sources. Extrapolation of static data to the flight condition is necessary and requires knowledge of noise source locations to improve the accuracy of static and flight data comparisons.

Flight effects determined from closed test section wind tunnels are affected by reverberation and ambient noise levels, as well as in flow measurement technique. Flight effects determined by free-jet tunnels require knowledge of sound propagation through the free-jet shear layer. The free-jet technique is presently limited to model-scale jets.

Flight effects on engine noise can be determined by testing an engine in a large wind tunnel such as the NASA Ames Research Center's 40- by 80-foot wind tunnel (40 by 80). As described in references 4 and 5, noise measurements are made relatively close to the engine sources. Knowledge of noise source locations, core stretching, and convection effects are necessary to analyze these near-field measurements and define the far-field flight effects.

The noise program conducted by Boeing in the 40 by 80 includes both model nozzle and full-scale engine tests to establish the feasibility of wind tunnel flight effects testing and to define specific flight effects for important engine noise sources. The full-scale test has been completed (ref. 5) and data obtained that define jet and fan noise flight effects for a JT8D-17 engine configured with baseline, 20-lobe ejector/suppressor, and internal mixer hardware. Of necessity, the noise measurements were made relatively close to the sources, similar to model nozzle tests conducted in the Boeing 9- by 9-foot wind tunnel (ref. 6).

The model nozzle program includes acoustic measurements on three sideline locations to establish a correlation between flight effects measured relatively near and far from the jet noise sources. The model nozzles were tested with uniform flow and included a 15.24-cm round convergent, 20-lobe, annular (plug), 20-lobe ejector/suppressor, annular ejector/suppressor, and a 57-tube ejector/suppressor. The model experimental program consisted of: a reverberation test in the 40 by 80 to define optimum nozzle and measurement locations (ref. 7); a noise test in the Boeing anechoic chamber to define static near-field and far-field jet noise relationships under free-field conditions; and a flight effects test in the 40 by 80.

This document describes the static near-field test and subsequent data analysis.

## ABBREVIATIONS AND SYMBOLS

a	speed of sound, m/s
A	area, m <sup>2</sup>
ARC	Ames Research Center
D	diameter, m
f	one-third-octave-band center frequency
FAA-DOT	Federal Aviation Administration, Department of Transportation
L	length, m
LTC	Boeing large anechoic test chamber
M	Mach number
NASA	National Aeronautics and Space Administration
NPR	nozzle pressure ratio
OASPL	overall sound pressure level, dB
1/3 OBSPL	one-third-octave-band sound pressure level, dB
P	pressure, N/m <sup>2</sup>
R	radial distance from sound source to observer, m
RC	round convergent
RH	relative humidity
S	Strouhal number, fD/V
SL	sideline distance, m
SPL	sound pressure level, dB
T	temperature, °C, K
V <sub>j</sub>	fully expanded jet velocity, m/s
X	axial distance from nozzle or ejector exit plane, m

$Y$	radial distance from nozzle centerline, m
$\gamma$	specific heat ratio
$\theta_I$	angle relative to nozzle or ejector exit plane center and inlet axis
$\theta_S$	angle relative to source location and inlet axis
$\lambda$	wavelength, m
$\rho$	density, $\text{kg}\cdot\text{m}^3$
$\rho_I$	fully expanded jet density, $\text{kg}\cdot\text{m}^3$

#### Subscripts

A	ambient
E	extrapolated
eq	flow equivalent
I	inlet
j	jet
M	measured, microphone
S	source
T	total

## TEST DESCRIPTION

### Boeing Large Anechoic Test Chamber Facility

The Boeing large anechoic test chamber consists of an acoustically treated room, 22.9 m wide, 19.8 m long, and 9.1 m high (75 by 65 by 30 ft). The acoustic treatment on the interior surfaces consists of 30.5-cm-square 32-kg/m<sup>3</sup> polyether/polyurethane foam wedges with a depth of 40.6 cm. The foam wedges have been treated with a chemical fire retardant. The chamber provides acoustic data within  $\pm 1$  dB of free field down to 200 Hz.

Room ambient conditions are maintained by inducing 14 200 m<sup>3</sup>/min ventilation airflow with a maximum wind velocity in the microphone arena of 8 km/hr. Intake and exhaust ducts have silencers installed to minimize internal and external extraneous noise sources.

The nozzle exit plane was located 1.8 m out from the nearest wall and 4.6 m above the floor. The nearest sidewall was a distance of 3 m from the nozzle centerline. The air heater for the jetflow is an inline gaseous propane burner capable of operating at pressure ratios up to 4.0, mass flows up to 13.6 kg/sec, and temperatures up to 1100 K. Airflow rates are measured using a critical flow venturi located well upstream of the burner. Mufflers are located between the venturi and burner to reduce this noise source.

### TEST HARDWARE

Six nozzle configurations were tested in the Boeing large anechoic test chamber and included:

- A 15.24-cm round convergent (RC) reference nozzle
- An annular (plug) nozzle
- A 20-lobe nozzle
- An annular nozzle with lined ejector
- A 20-lobe nozzle with lined ejector
- A 57-tube nozzle with lined ejector

The test nozzles have nearly equal flow areas, which are equivalent to a diameter of 15.24 cm. The nozzles are representative of 1/5-scale JT8D and 1/8-scale GE4 (SST) engine nozzle sizes.

### 15.24-cm $V_C$ NOZZLE

The baseline nozzle employed in this test was a 15.24-cm round convergent nozzle as shown in figure 1. The nozzle is 31.4 cm long and has a measured exit flow area of  $180.5 \text{ cm}^2$ . The nozzle contains an internal plug that has a diameter of 5.1 cm and is 16.5 cm long with the trailing edge located 14.9 cm upstream of the nozzle exit. The plug is the downstream centerbody fairing for the model charging station. The nozzle is composed of a series of straight and conical sections as shown in figure 1.

### ANNULAR (PLUG) NOZZLE AND EJECTOR

The annular nozzle has a flow area of  $185.2 \text{ cm}^2$  and a total-to-flow-area ratio of 2.0. The contoured plug, which extends 30.5 cm beyond the nozzle exit plane, forms an annular or throat height of 3.18 cm. A photograph of the annular nozzle and important dimensions are presented in figure 2 and table 1, respectively.

The annular (plug) nozzle was tested bare and with an area ratio 1.8 (ejector exit/flow area) acoustically lined ejector shroud (fig. 3). The lining is 2.0-cm-thick fiberglass contained between the solid outer wall and the perforated face sheet. The stainless shroud is contoured to maintain a constant area (ratio) through the ejector. The shroud has an overall length of 37.8 cm, a throat-to-exit length of 30.5 cm, and an exit diameter of 21.1 cm.

### 20-LOBE NOZZLE AND EJECTOR

This nozzle consists of a plug nozzle with an annular array of 20 lobes, 2.0 cm wide and 4.6 cm high. The 20 lobes encompass a flow area of  $179.9 \text{ cm}^2$  and a total-to-flow-area ratio of 2.7. The contoured plug extends 30.5 cm beyond the nozzle exit plane. The same ejector was used with the 20-lobe and annular nozzle.

Photographs of the 20-lobe nozzle and lined ejector are shown in figures 2 and 3. Important dimensions and geometric descriptions are provided in table 2.

### 57-TUBE EJECTOR/SUPPRESSOR

The 57-tube suppressor nozzle (56 tubes and a center hole) has a geometric-flow exit area of  $163.9 \text{ cm}^2$ . The nozzle area ratio, which is defined as the base area enclosed by the upstream periphery of the outer-tube row divided by the geometric flow area, is equal to 2.9. As shown in figure 4, the outer row consists of small, elliptical, constant cross-section tubes. The remaining tubes are round with round convergent exits, providing efficient internal performance. The baseplate design incorporates a 24.81-cm spherical radius, terminating in the circular central hole. The tube exits are noncoplanar to conform to stowage requirements of an SST suppressor nozzle installation.

The 24-sided, acoustically lined ejector used with the 57-tube nozzle (see fig. 5), has a flat-to-flat dimension across the lined ejector of 24.85 cm and a length of 27.7 cm ( $L/D_{eq} = 1.9$ ).

The ejector has an area ratio of 3.0 (where the ejector area ratio is defined as the cross-sectional area at the ejector throat divided by the primary nozzle exit area). The ejector was mounted 2.0 cm aft of the nozzle exit plane by means of four struts placed at 90° increments around the nozzle body, and located 45° from the nozzle vertical centerline.

The ejector lip consists of a 3.05/1.52-cm inner ellipse extending from the throat to the highlight, and a 1.52/1.26-cm outer ellipse from the highlight outward. The mounting struts attach to this outer portion of the ejector lip.

The lining has a 25% open-area face sheet with a 0.889-cm honeycomb backing, followed by an 8% open-area sheet with a 0.38-cm honeycomb backing, and closing out with a solid backing plate. The lining was tuned to have a flat frequency response between 6.3 and 12.5 kHz.

A summary of important 57-tube nozzle and ejector dimensions is presented in table 3.

## INSTRUMENTATION

### ACOUSTIC INSTRUMENTATION

All acoustic data were monitored by bare (without wind screens) 0.635-cm Bruel and Kjaer condenser microphones having a flat frequency response (after correction) from 50 to 80 000 Hz. A summary of the microphone locations is presented in table 4. Microphones located on the 0.6-m sideline were oriented for grazing incidence and were positioned below the horizontal plane of the nozzle axis. This was done so that microphone mounting hardware would not obstruct the source-receiver propagation paths for the 1.5-, 3.0- and 5.33-m sidelines. The microphones on the 1.5- and 3.0-m sideline locations were positioned for normal incidence and were oriented toward the nozzle exit plane. Photographs of the microphone installations and the anechoic chamber are shown in figures 6, 7, and 8.

For the RC (round convergent) nozzle, microphones were positioned initially on 0.6-, 1.5-, and 5.33-m sideline locations. The 5.33-m sideline array was then repositioned on the 3.0-m sideline for a second series of runs on the RC nozzle and the remainder of the test.

The RC nozzle and three nozzles with lined ejectors were designed with a common nozzle or ejector exit plane location, and all microphones were then positioned relative to an origin at this common nozzle or ejector plane location. In the case of the bare annular and 20-lobe nozzles, the 0.6-m sideline microphone array was shifted 7.62 cm downstream during the test to account for a change in nozzle exit plane location. However, the 1.5- and 3.0-m sideline microphone arrays were not moved, since the maximum error in angular location is 2.8° or less.

The analog data from each microphone was recorded for 20 sec on a 14-channel Ampex Type 1800L tape recorder, 12 microphones at a time. The taped data were reduced later

using a General Radio Model 1921 analyzer. The reduced data were presented in one-third-octave bands from 200 Hz to 80 kHz and stored on digital magnetic tape for subsequent analysis.

Prior to each run series on a nozzle, an "air ball" calibration noise source was used for functional checks of the noise data acquisition instrumentation. The airball (fig. 7) was removed from the chamber prior to jet noise testing.

The frequency response characteristics of the Bruel and Kjaer Model 4135 and 4136 microphones and of the Ampex FR-1800 tape recorder were determined prior to the test.

### FLOW INSTRUMENTATION

All models were tested using the single-flow rig, which contains facility charging station instrumentation rakes for the measurement of total pressure (10) and temperature (10). This facility charging station was located 1.5 m downstream of the burner and 1.5 m upstream of the nozzle. In addition to the facility charging station, all model installations except the 57-tube suppressor nozzle included a model charging station section that contained 10 total pressure and temperature probes.

The annular and 20-lobe nozzles contained two static pressure taps, and each ejector contained three total pressure probes used to determine the ejector inlet or entrainment velocity. The 57-tube suppressor nozzle contained four nozzle baseplate static pressures and four ejector lip static pressures (ejector throat) to define ejector inlet velocity.

### ACOUSTIC DATA REDUCTION

Acoustic data recorded on 14-track analog tape are reproduced and analyzed in one-third-octave bands. The basic analysis system consists of an analog tape reproducer, General Radio Model 1921 one-third-octave analyzer, time code reader, PDP8-1 computer, digital magnetic tape recorder, and associated monitor, control, interface, and peripheral service equipment.

The operator controls the analysis through a teletype keyboard used for entering calibration, frequency response, compensation, and measurement identification information into the computer. The General Radio analyzer includes a bank of 27 one-third-octave-band filters covering the frequency range of 200 Hz to 80 kHz. The filters are calibrated with both sinewave and random noise inputs. The true RMS detector section of the analyzer has a dynamic range of 60 dB and a resolution of +0.25 dB.

Frequency response compensation and sensitivity calibration information are added to the one-third-octave-band data in the computer and the output is a digital magnetic tape in a format compatible with existing CDC-6600 computer software.

All components of the recording and reduction system are periodically certified to manufacturer's specifications by the Boeing Flight Test Calibration Laboratory.

## TEST CONDITIONS

Five pressure ratios of 1.44, 1.58, 1.75, 1.965, and 2.25 were run for each nozzle configuration at a total temperature of 844 K. A few additional runs were conducted for the 15.24-cm RC and 57-tube nozzles. All test runs and corresponding test conditions are summarized in table 5. The jet velocity shown in table 5 and that used in this document is the ideally fully expanded value, which is calculated as follows:

$$V_j = 23.95 \left\{ \left( \frac{\gamma}{\gamma-1} \right) T_T \left[ 1 - \left( \frac{1}{\text{NPR}} \right)^{\frac{\gamma-1}{\gamma}} \right] \right\}^{1/2} \text{ m/s}$$

where  $\gamma$  is computed for products of combustion and hot flow, but at nozzle static conditions (ref. 8).

During the test, it became apparent that the two hygrometers in the anechoic chamber were functioning erratically. In order to provide accurate humidity and ambient temperature data, a psychrometer was utilized in addition to the two hygrometers. Ambient temperature and relative humidity values are presented in table 5.

## DATA ANALYSIS

### NEAR-FIELD JET NOISE PROBLEM

The jet noise generation and propagation problem can be broken into three regions: the flow field, the near field, and the far field. Siddon (ref. 9) defines the near field as the region from the line of maximum shear to the location where spherical divergence or 6 dB per doubling of distance begins. The near-field pressure fluctuations are composed of two parts: (1) the pseudosound or nonpropagating part, and (2) the acoustic or propagating fraction.

The near-field jet noise cannot be represented by a single-point source or by a series of point sources whose location is only a function of frequency. Assuming the jet can be represented by a cylindrical source, the noise at a given frequency is generated throughout the finite length cylindrical noise source and radiates sound in a highly directional manner. In a jet there are the additional effects of sound source convection and refraction, which influence sound directivity.

### PROPOSED MODEL AND METHOD OF ANALYSIS

A proposed model and method of analysis has been suggested by Strout (refs. 5 and 10). The jet noise generated at a given frequency is represented by a series of directional point sources. The sound radiates at a fixed angle relative to the jet axis and propagates from the source location in the jet through the near field and into the far field. The level is reduced by spherical divergence (with near-field corrections) and atmospheric absorption. The sound level distance relationship is assumed to be the same for all radiation or emission angles, excluding atmospheric absorption effects. This assumption of a constant SPL increment is based on the following considerations:

1.  $20 \log SL_2/SL_1 = \text{CONST}$
2.  $\Delta\text{SPL}$  due to near-field effects at a given frequency and sideline distance are constant
3. The differences in atmospheric attenuation over any two propagation paths is small (between the same two sidelines)

The latter requirement is not true for high frequencies, where atmospheric attenuation corrections are required.

The noise source locations and radiation angles are defined by acoustic measurements on multiple sidelines. The analysis is accomplished by plotting the one-third-octave-band SPL directivities for the multiple sidelines at a given jet condition as shown in figure 9. The four points indicated by the angles for the peak or maximum one-third-octave-band SPL specify a noise propagation path. Assuming the delta SPL between the peak for the far field and a near-field sideline remains constant for all locations or propagation paths, the nonpeak emission angles are defined in figure

9 by the dashed lines. To illustrate the procedure, assume an angle of 90° on the 5.33-m sideline and then add the ΔSPL between the peak 5.33-m and 3-m sidelines to the SPL at 90° on the 5.33-m sideline. One then determines where this corrected SPL intersects the 3-m sideline, which is 93° for this case. This procedure is repeated for the remaining two sidelines to complete the tracing of the noise propagation path. This procedure is then repeated for other propagation paths to determine the variation of source location as a function of noise radiation angle for a given frequency or Strouhal number.

The procedure illustrated in figure 9 is repeated for each frequency to define a series of emission angles and apparent axial source locations for each jetflow condition. The noise sources were assumed to be located radially along a line of maximum shear, or at a radial position (Y) equal to the nozzle radius as shown in figure 10. The source locations and emission angles for a given frequency or Strouhal number are shown in figure 11.

Application of the apparent jet noise source locations to the extrapolation of near-field data requires the assumption of a noise/distance scaling relationship, namely spherical divergence. Near a jet this assumption breaks down due to:

1. Pseudosound (nonpropagating), which increases the noise above spherical divergence close to the jet source region.
2. Noise generation and sources are distributed over a volume in the jet. This is related to the differences between a point and line source as discussed by Rathe (ref. 11). The sound emitted by a line source falls off by a 10-log relation and then by a 20-log relation. The sound attenuation with distance is a function of the sideline distance and the position of the observer (i.e., the viewing angle, which spans the length of the source). The results of Rathe, though not directly applicable, are informative.

To account for the two effects, peak near-field noise levels at varying frequencies or wavelengths were correlated as presented in figure 12. The correlation indicates the deviation of the peak near-field one-third-octave-band SPL from the peak far-field SPL extrapolated to the near-field location using spherical divergence. This near-field noise increment was found to be a function of the following correlation parameters:

1. SL/D, sideline distance to jet diameter
2.  $(R/\lambda)(V_j/a_A)$ , ratio of path length from noise source location to observer (R) to the wavelength ( $\lambda$ ) multiplied by the acoustic Mach number ( $V_j/a_A$ )

The dimensionless ratio group (item 2) can be transformed as follows:

$$\left[ \frac{R}{\lambda} \right] \left[ \frac{V_j}{a_A} \right] = \left[ \frac{rD_j}{V_j} \right] \left[ \frac{R}{D_j} \right] \left[ \frac{V_j}{a_A} \right]^2$$

The section of the curves to the right of the peak is attributed to the distributed source effects, while the left part of the curve is due to near-field effects. The near-field and

distributed source effects on the acoustic spreading loss diminish for sideline distances ( $SL/D_j$ ) greater than 20 diameters.

### 15.24-cm RC NOZZLE RESULTS

The simplest of the nozzle configurations tested was the round convergent (RC) nozzle. Jet noise was measured at up to 12 angles on each of four sidelines to accurately define the one-third-octave directivities as shown in figure 13. The jet noise at the low frequencies peaks at angles close to the jet axis, while the high frequencies peak at angles away from the jet axis. The peak low-frequency noise appears to be generated and located well downstream from the nozzle exit. Peak axial noise source locations have been previously determined by numerous techniques, one of which is the wall isolation technique of reference 12.

The peak sound power source location data of McGregor and Simcox (ref. 12) have been normalized and are displayed in figure 14. The peak axial noise source locations that were determined for an RC nozzle at supersonic conditions are indicated by the solid lines. The dashed lines at the subsonic conditions are extrapolations of the supersonic data. The source locations are observed to be a strong function of nozzle pressure ratio or Mach number.

The wall isolation results from Reference 12 are compared with peak noise source locations from the multiple sideline technique in figure 15. Although the two sets of results are nearly equal in magnitude, the detail trends are quite different. The noise source locations from the multiple sideline technique do not stratify with Mach number and exhibit a flat region that indicates most of the peak noise is generated at the tip of the potential core at  $X/D = 5.0$ .

In order to verify the multiple sideline results, peak power source locations for the RC nozzle were determined analytically using the Lu-Berman flow/noise analysis (refs. 13 and 14). The analytical results are presented in figure 16 for nozzle pressure ratios of 1.44 and 2.25. The analytical results collapse into a single line, and also show the concentration of peak noise sources at or slightly downstream from the tip of the potential core. The analytical results indicate the high frequencies are located closer to the nozzle exit than shown by the measurements. This is due to the analytical method, which at present does not include the sound propagation internal to the jet. The analytical results confirm the multiple sideline technique. Further, the multiple sideline technique appears to provide greater resolution of source locations than the wall isolation technique.

Peak noise source locations are only one piece of information required in the near-field/far-field analysis of jet noise data. Knowledge of the noise source radiation angles is also required to perform a near-to-far-field extrapolation of jet noise results. The peak noise radiation angles, like the noise source locations, were found to correlate with Strouhal number as presented in figure 17. The peak OASPL has a sound radiation angle of  $141^\circ$  as shown in figure 17, which is representative of a Strouhal number of 0.3 and an apparent noise source location of  $X/D = 5.0$ .

The peak noise source locations and radiation angles only partially define the noise generation in the jet. The noise at one frequency or Strouhal number is generated throughout the jet, and different parts of the jet radiate at different angles, as was shown earlier in figure 11. The previous correlations for peak noise source locations and radiation angles as functions of Strouhal number suggest a means of correlating the distributed noise source effects. The nondimensional noise source locations ( $X_S/D$ ) can be correlated as a function of radiation angle ( $\theta_S$ ), but at constant Strouhal number ( $fD/V$ ), as shown in figure 18, using the procedures and results of figures 9 and 11.

The distributed source location correlations indicate that for a given nozzle diameter, if the jet velocity and frequency are both doubled, the source locations ( $X_S/D$ ) and radiation angles for the two cases are equal. This occurs because as frequency is increased, the noise sources tend to shift toward the nozzle exit, but as velocity is increased the jet core length is increased and the noise sources tend to move downstream.

These distributed noise source correlations indicate that the noise generation region at a given Strouhal number is limited in size, and extends from a point just downstream of the nozzle exit to a point near the end of the jet plume. These results are consistent with jet noise and flow phenomena.

The results of figures 12 and 18 plus the atmospheric attenuation from ARP 866 (ref. 15) can be used to extrapolate jet noise data measured in the near field into the far field as follows:

$$1/3 \text{ OBSPL (far field)} = 1/3 \text{ OBSPL (near field)}$$

$$-20 \log_{10} \frac{R_{S,E}}{R_{S,M}} - \frac{\Delta \text{dB}}{305} \left[ \frac{R_{S,E} - R_{S,M}}{305} \right] + \Delta \text{SPL}_1 - \Delta \text{SPL}_2$$

where

$R_{S,M}$  = acoustic path length from source location to near-field microphone, m

$R_{S,E}$  = acoustic path length from source (through near-field location) to far-field sideline, m

$\Delta \text{dB}/305$  = atmospheric attenuation (ARP 866), dB/305 m

$\Delta \text{SPL}_1$  = from figure 12, where  $R = R_{S,M}$  and  $SL = SL_M$

$\Delta \text{SPL}_2$  = from figure 12, where  $R = R_{S,E}$  and  $SL = SL_E$

Jet noise measurements on 0.6-, 1.5-, and 3.0-m sidelines have been extrapolated to 5.33 m and compared with measurements on a 5.33-m sideline in figures 19, 20, and 21 for pressure ratios of 1.44, 1.75, and 2.25. The measured and extrapolated OASPL and one-third-octave SPL directivities are in good agreement. To further test the extrapolation procedure, the data from the four sideline locations have been extrapolated to a 15-m far-field location ( $R_E/D_j \geq 100$ ) and compared on a spectral basis as shown in figure 22. Again, the data sets are in good agreement.

Data from the 5.33-m sideline extrapolated to 15 m are compared with an empirical, far-field, "clean," shock-free jet noise prediction procedure (ref. 16) in figure 23. The good agreement in the low frequencies indicates an absence of burner can and combustion related noise. The difference between the data and predictions in the high frequency is assumed to be due to the presence of increased turbulence due to the internal upstream struts, possible flow separation on the plug, and velocity profile distortion by the plug. The effect of an outer high-velocity region in the jet produces low-frequency suppression, and high-frequency noise increases (see refs. 17 and 18). These effects are evident in the data/prediction comparison at a pressure ratio of 2.25. At an NPR = 2.25 some of the high frequency differences are due to shock-cell-related phenomena.

The analysis of the RC nozzle jet noise data confirms:

- The multiple sideline technique for noise source locations
- Correlations of noise source locations and radiation angles
- The near-field/far-field extrapolation procedure for jet noise

However, further confirmation of the data analysis techniques and near-field/far-field extrapolation procedures is required for more complex nozzles and jet flow fields, which will now be provided with the analysis of data from:

- The annular (plug) nozzle with and without lined ejector
- The 20-lobe (plug) nozzle with and without lined ejector
- The 57-tube composite nozzle with lined ejector

### ANNULAR NOZZLE RESULTS

The one-third-octave directivities and source locations for the annular nozzle at an NPR = 1.44 are presented in figures 24 to 27. The peak axial noise source locations and radiation angles that are displayed in figures 25 and 26 exhibit a gradual falloff with Strouhal number. This differs from the peak source location distribution observed for the RC nozzle. The data, however, do correlate with distance ( $X/D_{eq}$ ) and Strouhal number, where  $D_{eq}$  in each case is the equivalent flow diameter.

The measured noise data for the annular nozzle on the 0.6- and 1.5-m sidelines were extrapolated to the 3.0-m sideline using the results of figure 12 and the distributed source locations shown in figure 27. The extrapolated OASPL and one-third-octave-band SPL's are observed to be in good agreement with the measured results, as shown in figures 28, 29, and 30 for NPR = 1.44, 1.75, and 2.25.

The measured annular nozzle results were also extrapolated to the far-field 15-m location and compared with the empirical, "clean," far-field RC nozzle jet noise predictions as presented in figure 31. The annular nozzle compared to the RC nozzle

predictions show low-frequency noise suppression and high-frequency noise generation. The low frequencies are suppressed as a result of the larger nozzle diameter, which results in increased air entrainment and a velocity profile distortion. The high-frequency noise increases as a result of a frequency shift due to noise scaling with annulus height rather than equivalent flow diameter.

## 20-LOBE NOZZLE RESULTS

A 20-lobe nozzle with a centerbody was tested in this study as one example of a suppressor nozzle. The multilobe nozzle is used to break up a large jet into smaller elements with smaller potential cores and noise sources located much closer to the nozzle exit. The jet from a multilobe or multitube nozzle consists of three regions:

- The premerged region where the elemental jets exist but are entraining ambient air
- The transition region where the high velocity hot jets interact and mix with the cool, low-velocity, ambient air
- The postmerged region that acts like a new jet having the properties of a fully mixed jet but with a lower velocity and temperature than the original jet

Low-frequency jet noise suppression is achieved through the lower postmerged velocity. The multielements or premerged jets produce a frequency shift and a noise increase in the high frequencies.

One-third-octave-band directivities, noise source locations, and radiation angles for the 20-lobe nozzle are presented in figures 32 to 34. The peak noise source locations stratify with jet velocity as shown in figure 33. The jet exit or premerged normalizing parameters selected produce a collapse of the data in the high-frequency region. No single set of normalizing conditions will collapse the premerged, transition, and postmerged source locations. The peak noise source radiation angles do correlate with the use of a single parameter; namely, jet exit Strouhal number.

The distributed source results shown in figure 34 were used to extrapolate data from the near field into the far field as presented in figures 35, 36, and 37. The agreement between the extrapolated and measured data on both an overall and spectral basis is excellent.

Figure 38 shows the measured data for the bare 20-lobe nozzle at a pressure ratio of 1.75 extrapolated to a 15-m sideline, and compared with pre- and postmerged empirical jet noise predictions. The data collapse is excellent and the postmerged prediction is in good agreement with the data. The postmerged jet conditions for the predictions were based on one-dimensional ejector calculations with the following assumptions:

- The air entrained by a multilobe/tube nozzle is not affected by a lossless, frictionless ejector with a diameter equal to that of the nozzle exterior
- The flow is one-dimensional, with constant and equal gas properties

The one-dimensional ejector calculations solve the equations of continuity, momentum, and energy to obtain the ejector entrained airflow and velocity, as well as the fully mixed conditions at the ejector exit.

The premerged predictions are based on the assumption of 20 equivalent, isolated, noninteracting jets. The difference between the data and predictions at angles of 140° and 160° is an indication of the effect of the jet interaction and ambient air entrainment on jet noise. The agreement between the predictions and data at the very high frequencies indicates presence of the elemental jets, since this noise is generated at or near the nozzle exit before any interaction or mixing occurs.

This completes the analyses of the three "bare" nozzles. The analyses of the annular and 20-lobe nozzles with a lined ejector follows.

### ANNULAR AND 20-LOBE NOZZLES WITH LINED EJECTOR

A simple method of reducing the exhaust noise of a jet is to place a shield or ejector immediately downstream of the nozzle, but surrounding the jet. The ejector allows entrainment of ambient air and shields or absorbs the high-frequency noise. The ejector may produce thrust augmentation at takeoff, but added weight and drag penalize aircraft cruise performance.

The annular and 20-lobe nozzles were tested with the same lined ejector as described in an earlier section. The results of the analyses are presented in figures 39 through 53. To determine ejector performance, total and static pressure in the entrained airstream were measured. These measurements are presented in figure 39 and compared with ideal one-dimensional ejector calculations. The measured ejector inlet Mach number for the 20-lobe nozzle approaches the predictions, while the annular nozzle inlet Mach number is significantly lower. These differences are due to deviations in the actual ejector exit velocity profile from the flat, fully mixed profile used in the predictions.

The calculated, fully mixed, ejector exit pressure ratio and total temperature, and the ejector entrained airflow are displayed in figure 39. The entrained airflow for this area ratio 1.8 ejector is equal to 50% of the jetflow rate and results in a fully mixed or postmerged velocity ( $V_{\text{mixed}}/V_j$ ) of 0.68.

The measured and extrapolated one-third-octave-band directivities and noise source distributions for the annular nozzle with lined ejector are presented in figures 40 to 46. The noise source characteristics for the 20-lobe nozzle with ejector are shown in figures 48 to 50. The noise source locations indicated are measured relative to the ejector exit. The normalizing parameters have been based on nozzle exit conditions. In general, the ejector tends to shift the high-frequency noise sources closer to the nozzle exit, but the changes are small.

The extrapolated one-third-octave-band directivities are in good agreement for all frequencies and pressure ratios for both nozzles, as shown in figures 44 to 46 and 51 to 53.

## 57-TUBE NOZZLE WITH LINED EJECTOR

The 57-tube suppressor was developed during the FAA-DOT Phase II program as a jet noise suppression system for an SST turbojet engine. This system was considered the best design to provide low noise levels with high performance. The unequal tube sizes were selected to obtain a desired high-frequency content from the outer tubes to maximize ejector lining effectiveness. Tube shape and spacing were selected to provide ventilation airpaths across the nozzle base to minimize base pressure losses. Also, the tube size and locations were selected to shape the velocity distribution across the array.

The 57-tube suppressor has been statically tested model scale, and full scale on the J-58 engine (refs. 19 and 20). The 57-tube nozzle with ejector was selected for this study as a representative example of a complex flow/noise suppressor system.

The measured and predicted ejector performance is presented in figure 54. The predictions are in good agreement with the measurements. The area ratio 3.0 ejector produces an entrained airflow equal to 110% to 120% of the jetflow and results in a low postmerged velocity ( $V_{\text{mixed}}/V_j$ ) of 0.515.

The acoustic characteristics of the 57-tube composite nozzle with lined ejector are presented in figures 55 to 63. The apparent peak and distributed noise source locations are presented in figures 56, 57, and 58 for pressure ratios of 1.44, 1.75, 2.25, and 2.60. The distributed source locations presented in figure 58, plus the correlation presented in figure 12, were used to extrapolate near-field jet noise measurements into the far field (3-m) as shown in figures 59 to 62. The extrapolated data are in agreement with the measured OASPL's and the one-third-octave-band SPL's.

The measured data extrapolated to a 15-m sideline are compared to predictions in figure 63. The low-frequency postmerged prediction is based on the ejector calculations shown in figure 54. The predictions in the postmerged region underpredict the data at angles of  $100^\circ$  and  $120^\circ$  due to possible burner noise or a non-square-velocity profile. The results from the 20-lobe nozzle and RC nozzle indicated that there was little or no burner/combustion noise present.

The premerged prediction is based on 61 equivalent (outer tube area) tubes and jet exit conditions. The differences between the measured and predicted results indicates the effect of the following suppression mechanisms:

- Fluid shielding
- Interaction of the elemental jets
- Shielding by the ejector
- Absorption of sound by the ejector lining

These effects are maximum at angles near the jet axis, and minimum at  $100^\circ$ . The agreement between sets of extrapolated data and predictions for this complex suppressor provides further verification of the source locations and extrapolation procedure.

## CONCLUDING REMARKS

A study of the near-field/far-field noise characteristics of baseline and suppressor nozzles under static conditions has been completed. This study has:

- Verified the multiple sideline technique for determination of apparent jet noise source locations, on both a peak and distributed basis
- Determined and correlated noise source locations for six baseline and suppressor nozzles operating at subsonic and supersonic Mach numbers
- Established a technique for extrapolating static near-field jet noise measurements into the far field

The techniques established will now be verified for wind tunnel conditions with ambient air velocity. The presence of ambient velocity adds an effect of convection on noise source radiation angles and results in a shifting of the noise sources downstream due to a stretching of the potential core. These effects of forward speed on jet noise were studied by tests in the NASA-Ames 40- by 80-foot wind tunnel. A description of the test and subsequent analysis are presented in volume 2 of this report.

Boeing Commercial Airplane Company  
P.O. Box 3707  
Seattle, Washington 98124  
September 1976

## REFERENCES

1. Bushell, K.: *Measurement and Prediction of Jet Noise in Flight*. AIAA paper 75-461, March 1975.
2. Cocking, B. J.; and Bryce, W. D.: *Subsonic Jet Noise in Flight Based on Some Recent Wind Tunnel Results*. AIAA paper 75-462, March 1975
3. Atencio, A., Jr.; and Soderman, P. T.: *Comparison of Aircraft Noise Measured in Flight Test and in the NASA-Ames 40- by 80-Foot Wind Tunnel*. AIAA paper 73-1047, October 1973.
4. Atencio, A., Jr.: *Wind Tunnel Measurements of Forward Speed Effects on Jet Noise From Suppressor Nozzles and Comparison With Flight Test Data*. AIAA paper 75-870, June 1975.
5. Strout, F. G.: *Flight Effects on Noise Generated by the JT8D-17 Engine in a Quiet Nacelle and a Conventional Nacelle As Measured in the NASA-Ames 40- by 80-Foot Wind Tunnel*. Boeing document D6-42813 (NASA CR-137(97), January 1976.
6. Strout, F. G.: *Summary of Wind Tunnel Jet Noise Tests—Baseline and Suppressor Nozzles*. Boeing document D6-40924, April 1973.
7. Jaeck, C. L.: *Analysis of Data From a Reverberation Test Conducted in the NASA-Ames 40- by 80-Foot Wind Tunnel Including Acoustic Lining on the Internal Tunnel Floor*. Boeing document D6-42566, October 1975.
8. Minassian, B.: *Design Charts for Ramjet Analysis*. Boeing document D-7066 volume 2, 1947 (revised 1956).
9. Siddon, T. E.: *Comments—Noise Mechanisms*. AGARD Conference No. 131, AGARD CP-131, pp A2 to A4.
10. Strout, F. G.: *Procedure for Evaluating Near Field Wind Tunnel Noise Data for Flight Effects*. Boeing document D6-42745TN, November 1975.
11. Rathe, E. J.: "Note on Two Common Problems of Sound Propagation." *J. Sound Vibration*, (1969) 10 (3), pp 472-479.
12. McGregor, G. R.; and Simcox, C. D.: *Location of Acoustic Sources in Jet Flows by Means of "Wall Isolation Technique"*. AIAA paper no. 73-1041, presented at AIAA Aero-Acoustics Conference, Seattle, Washington, October 1973.
13. Lu, H.: *Multiannular Axisymmetric Jet Flow Prediction Using a Two Equation Model of Turbulence*. Boeing document D6-42606, September 1975.

14. Berman, C.; Jaeck, C.; and Lu, H.: *Analytical Prediction of Jet Noise Generation*. Boeing document D6-40614TN, July 1974.
15. Coordination Sheet AMEP-S-461, dated November 27, 1972 by R. M. Masters; and Aerospace Recommended Practice 866 by the Society of Automotive Engineers, Inc., issued August 31, 1964.
16. Jaeck, C.: *Empirical Jet Noise Predictions for Single and Dual Flow Jets With and Without Suppressor Nozzles—Volume I: Single Flow Subsonic and Supersonic Jets*. Boeing document D6-42929, April 1976.
17. Crouch, R. W.; Coughlin, C. L.; and Paynter, G. C.: *Nozzle Exit Profile Shaping for Jet Noise Reduction*. AIAA paper 76-511, July 1976.
18. Packman, A. B.; Kozlowski, H.; and Gutierrez, O.: *Jet Noise Characteristics of Unsuppressed Duct Burning Turbofan Exhaust System*. AIAA paper 76-149, January 1976.
19. Atvars, J.; Wright, C. P.; and Simcox, C. D.: *Supersonic Jet Noise Suppression With Multitube Nozzle/Ejectors*. AIAA paper 75-507, March 1975.
20. Armstrong, R. S.; Atvars, J.; Fullerton, C. R.; and Wright, C. P.: *Noise Suppressor/Nozzle Development—Volume 10: Advanced Suppressor Concepts and Full Scale Tests*. FAA-SS-73-11-10 (Boeing document D6-42445), March 1975 (U.S. Government use only, export restricted).

*Table 1.—Annular Nozzle Dimensions*

Nozzle flow area	186.1 cm <sup>2</sup>
$\frac{\text{Ejector inlet area}}{\text{Nozzle flow area}}$	1.8
Ejector length (nozzle exit to ejector exit)	30.5 cm
Overall ejector length	37.8 cm
Plug diameter	15.3 cm
Annular nozzle diameter	21.7 cm
Ejector exit diameter	21.1 cm

*Table 2.—Dimensions for 20-Lobe Nozzle*

Nozzle flow area	179.9 cm <sup>2</sup>
$\frac{\text{Ejector inlet area}}{\text{Nozzle flow area}}$	1.8
$\frac{\text{Ejector exit area}}{\text{Nozzle flow area}}$	1.8
Ejector length (nozzle exit to ejector exit)	30.5 cm
Overall ejector length	37.8 cm
Diameter of plug	15.2 cm
Maximum diameter of lobes	25.1 cm
Ejector exit diameter	21.1 cm
Lobe width	2.0 cm
Lobe height	4.6 cm
Lobe radius (crown)	1.0 cm

ORIGINAL PAGE IS  
OF POOR QUALITY

*Table 3.—Dimensions for 57-Tube Nozzle*

Nozzle flow area	163.9 cm <sup>2</sup>
Nozzle base area (outer edge of tubes)	475.2 cm <sup>2</sup>
Ejector area	489.0 cm <sup>2</sup>
Ejector length (nozzle exit to ejector exit)	29.7 cm
Ejector set back (tube exit to ejector lip)	2.0 cm
Overall ejector length	27.7 cm
Nozzle base area/nozzle flow area	2.9
Ejector area/nozzle flow area	3.0

	Number
Row 5	24 (elliptical)
4	12
3	12
2	8
1	1

Table 4.—Summary of Microphone Locations

Nozzle description	Sideline distance,	Microphone angles, deg <sup>a</sup>
15.24-cm RC, annular, annular/ejector	0.6	90,100,110,120,130,135,140,145,150,155,160,165
	1.5	90,100,110,120,130,135,140,145,150,155,160,165
	3/5.33	90,100,110,120,130,135,140,145,150,155,160
20-lobe, 20-lobe/ejector, 57-tube/ejector	0.6	90,100,110,115,120,125,130,140,150,155,160,165
	1.5	90,100,110,115,120,125,130,140,150,155,160,165
	3.0	90,100,110,115,120,125,130,140,150,155,160

<sup>a</sup>The microphone angles are relative to the inlet axis and with the origin at the nozzle or ejector exit.

Table 5.—Model Conditions for Static Near-/Far-Field Test

Nozzle description	Flow Area, cm <sup>2</sup>	Run no.	Ambient Temp, °C	Relative humidity, %	Jet total temperature K	Ideal jet velocity, m/s	Nozzle pressure ratio	Measured nozzle flow rate, kg/sec
Round convergent	187.1	3	14.4	32	820	404	1.44	3.38
					830	450	1.57	3.84
					829	500	1.74	4.36
					826	538	1.94	4.95
					834	588	2.23	5.69
		6	15.5	40	839	408	1.44	3.36
					848	454	1.57	3.83
					850	500	1.74	4.33
					861	547	1.936	4.88
		4	14.4	32	859	600	2.25	5.66
					589	447	1.91	5.79
					528	395	1.74	5.49
					480	319	1.48	4.63
Annular/plug	186.1	16	21.1	36	806	402	1.44	3.42
					828	450	1.57	3.94
					823	494	1.74	4.45
					828	536	1.93	4.96
					820	585	2.24	5.84
20-lobe	179.9	13	18.3	37	822	401	1.43	3.37
					833	451	1.57	3.76
					838	501	1.75	4.32
					844	545	1.95	4.93
					848	593	2.23	5.63
Annular/plug nozzle with lined ejector	186.1	9	13.3	54	841	408	1.435	3.44
					849	450	1.57	3.89
					850	503	1.743	4.44
					833	541	1.95	5.11
					844	596	2.26	5.80

Table 5.—(Concluded)

Nozzle description	Flow Area, cm <sup>2</sup>	Run no.	Ambient Temp, °C	Relative humidity, %	Jet total temperature K	Ideal jet velocity m/s	Nozzle pressure ratio	Measured nozzle flow rate, kg/sec
20-lobe nozzle with lined ejector	179.9	10	22.8	24	827	403	1.434	3.44
					835	450	1.567	3.86
					836	495	1.731	4.34
					844	546	1.959	4.88
					843	591	2.231	5.59
57-tube nozzle with lined ejector	163.9	11	22.2	24	826	404	1.434	3.10
					831	449	1.563	3.52
					839	501	1.754	3.94
					833	541	1.95	4.53
					836	588	2.23	5.12
		12	22.2	24	825	632	2.58	5.83

PRECEDING PAGE BLANK NOT FILMED

ORIGINAL PAGE IS  
OF POOR QUALITY

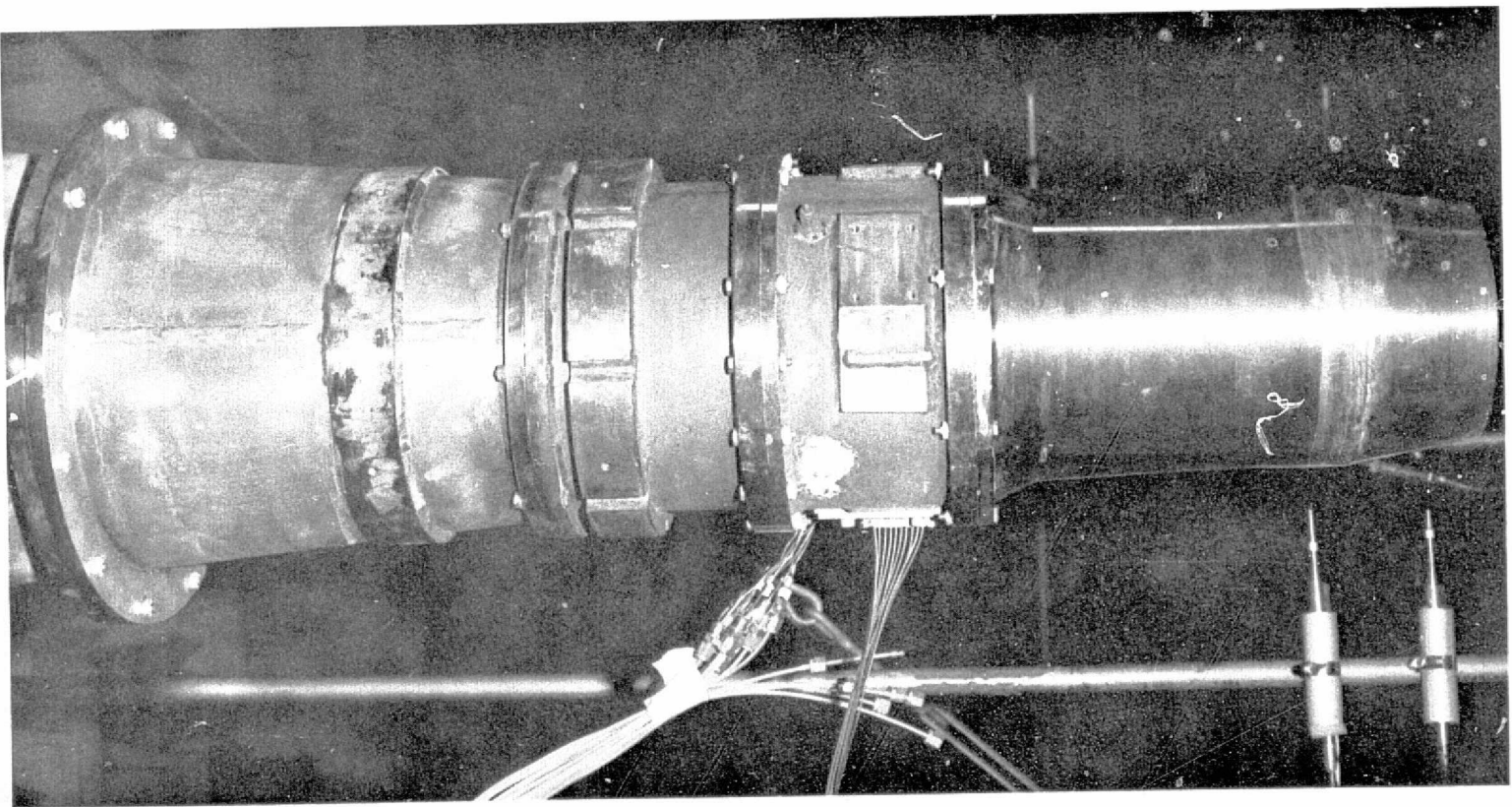
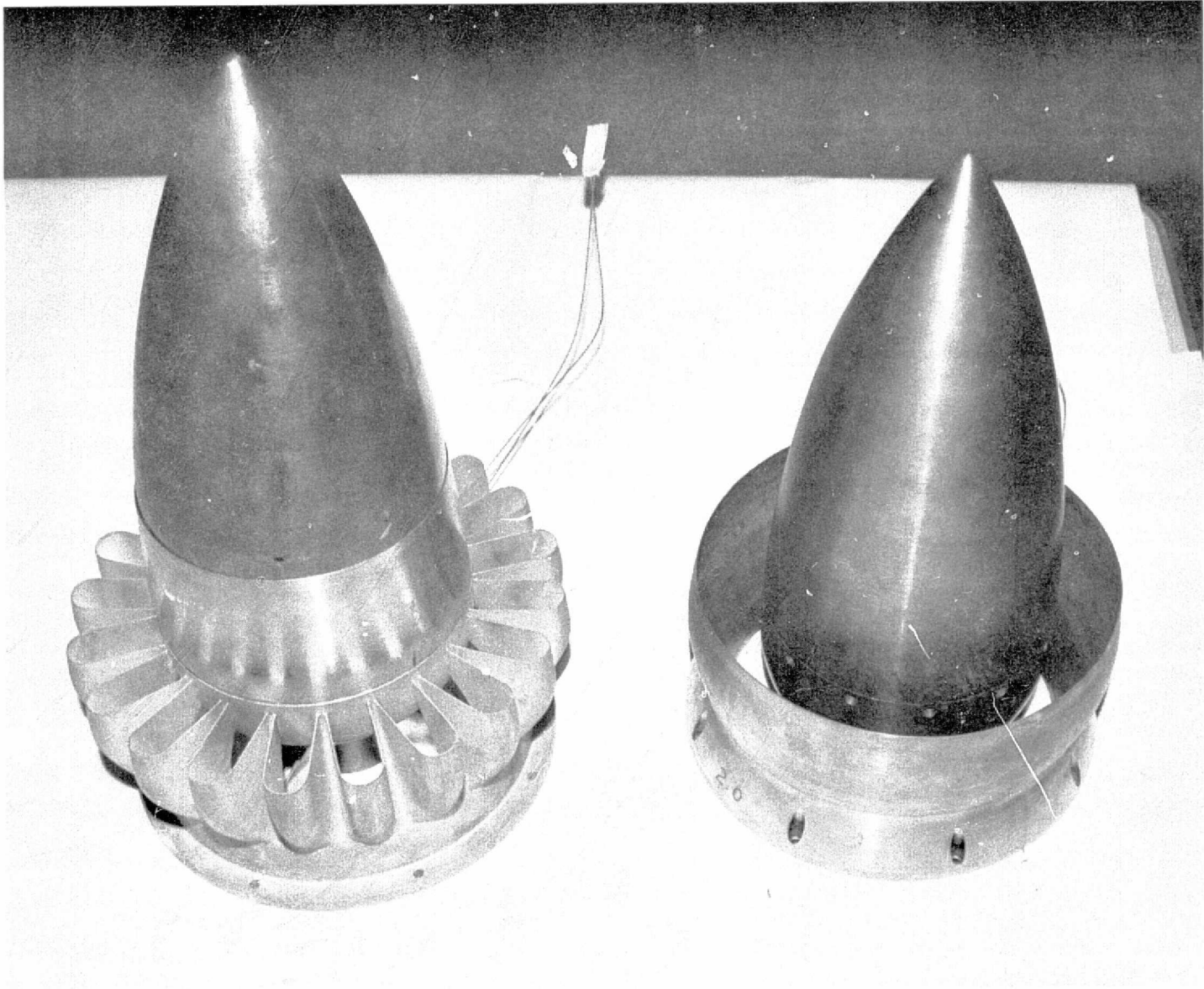


Figure 1.—15.24-cm RC Nozzle



*Figure 2.—20-Lobe and Annular Nozzles*

ORIGINAL PAGE IS  
OF POOR QUALITY

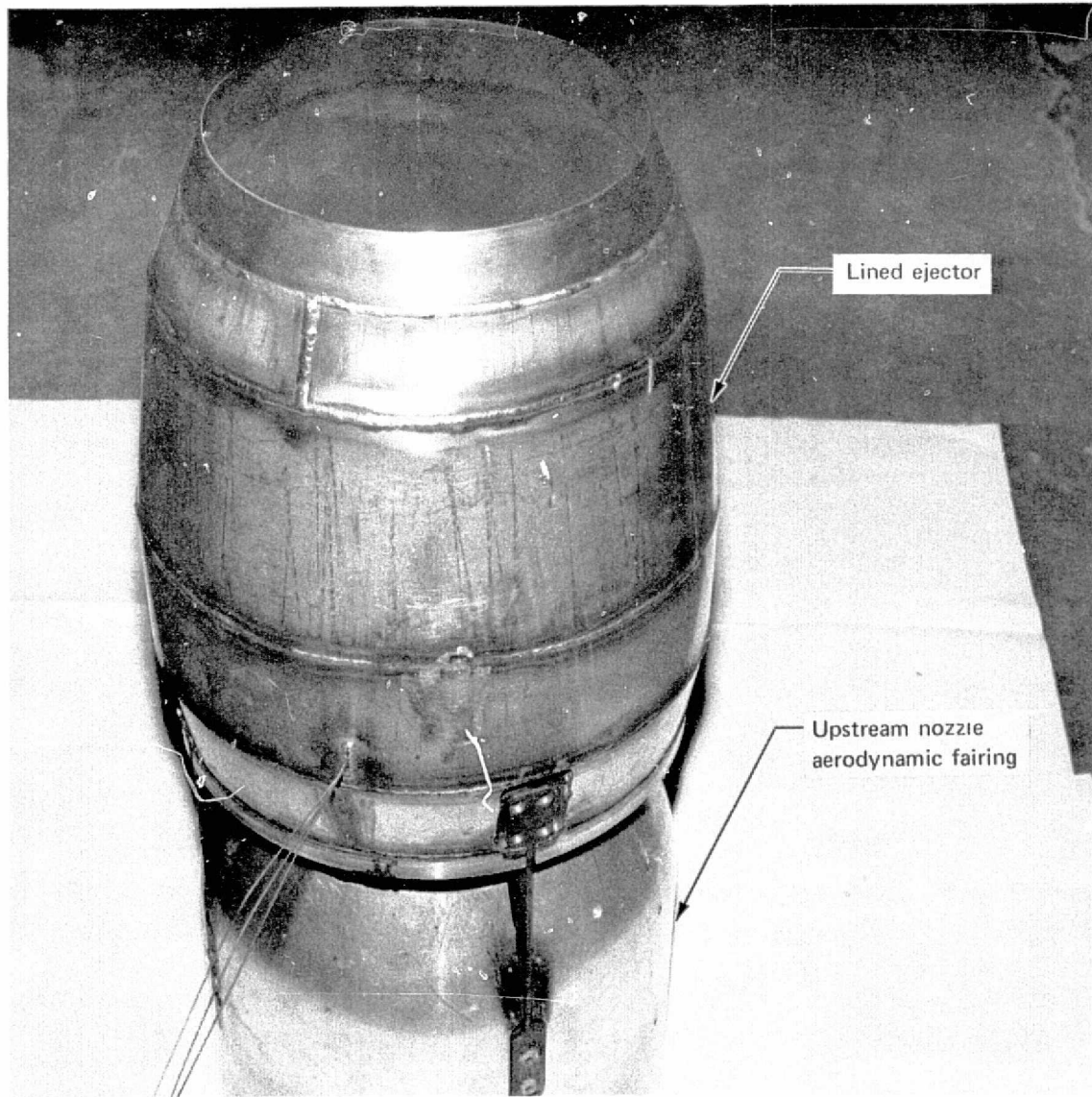
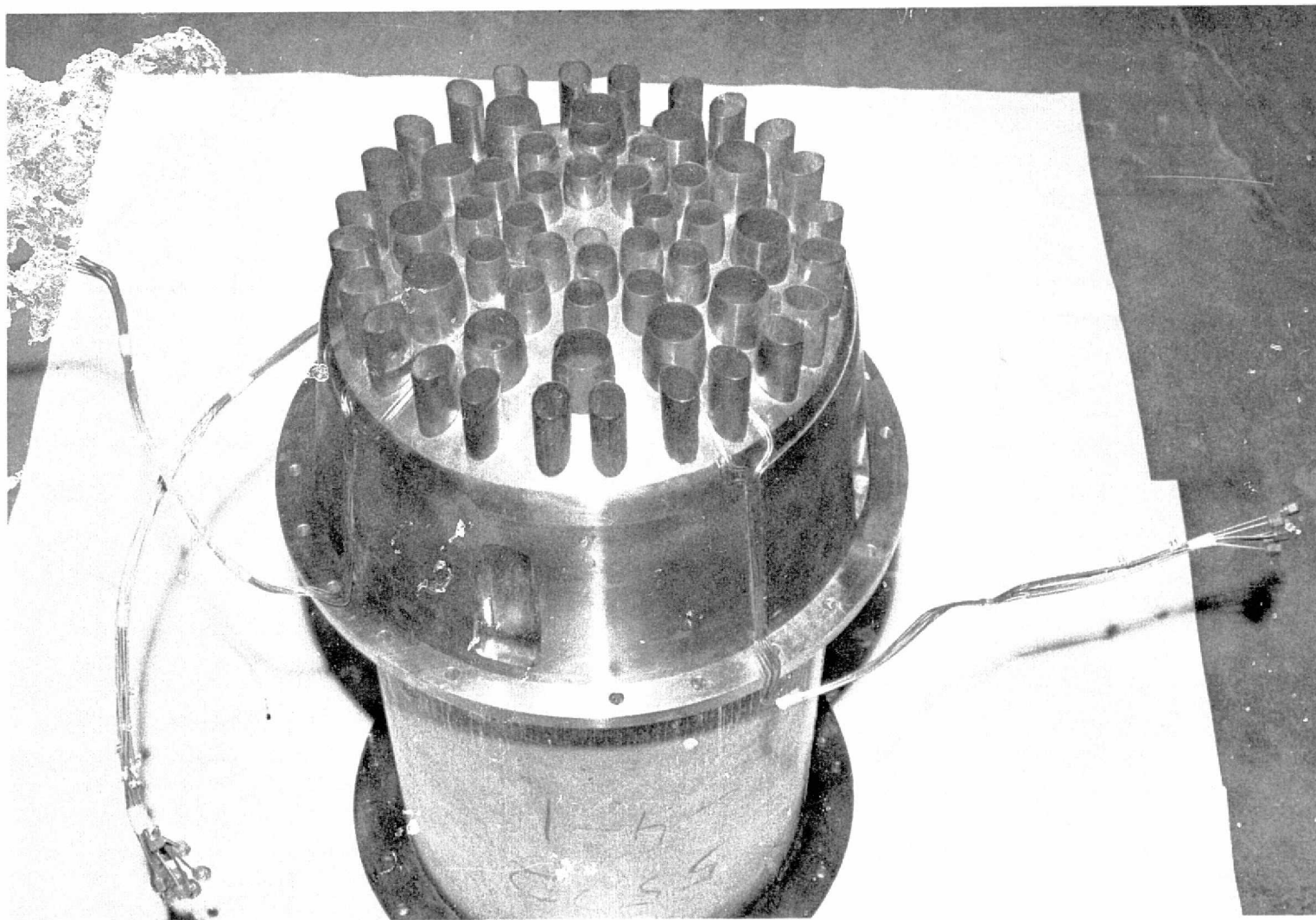


Figure 3.—Lined Ejector for 20-Lobe and Annular Nozzles



*Figure 4.—57-Tube Composite Nozzle*

ORIGINAL PAGE IS  
OF POOR QUALITY

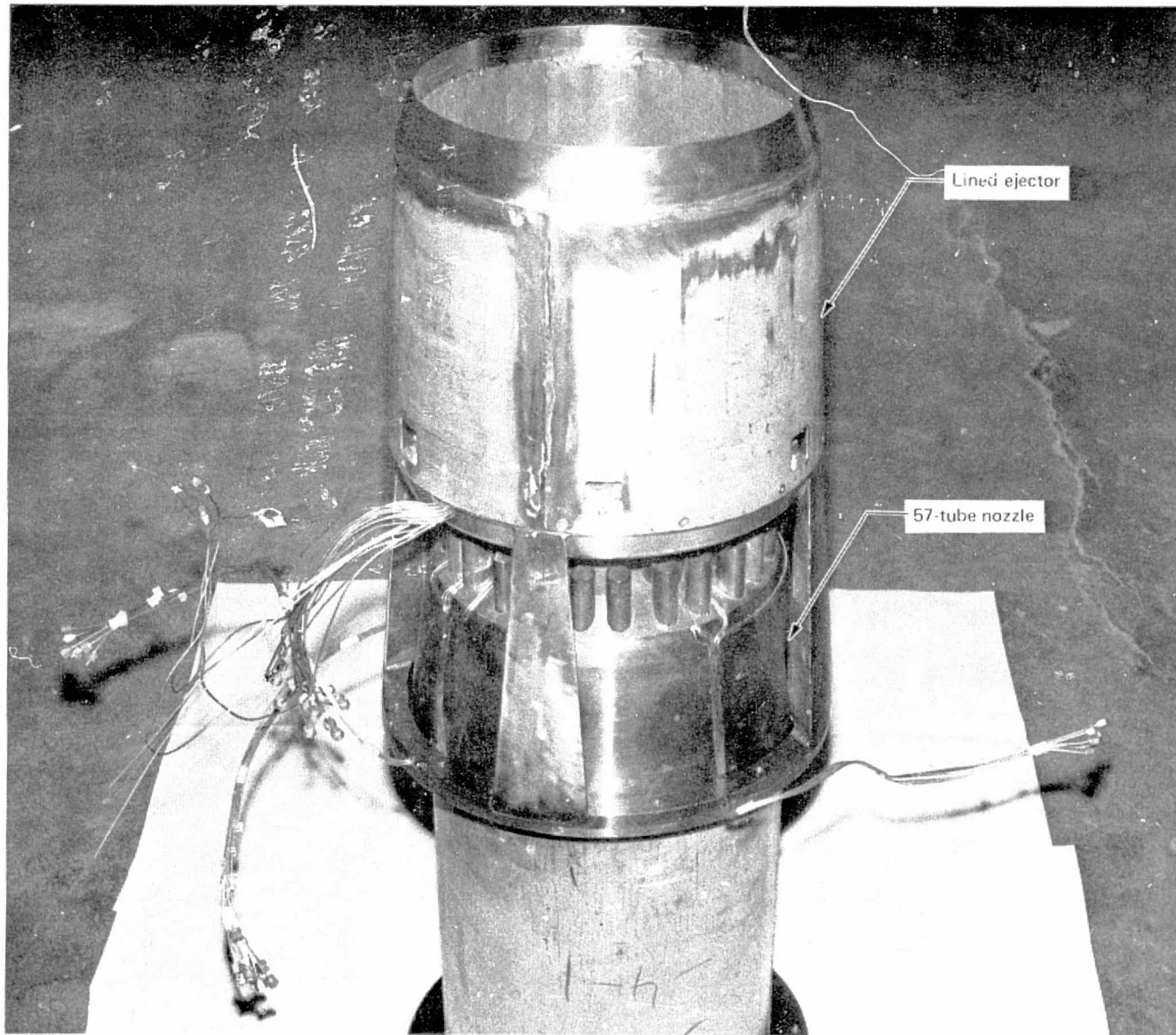
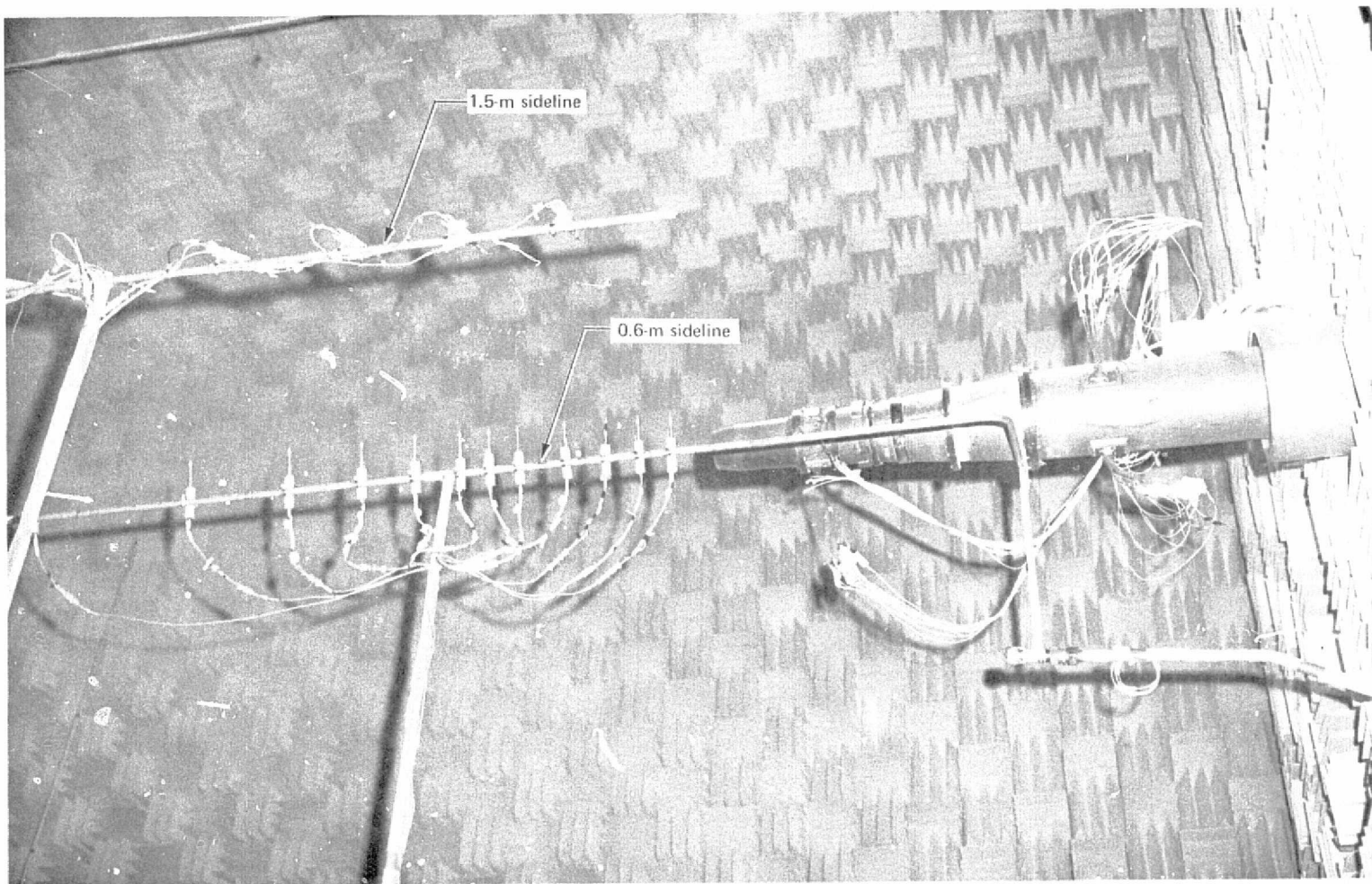
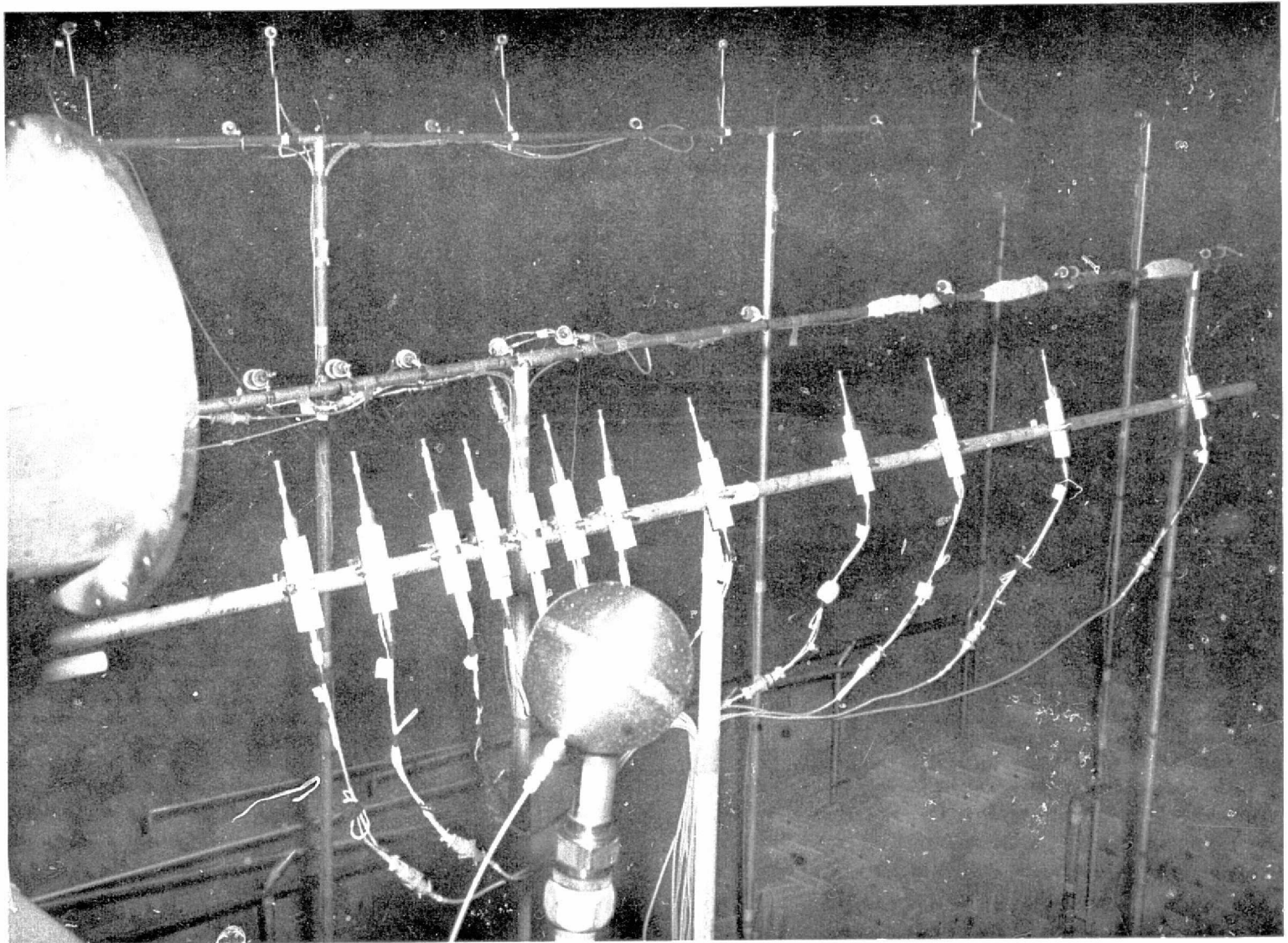


Figure 5.—Lined Ejector for 57-Tube Nozzle



*Figure 6.—Near-Field Microphone Array*

ORIGINAL PAGE IS  
OF POOR QUALITY



*Figure 7.—0.6-, 1.5-, and 3-m Sideline Microphone Arrays*

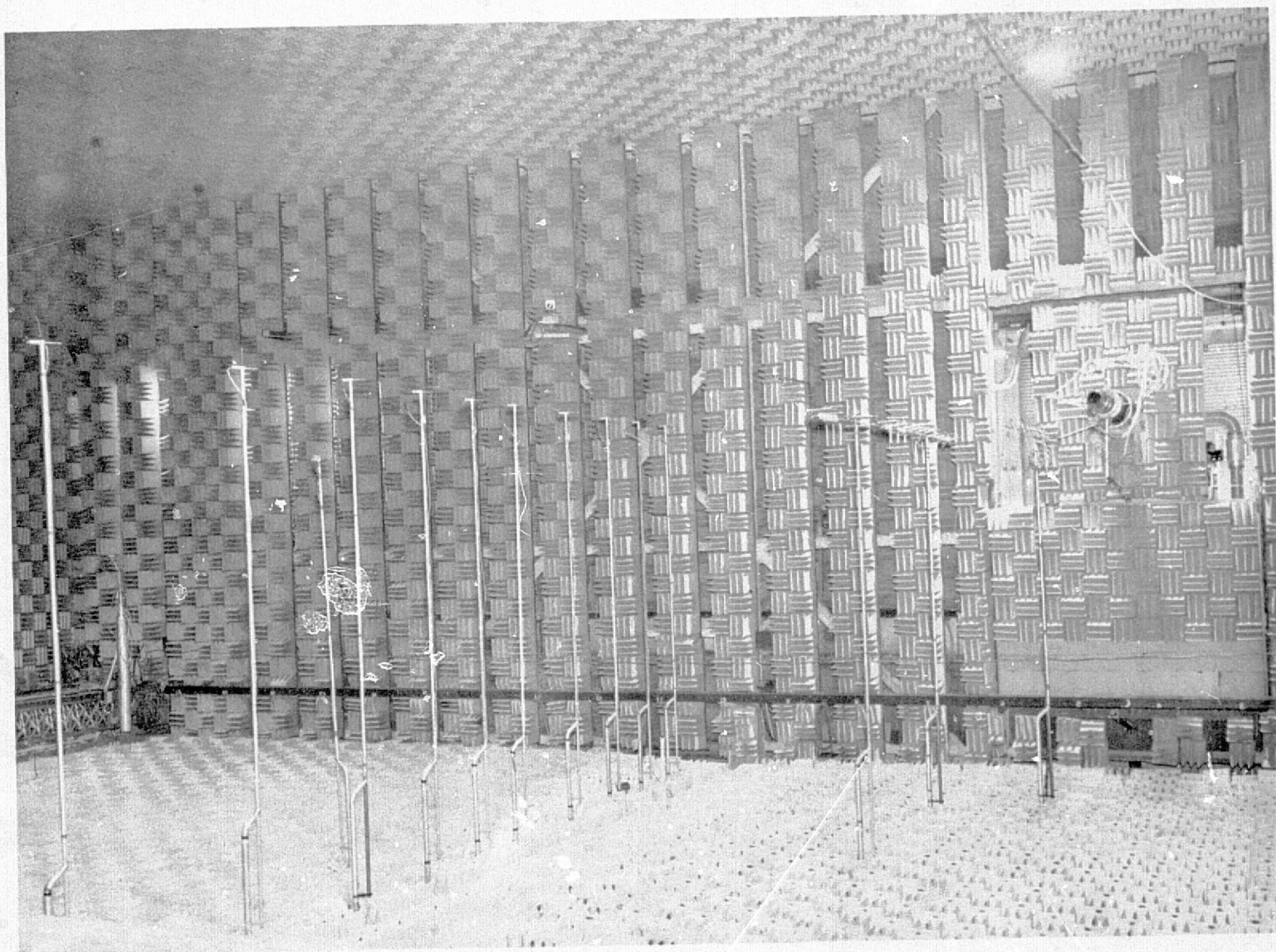


*Figure 8.—Anechoic Chamber With 0.6-, 1.5-, and 5.33-m Sideline Arrays*

- 15.24-cm RC nozzle
- NPR = 1.75
- $T_T = 844$  K
- Frequency = 250 Hz
- $S = 0.075$

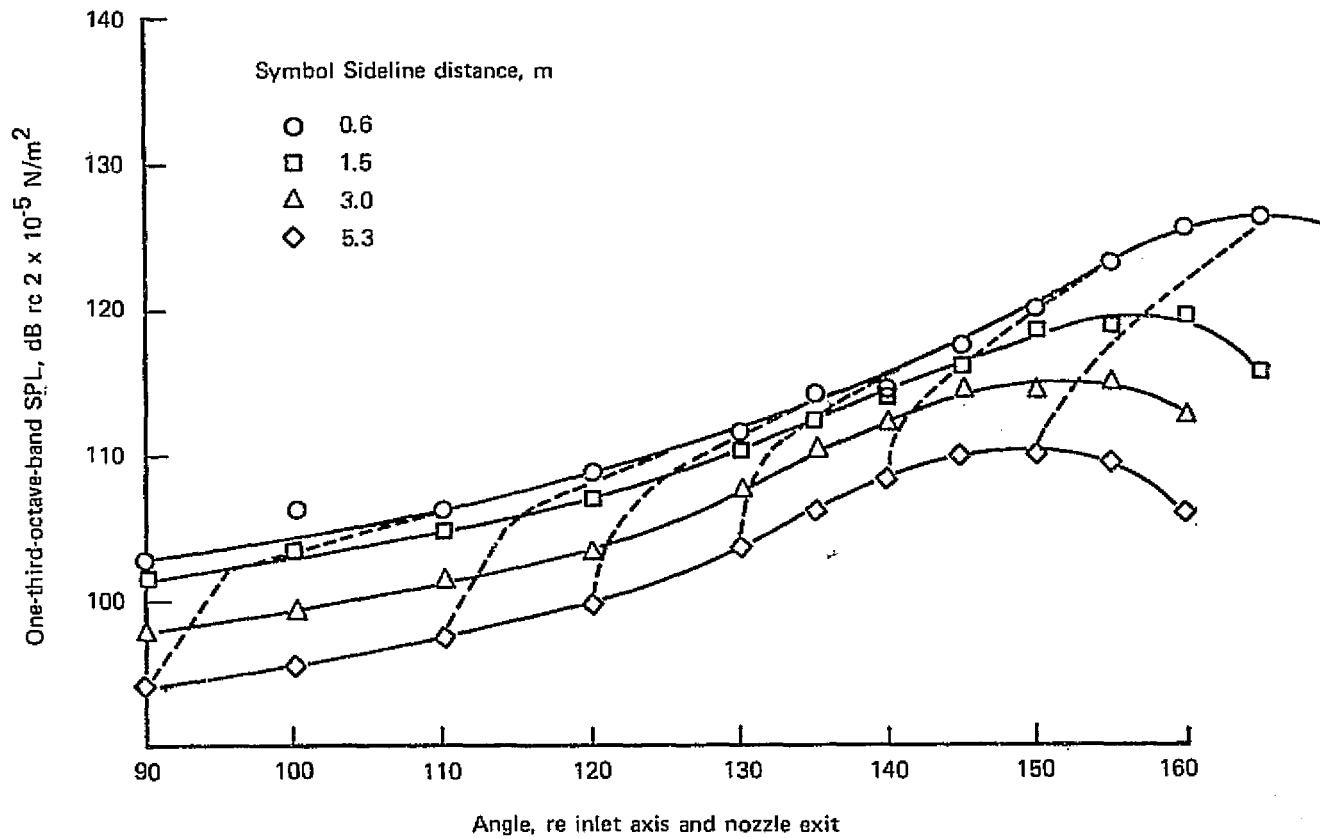


Figure 9.—Multiple Sideline Source Location Technique

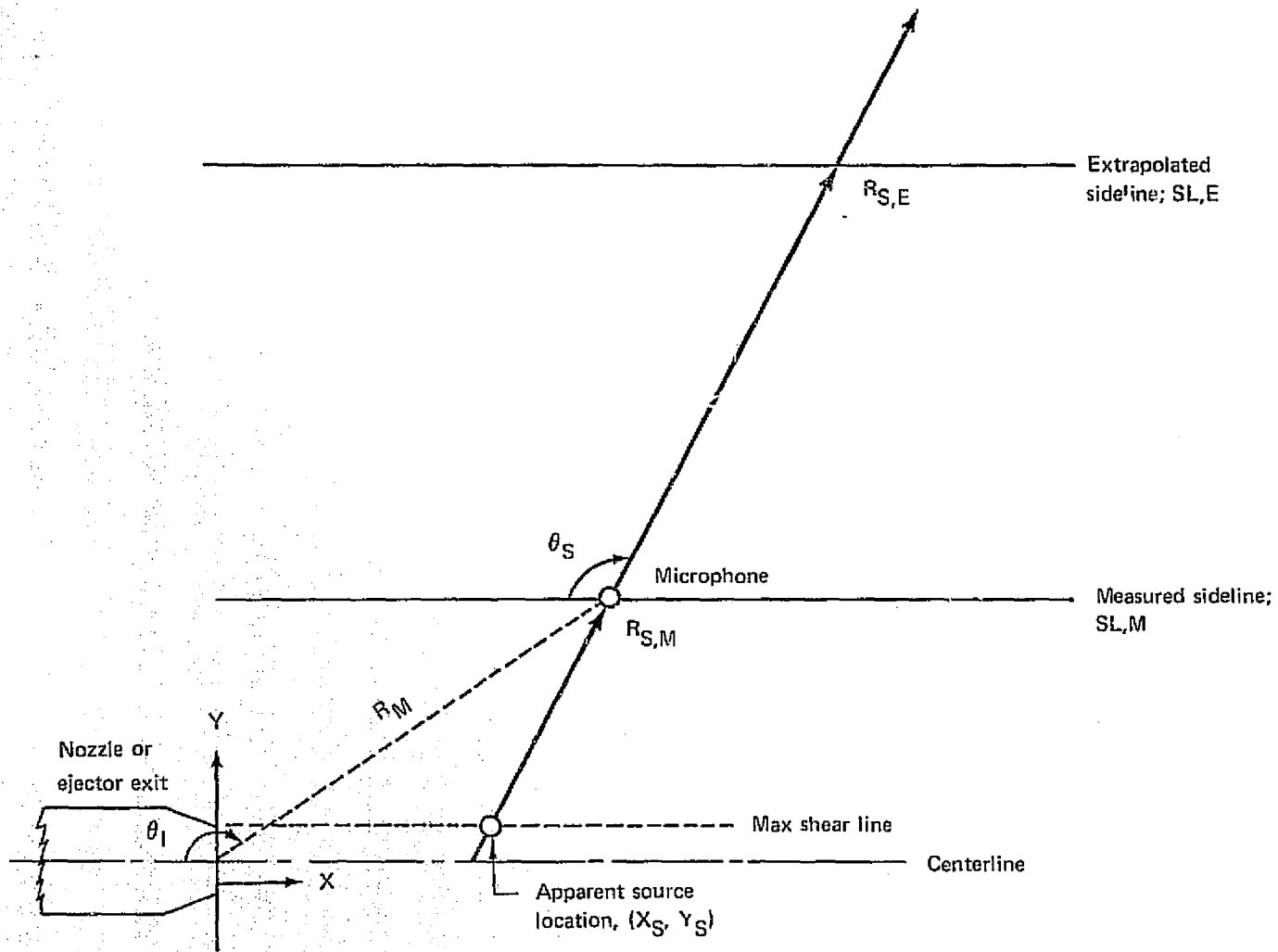


Figure 10.—Coordinate System

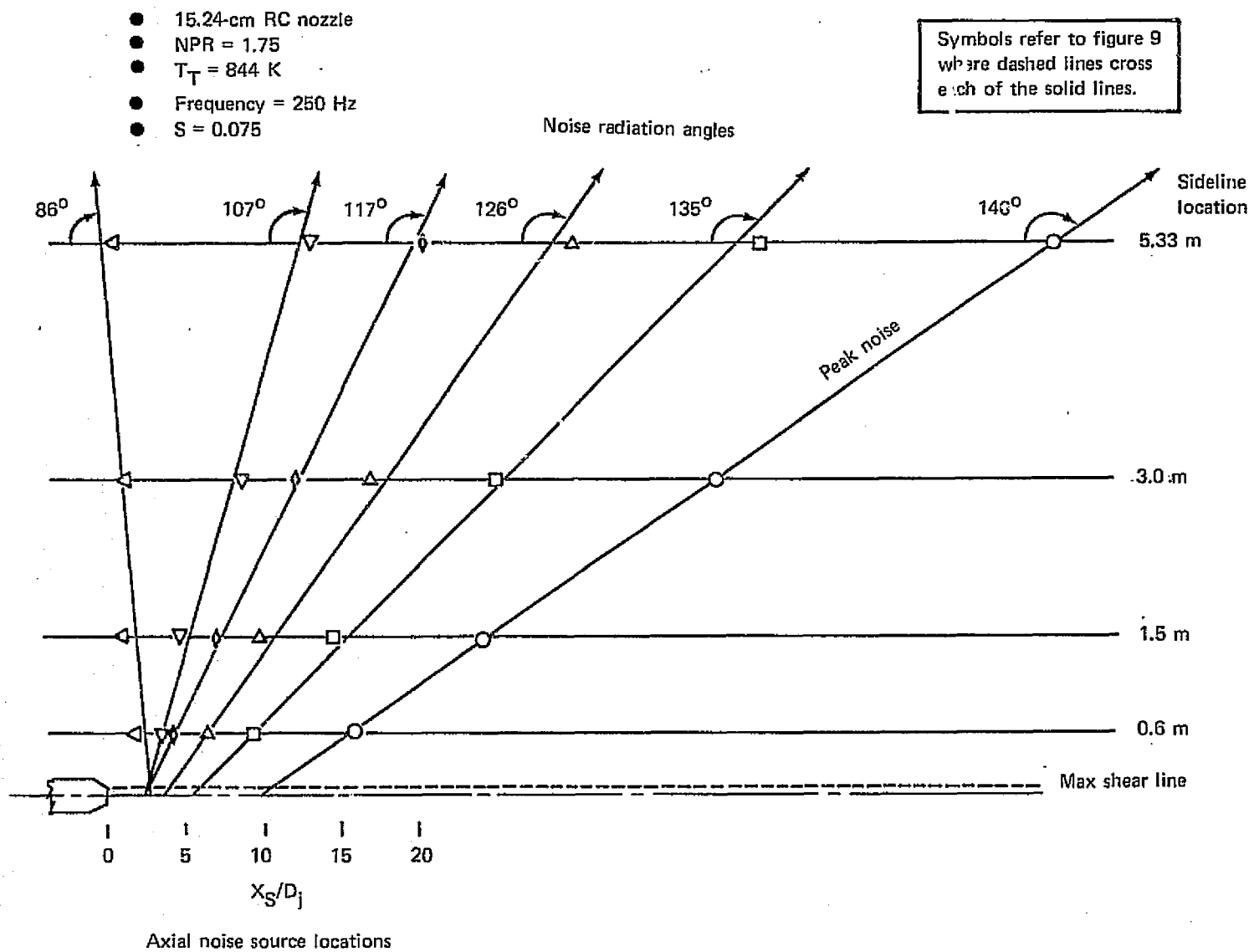


Figure 11.—Determination of Apparent Noise Source Locations and Noise Radiation Angles

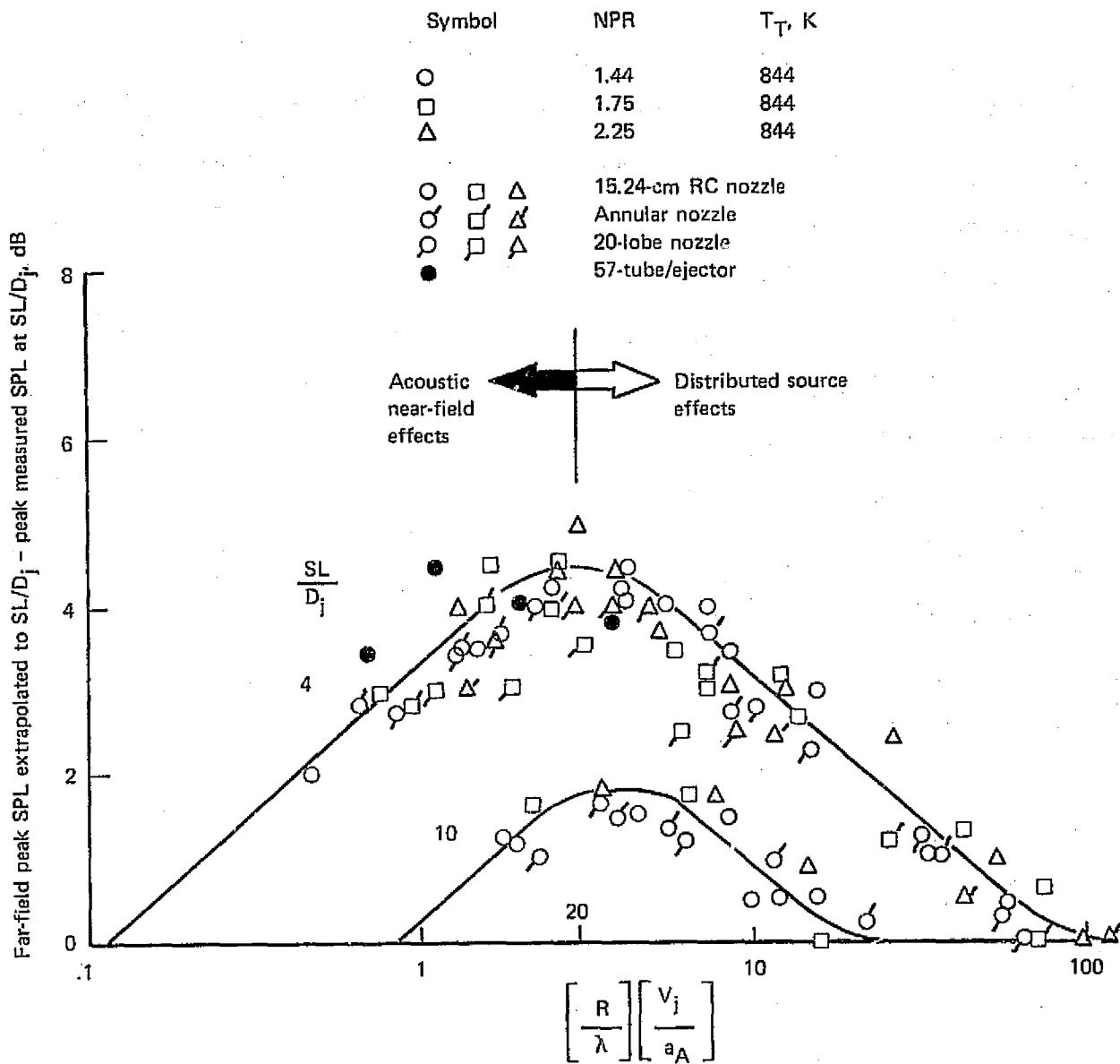


Figure 12.—Deviation of Jet Noise Measurements From the Spherical Divergence/Point Source Assumption

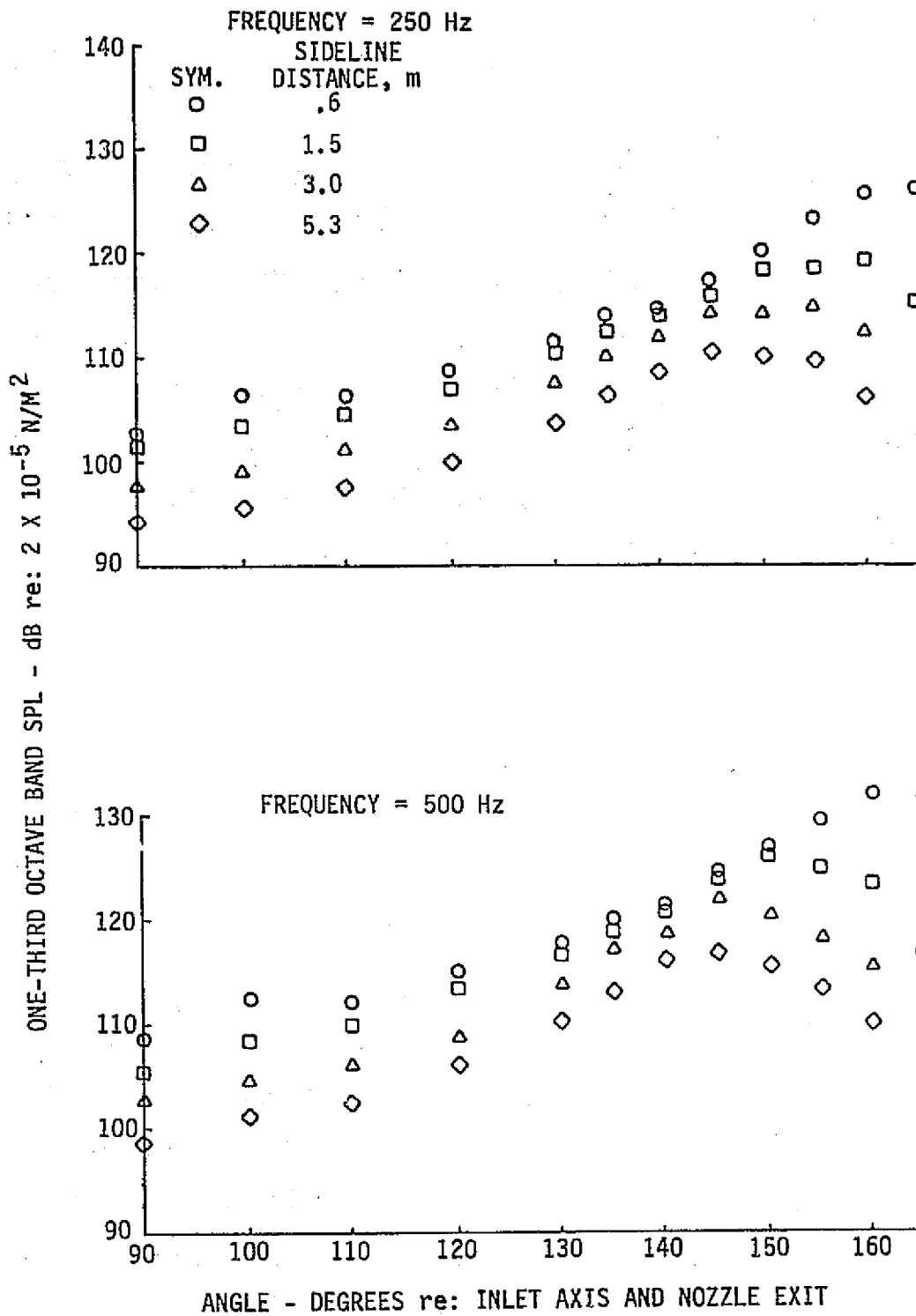


Figure 13.—One-Third-Octave-Band SPL Directivities for a 15.24-cm RC Nozzle—NPR = 1.75,  $T_T = 844$  K

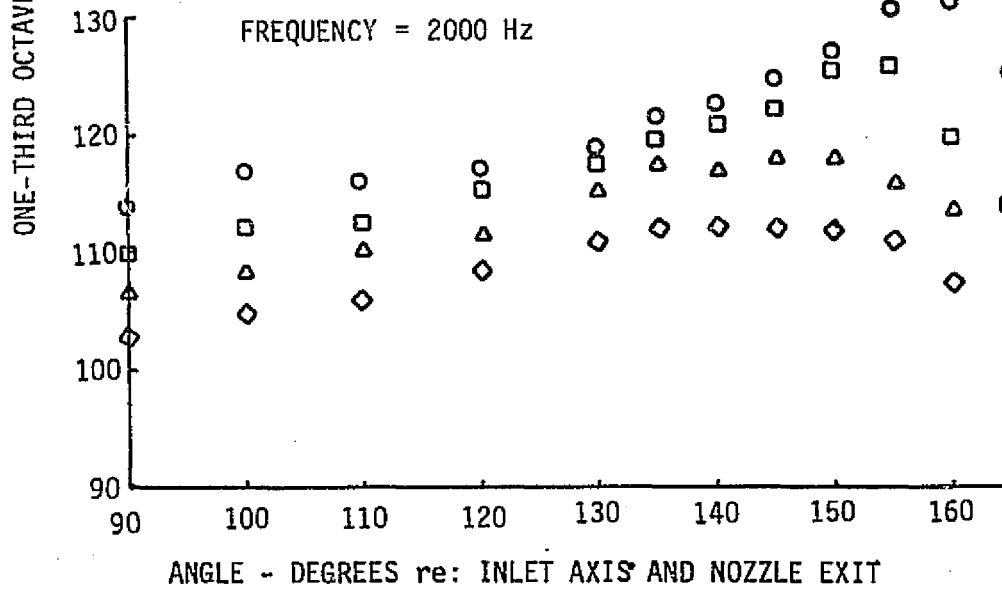
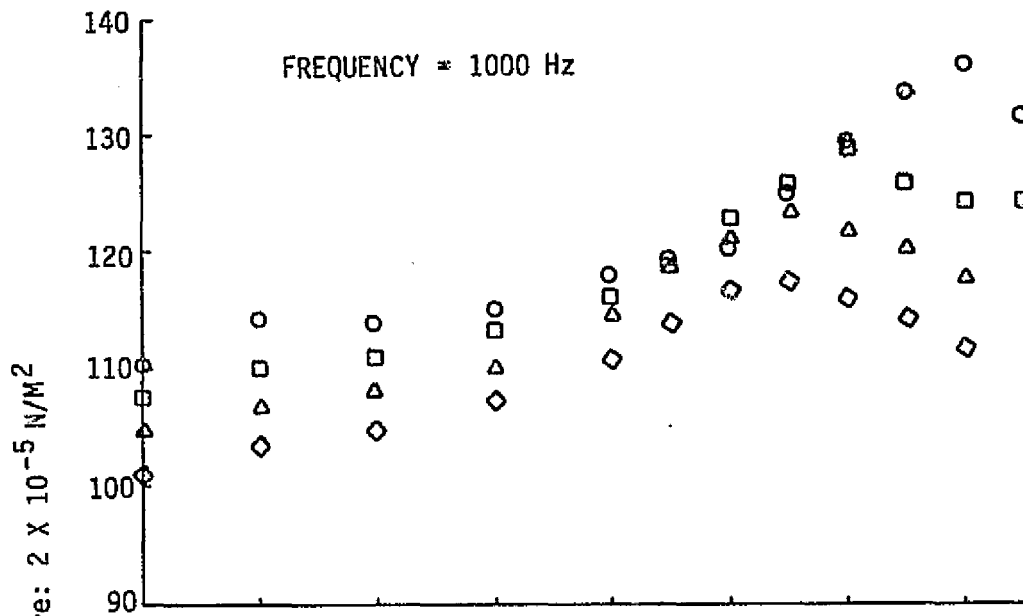


Figure 13.- (Continued)

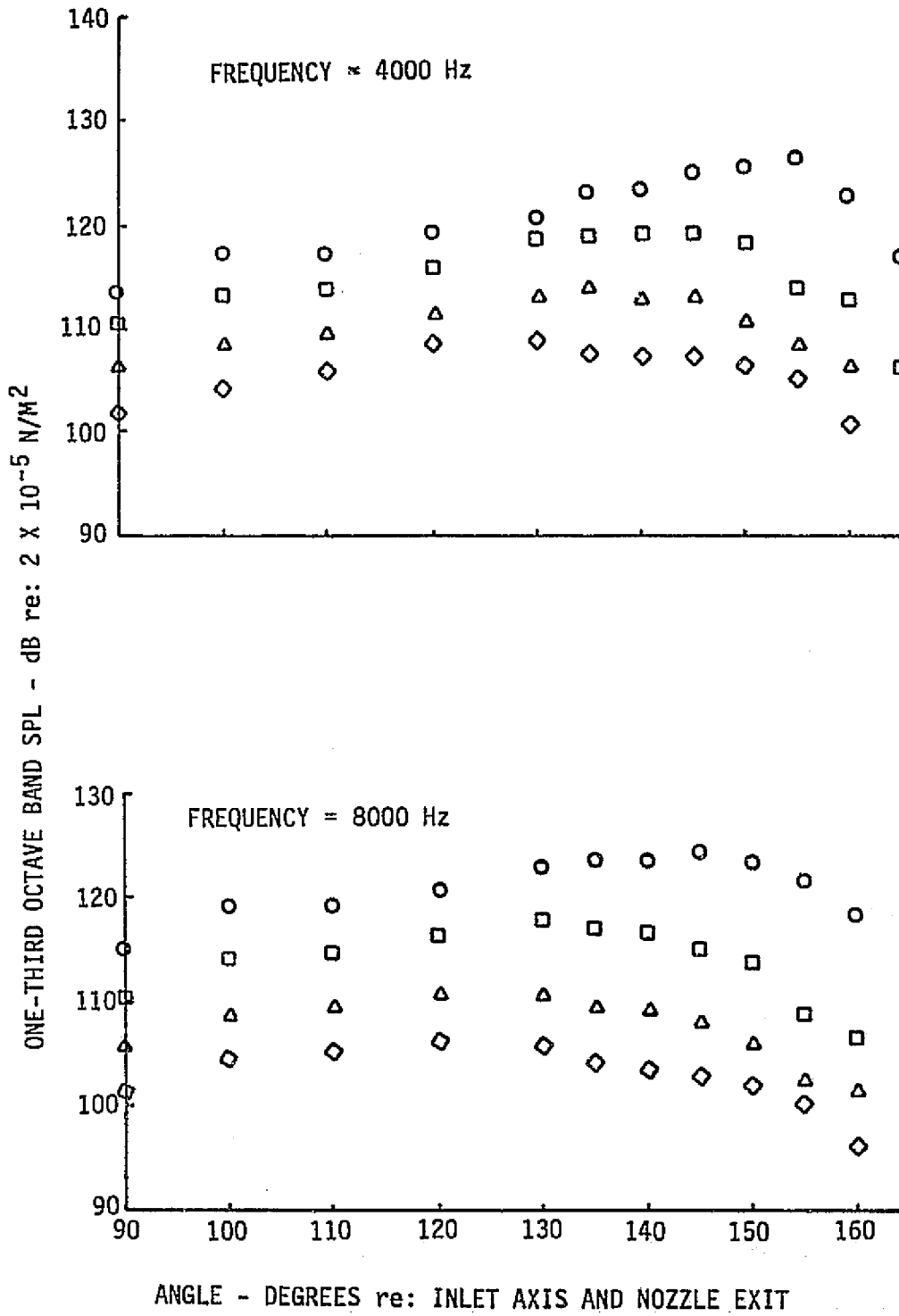


Figure 13.—(Continued)

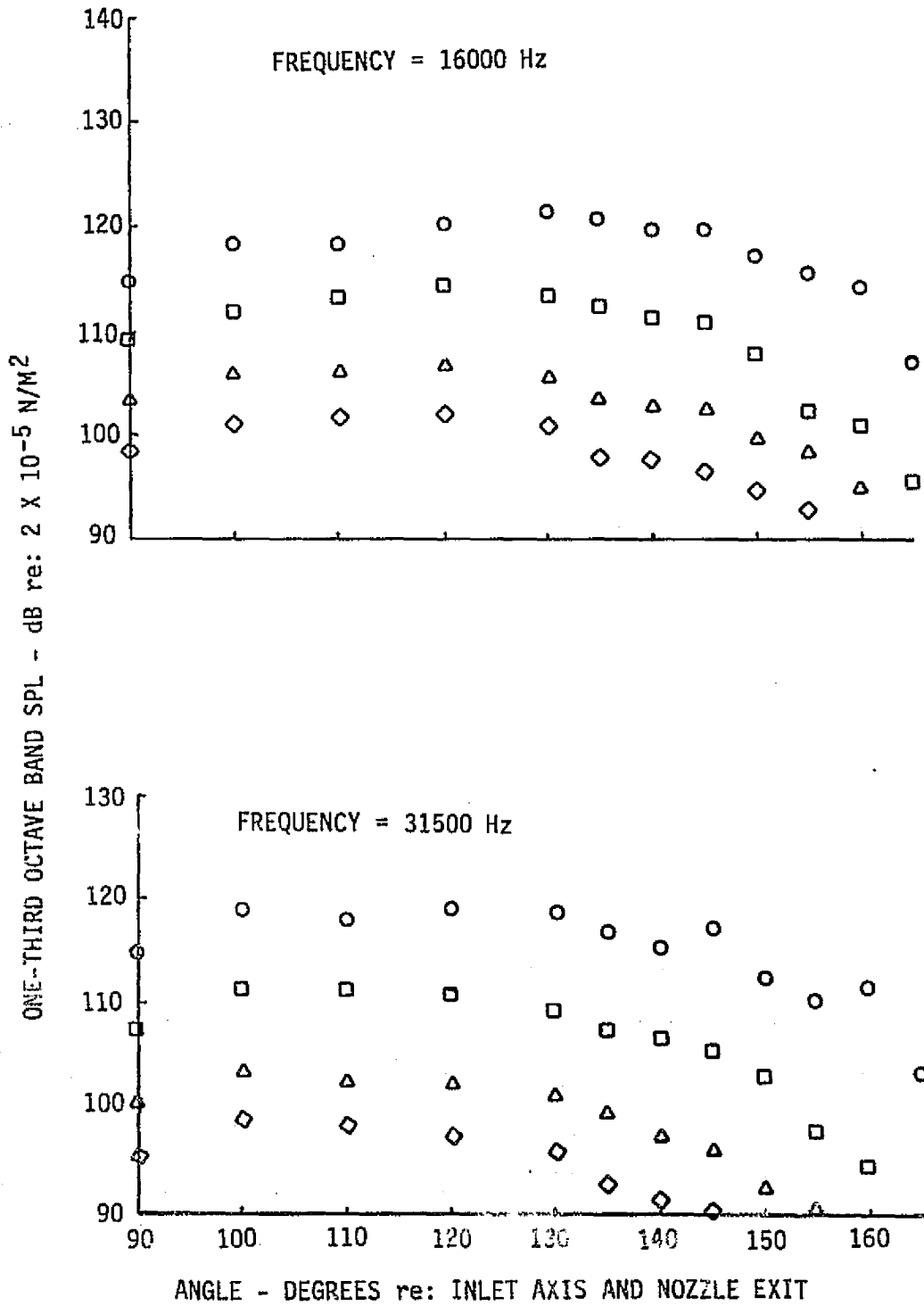


Figure 13.—(Concluded)

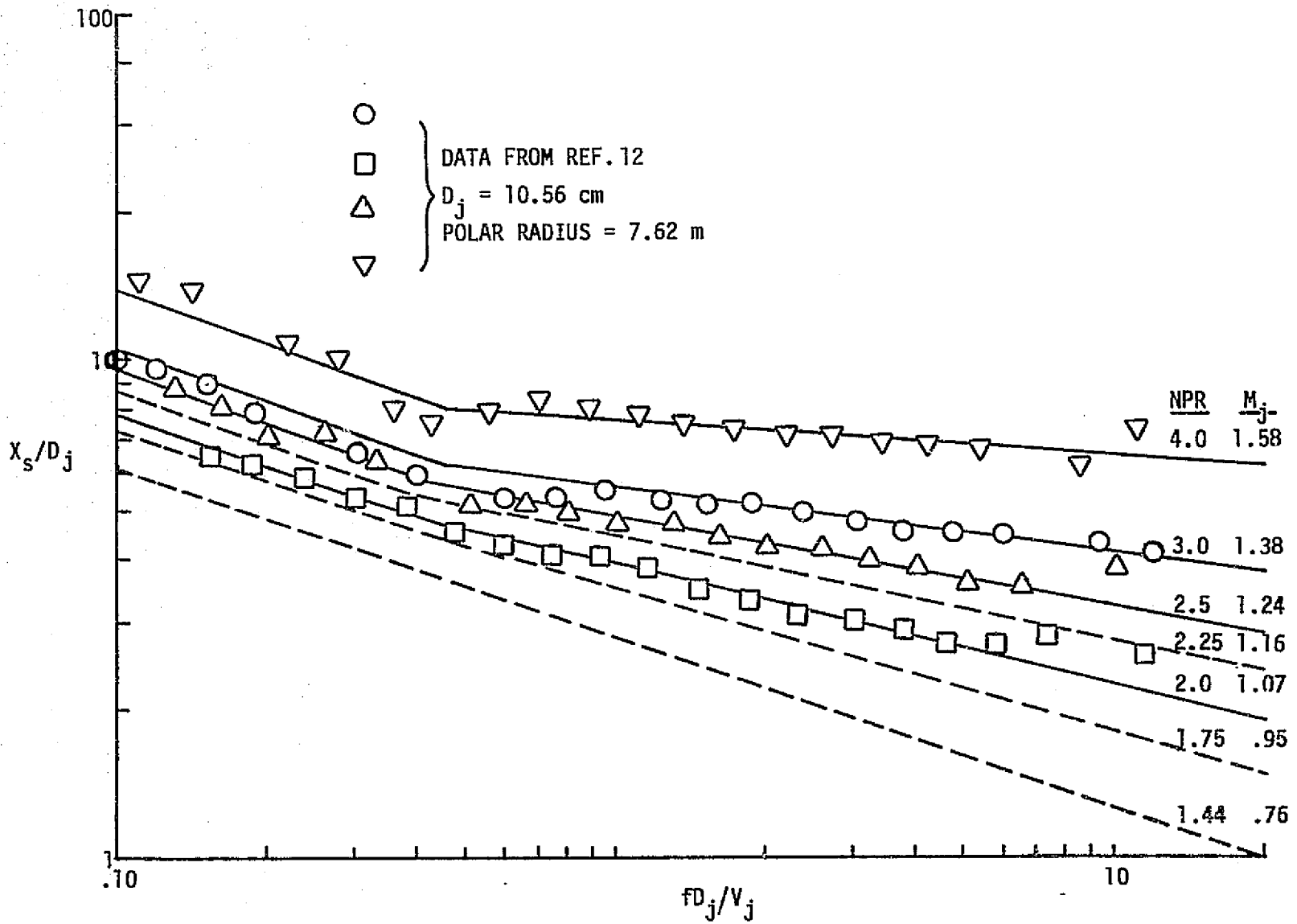


Figure 14.—Peak Noise Source Locations for an RC Nozzle at  $T_T = 900 \text{ K}$  Using the Wall Isolation Technique

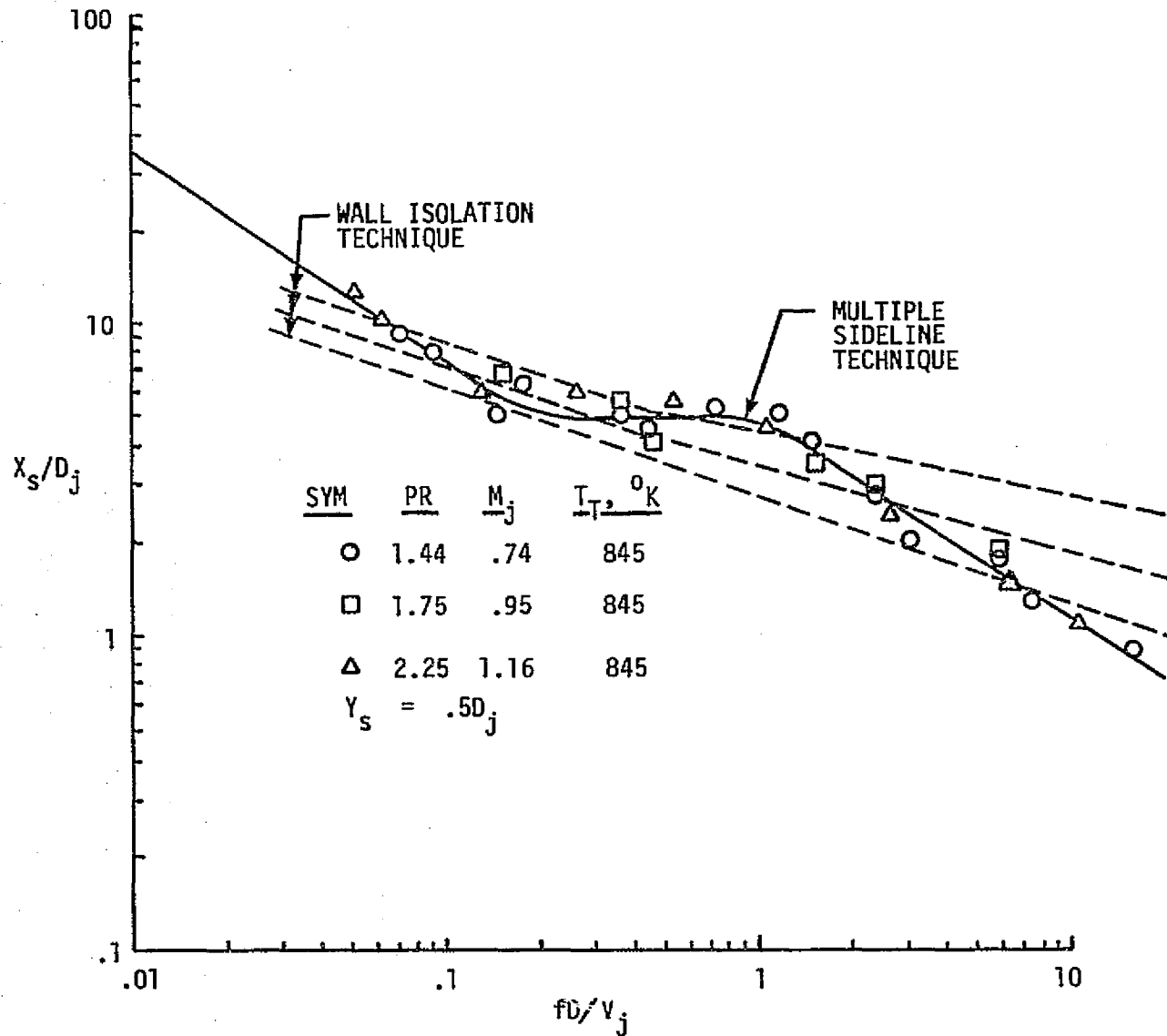


Figure 15.—Comparison of Peak Axial Noise Source Location for a 15.24-cm RC Nozzle Using the Wall Isolation and Multiple Sideline Techniques

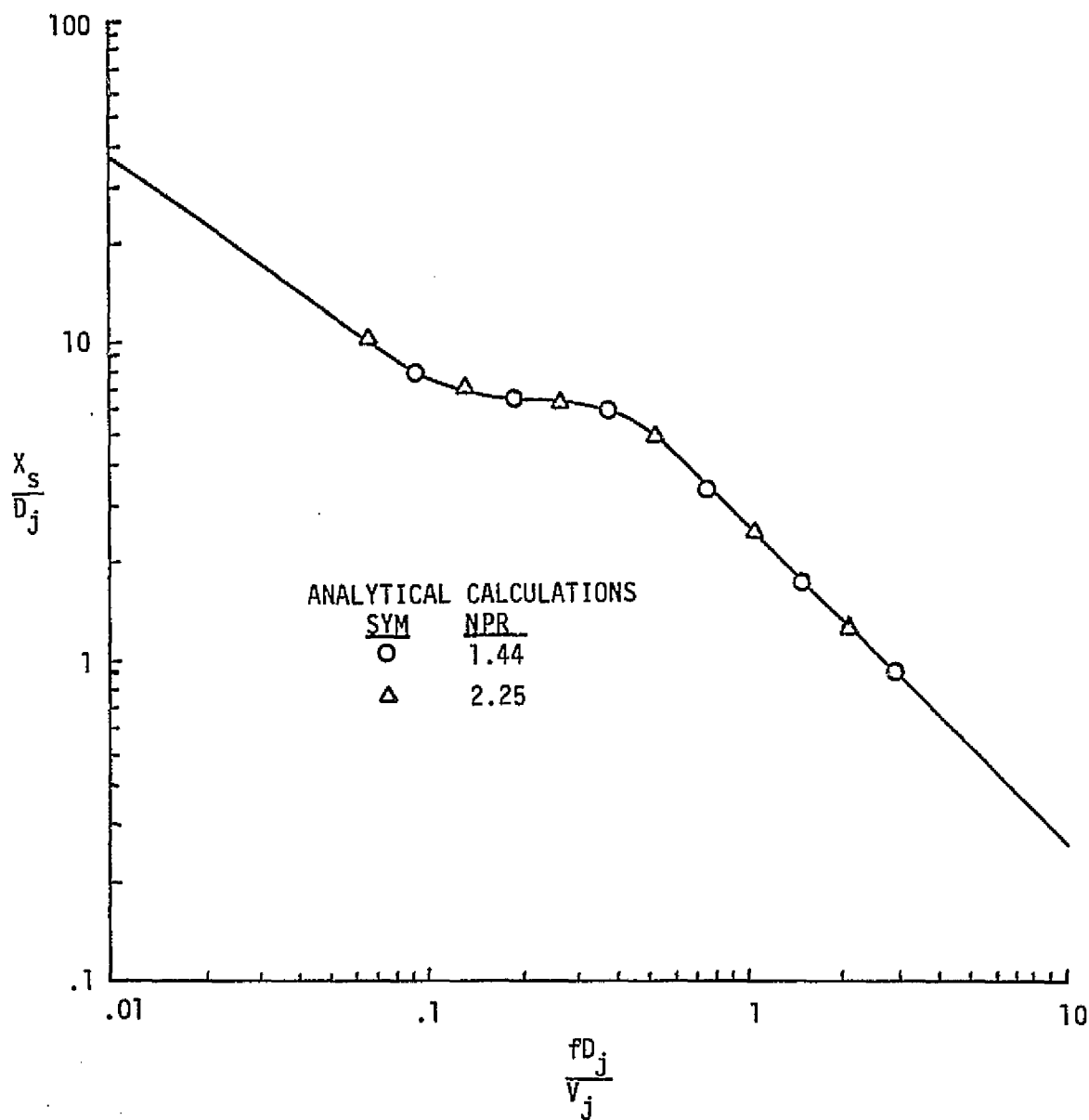


Figure 16.—Analytical Prediction of Noise Source Locations for a 15.24-cm Nozzle Using the Lu/Berman Flow/Noise Analysis

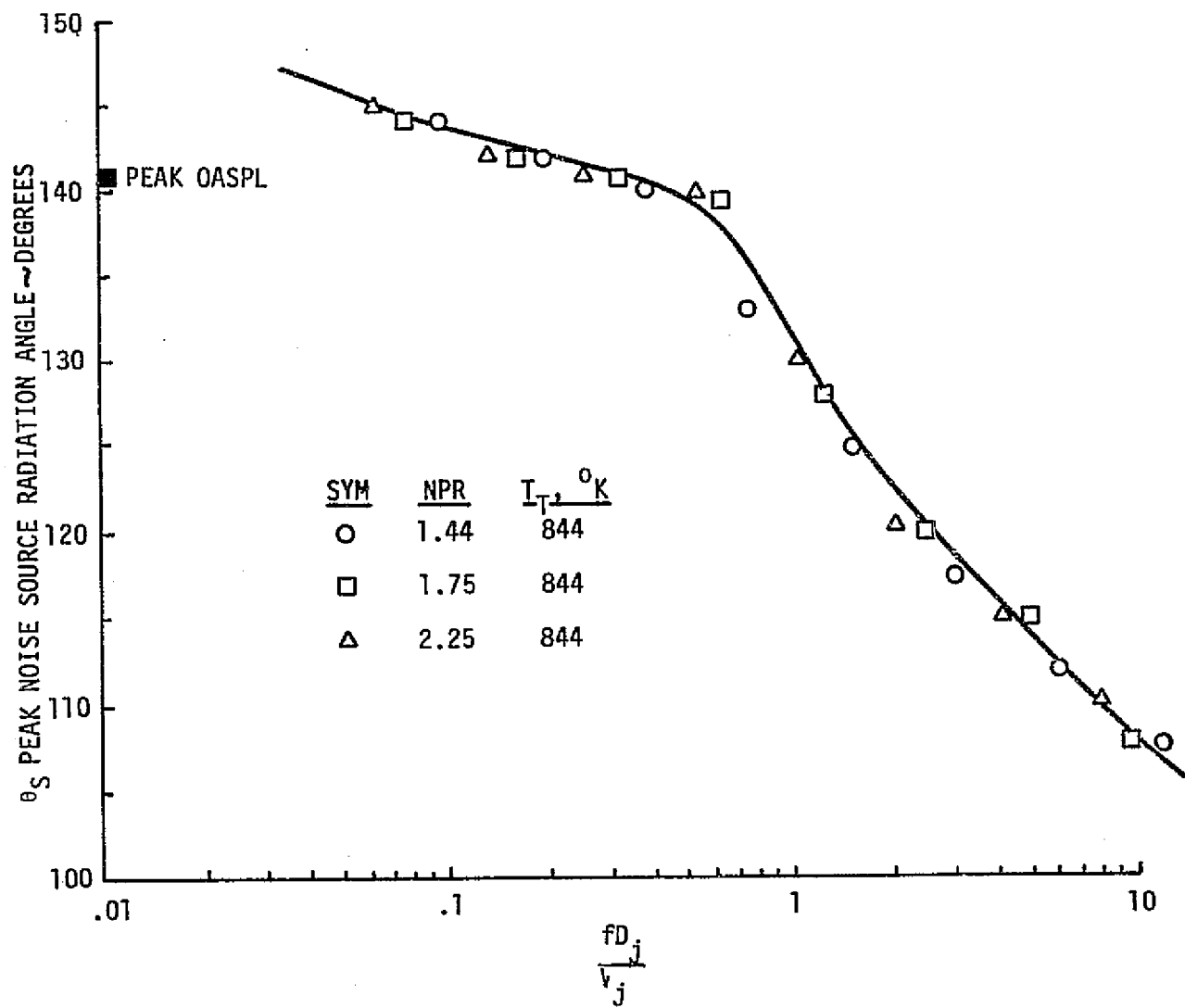


Figure 17.—Correlation of Peak Noise Source Radiation Angle for a 15.24-cm RC Nozzle

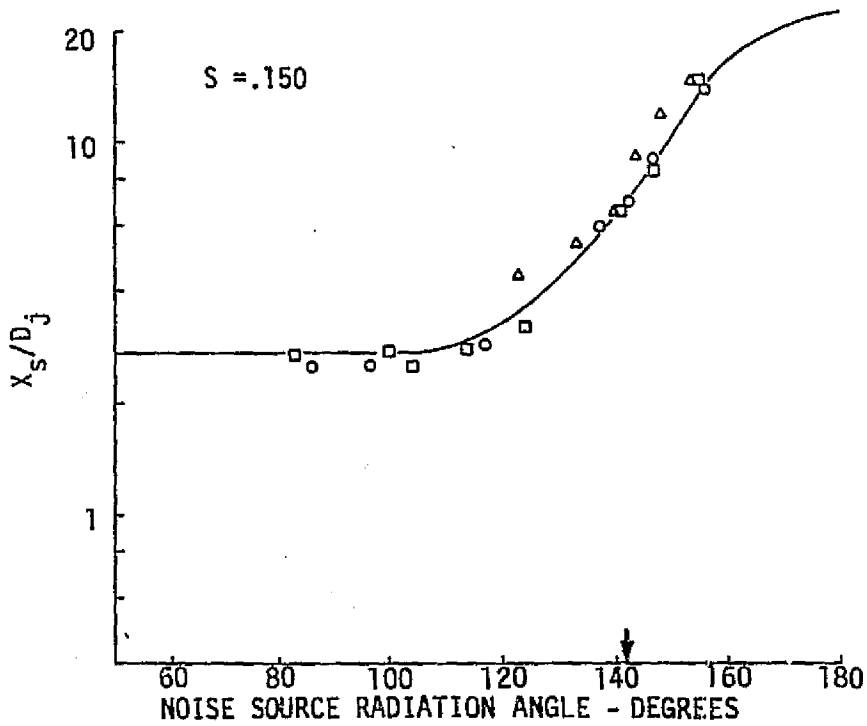
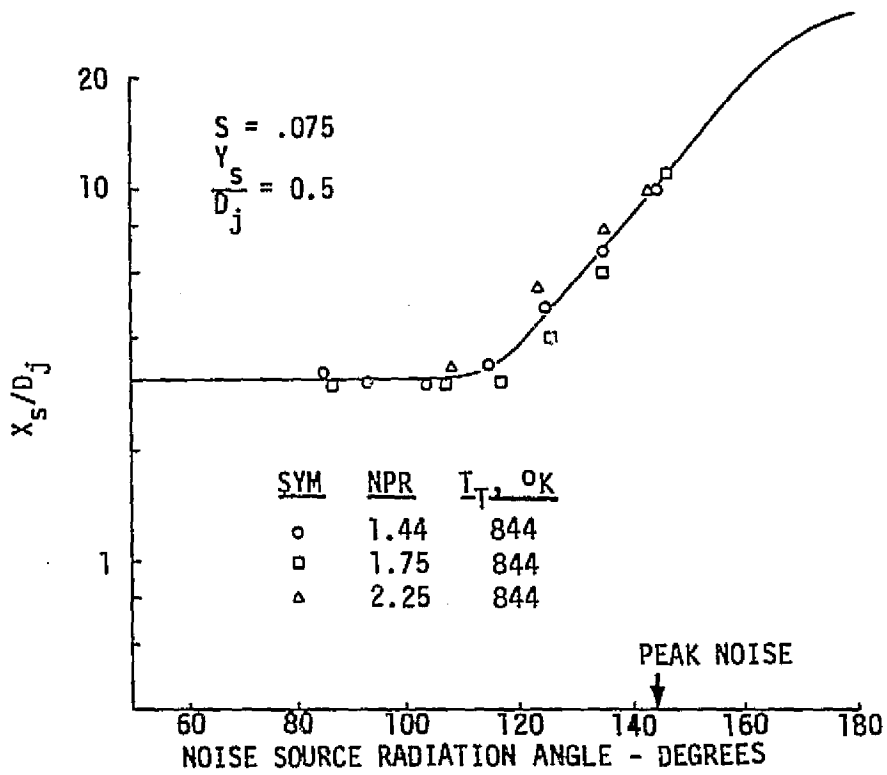


Figure 18.—Distributed Noise Source Locations for a Jet From a 15.24-cm RC Nozzle

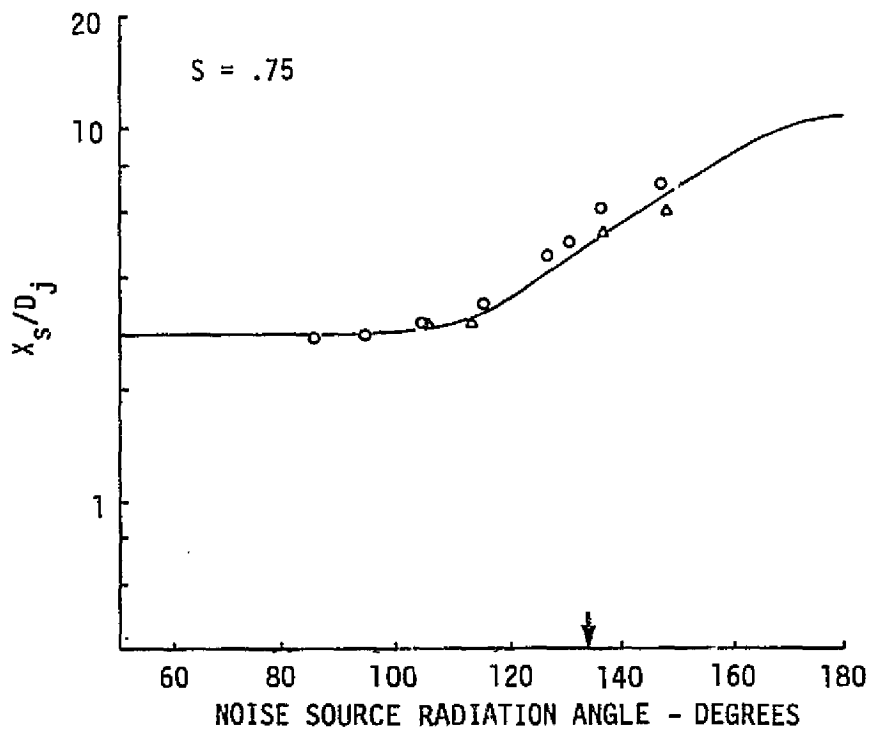
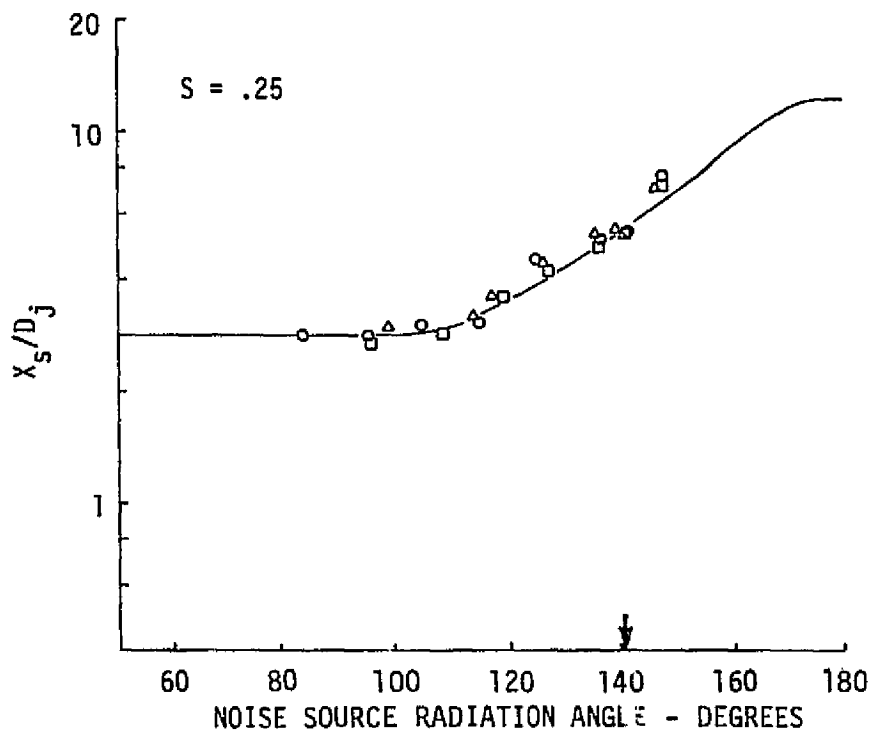


Figure 18.—(Continued)

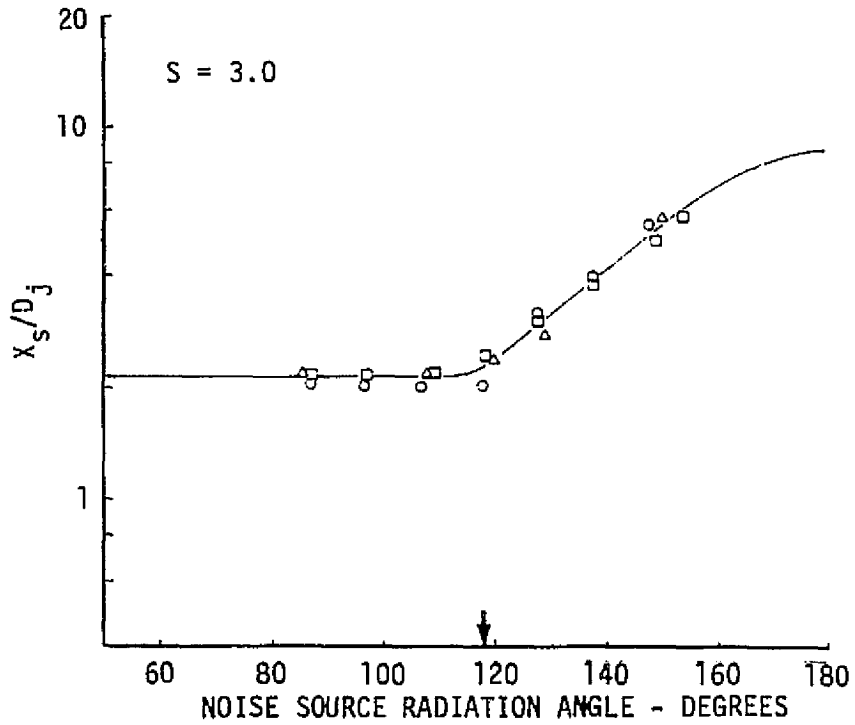
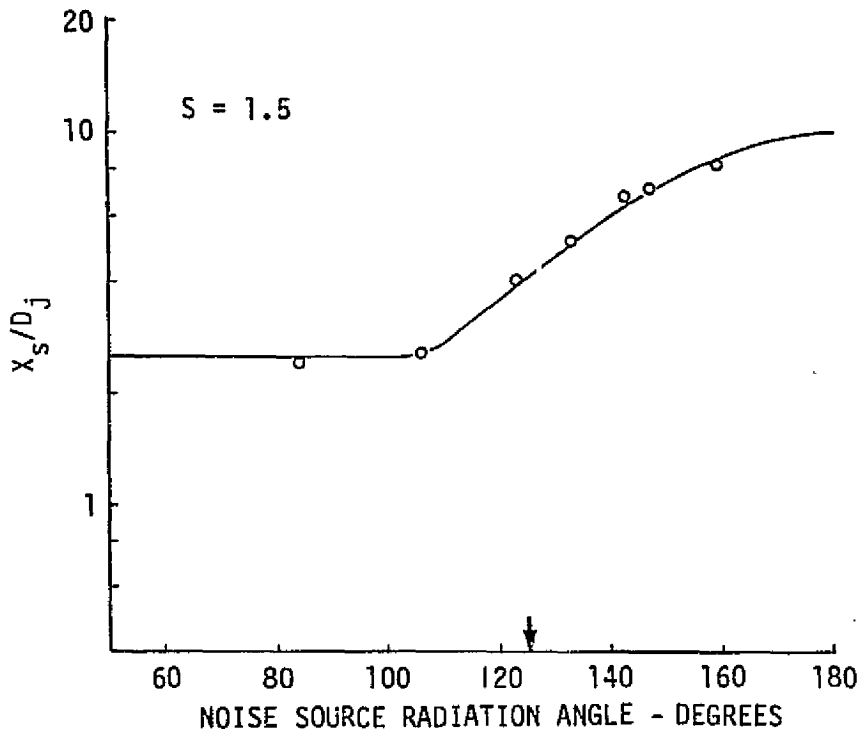


Figure 18.—(Continued)

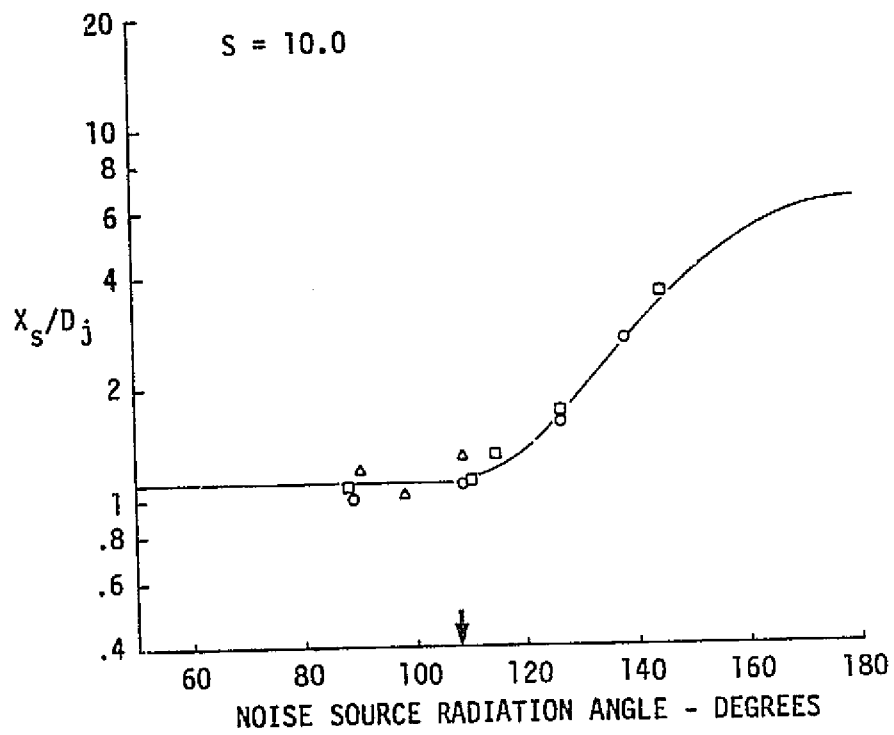


Figure 18.—(Concluded)

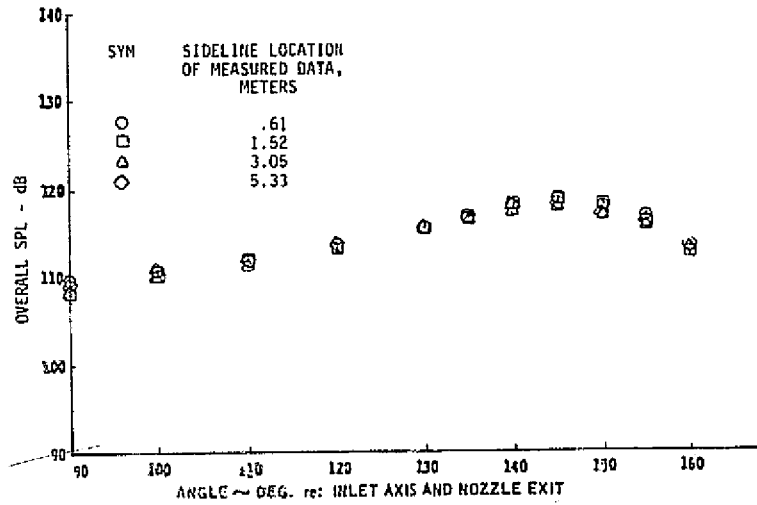


Figure 19.—OASPL and One-Third-Octave-Band SPL Directivity Data for a 15.24-cm RC Nozzle Extrapolated to a 5.33-m Sideline—NPR = 1.44,  $T_T = 844$  K

ORIGINAL PAGE IS  
OF POOR QUALITY

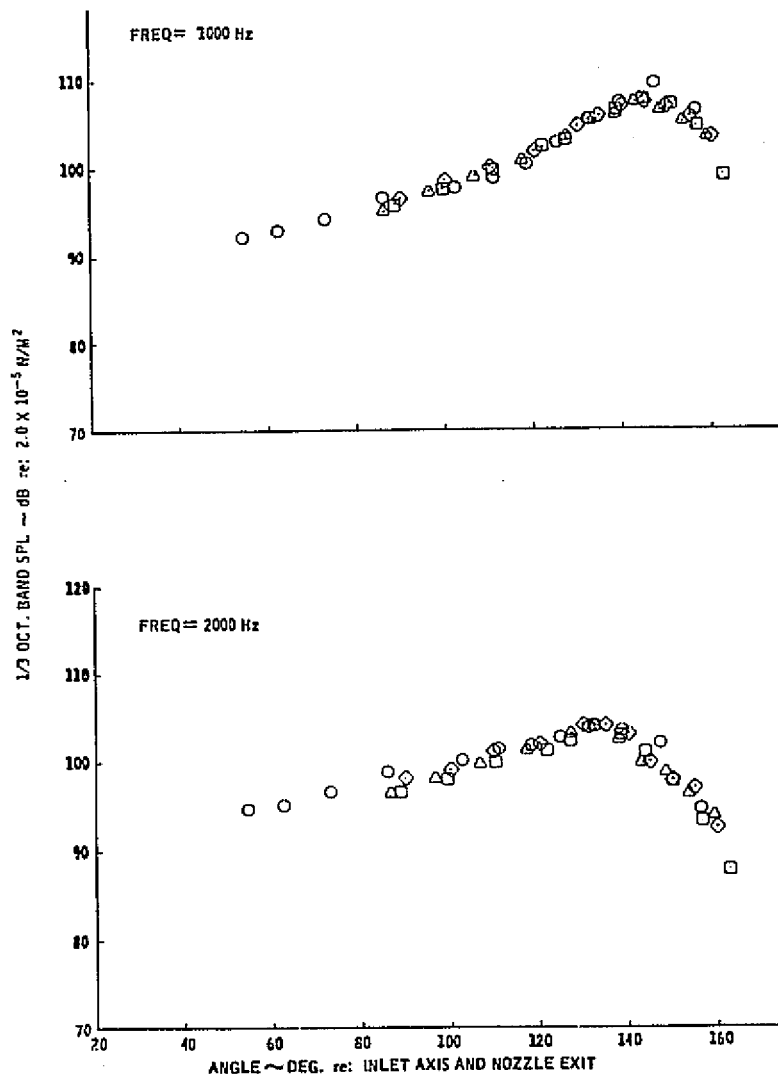
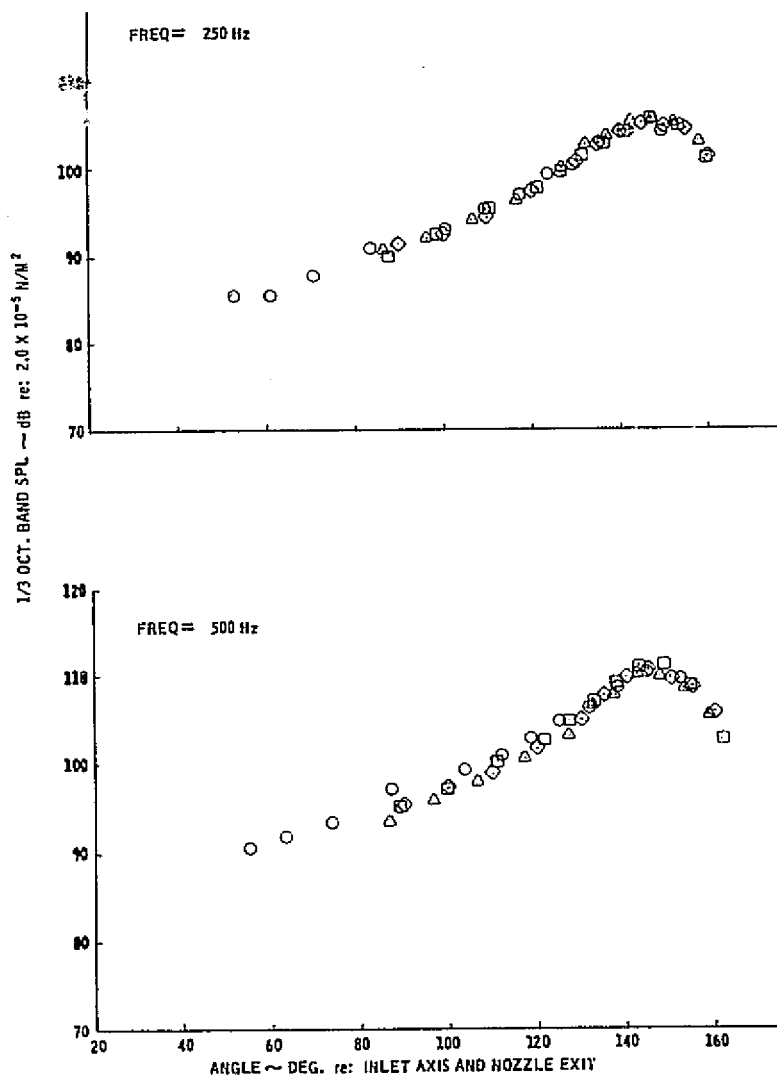


Figure 19.—(Continued)

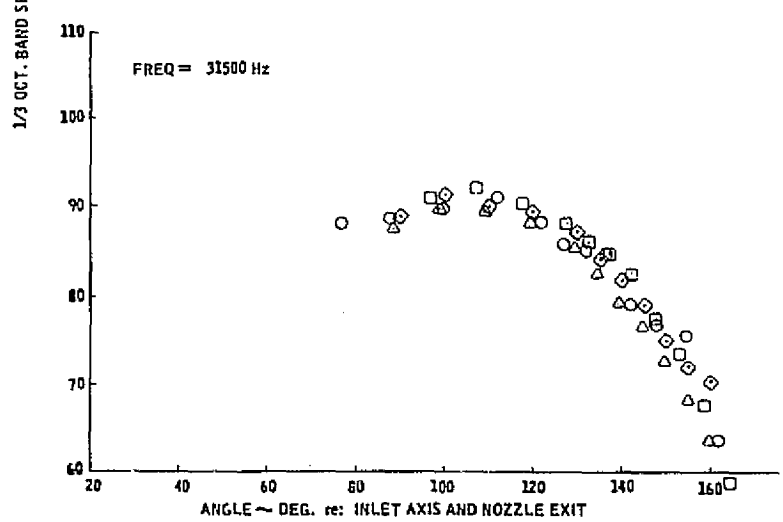
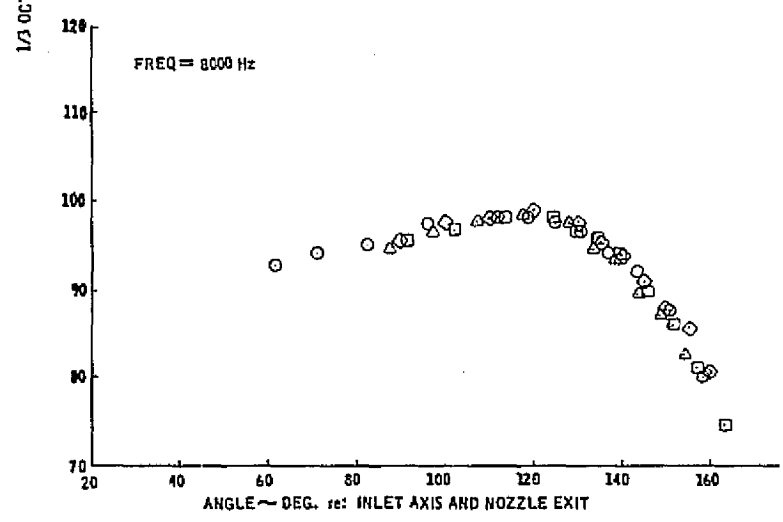
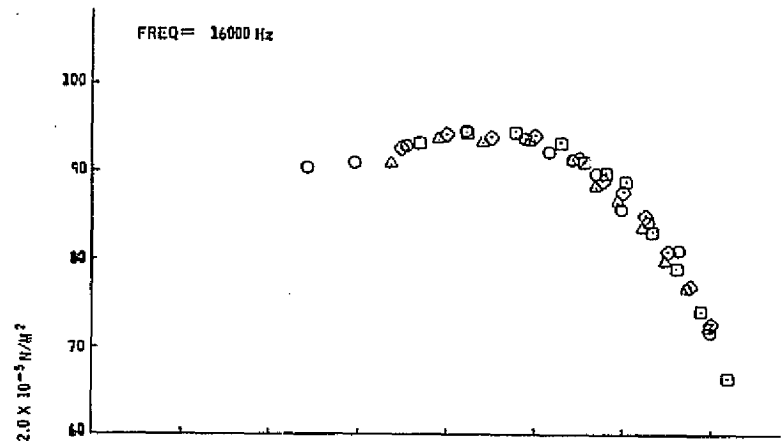
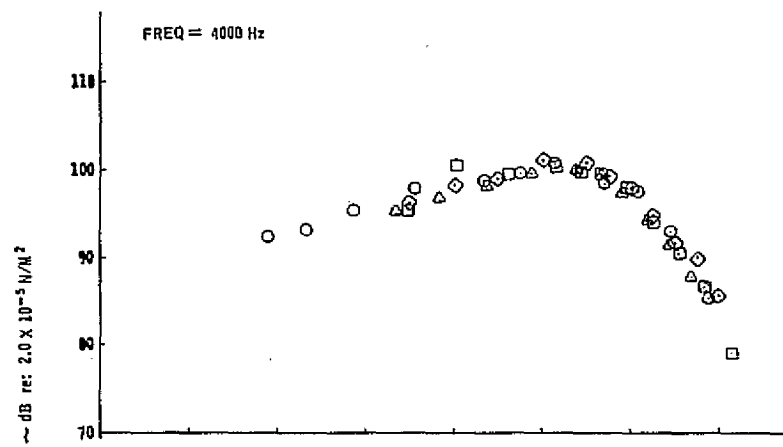


Figure 19.-(Concluded)

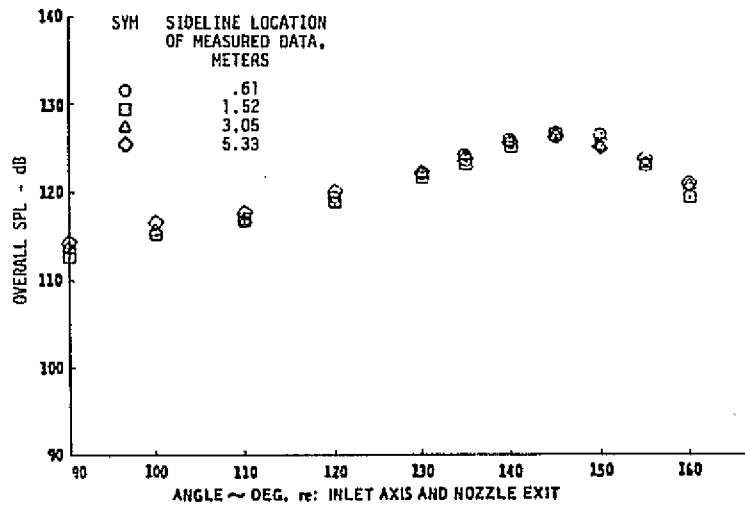


Figure 20.—OASPL and One-Third-Octave-Band SPL Directivity Data for a 15.24-cm RC Nozzle Extrapolated to a 5.33-m Sideline—NPR = 1.75,  $T_T = 844$  K

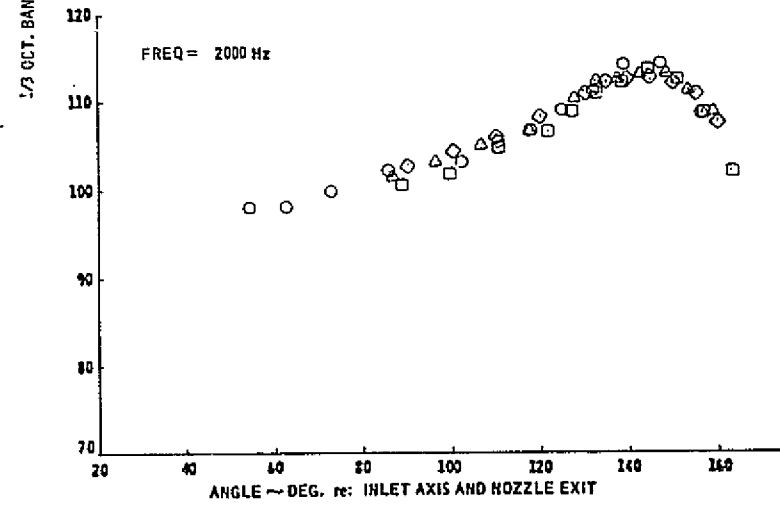
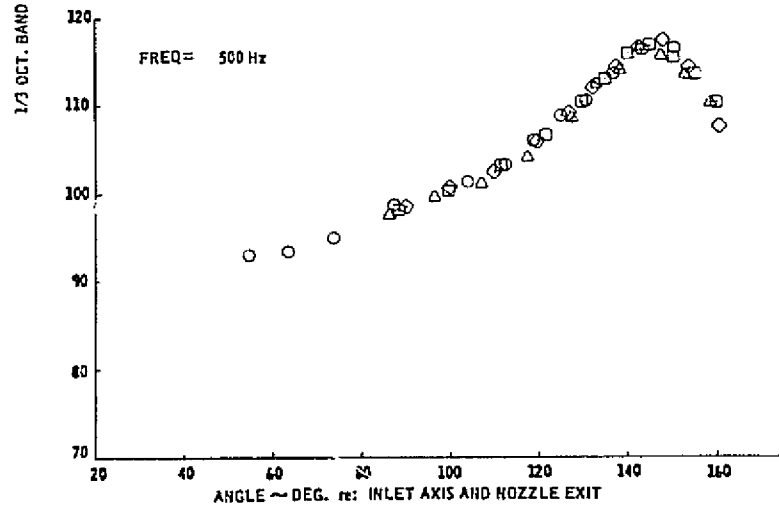
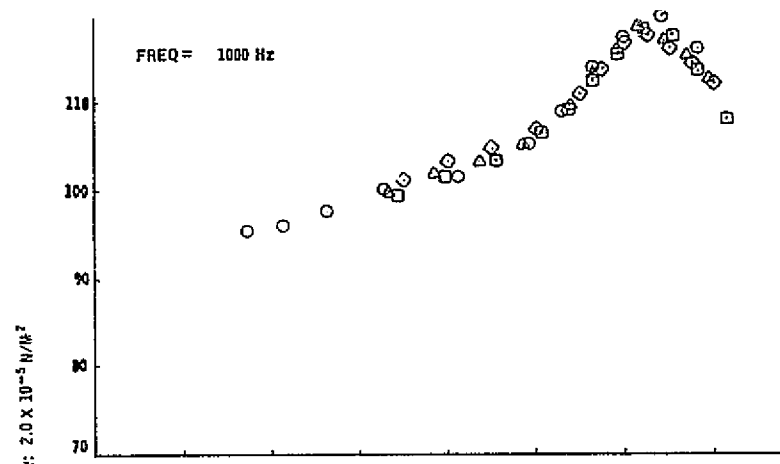
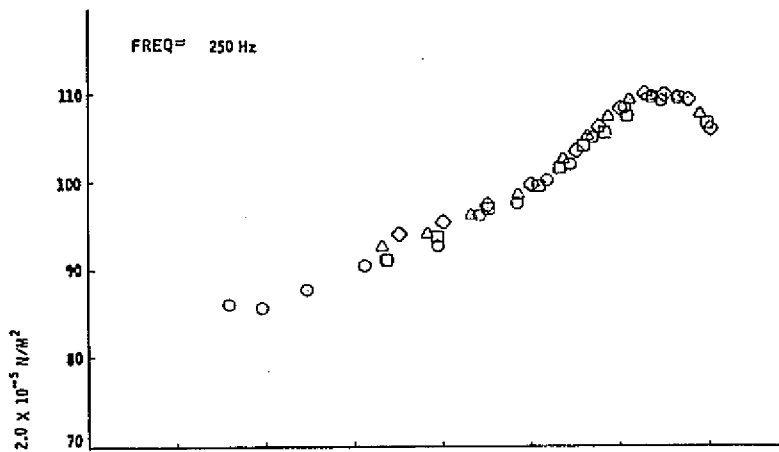


Figure 20.—(Continued)

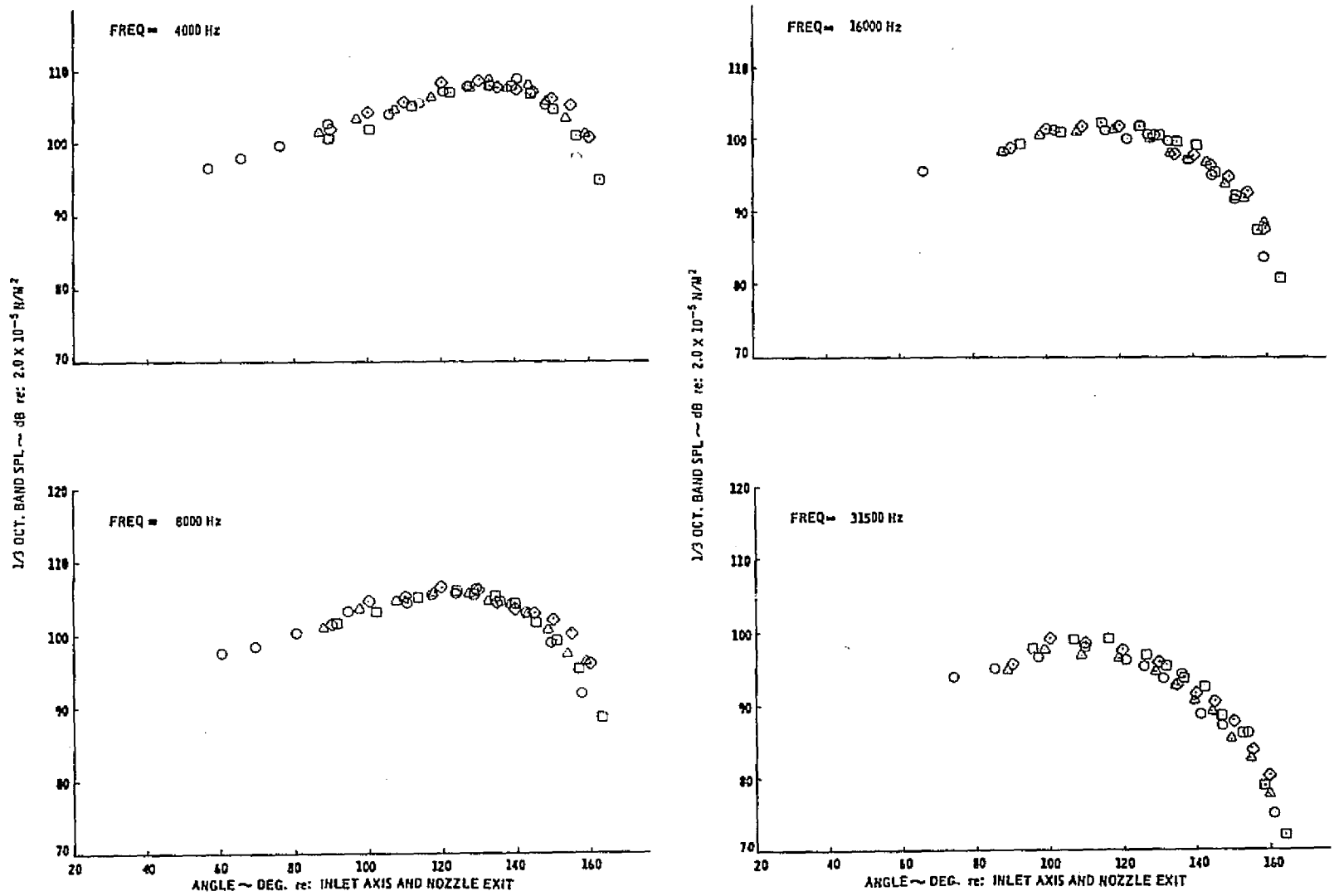


Figure 20.—(Concluded)

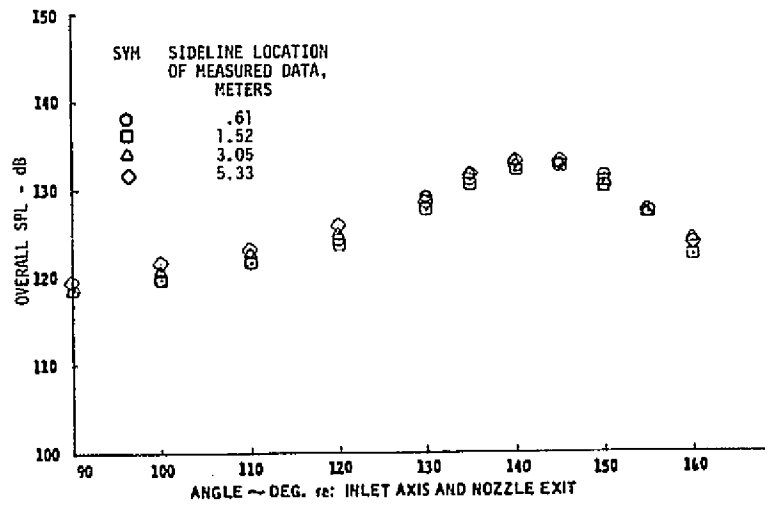


Figure 21.—OASPL and One-Third-Octave-Band SPL Directivity Data for a 15.33-cm RC Nozzle Extrapolated to a 5.33-m Sideline—NPR = 2.25,  $T_T = 841$  K

ORIGINAL PAGE IS  
OF POOR QUALITY

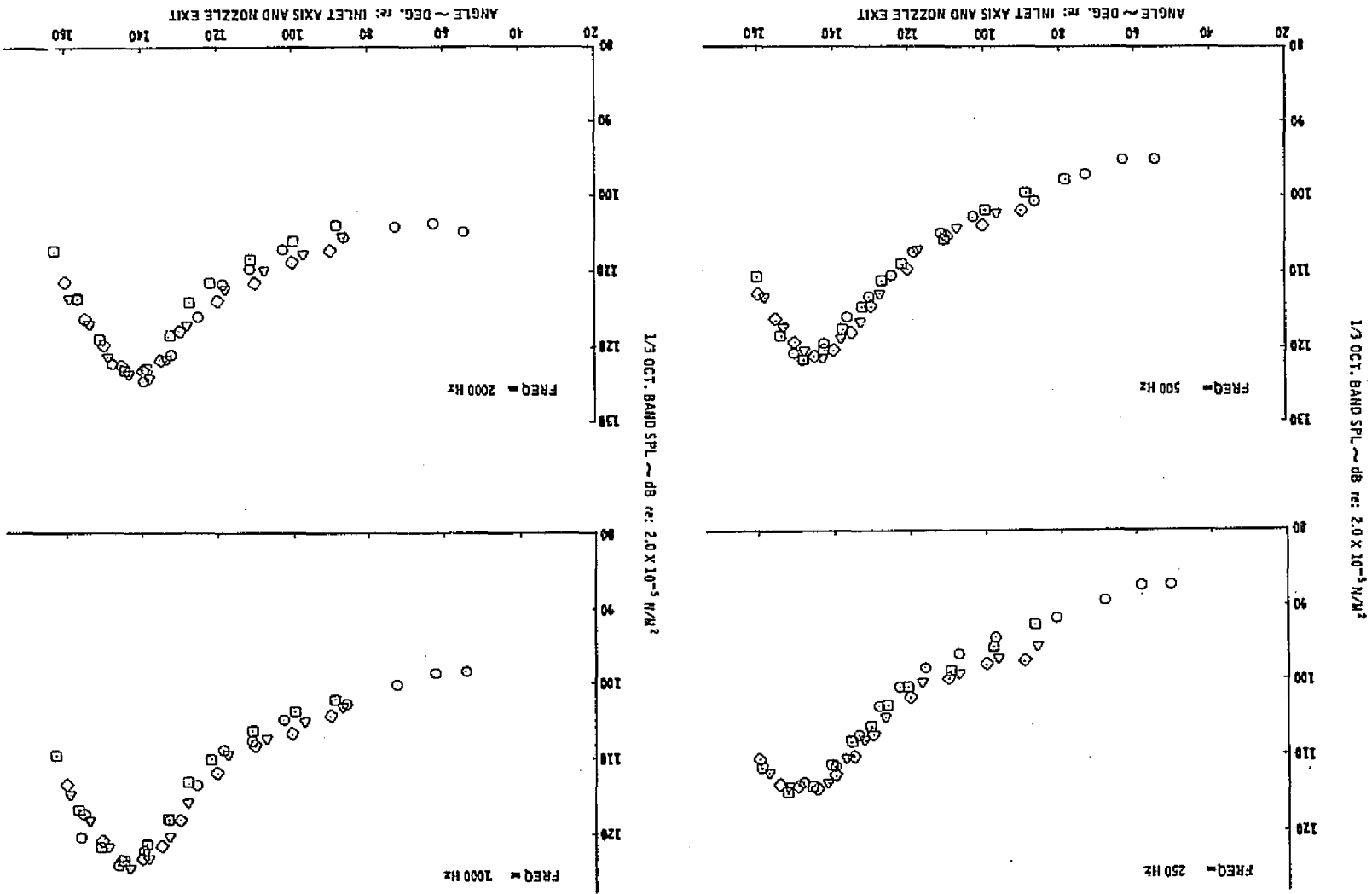


Figure 21.—(Continued)

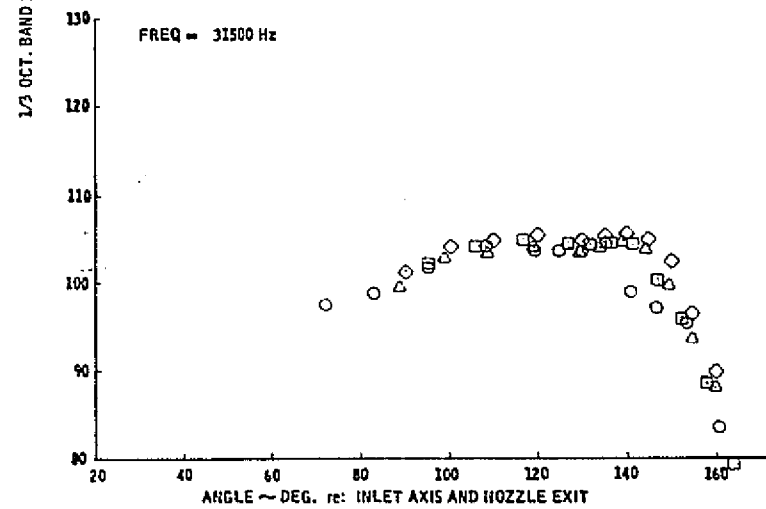
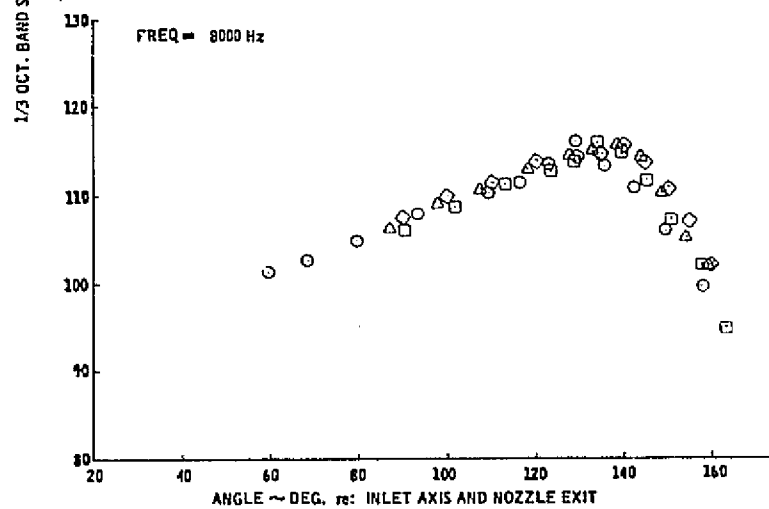
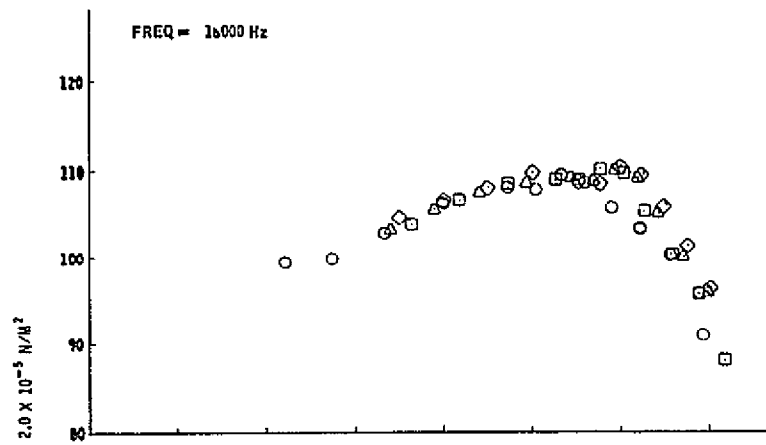
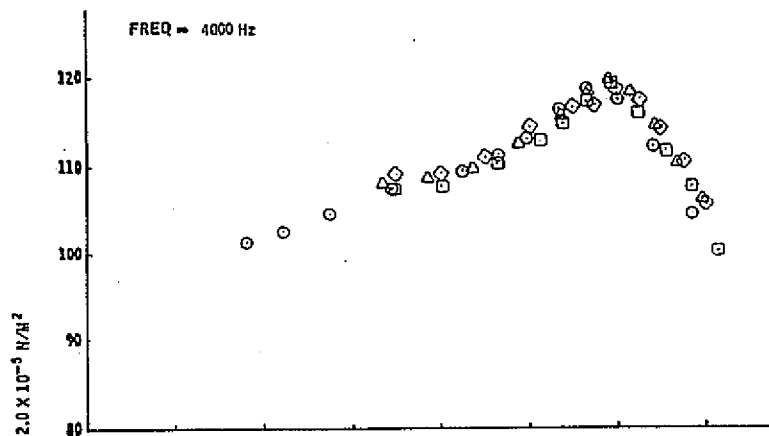


Figure 21.—(Concluded)

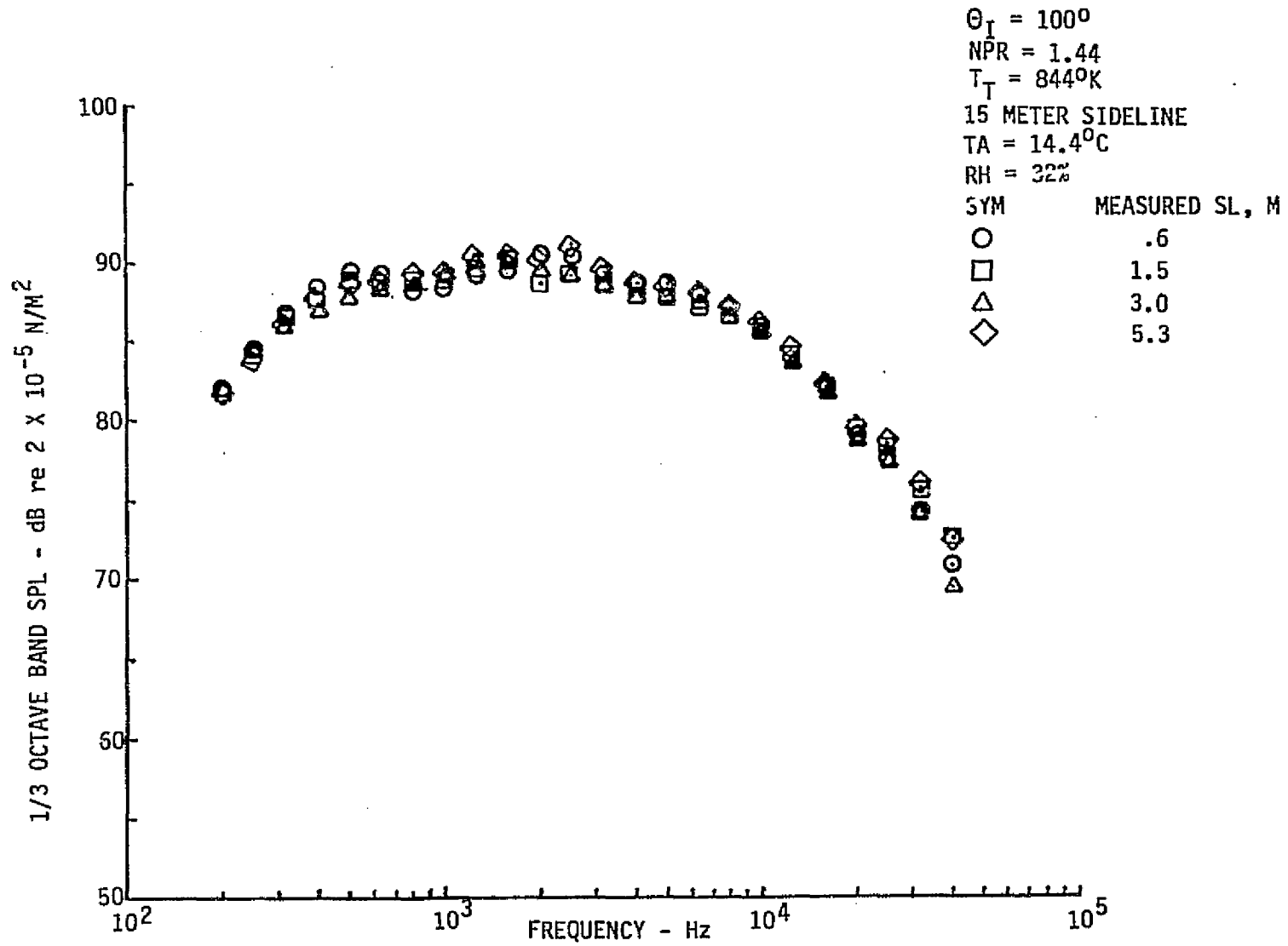


Figure 22.—Measured One-Third-Octave-Band Spectra for a 15.24-cm RC Nozzle Extrapolated to a 15-m Sideline

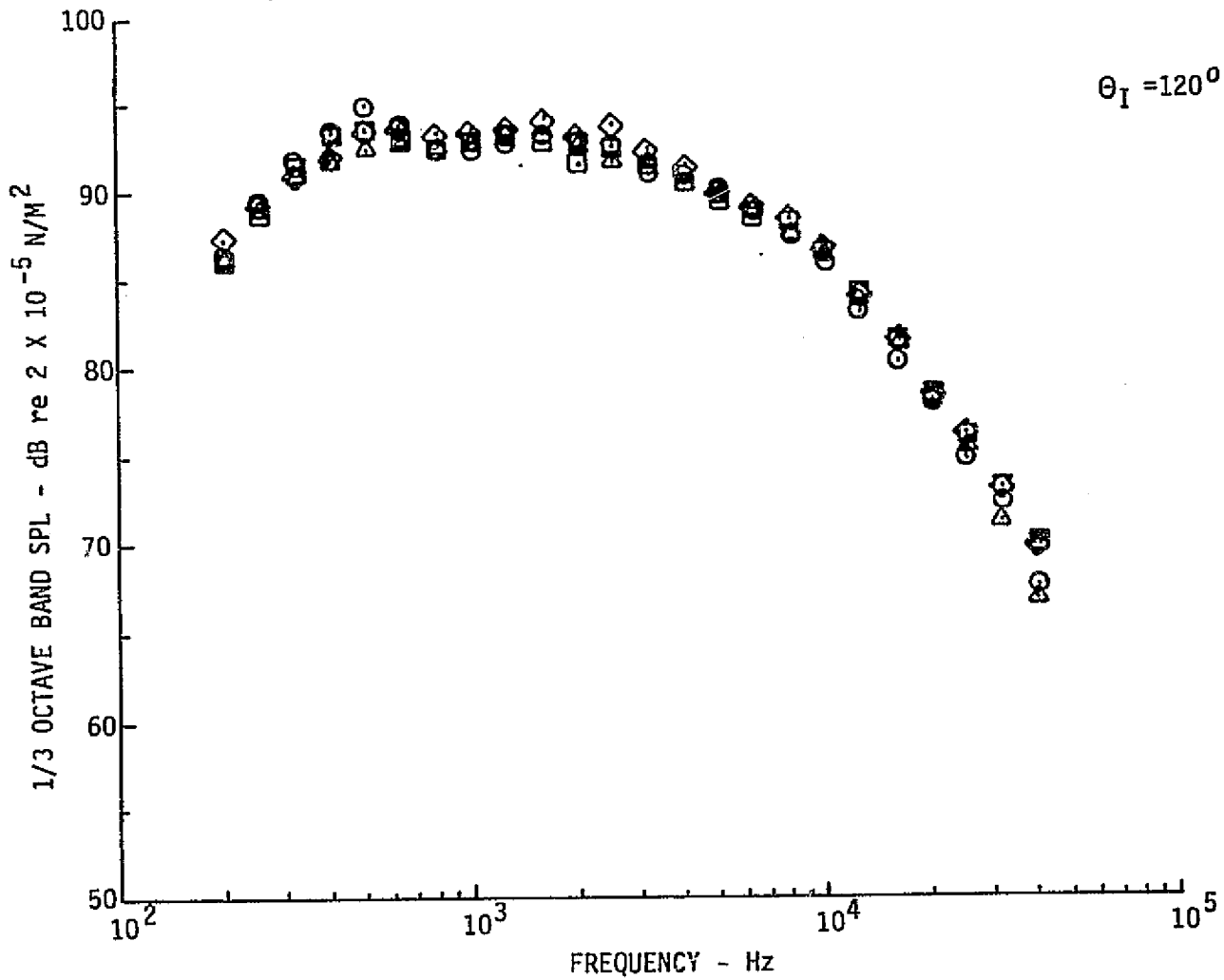


Figure 22.--(Continued)

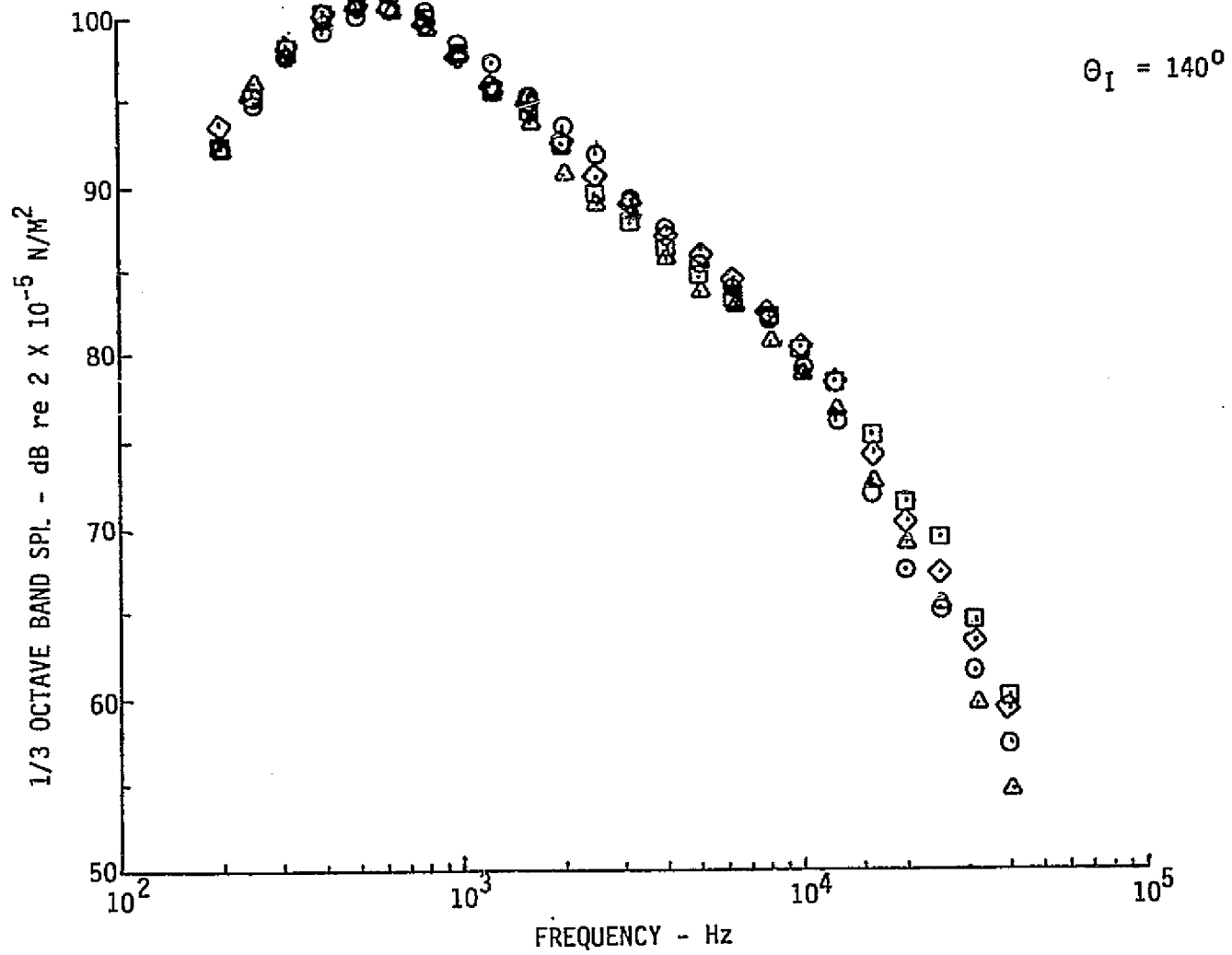


Figure 22.—(Continued)

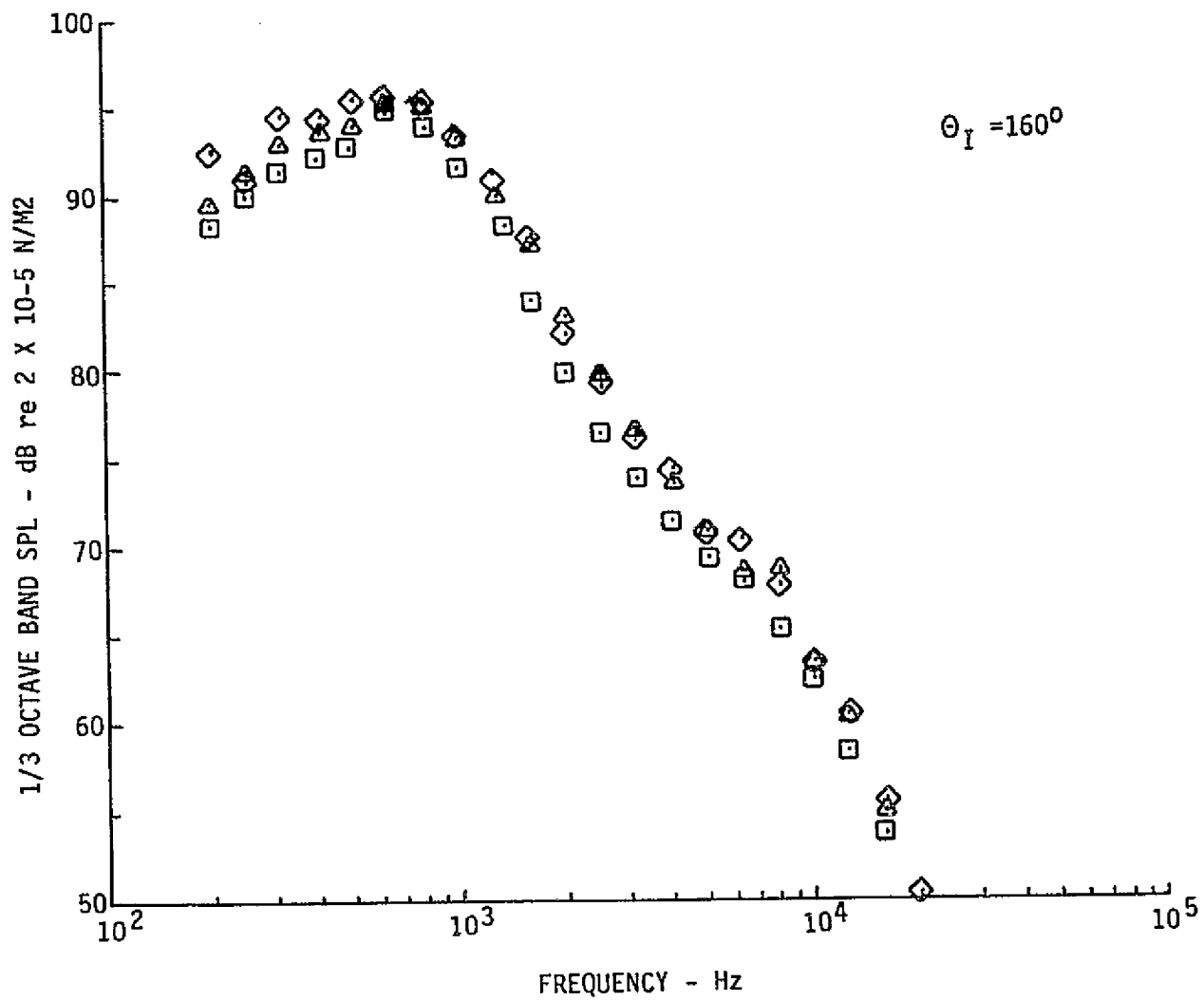


Figure 22.—(Concluded)

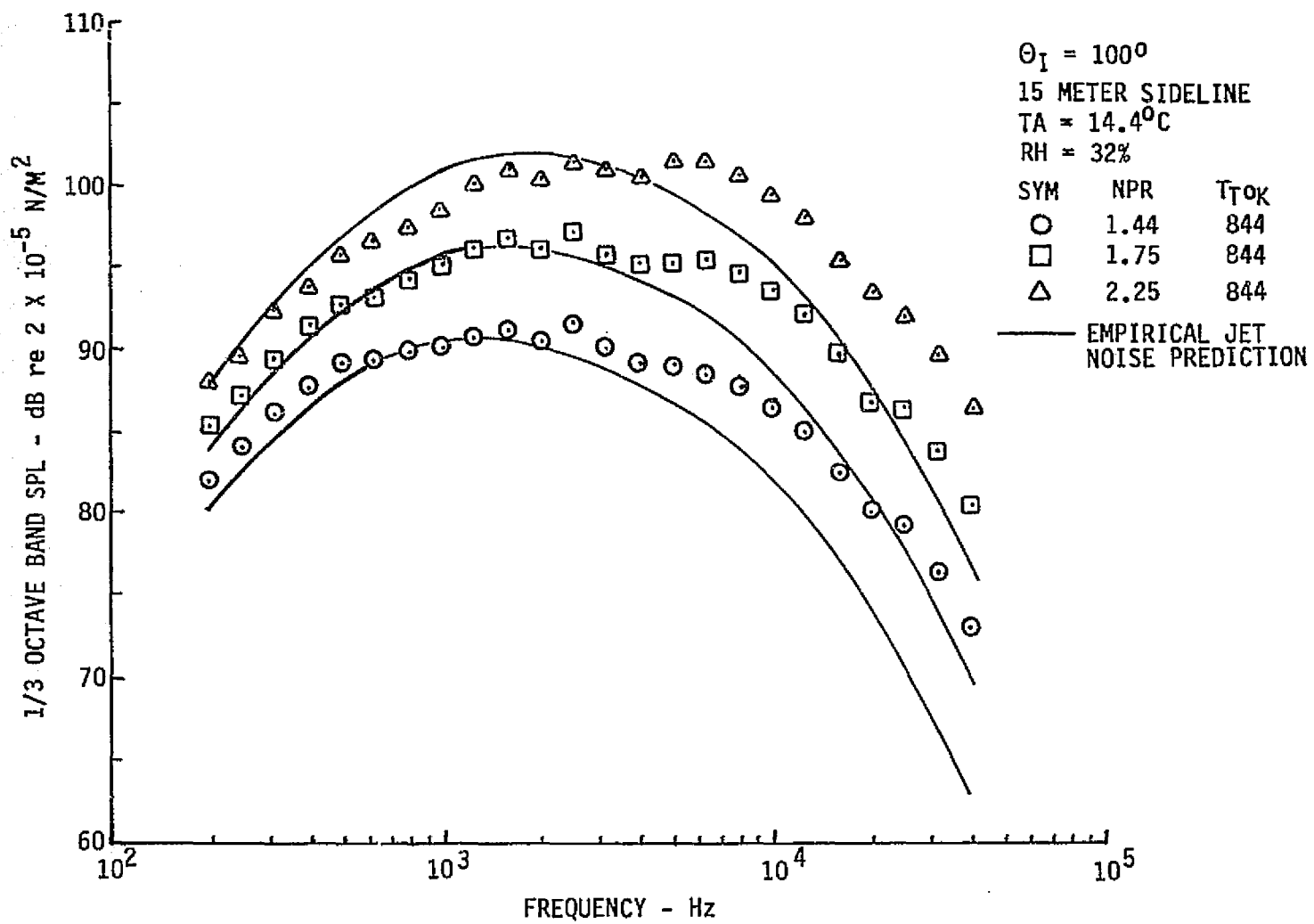


Figure 23.—Comparison of 15-m Sideline Extrapolated Data for the 15.24-cm RC Nozzle and Empirical, Clean, Far-Field Jet Noise Predictions

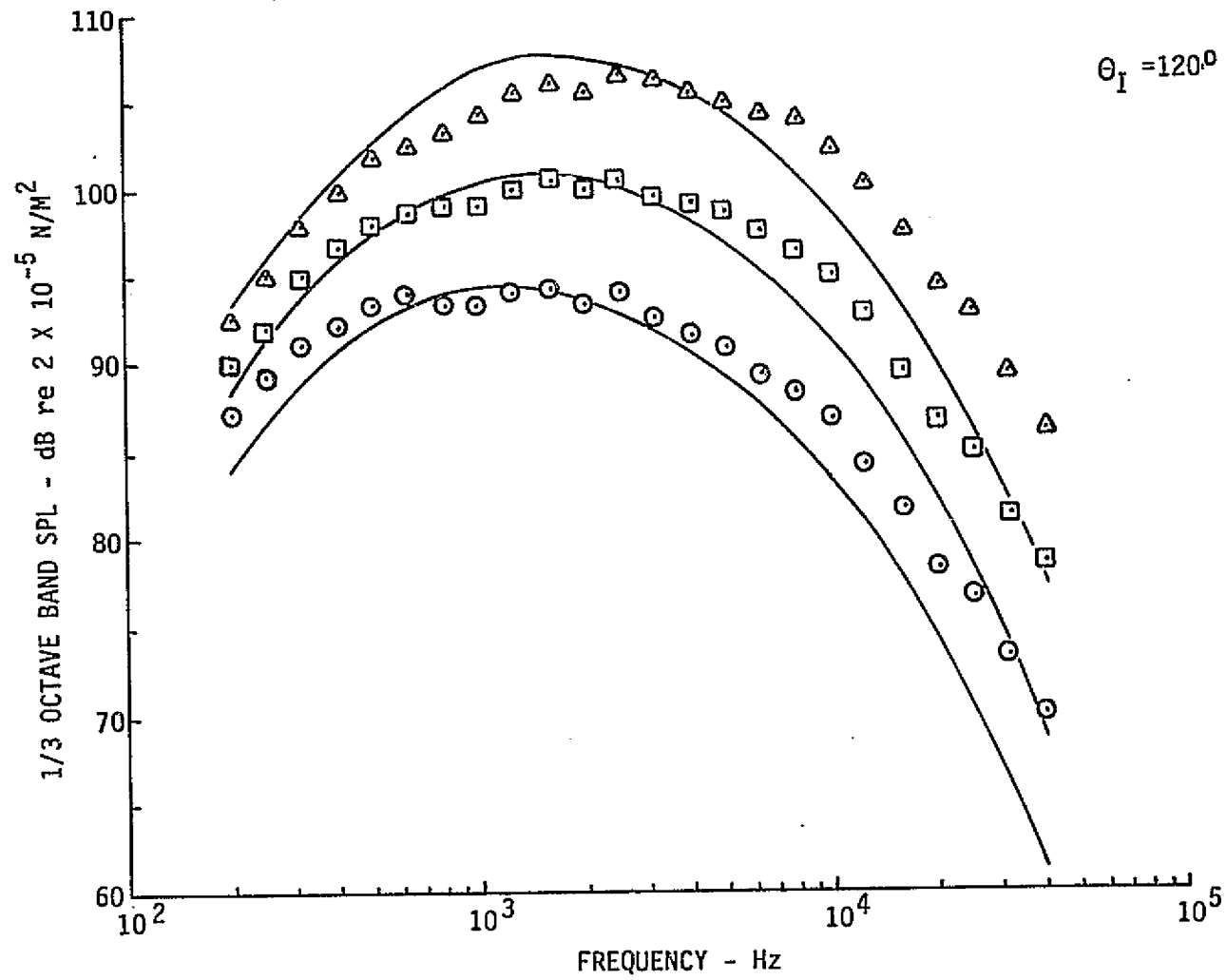


Figure 23.—(Continued)

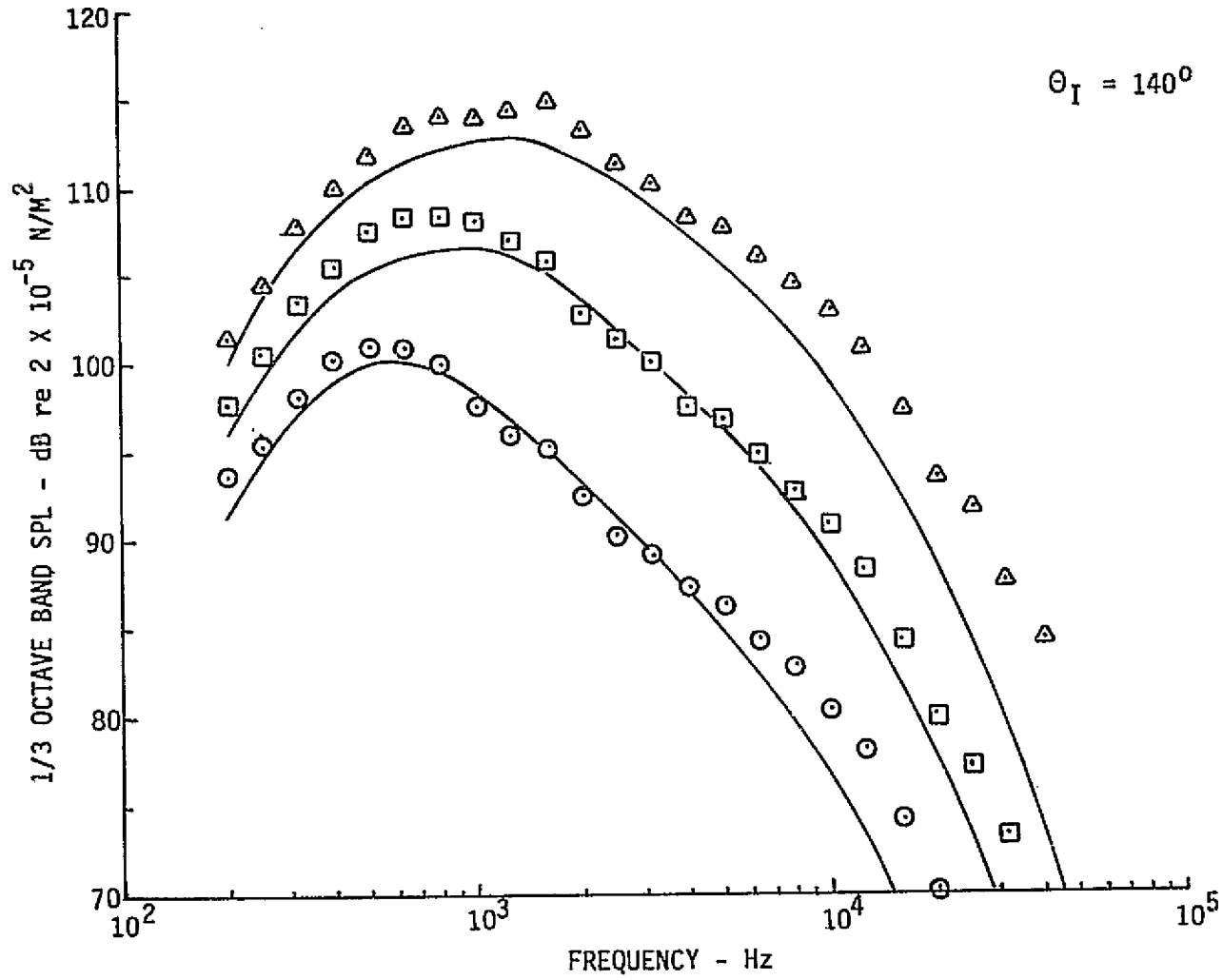


Figure 23.—(Continued)

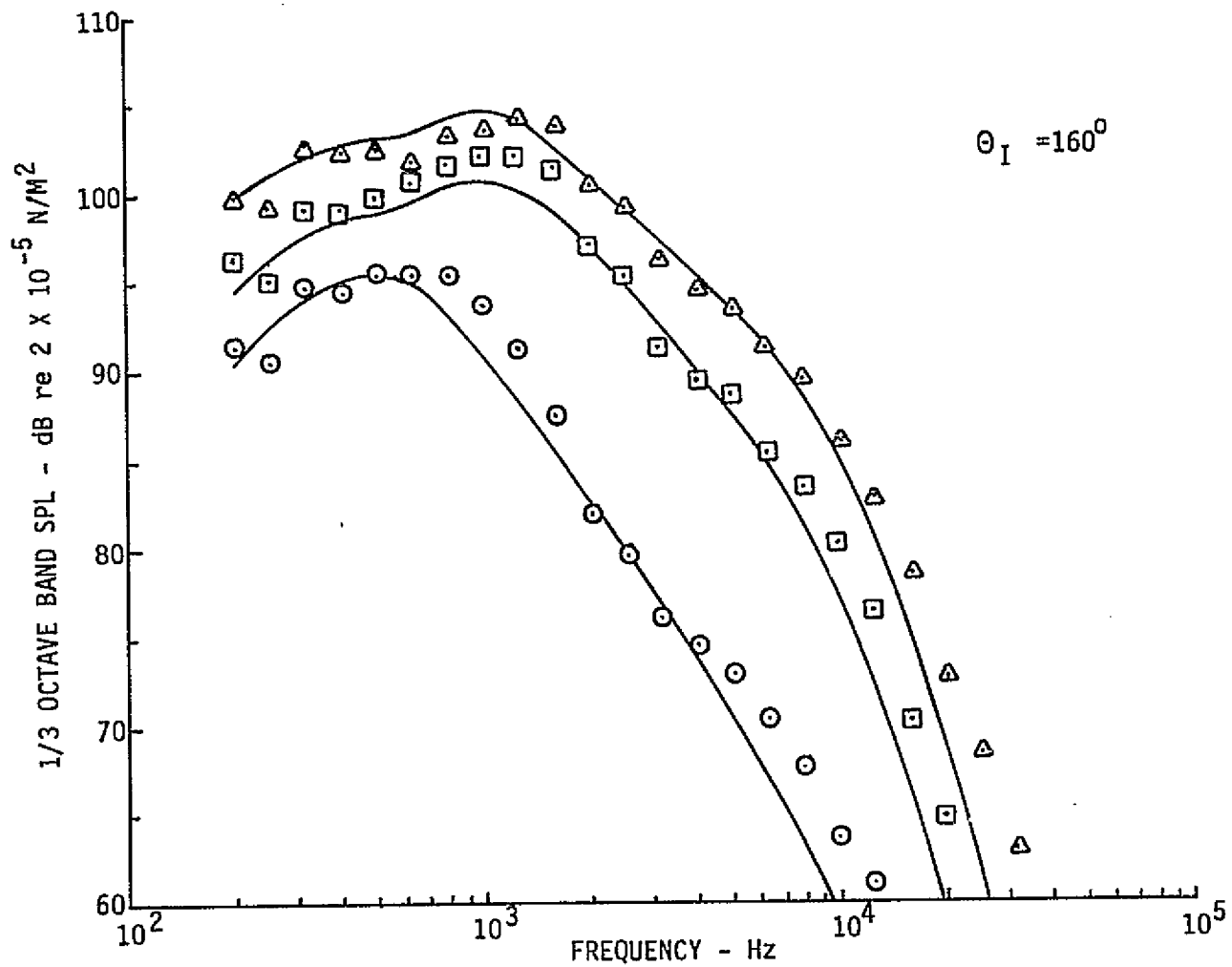


Figure 23. (Concluded)

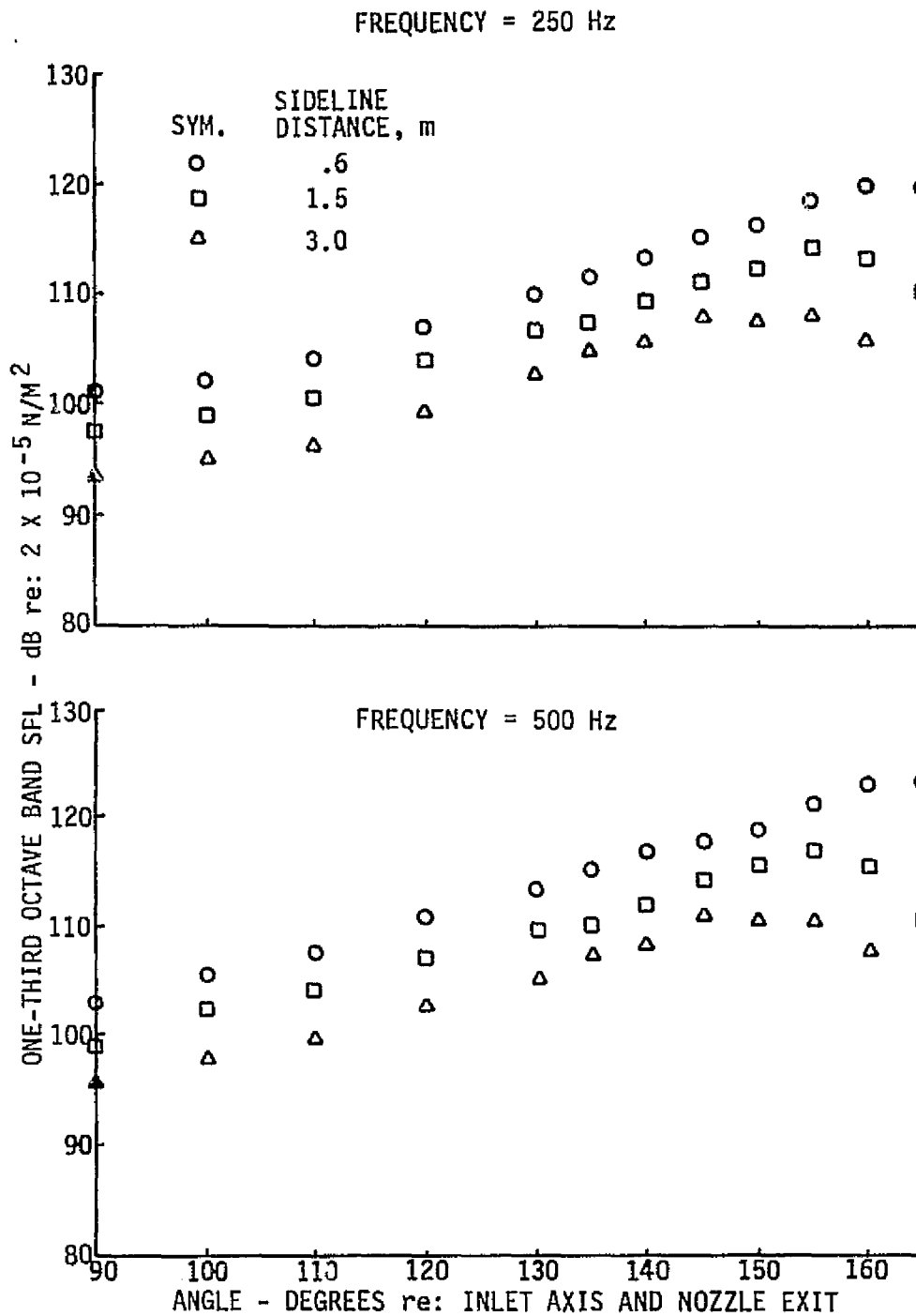


Figure 24.—One-Third Octave Band SPL Directivities for the Annular Nozzle— NPR=1.44,  $T_T=844$  K

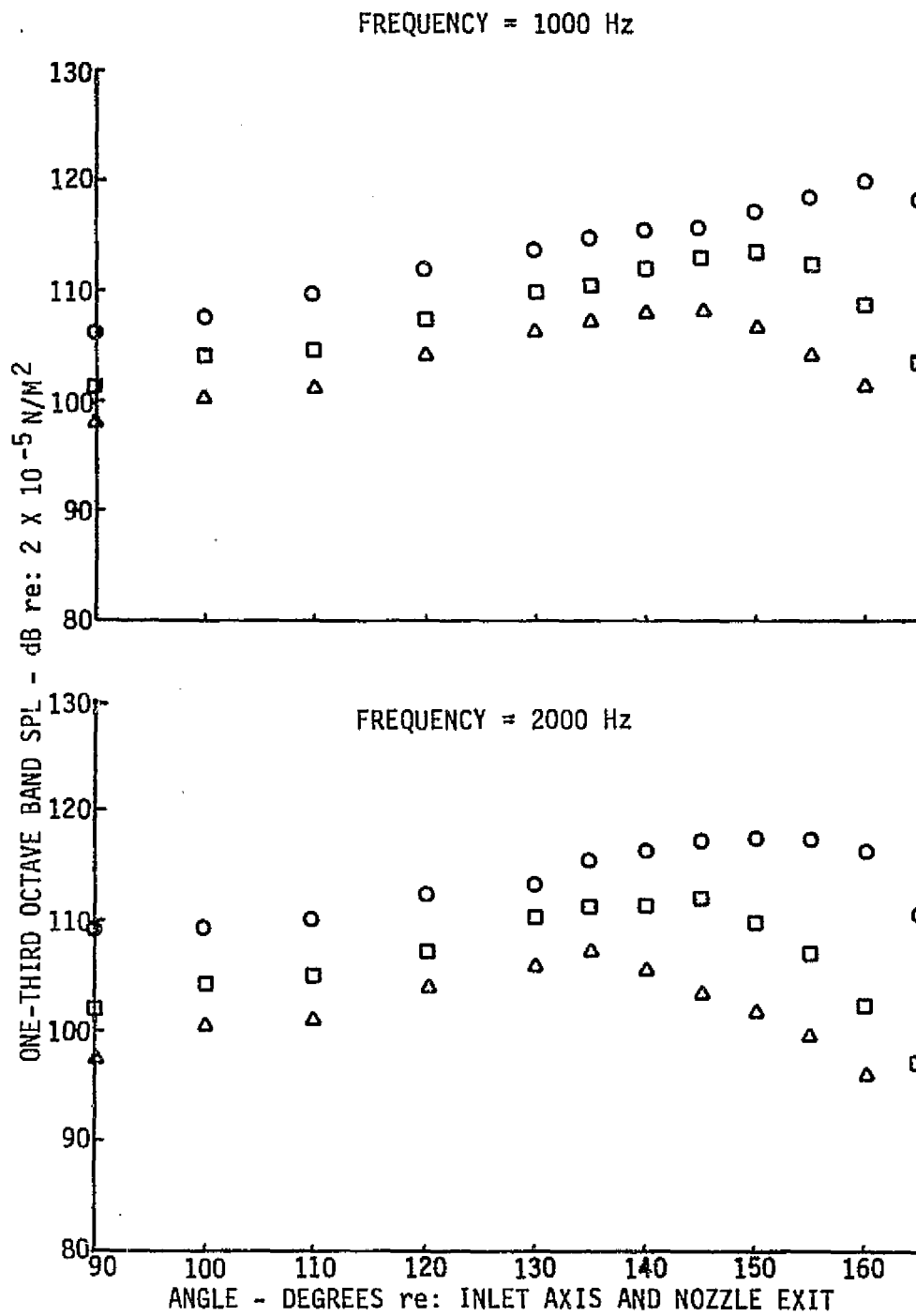


Figure 24.(Continued)

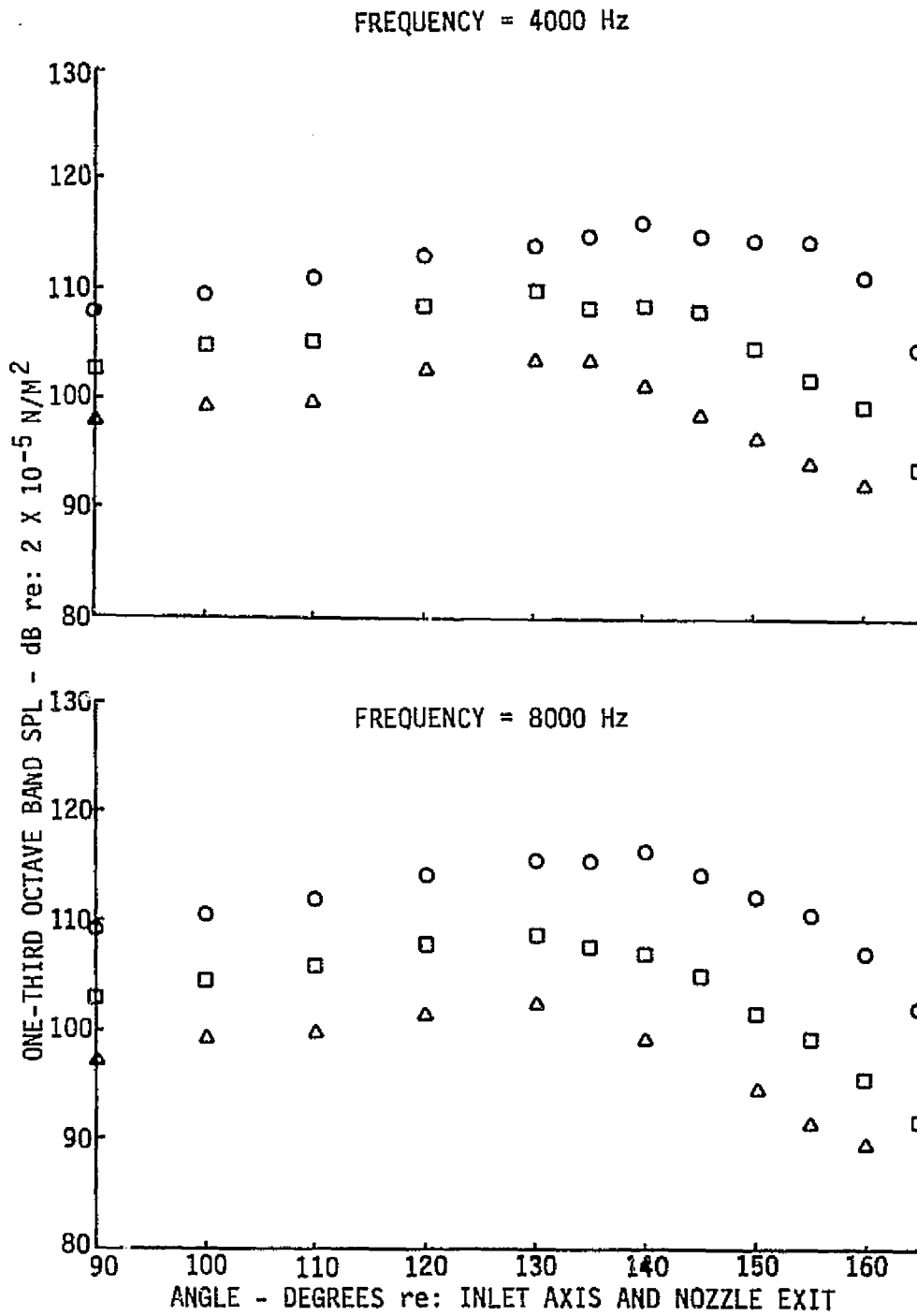


Figure 24.—(Continued)

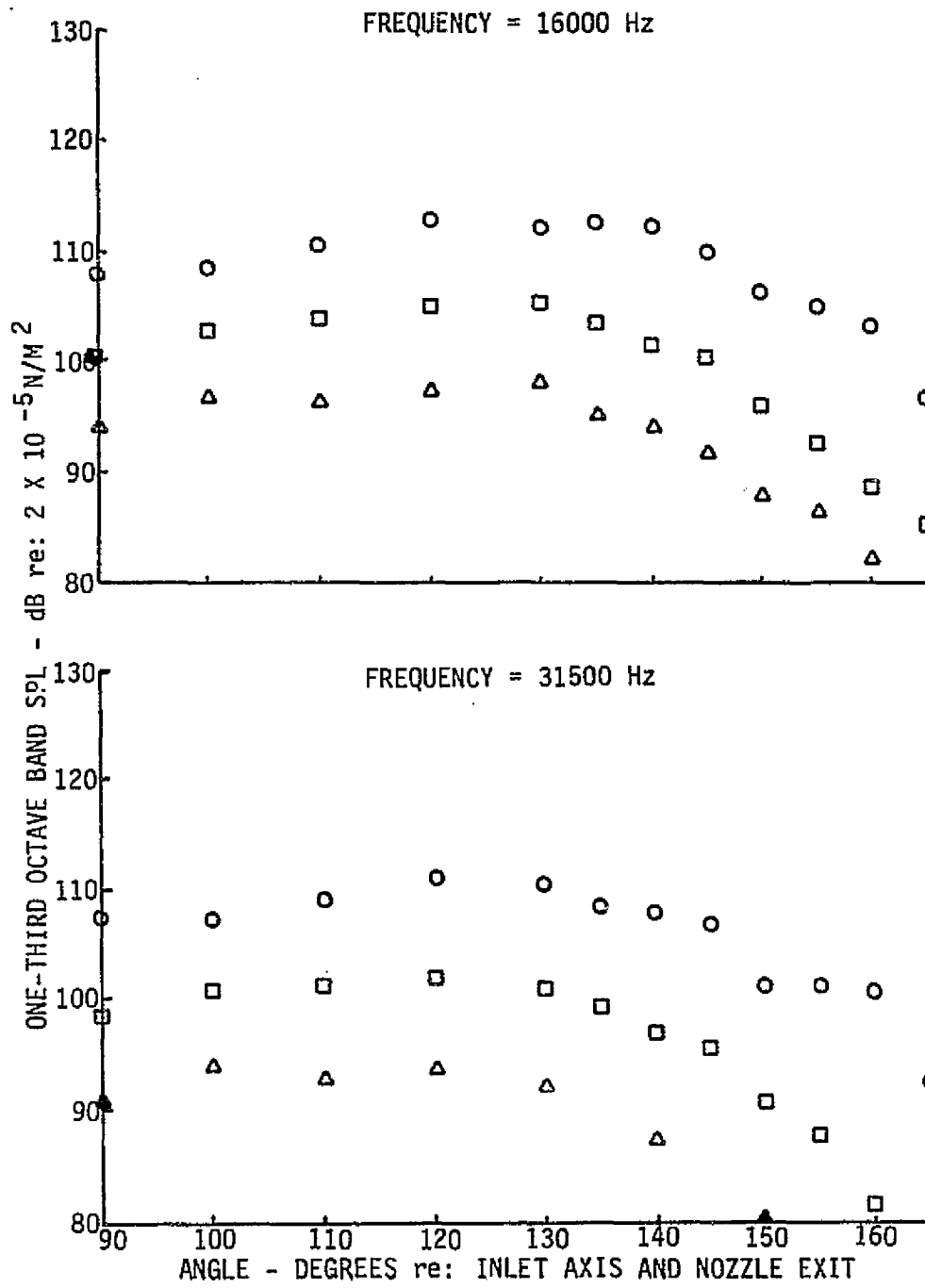


Figure 24.—(Concluded)

$$Y_s/D_{eq} = .7$$

<u>SYM</u>	<u>NPR</u>	<u>T<sub>T2</sub></u> °K
○	1.44	844
□	1.75	844
△	2.25	844

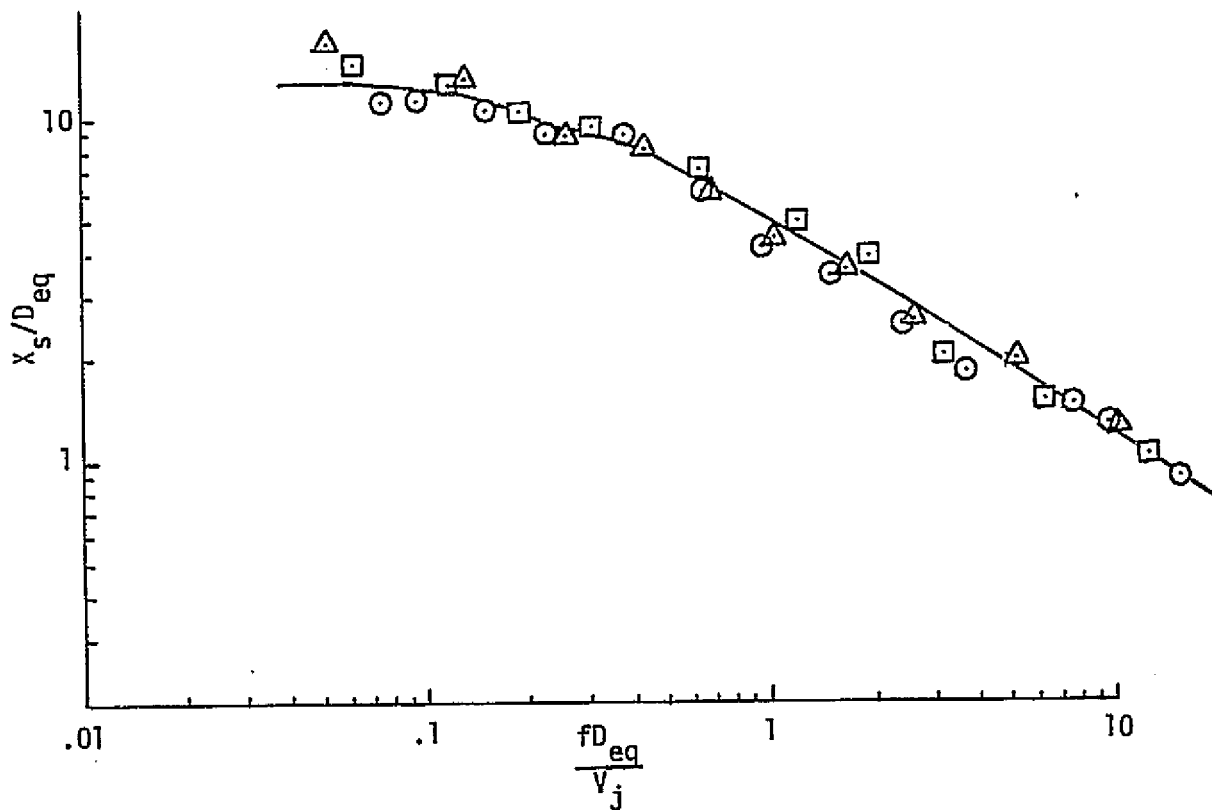


Figure 25.—Peak Noise Source Locations for an Annular Nozzle

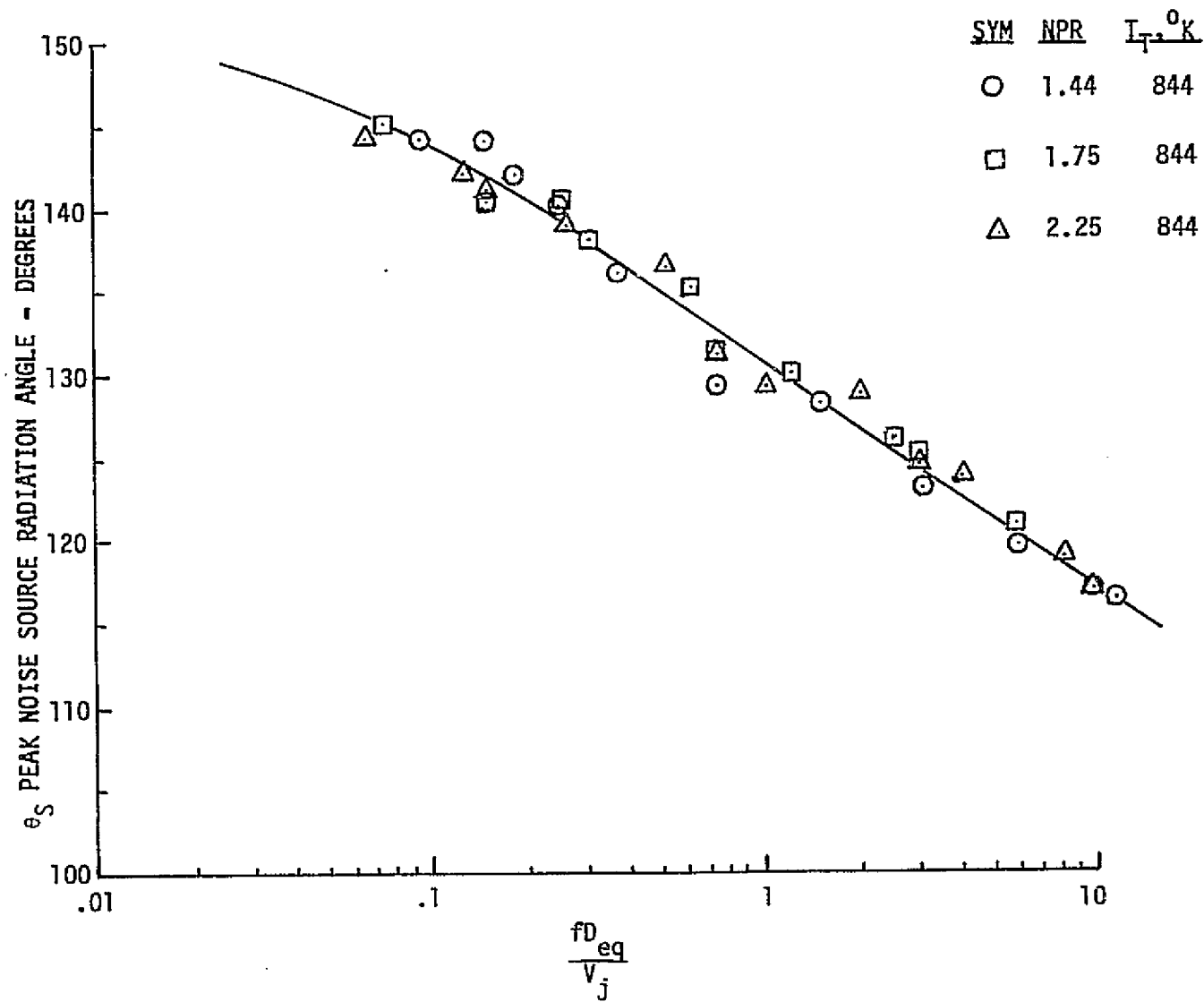


Figure 26.—Peak Noise Source Radiation Angles for the Annular Nozzle

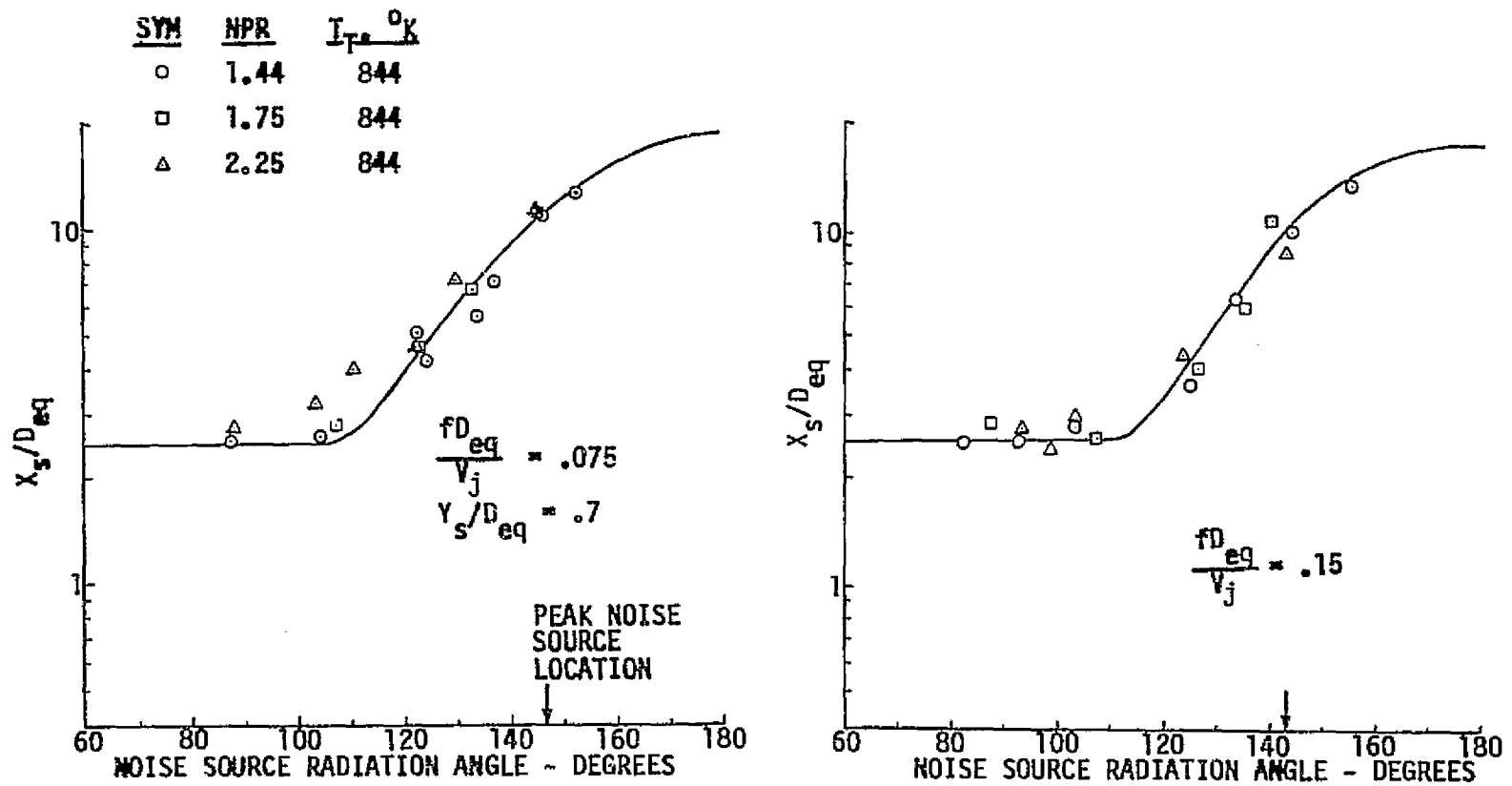


Figure 27.—Distributed Noise Source Locations for a Jet From an Annular Nozzle

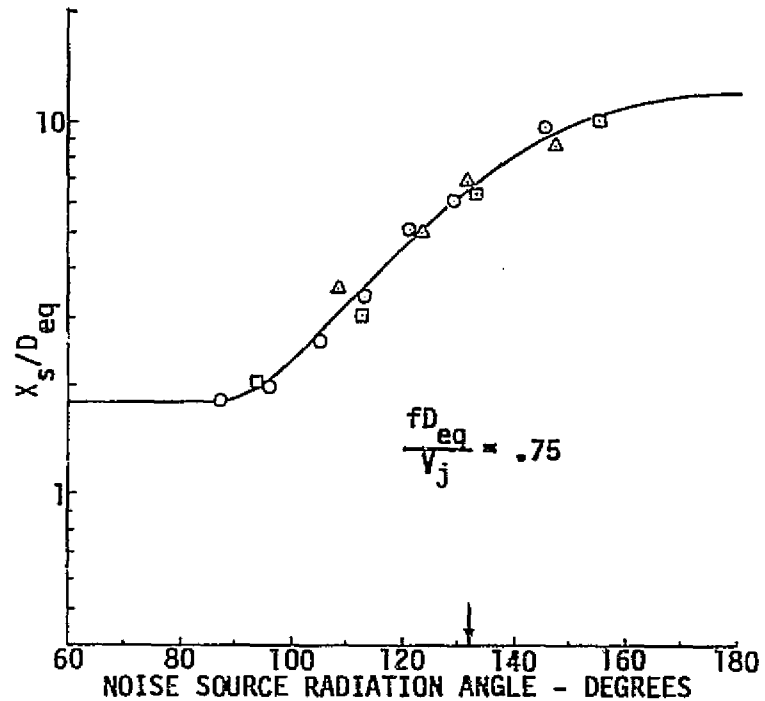
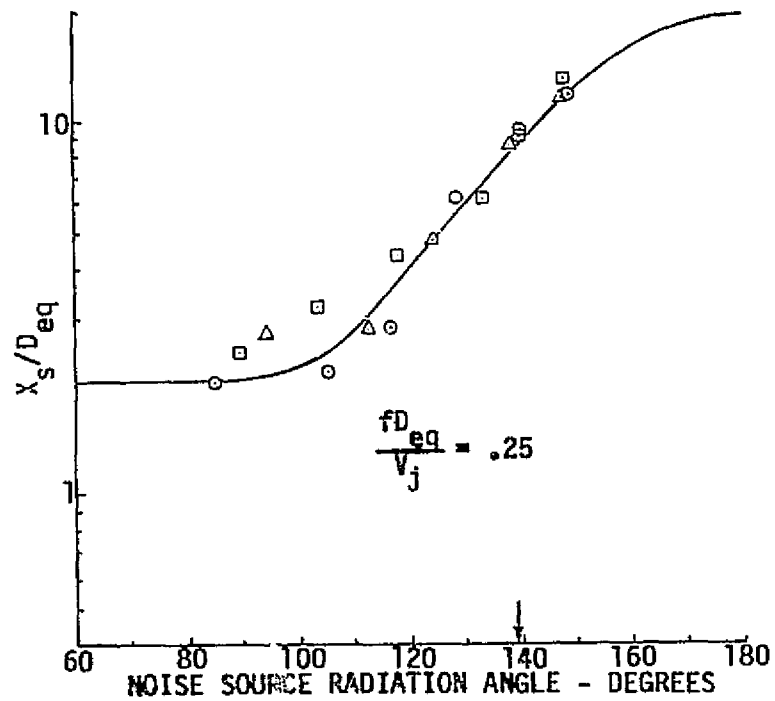


Figure 27.—(Continued)

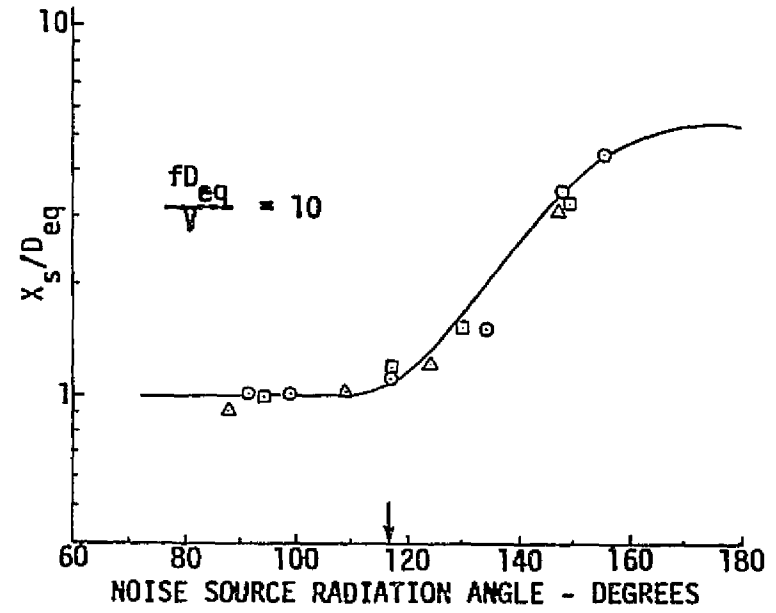
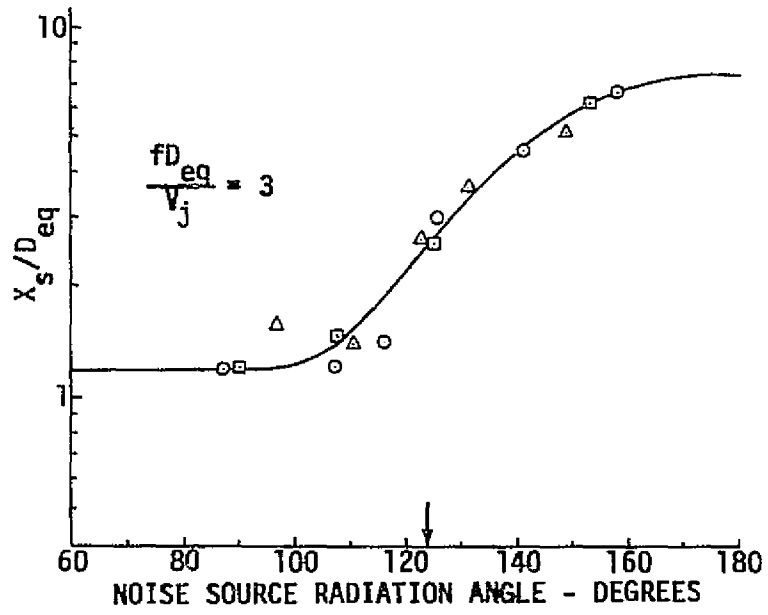


Figure 27.—(Concluded)

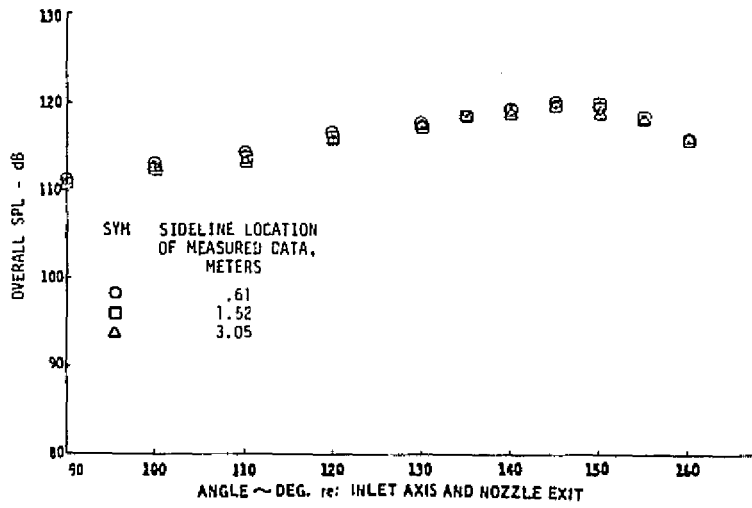


Figure 28.—OASPL and One-Third-Octave-Band SPL Directivity Data for the Annular Nozzle Extrapolated to a 3.0-m Sideline—NPR = 1.44,  $T_T = 844$  K

ORIGINAL PAGE IS  
OF POOR QUALITY.

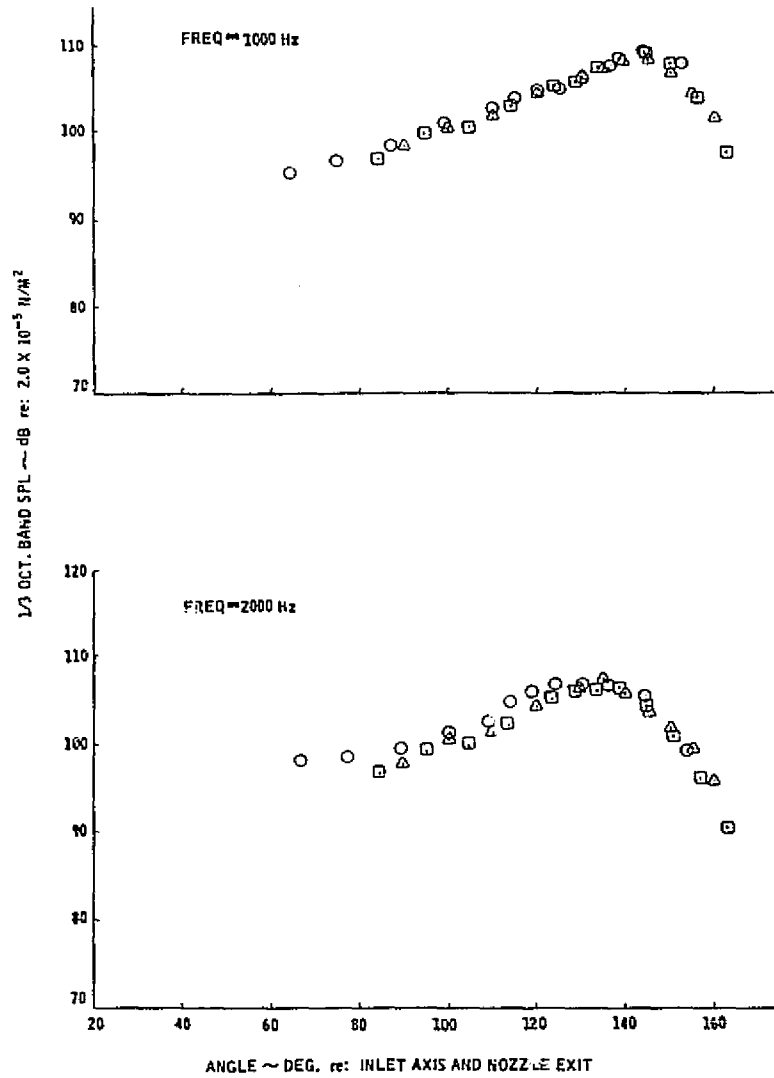
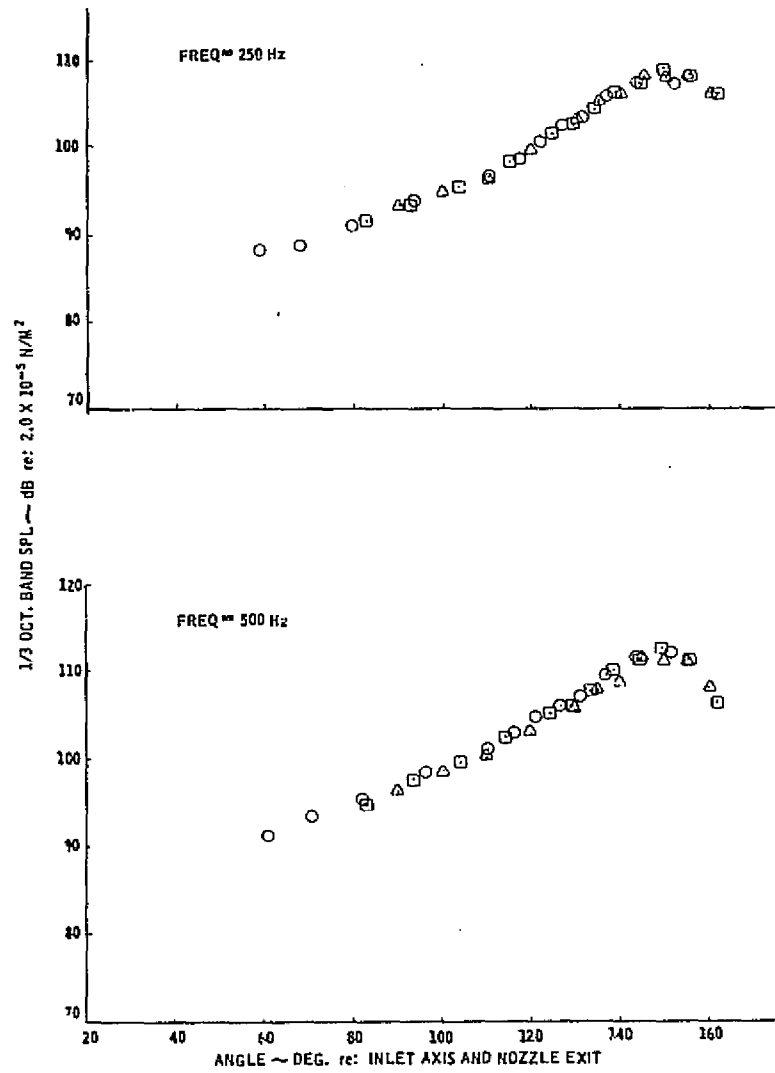


Figure 28.—(Continued)

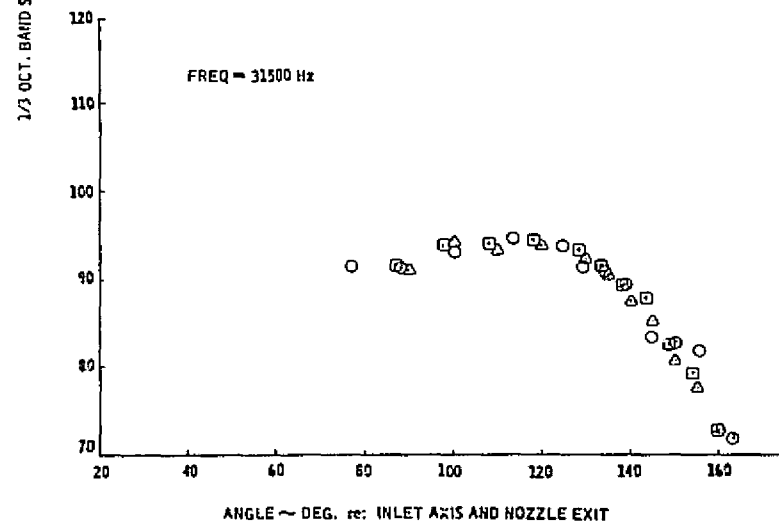
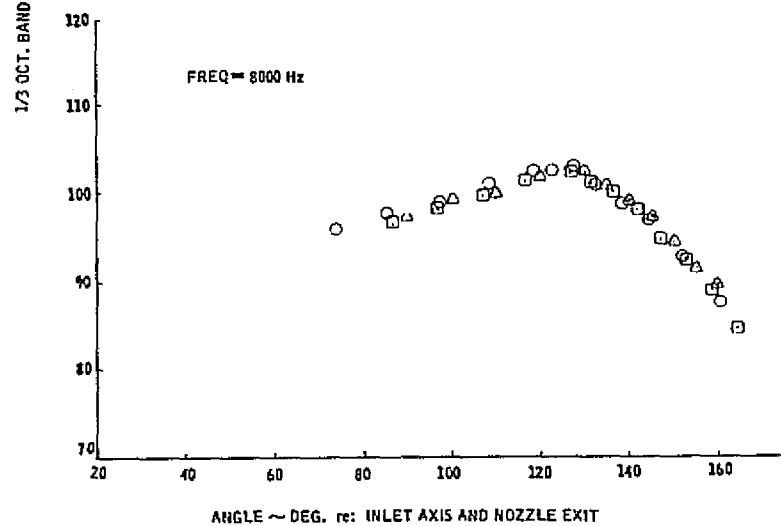
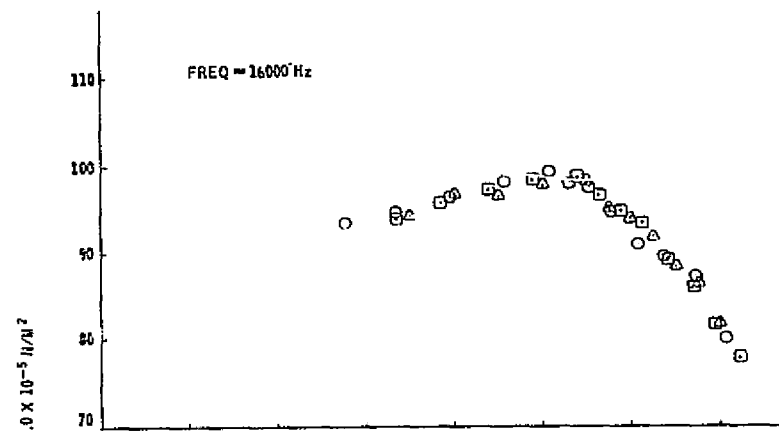
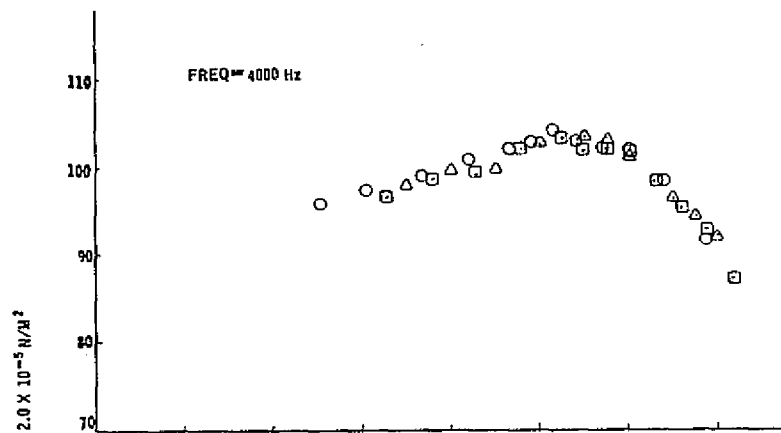


Figure 28.—(Concluded)

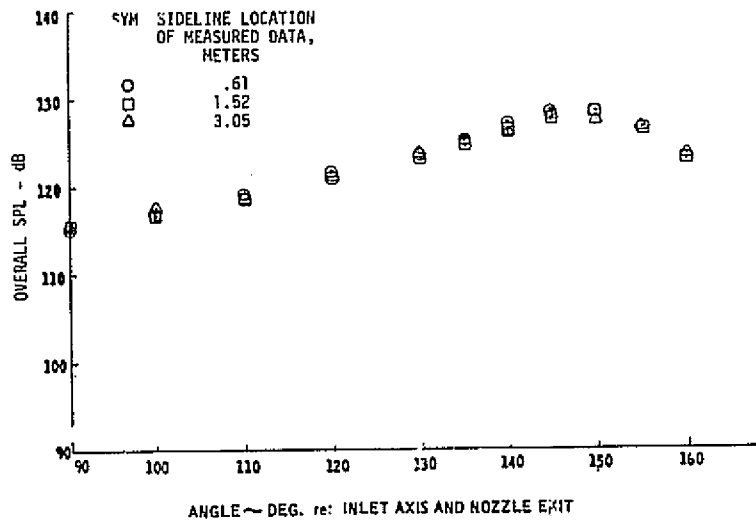


Figure 29.—OASPL and One-Third-Octave-Band SPL Directivity Data for the Annular Nozzle Extrapolated to a 3.0-m Sideline—NPR = 1.75,  $T_T = 844$  K

ORIGINAL PAGE IS  
 OF POOR QUALITY

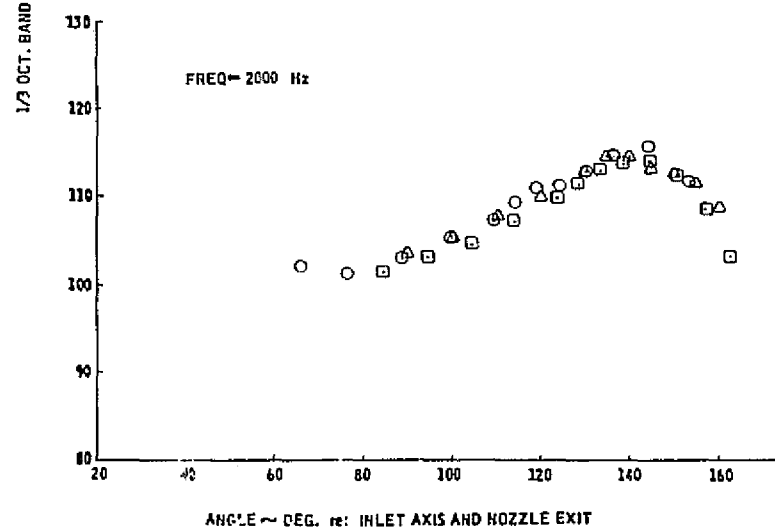
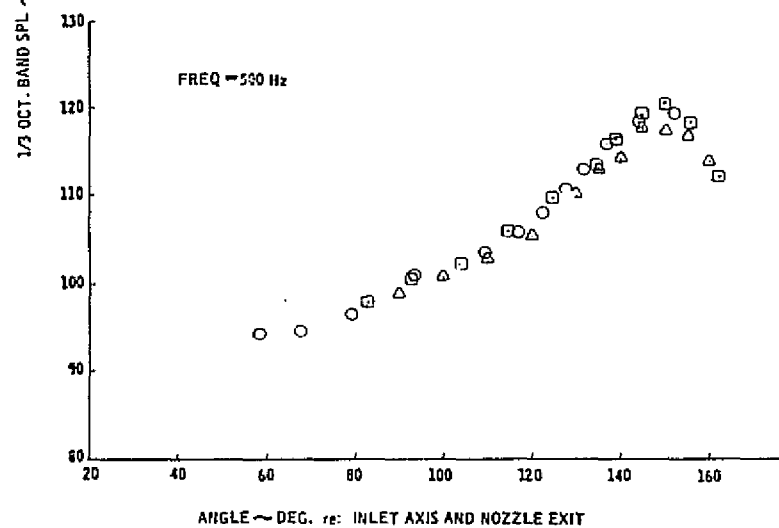
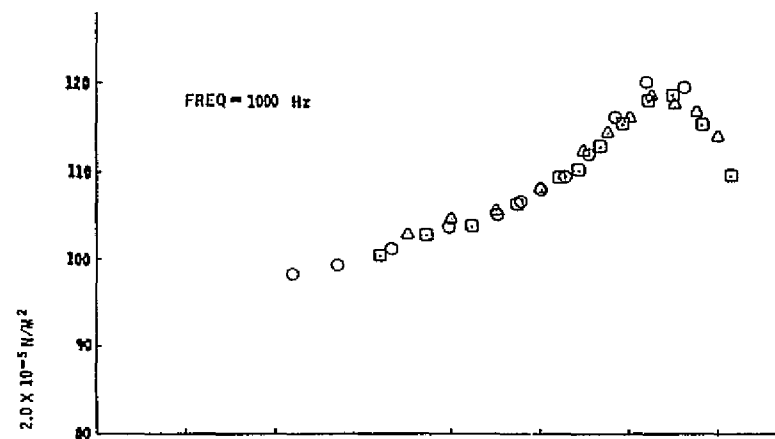
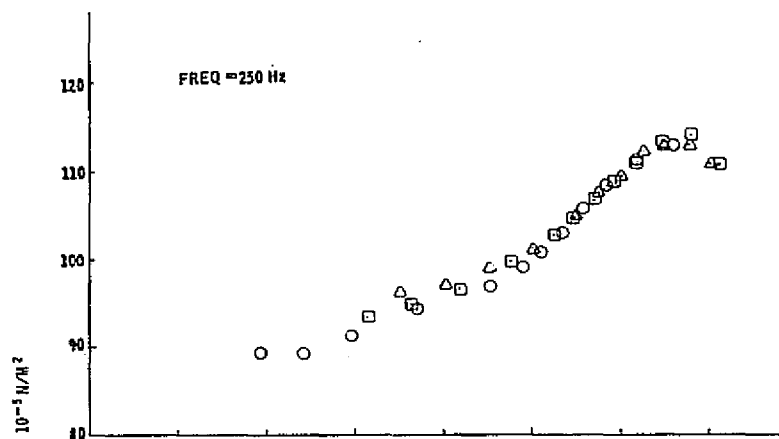


Figure 29.—(Continued)

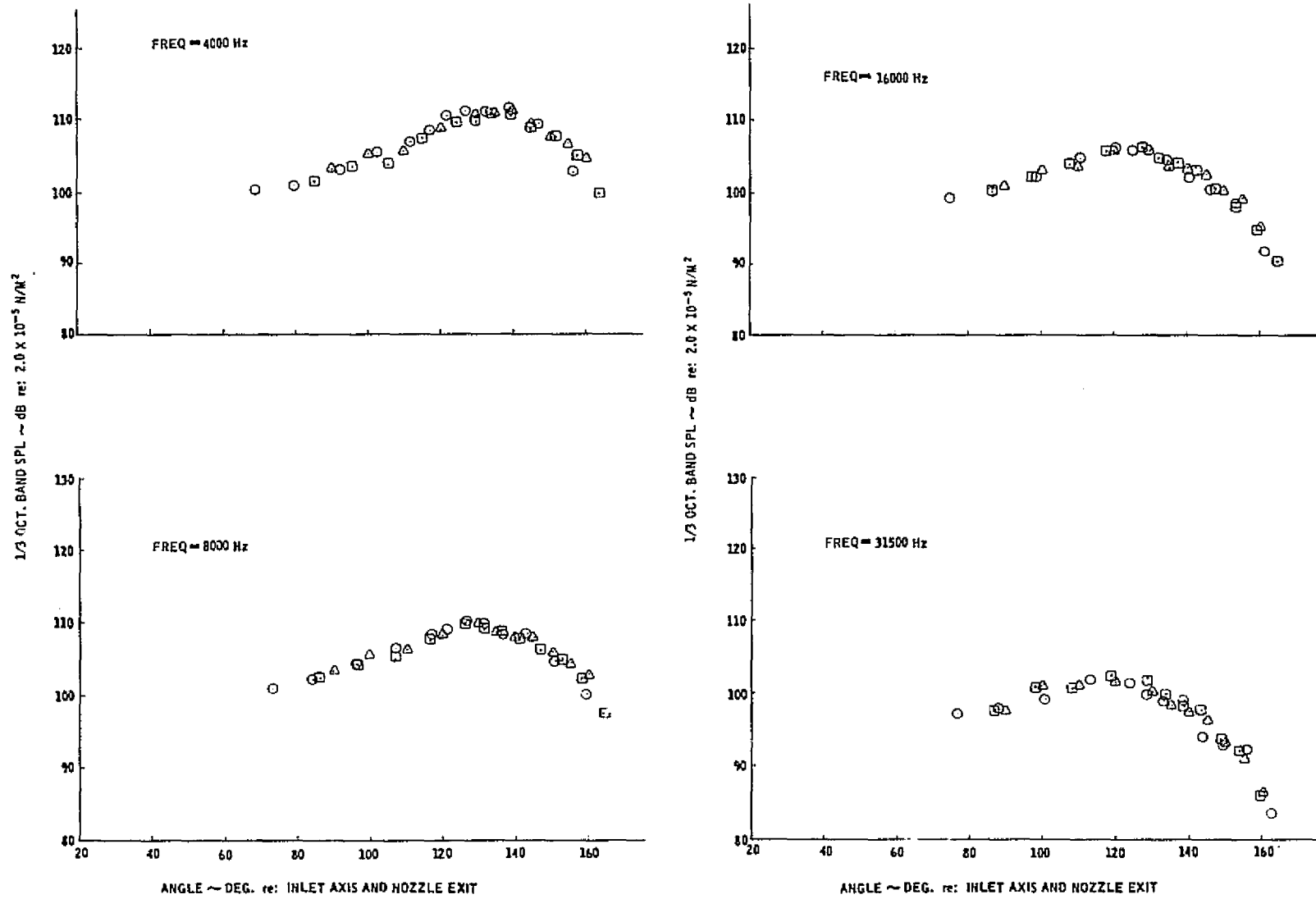


Figure 29.--(Concluded)

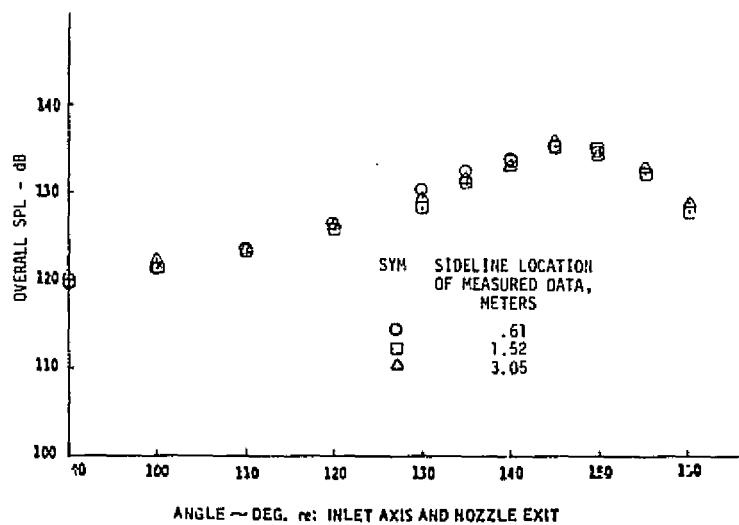


Figure 30.—OASPL and One-Third-Octave-Band SPL Directivity Data for the Annular Nozzle Extrapolated to a 3.0-m Sideline—NPR = 2.25,  $T_T = 344$  K

ORIGINAL PAGE IS  
OF POOR QUALITY.

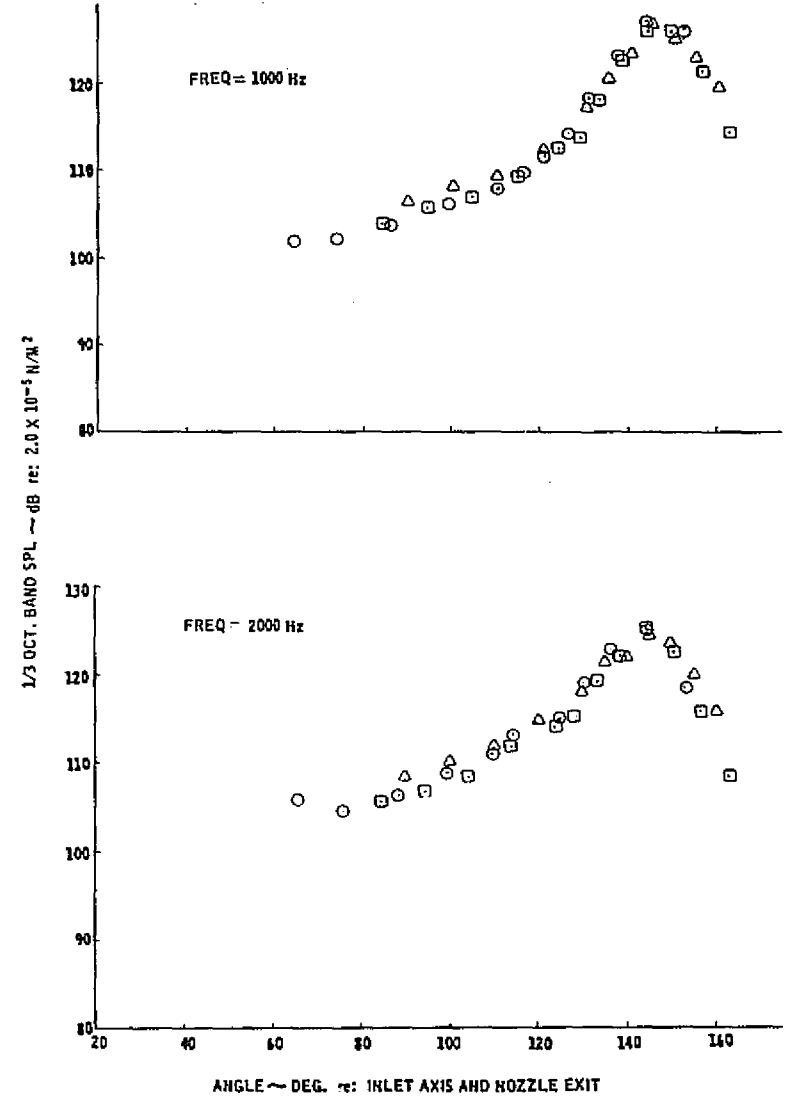
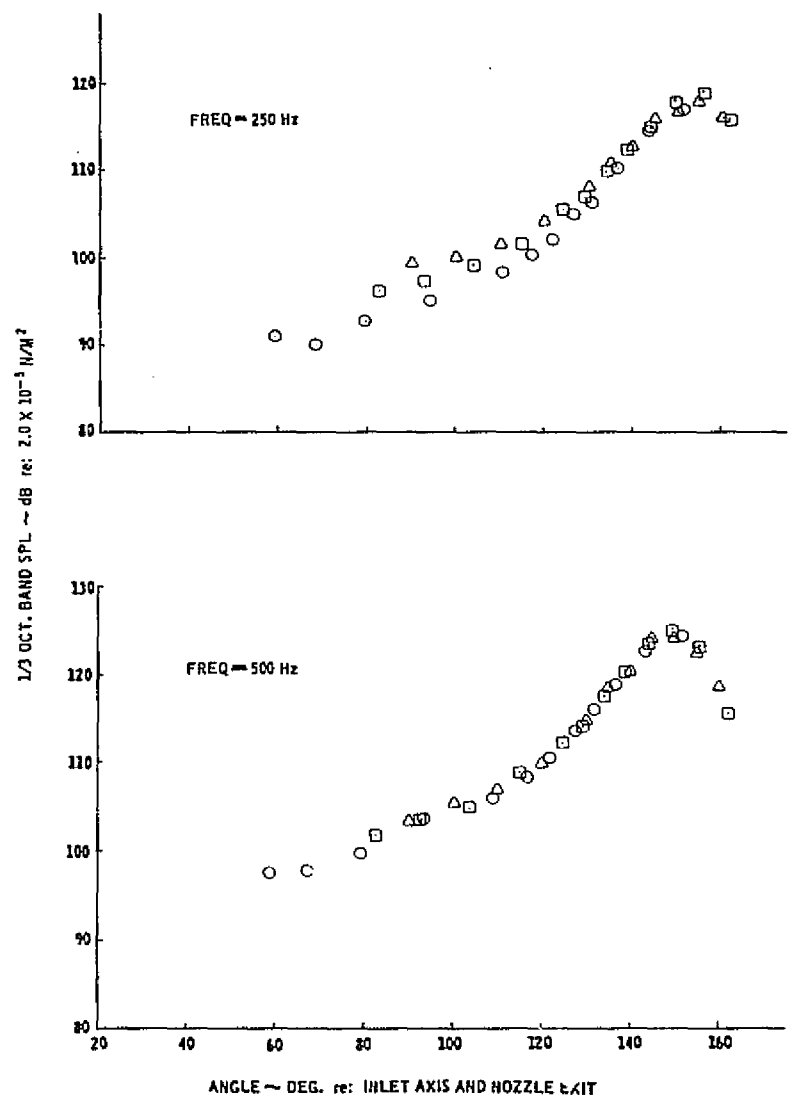


Figure 30.-(Continued)

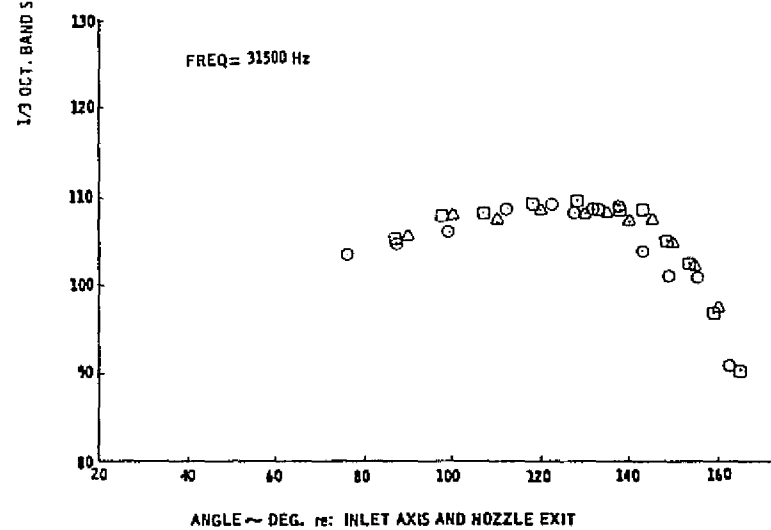
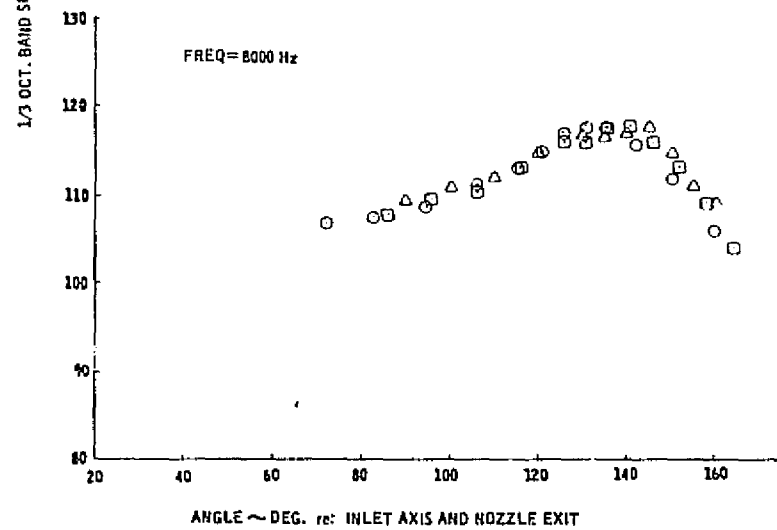
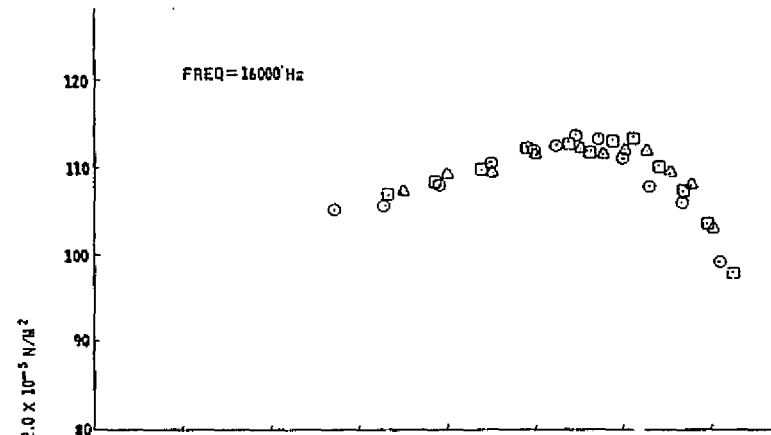
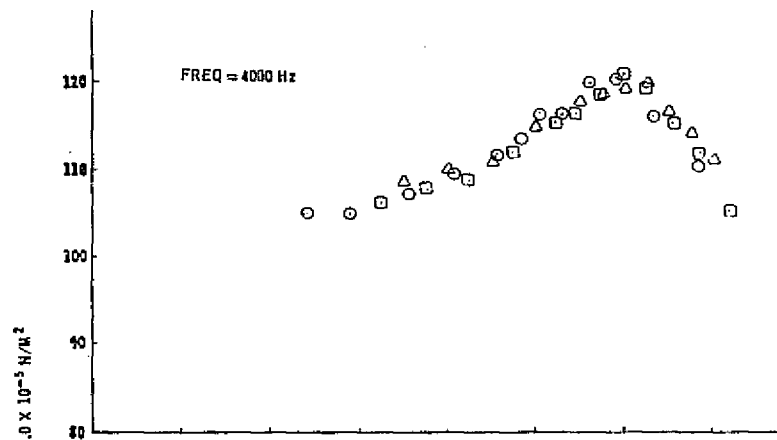


Figure 30.-(Concluded)

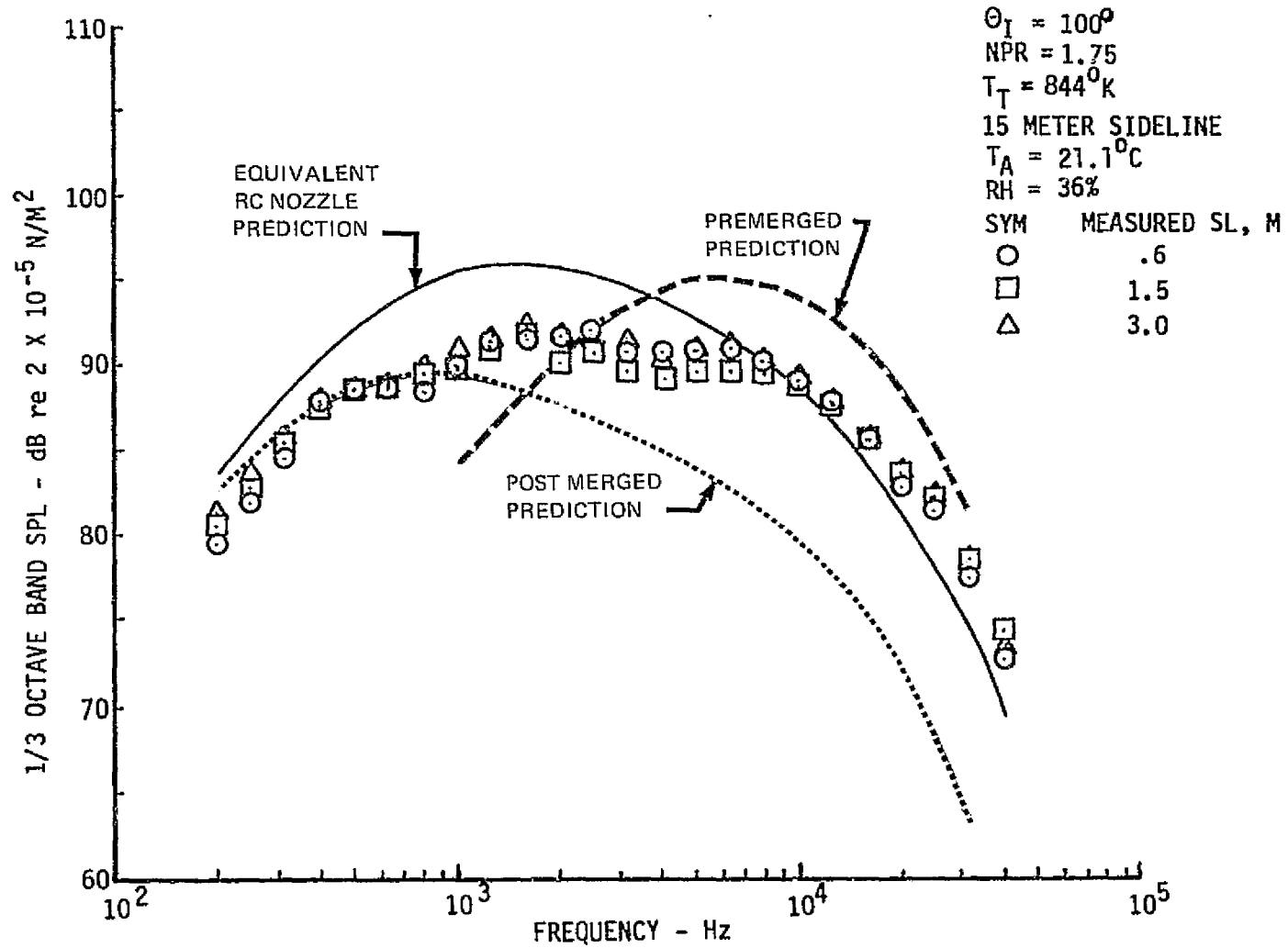


Figure 31.—Comparison of 15-m Sideline Extrapolated Data for the Annular Nozzle and Clean, Far-Field Jet Noise Predictions

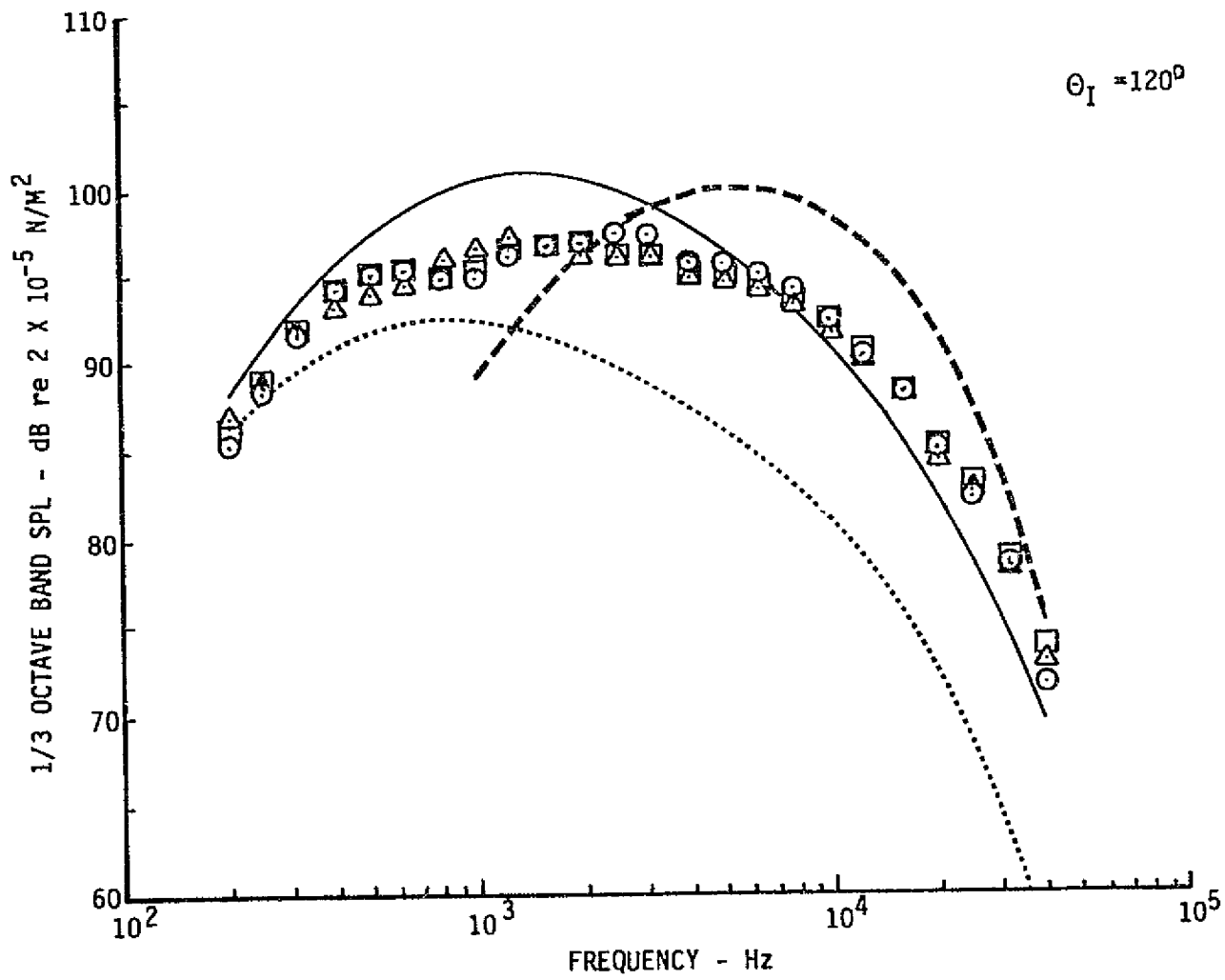


Figure 31. -(Continued)

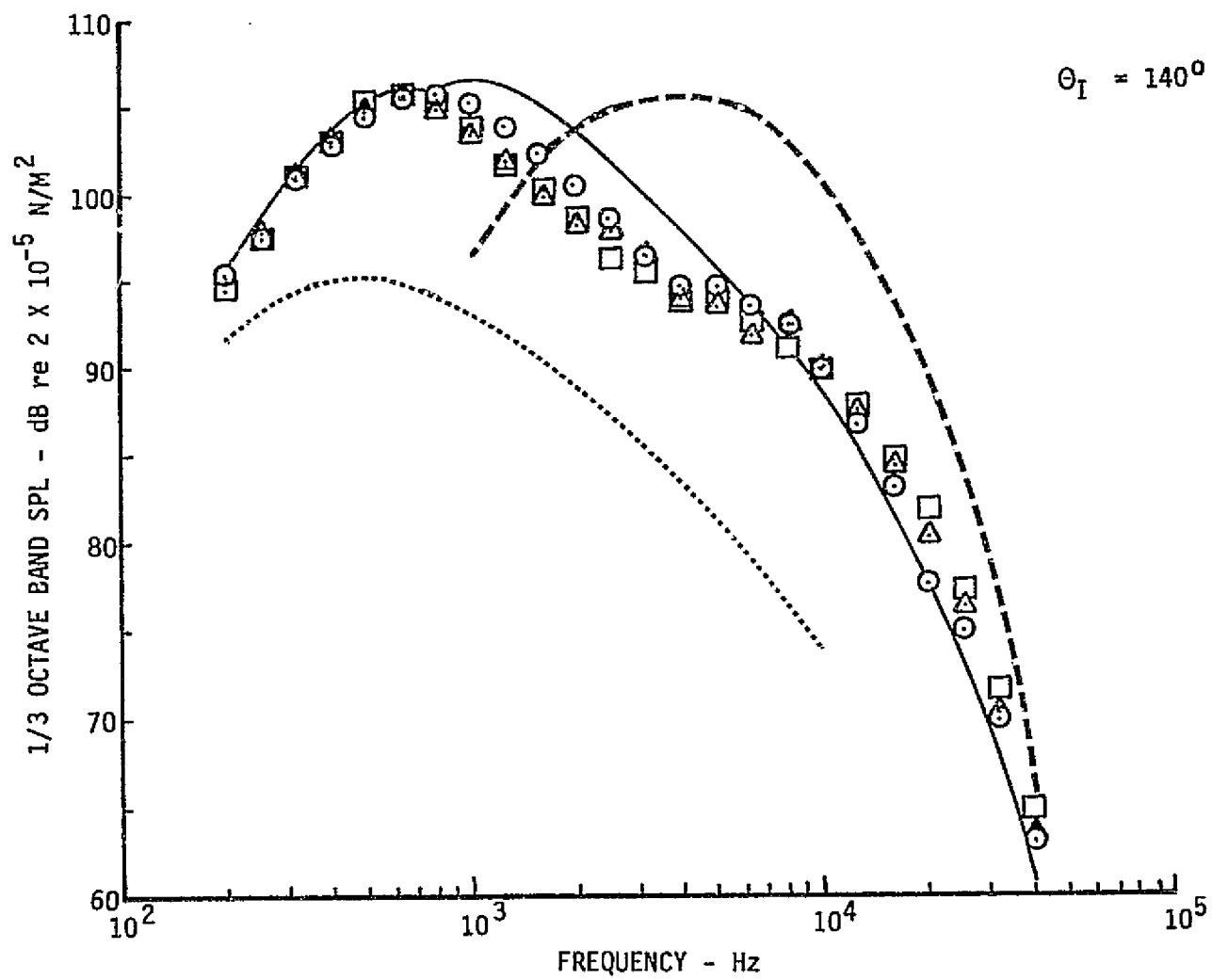


Figure 31.—(Continued)

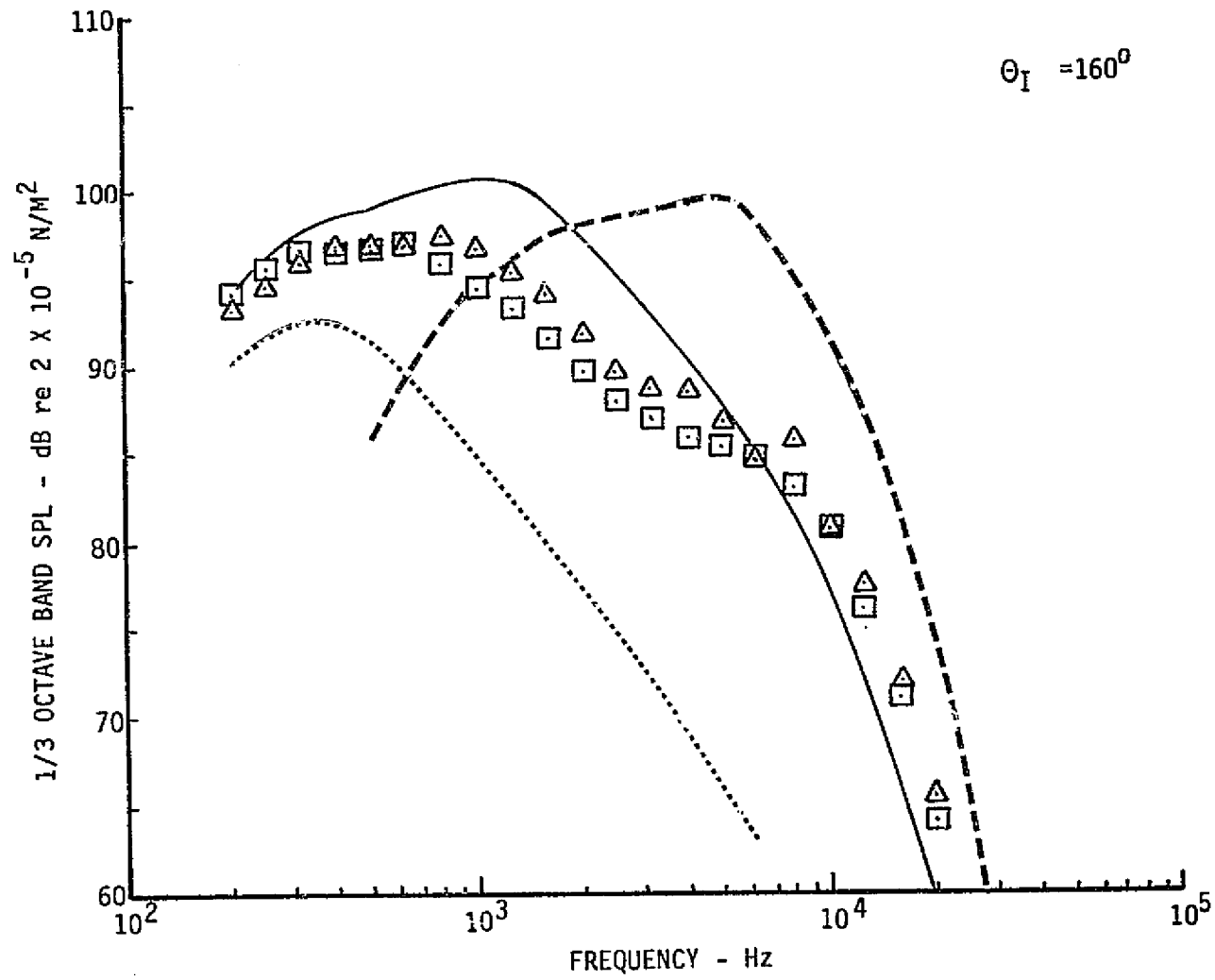


Figure 31.—(Concluded)

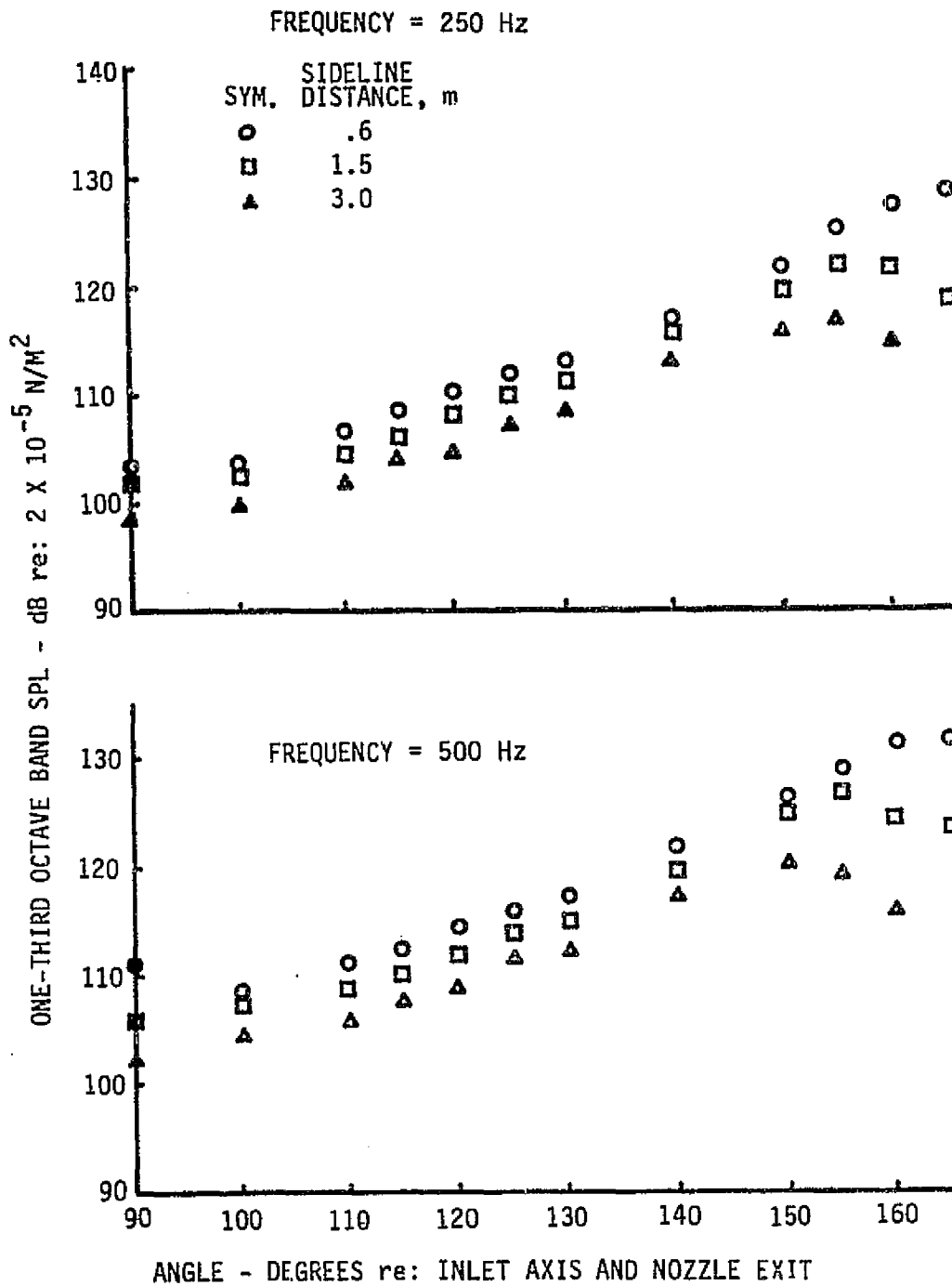


Figure 32.—One-Third-Octave-Band SPL Directivities for the 20-Lobe Nozzle—  
 NPR = 2.25,  $T_T = 844 \text{ K}$

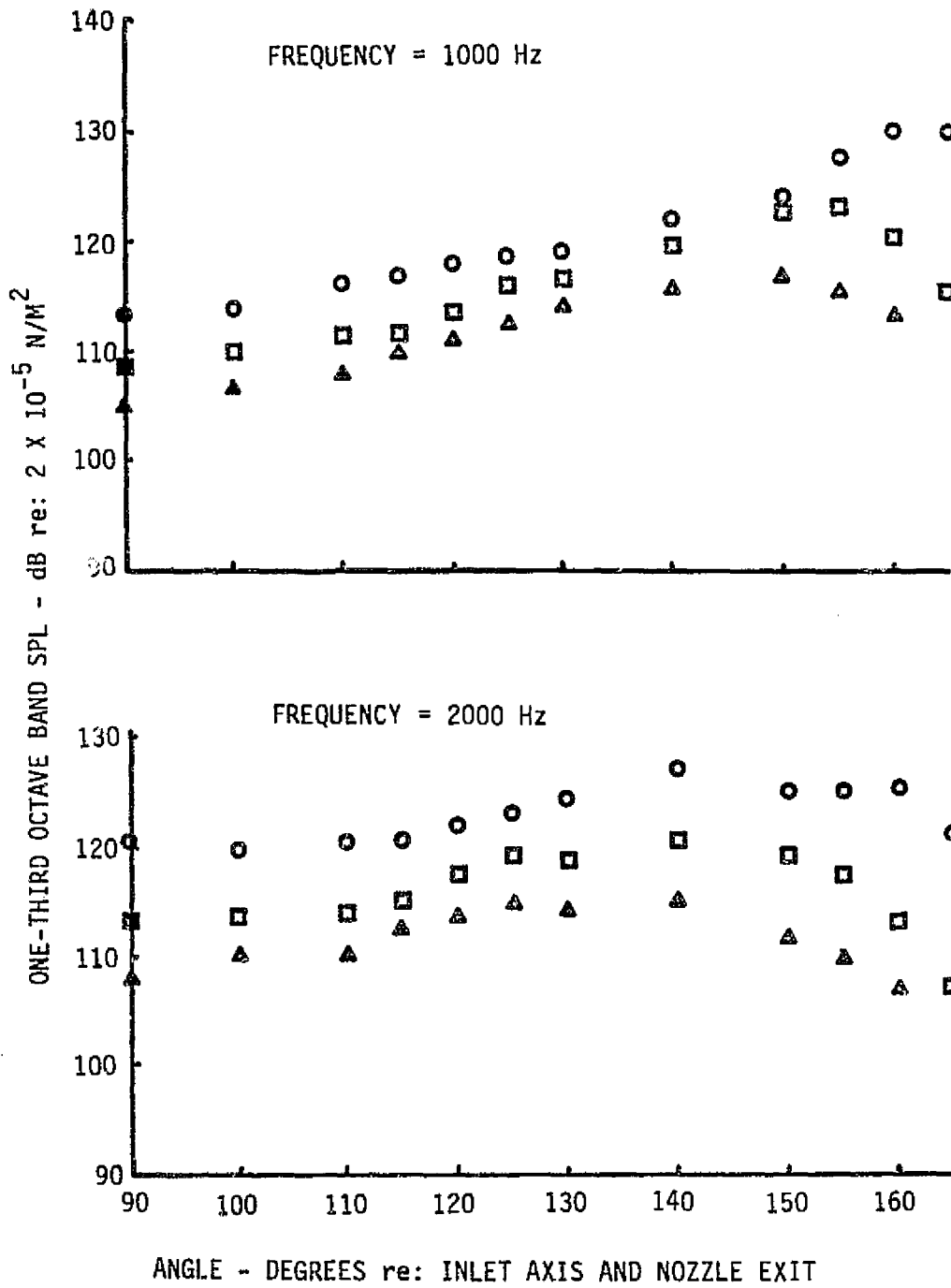
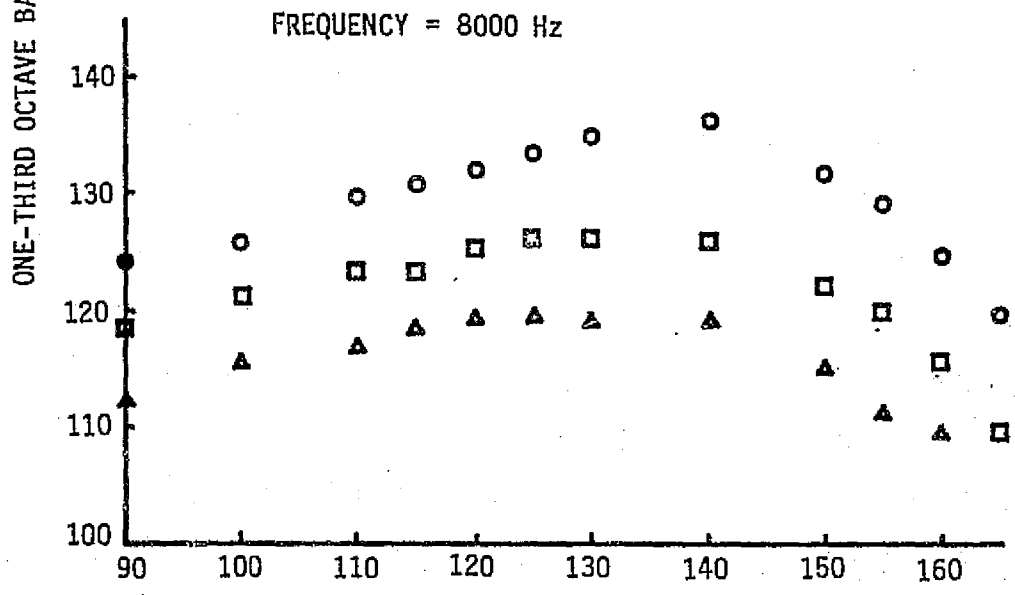
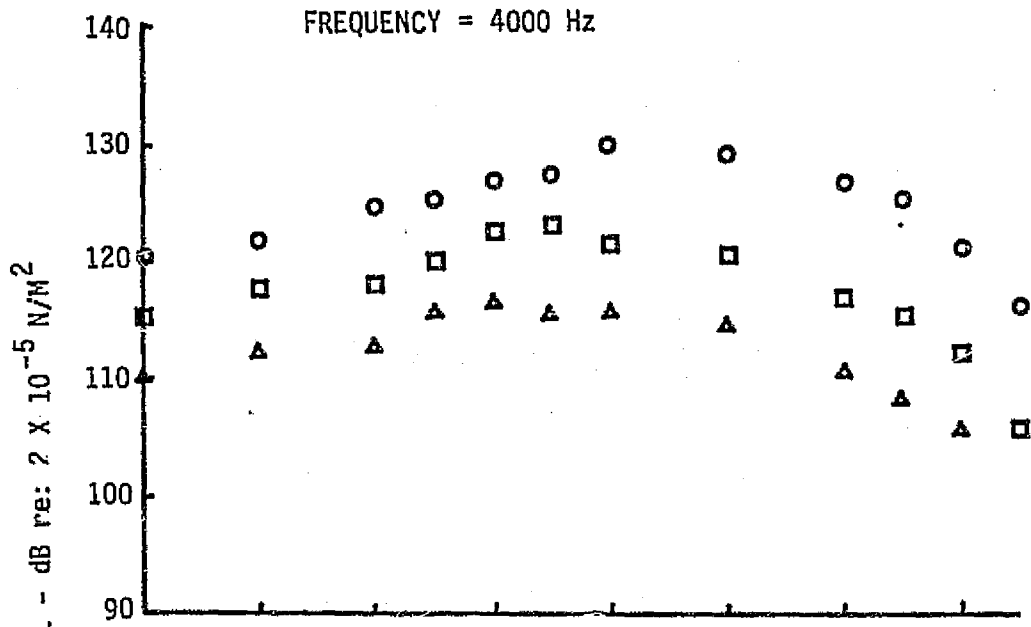


Figure 32.--(Continued)



ANGLE - DEGREES re: INLET AXIS AND NOZZLE EXIT

Figure 32.-(Continued)

C. 2

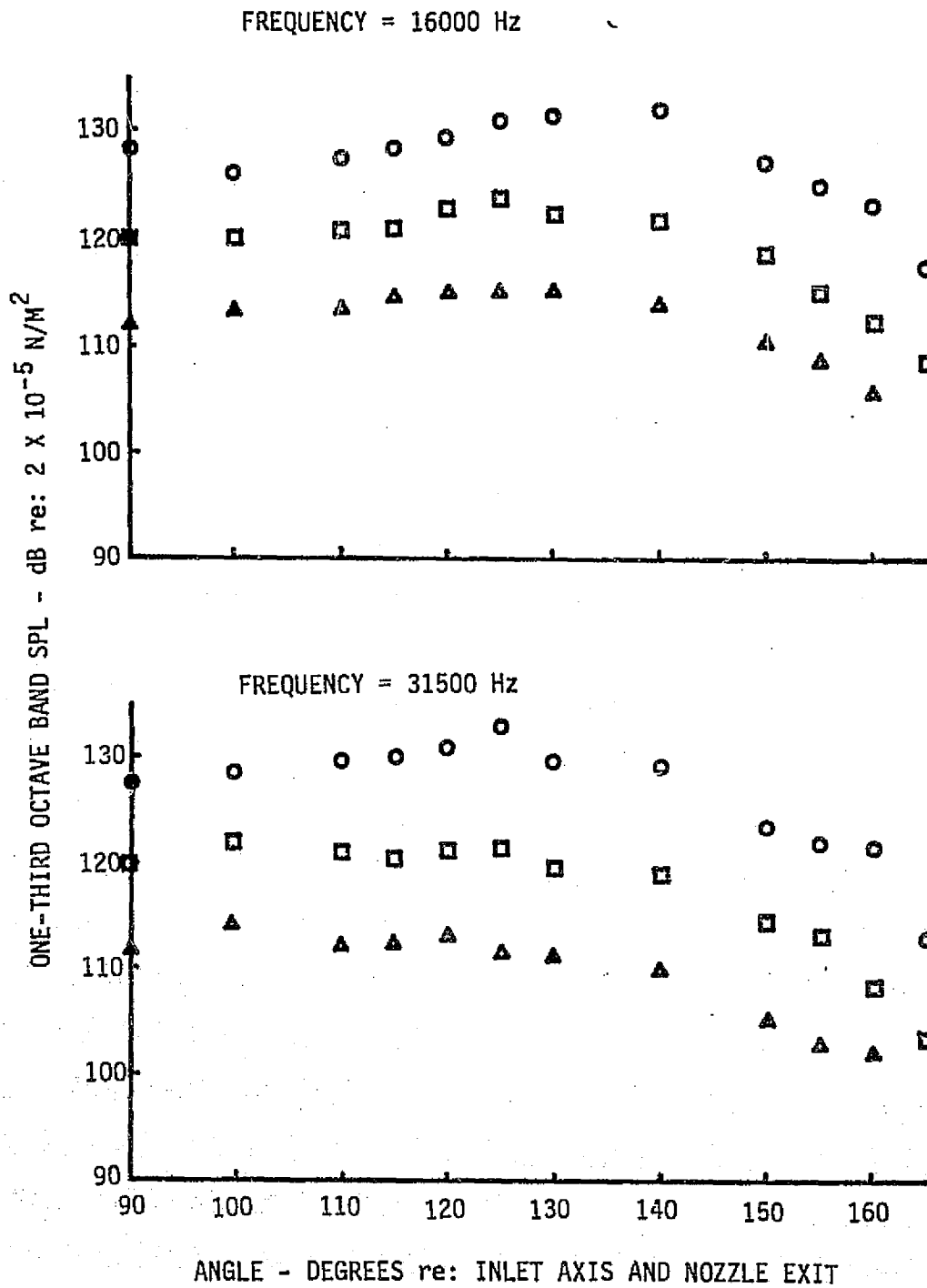


Figure 32.—(Concluded)

$$Y_s/D_{eq} = .8$$

<u>SYM</u>	<u>NPR</u>	<u>T<sub>Tz</sub></u> °K
○	1.44	844
□	1.75	844
△	2.25	844

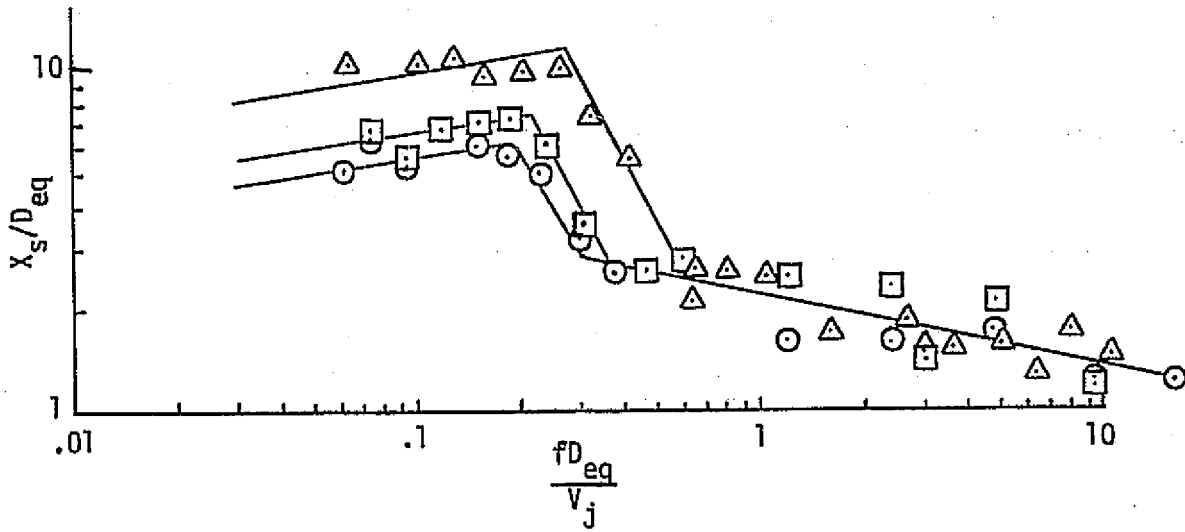


Figure 33.—Peak Noise Source Locations and Radiation Angles for the 20-Lobe Nozzle

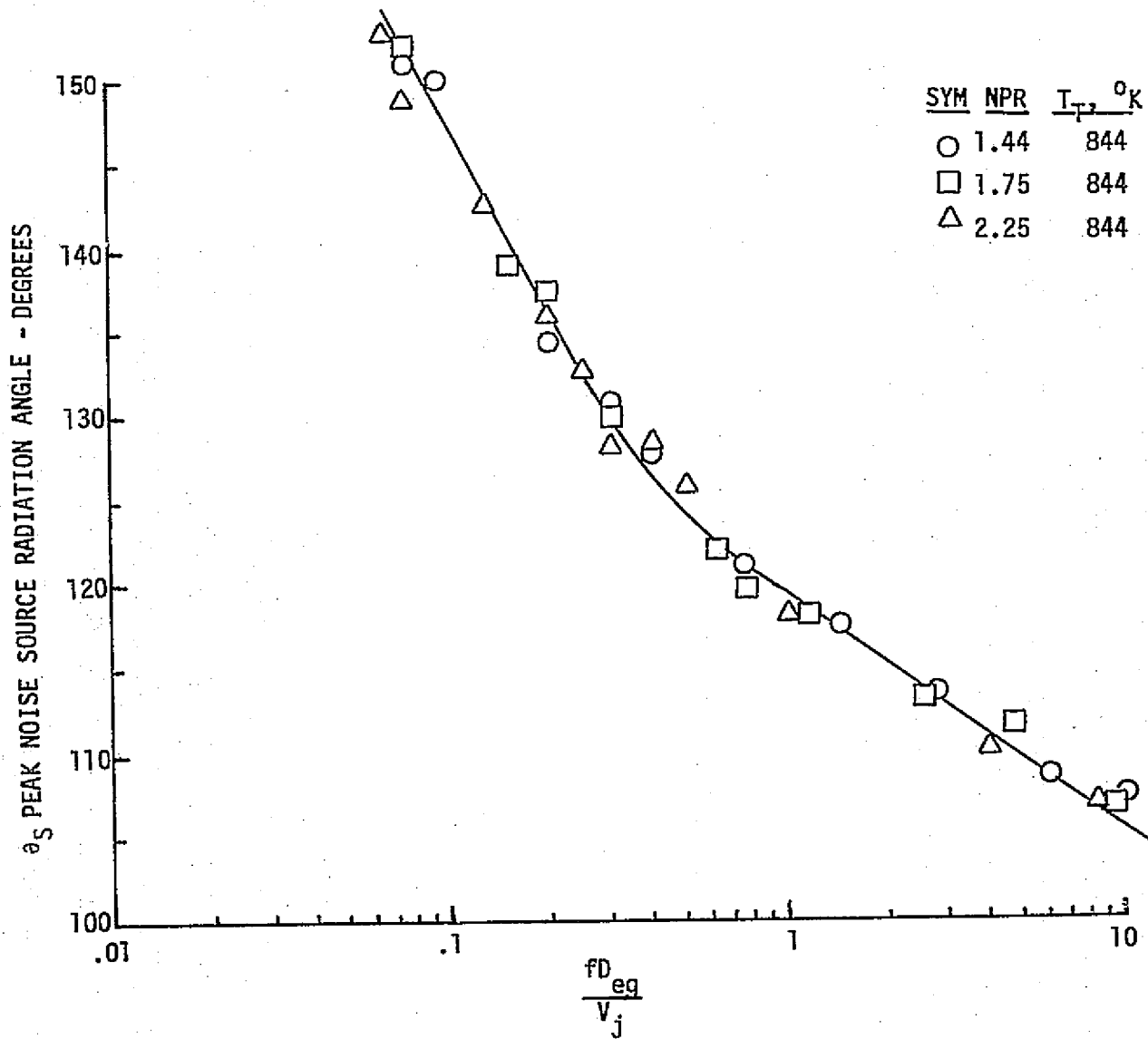


Figure 33.—(Concluded)

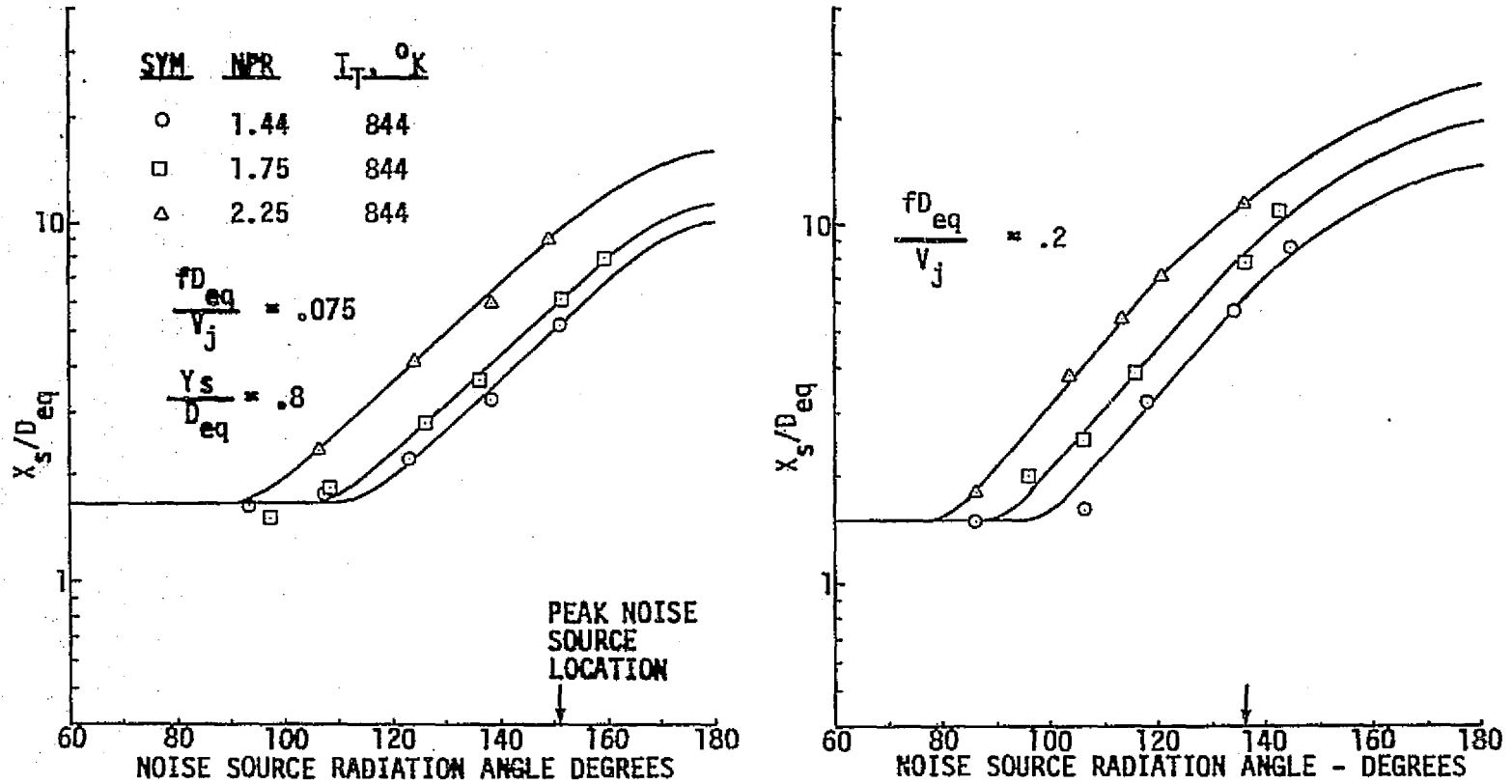


Figure 34.—Distributed Noise Source Locations for the 20-Lobe Nozzle

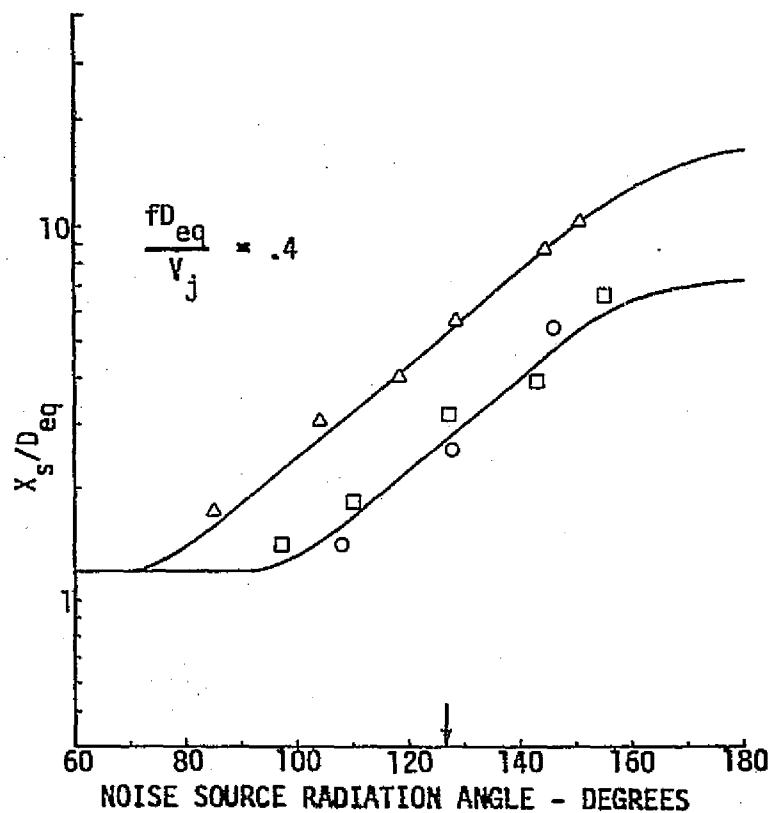
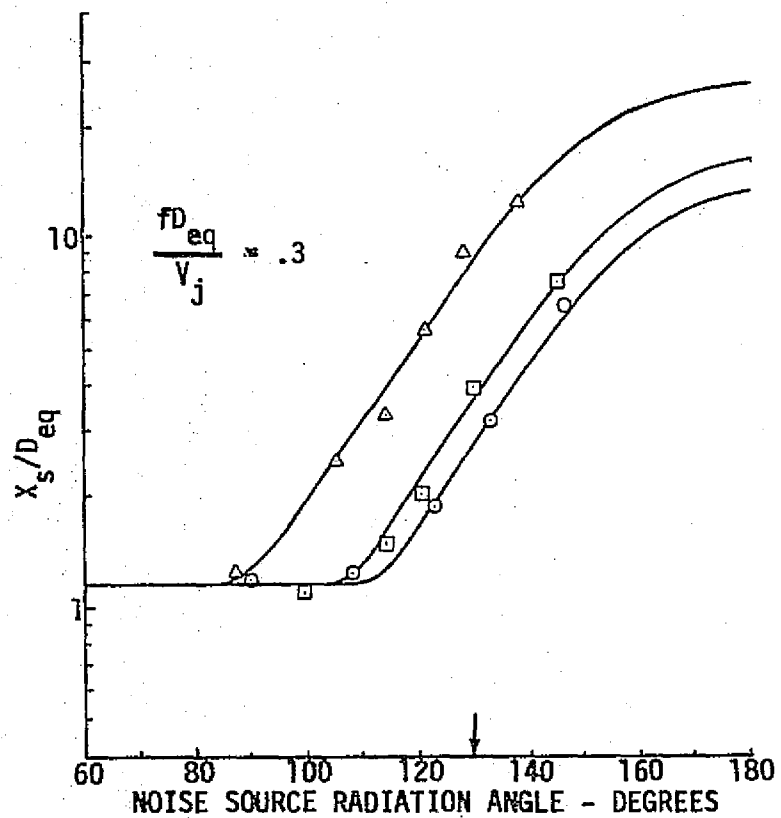


Figure 34.—(Continued)

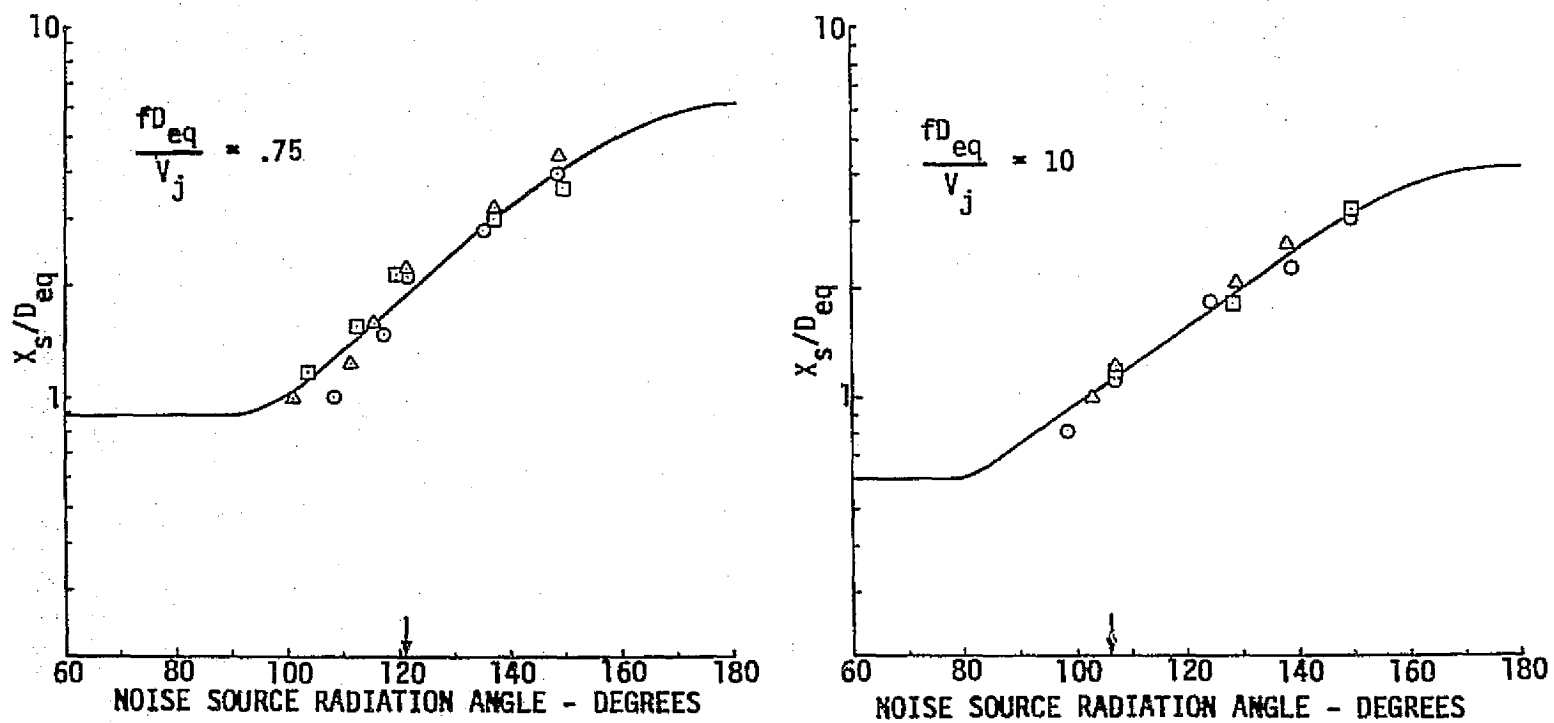


Figure 34.—(Concluded)

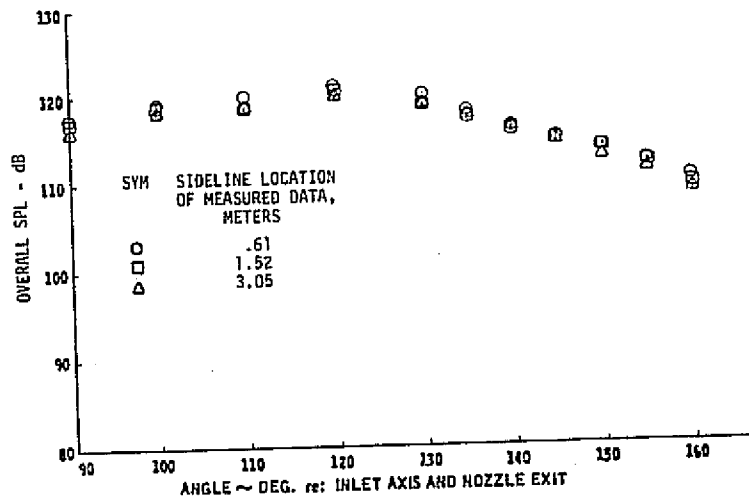


Figure 35.—OASPL and One-Third-Octave-Band Directivity Data for the 20-Lobe Nozzle Extrapolated to a 3.0-m Sideline—NPR = 1.44,  $T_T = 844$  K

ORIGINAL PAGE IS  
OF POOR QUALITY.

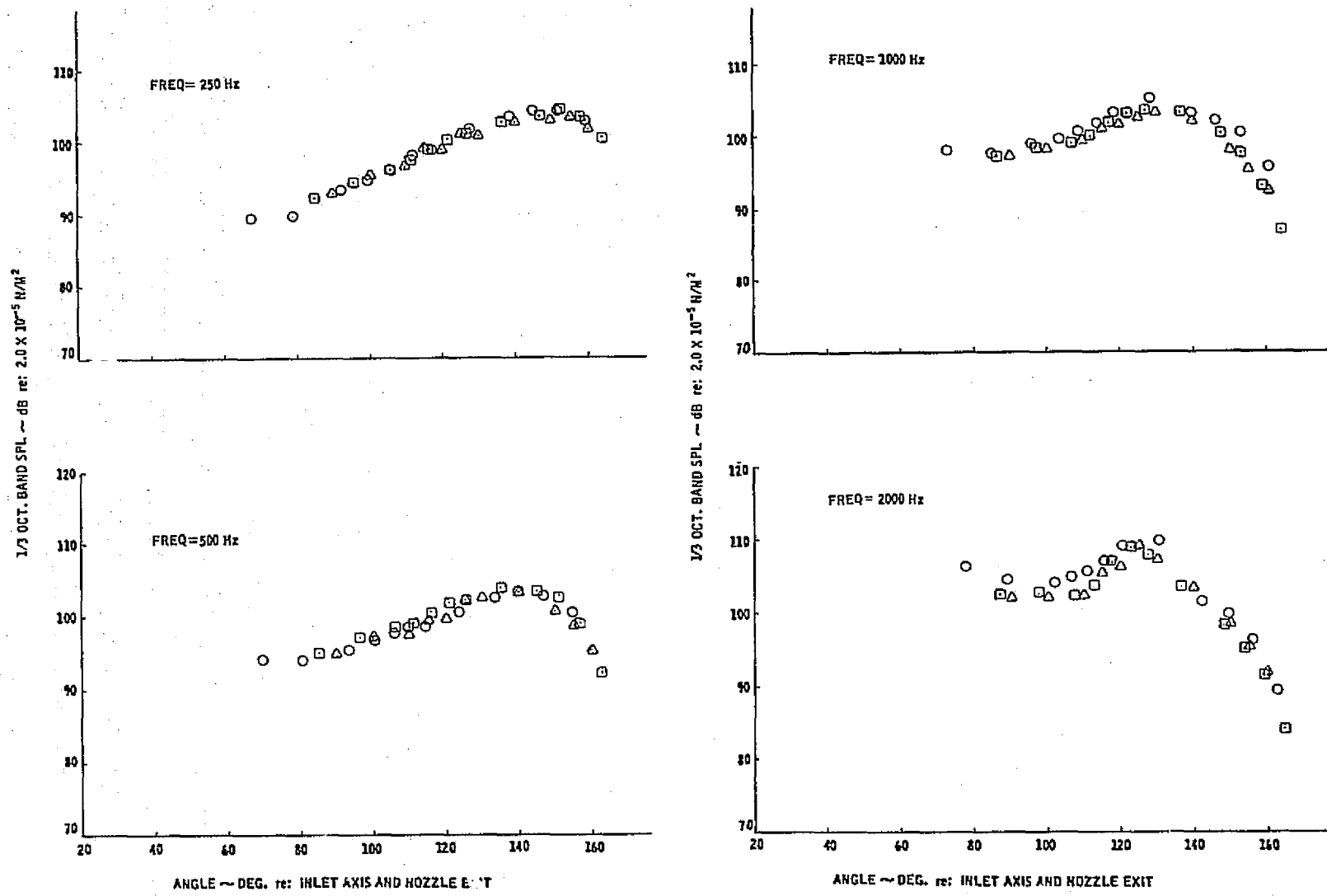


Figure 35.—(Continued)

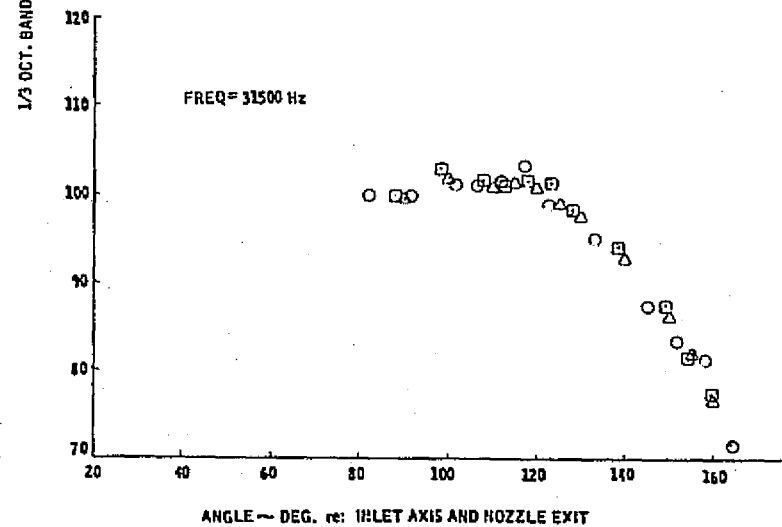
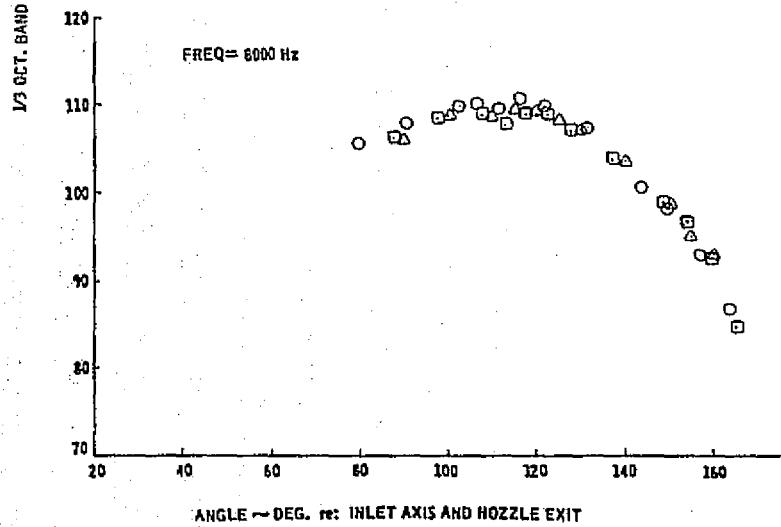
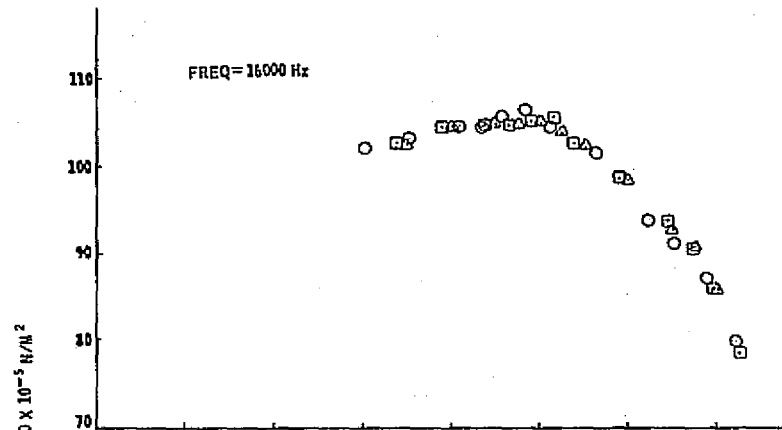
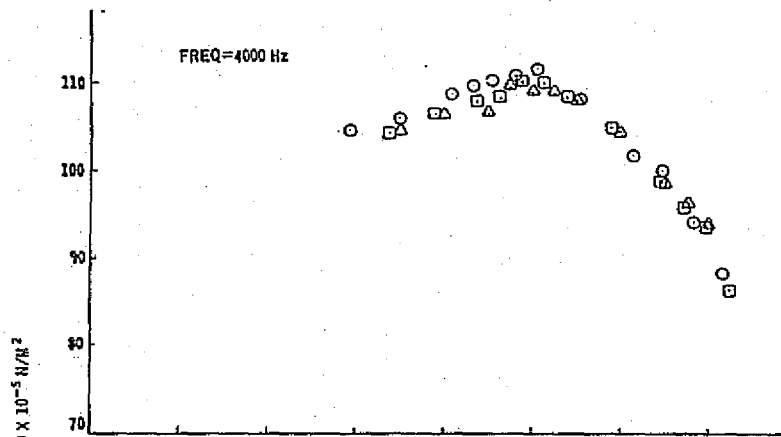


Figure 35.--(Concluded)

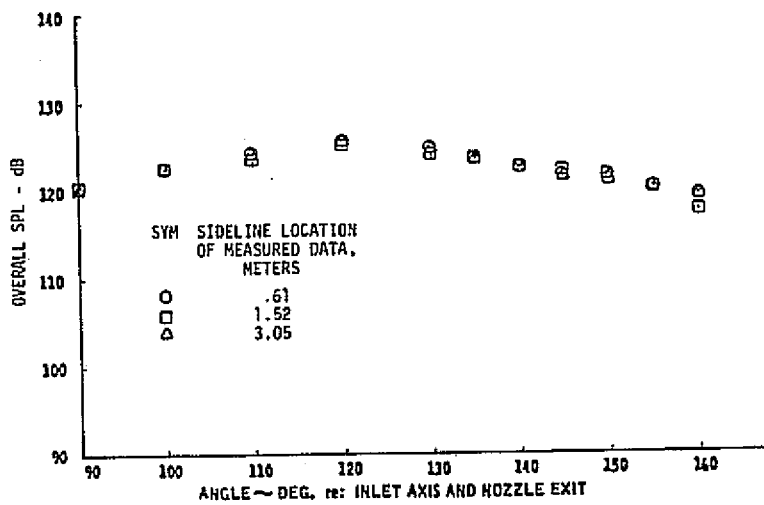


Figure 36.—OASPL and One-Third-Octave-Band SPL Directivity Data for the 20-Lobe Nozzle Extrapolated to a 3.0-m Sideline—NPR = 1.75,  $T_T = 844$  K

ORIGINAL PAGE IS  
OF POOR QUALITY

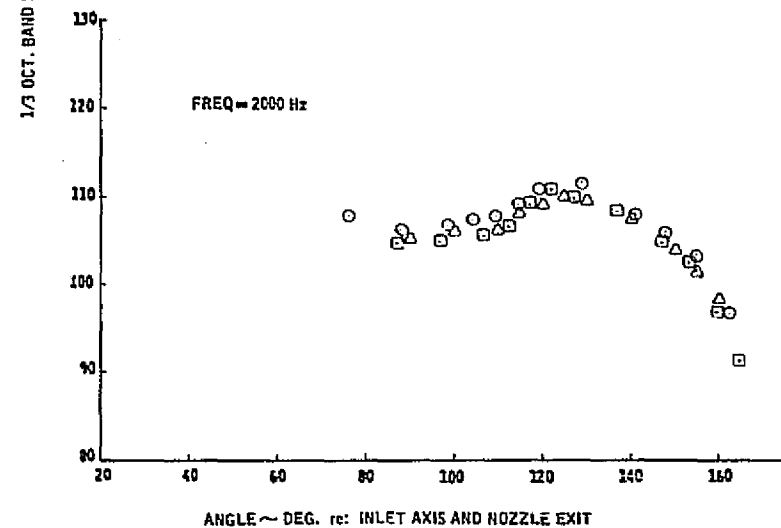
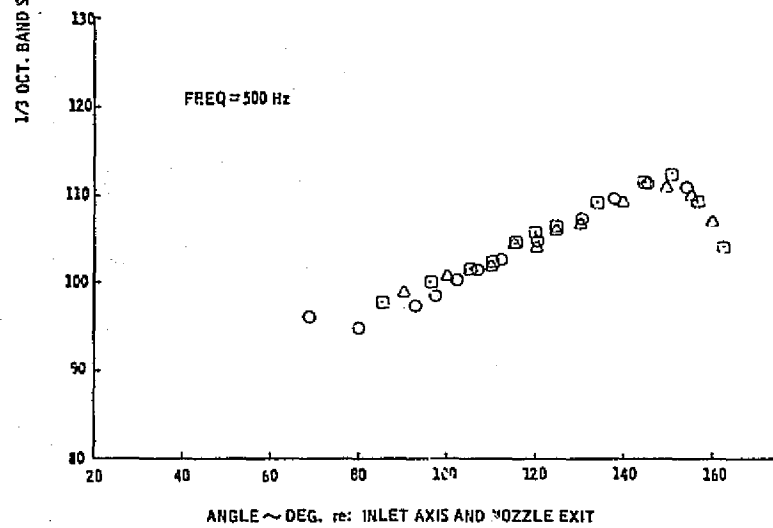
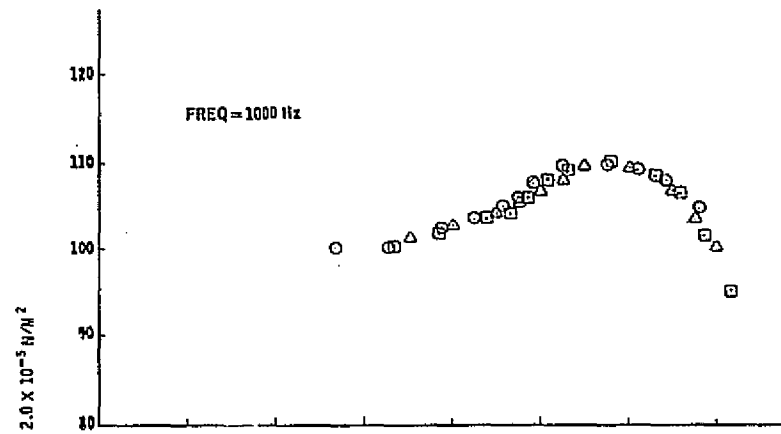
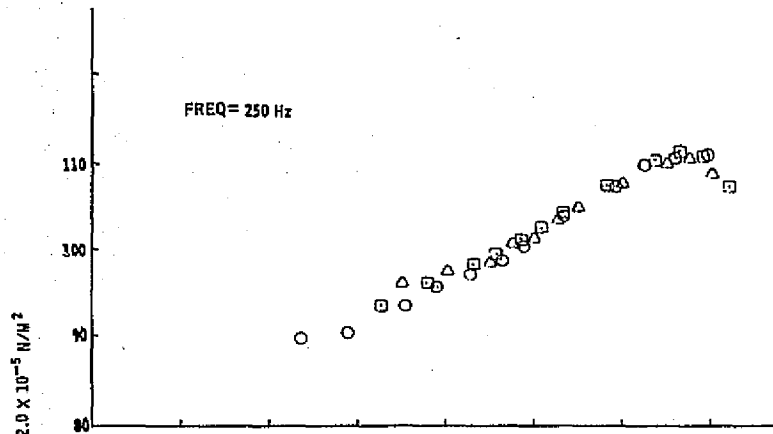


Figure 36.—(Continued)

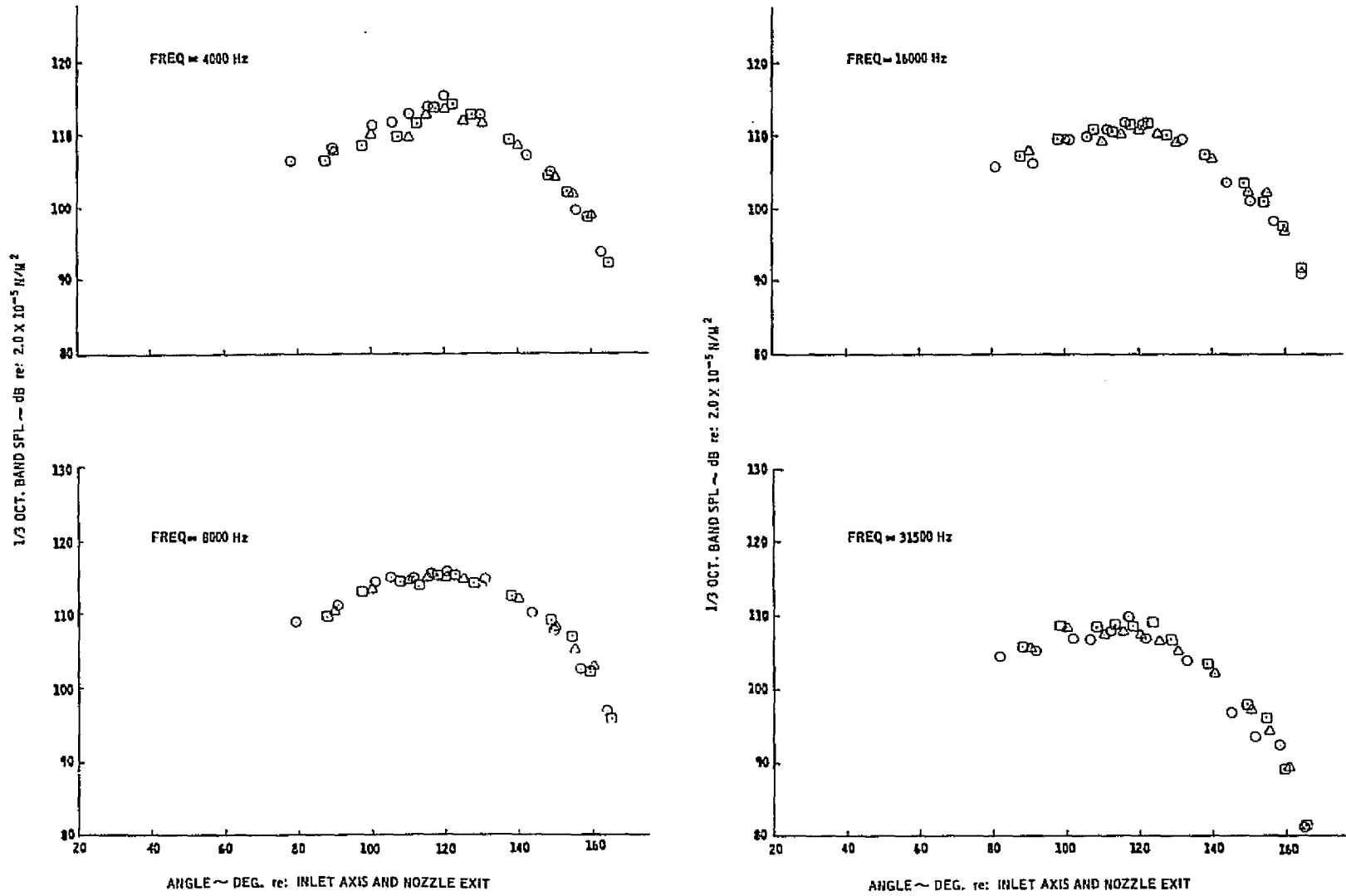


Figure 36.—(Concluded)

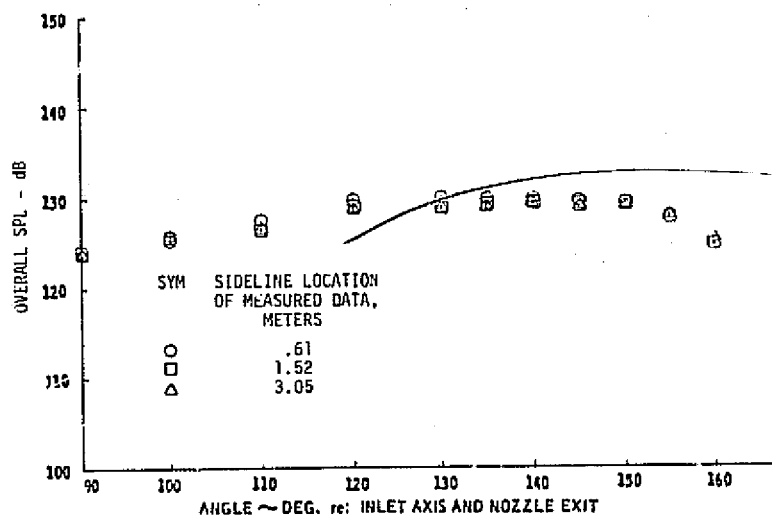


Figure 37.—OASPL and  $O_{1e}$  Third-Octave-Band SPL Directivity Data for the 20-Lobe Nozzle Extrapolated to a 3.0-m Sideline—NPR = 2.24,  $T_T = 844$  K

ORIGINAL PAGE IS  
OF POOR QUALITY

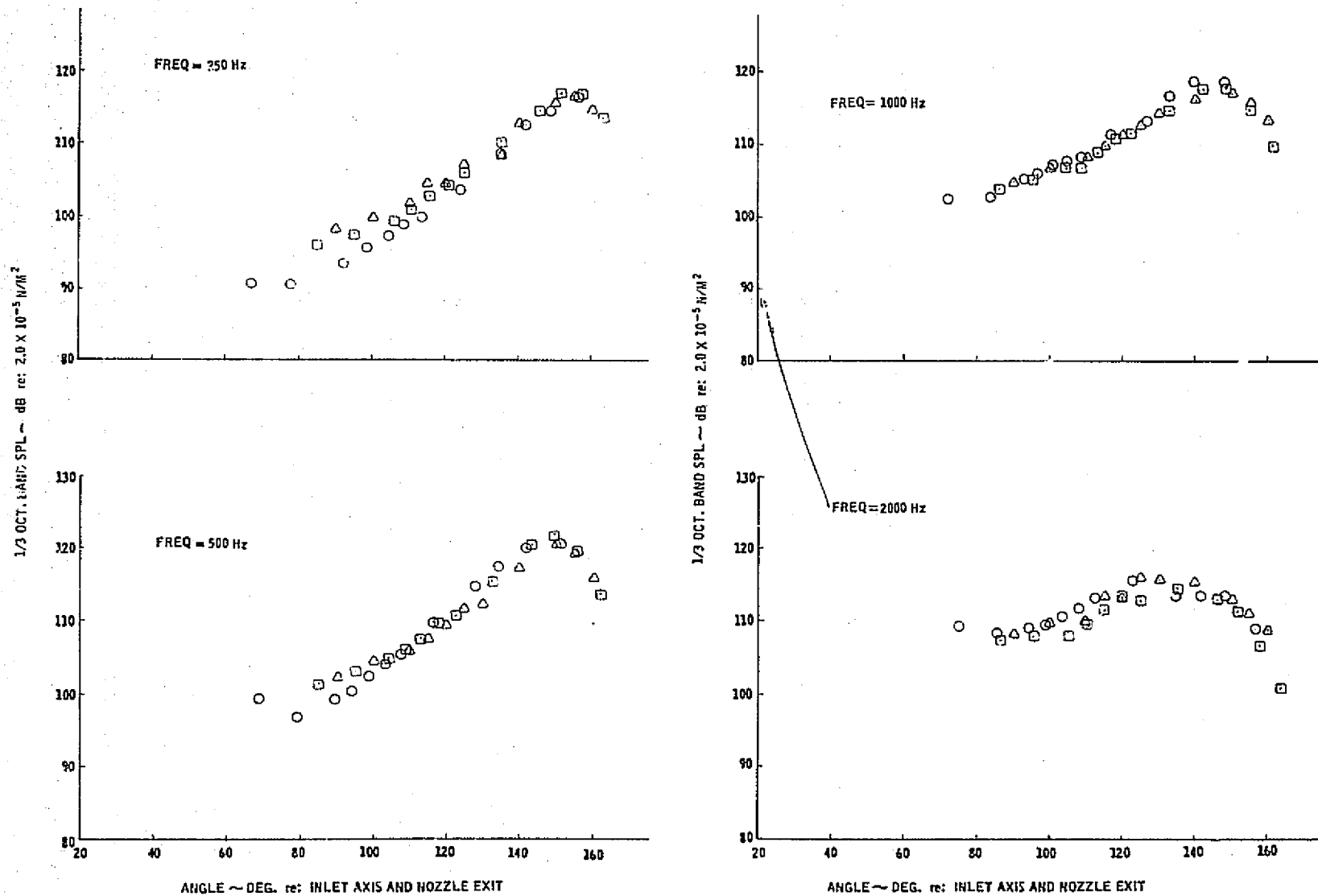
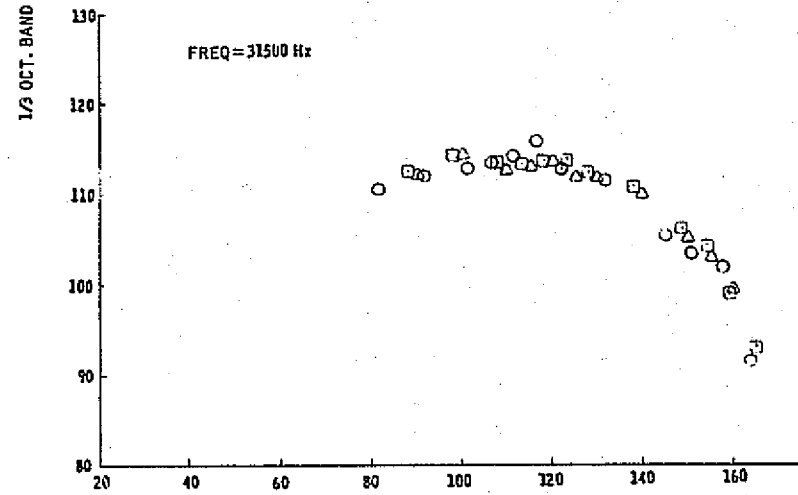
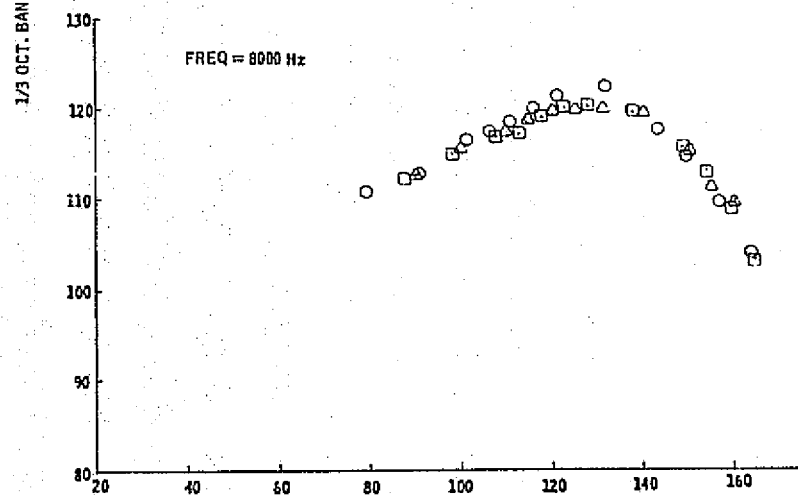
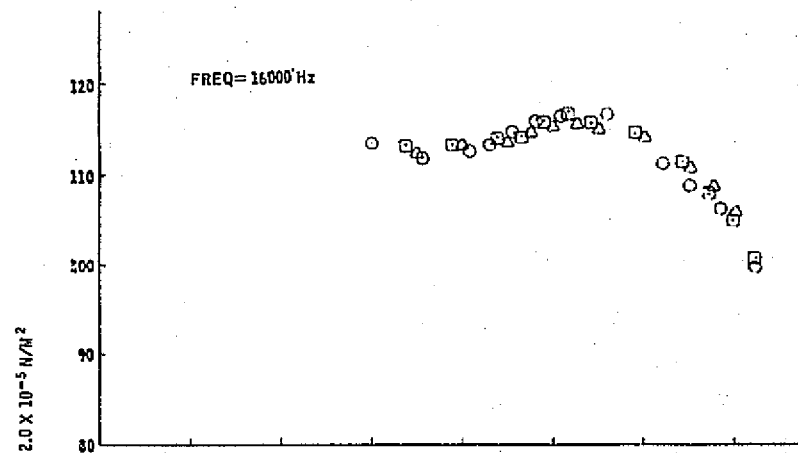
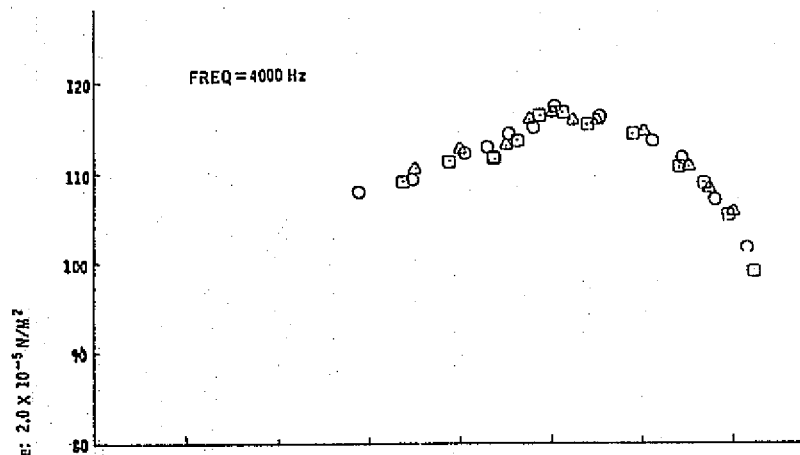


Figure 37.—(Continued)



ANGLE ~ DEG. re: INLET AXIS AND NOZZLE EXIT

ANGLE ~ DEG. re: INLET AXIS AND NOZZLE EXIT

Figure 37.—(Concluded)

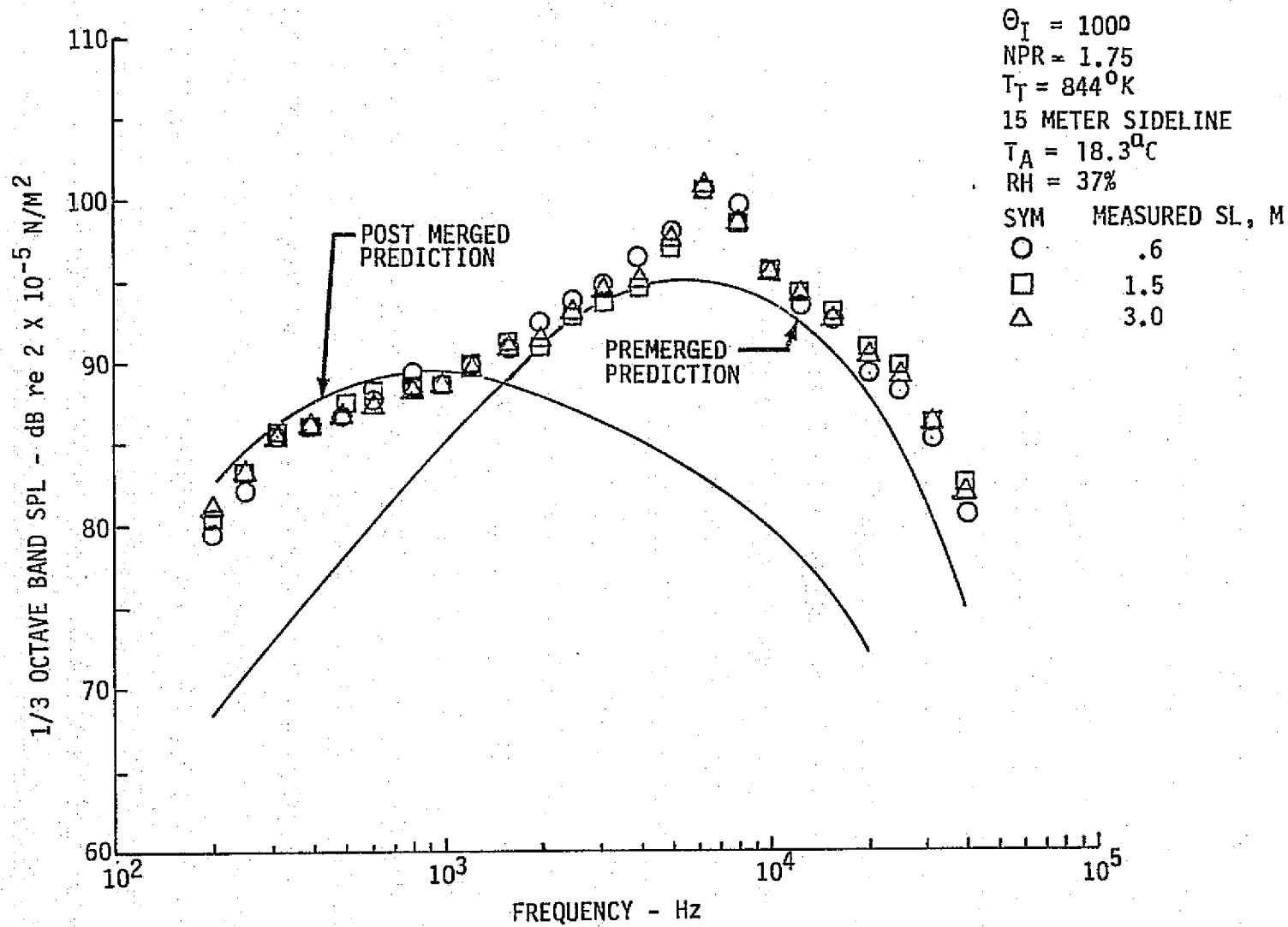


Figure 38.—Comparison of 15-m Sideline Extrapolation Data for the 20-Lobe Nozzle and Clean, Far-Field Jet Noise Predictions

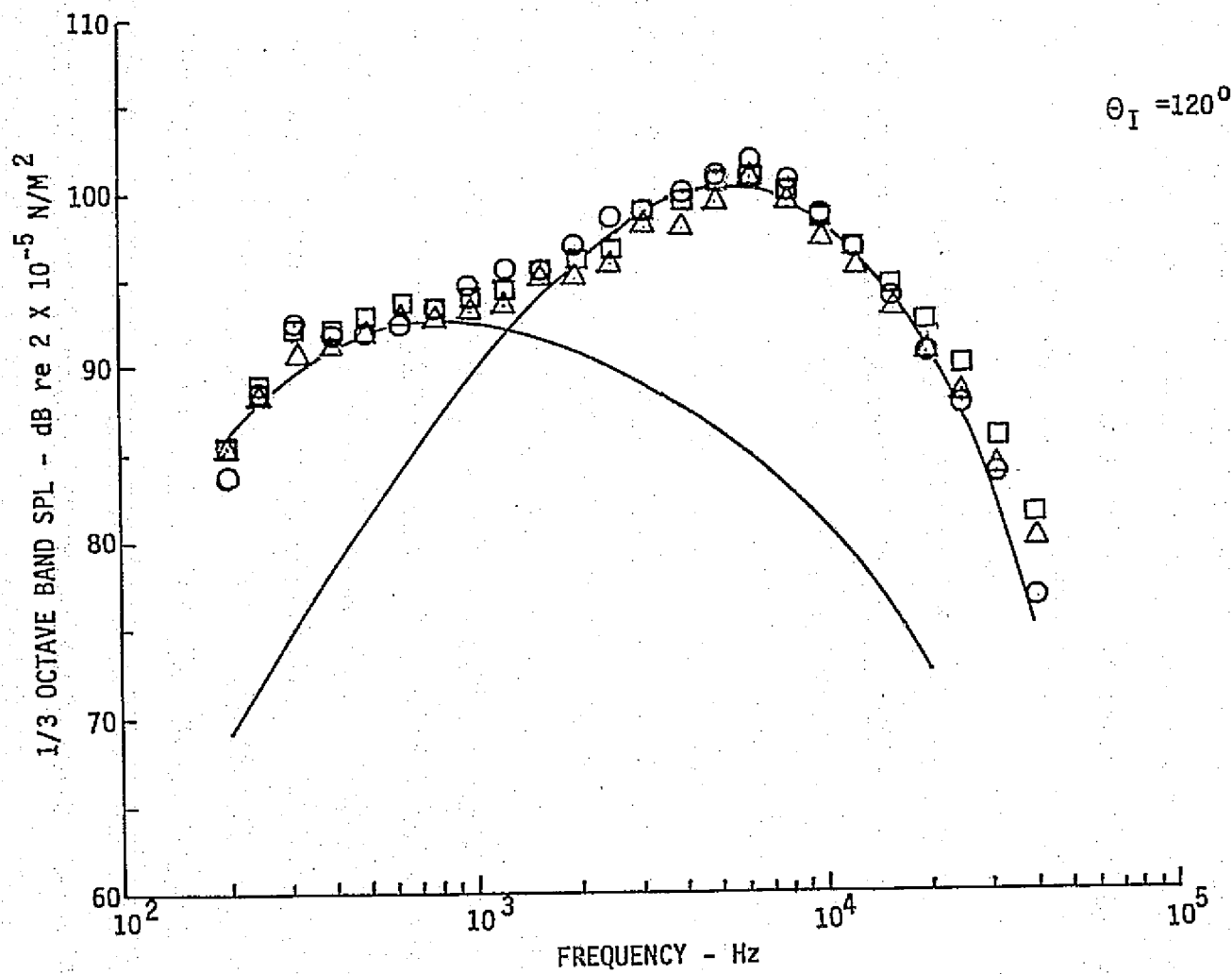


Figure 38.--(Continued)

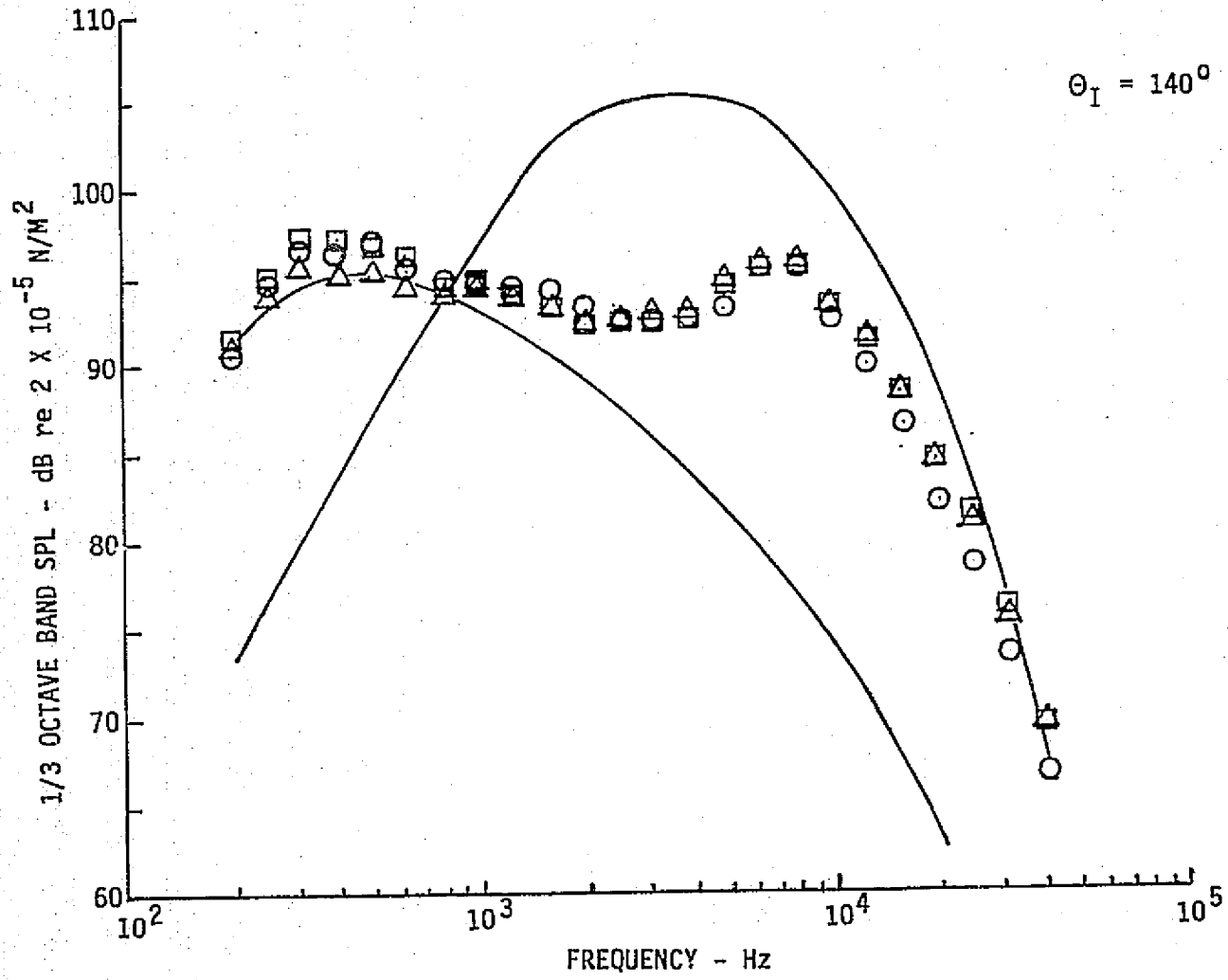


Figure 38.—(Continued)

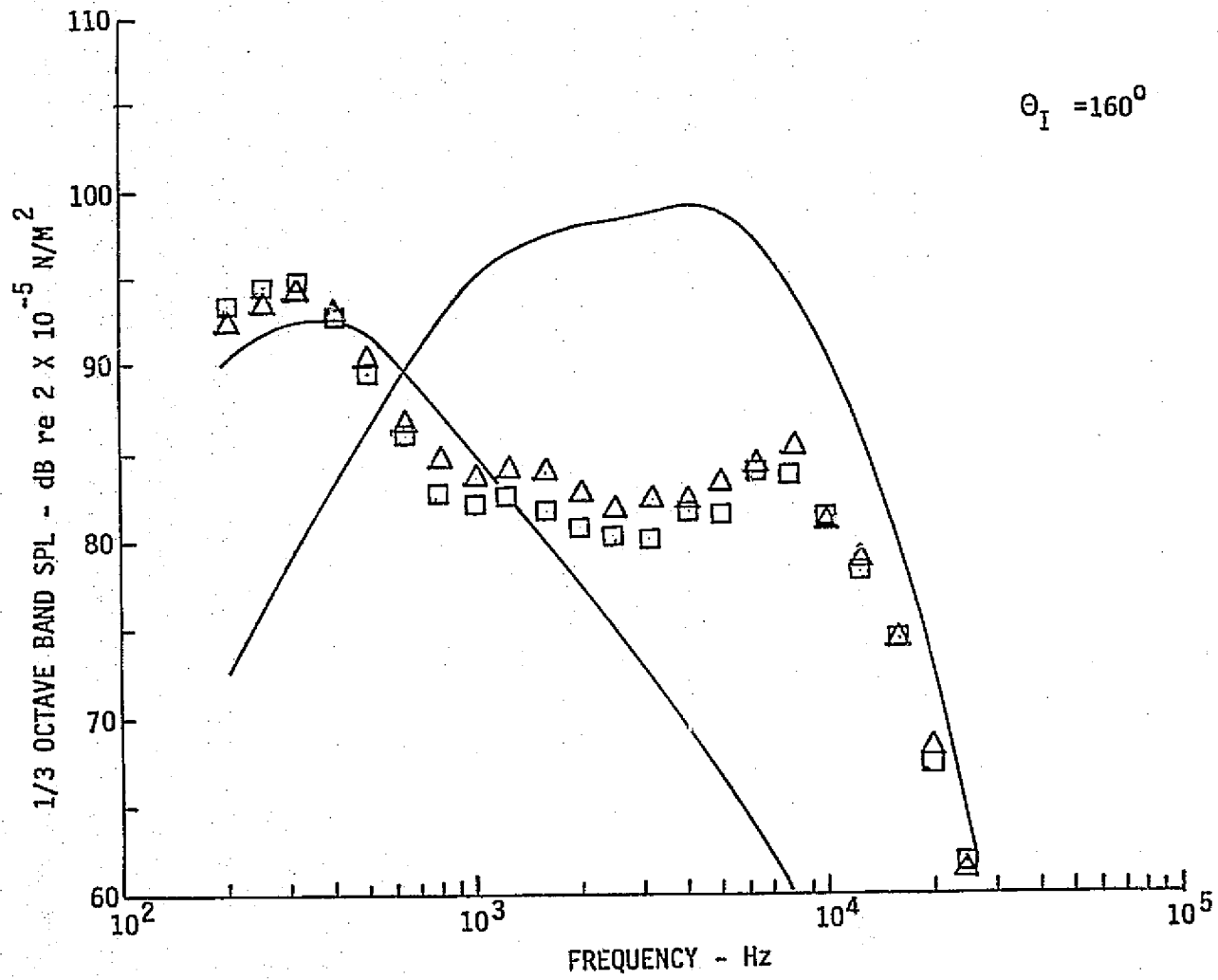


Figure 38.—(Concluded)

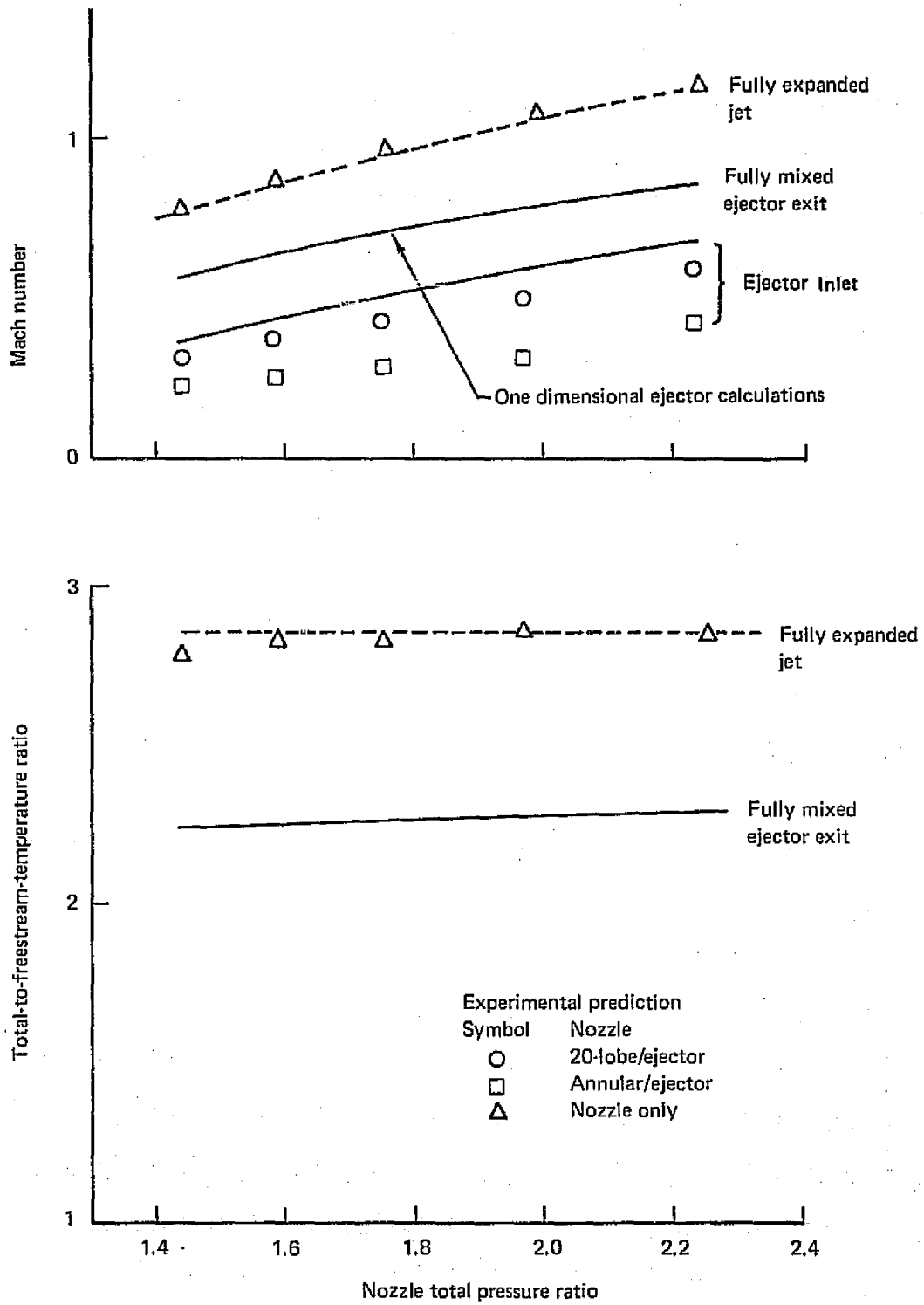


Figure 39.—Ejector Performance With Annular and 20-Lobe Nozzles

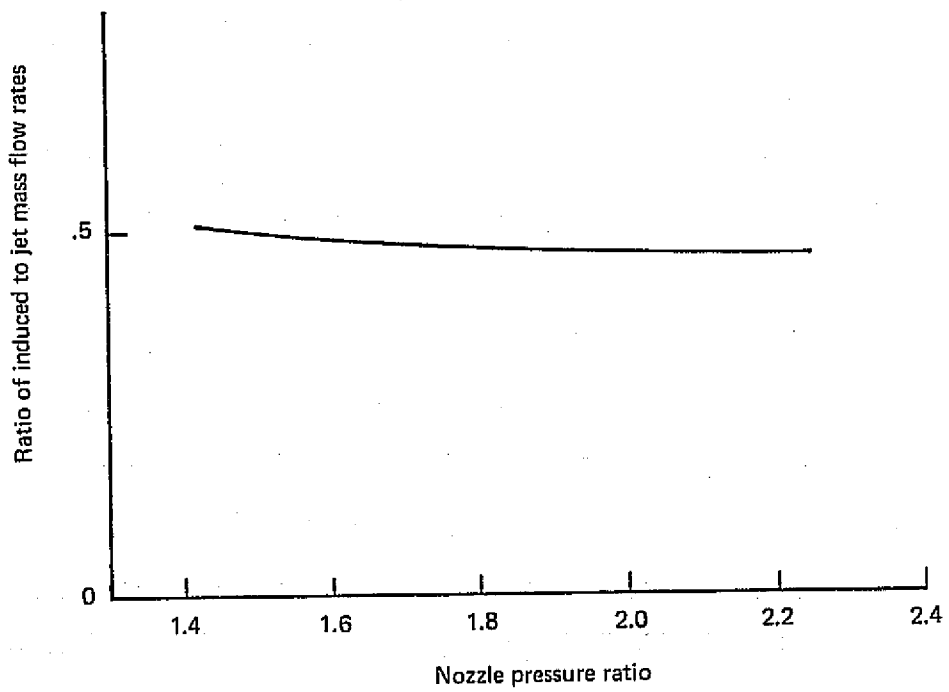
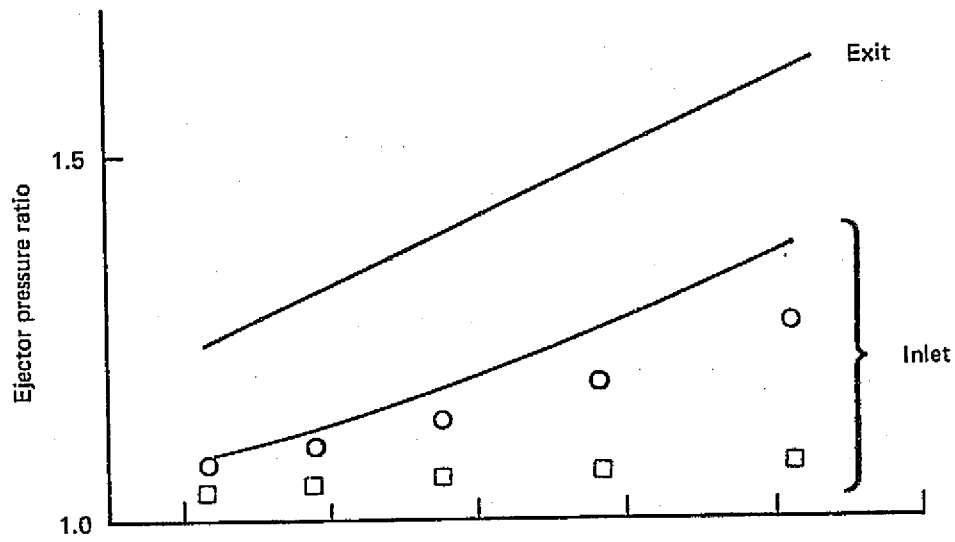


Figure 39.—(Concluded)

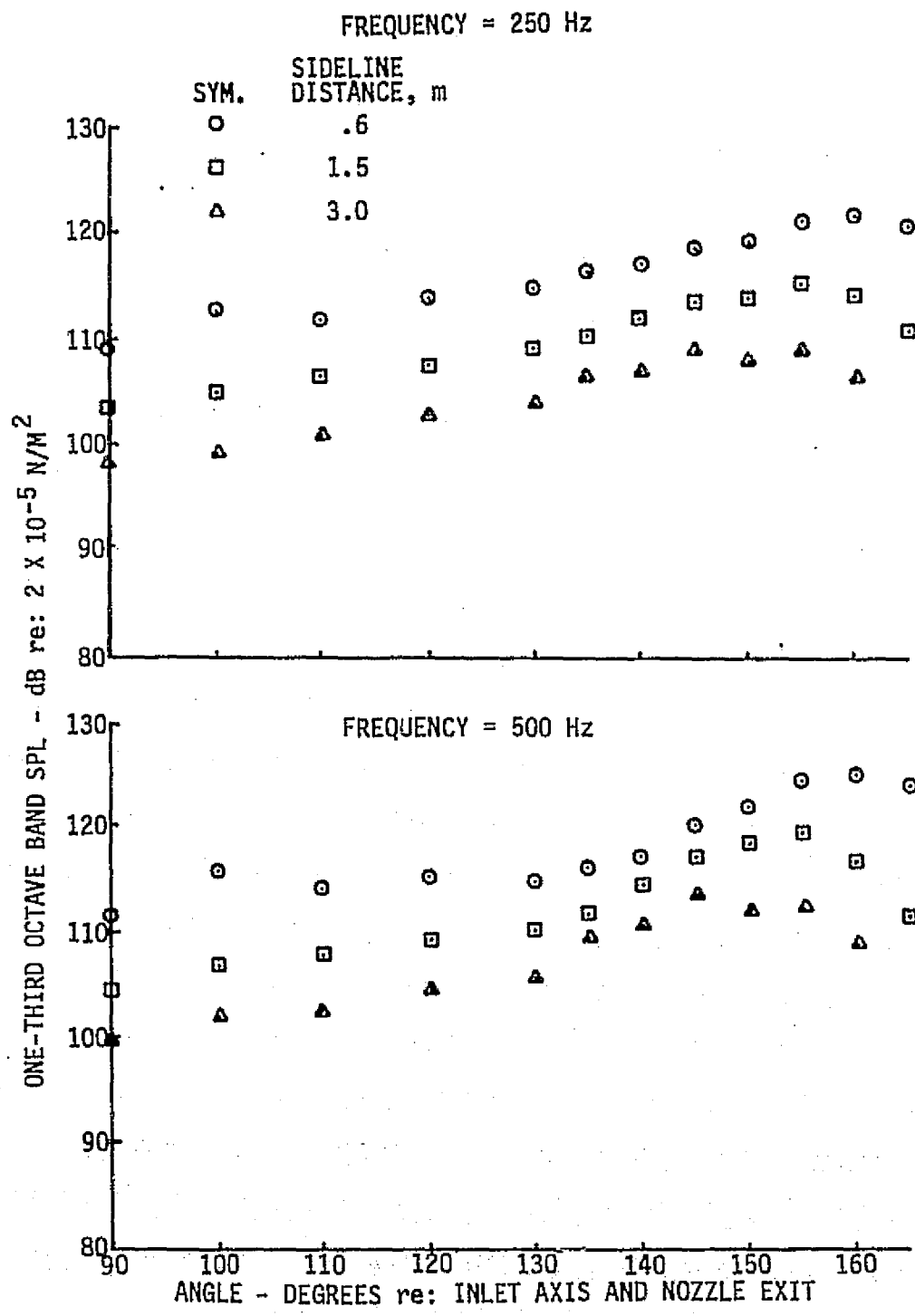
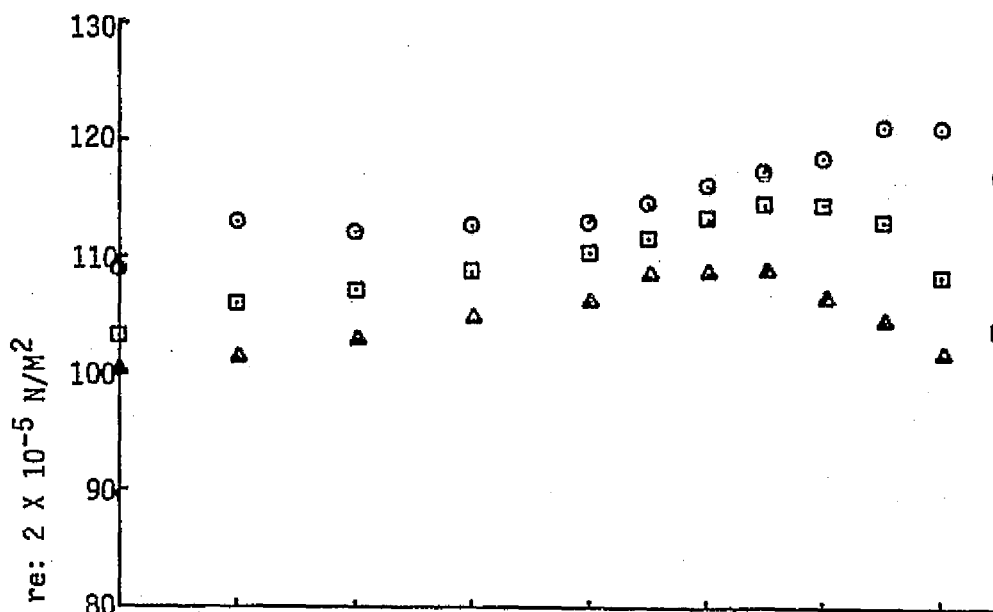


Figure 40.—One-Third-Octave-Band SPL Directivities for the Annular Nozzle With Lined Ejector—NPR = 1.44,  $T_T = 844$  K

FREQUENCY = 1000 Hz



FREQUENCY = 2000 Hz

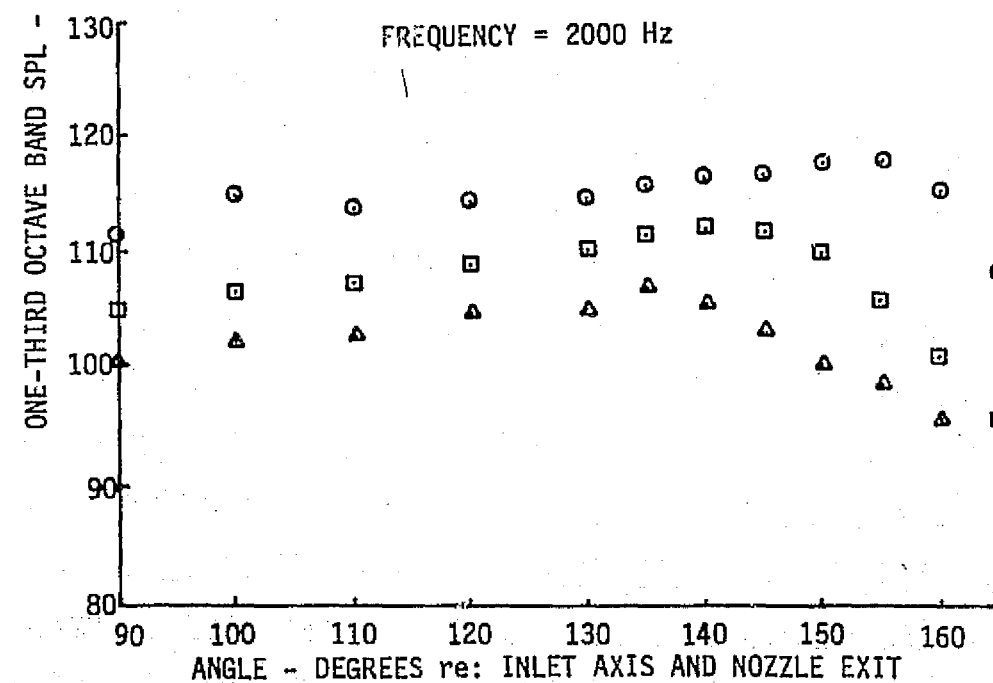
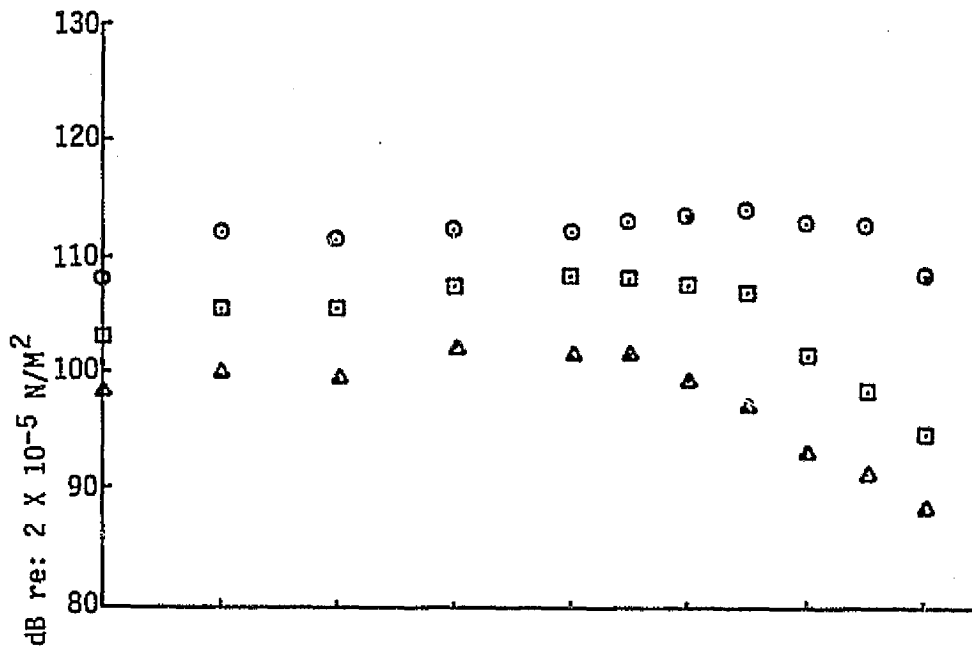


Figure 40.—(Continued)

FREQUENCY = 4000 Hz



FREQUENCY = 8000 Hz

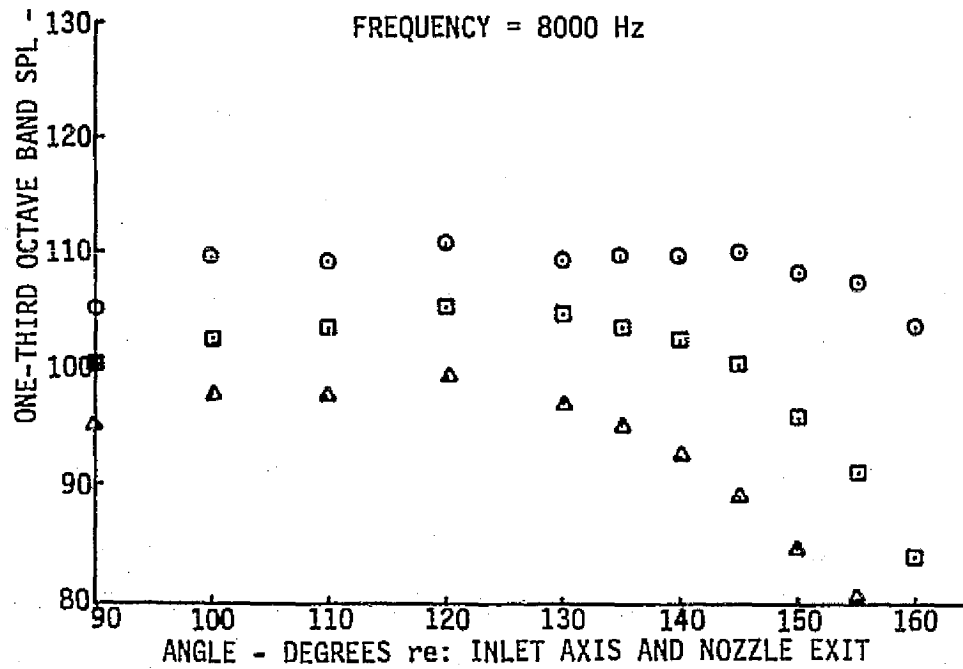
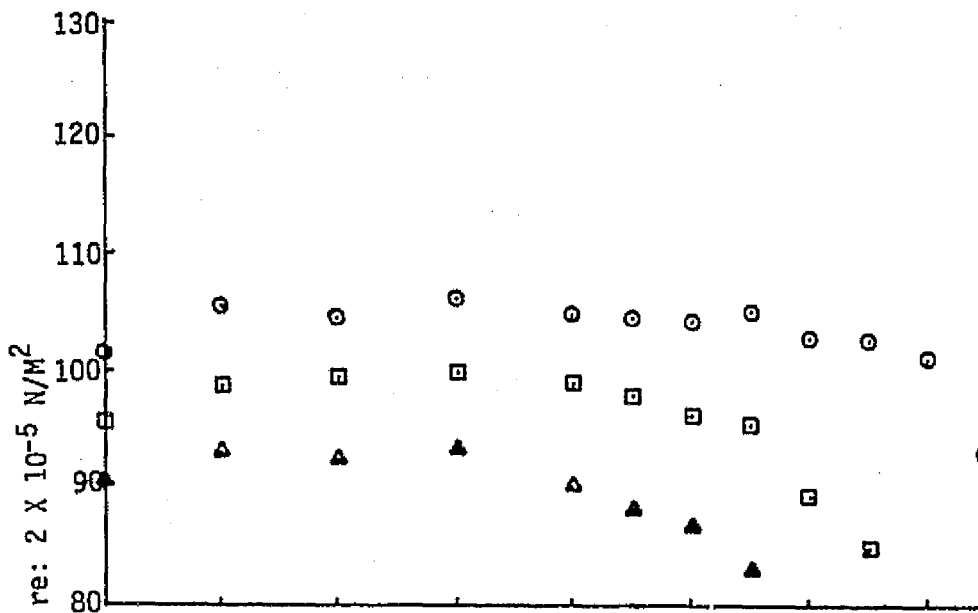


Figure 40.—(Continued)

FREQUENCY = 16000 Hz



FREQUENCY = 31500 Hz

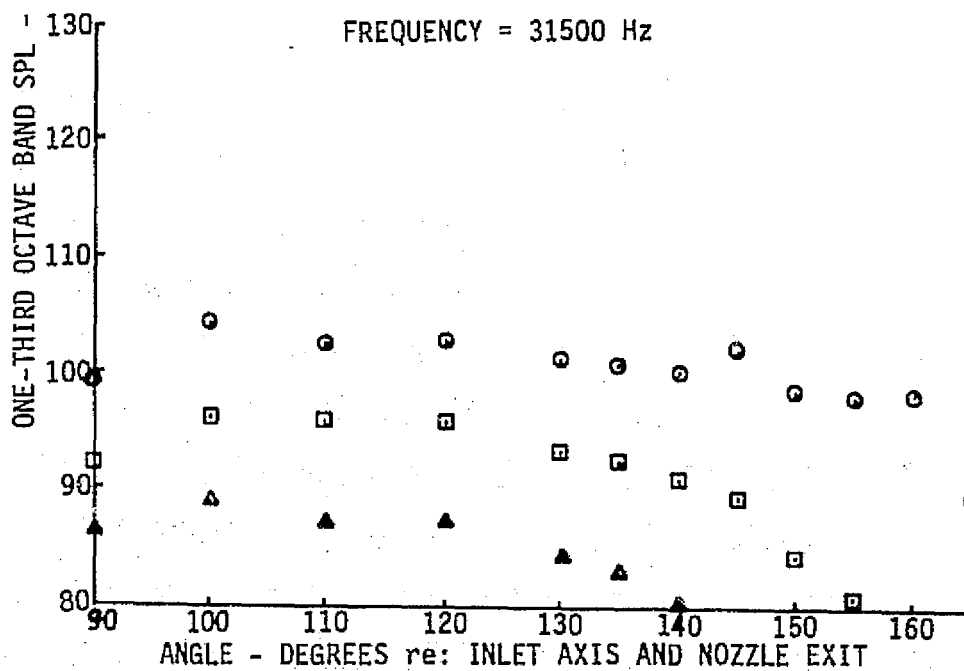


Figure 40.—(Concluded)

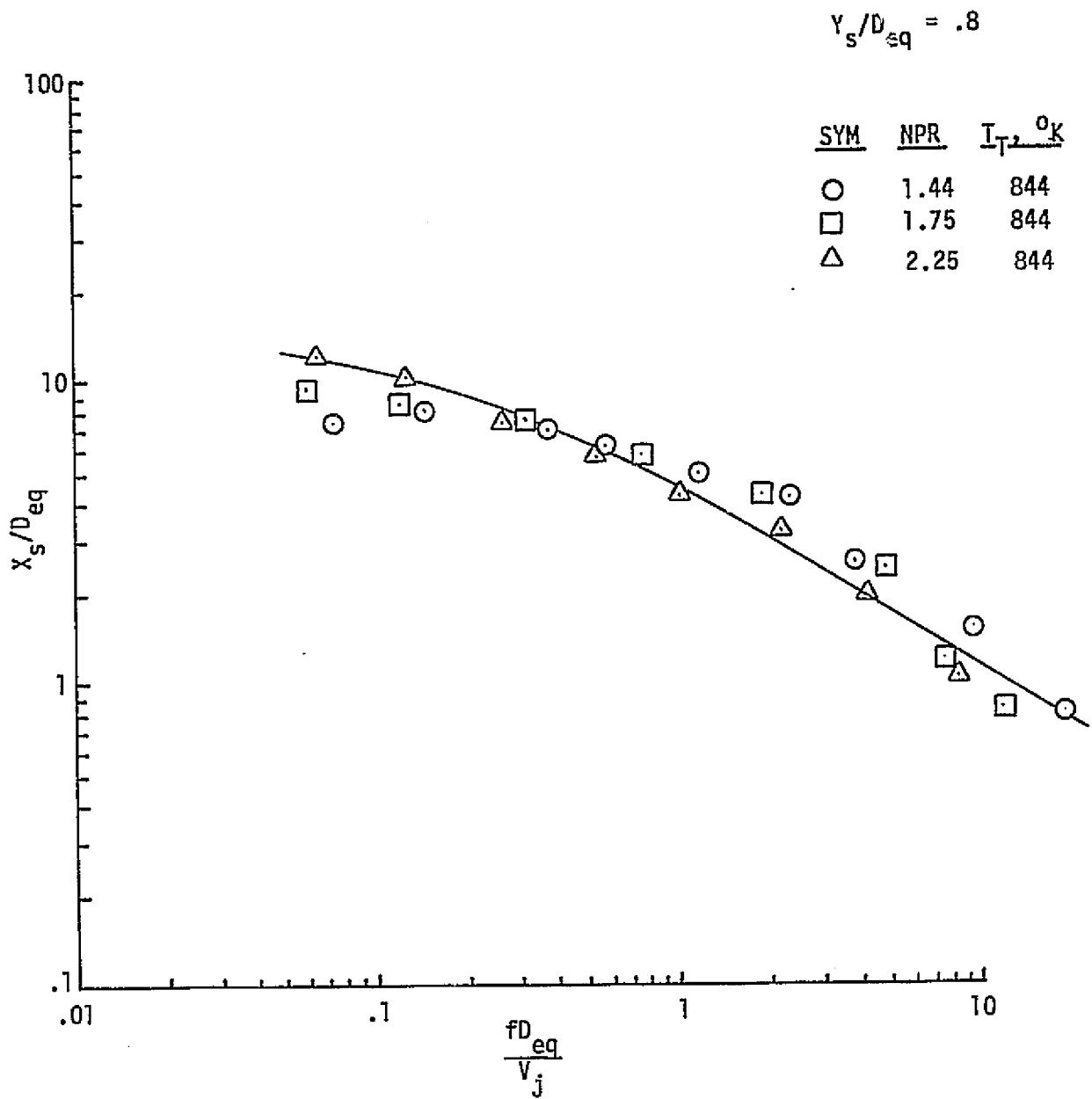


Figure 41.—Peak Noise Source Locations for the Annular Nozzle With Lined Ejector

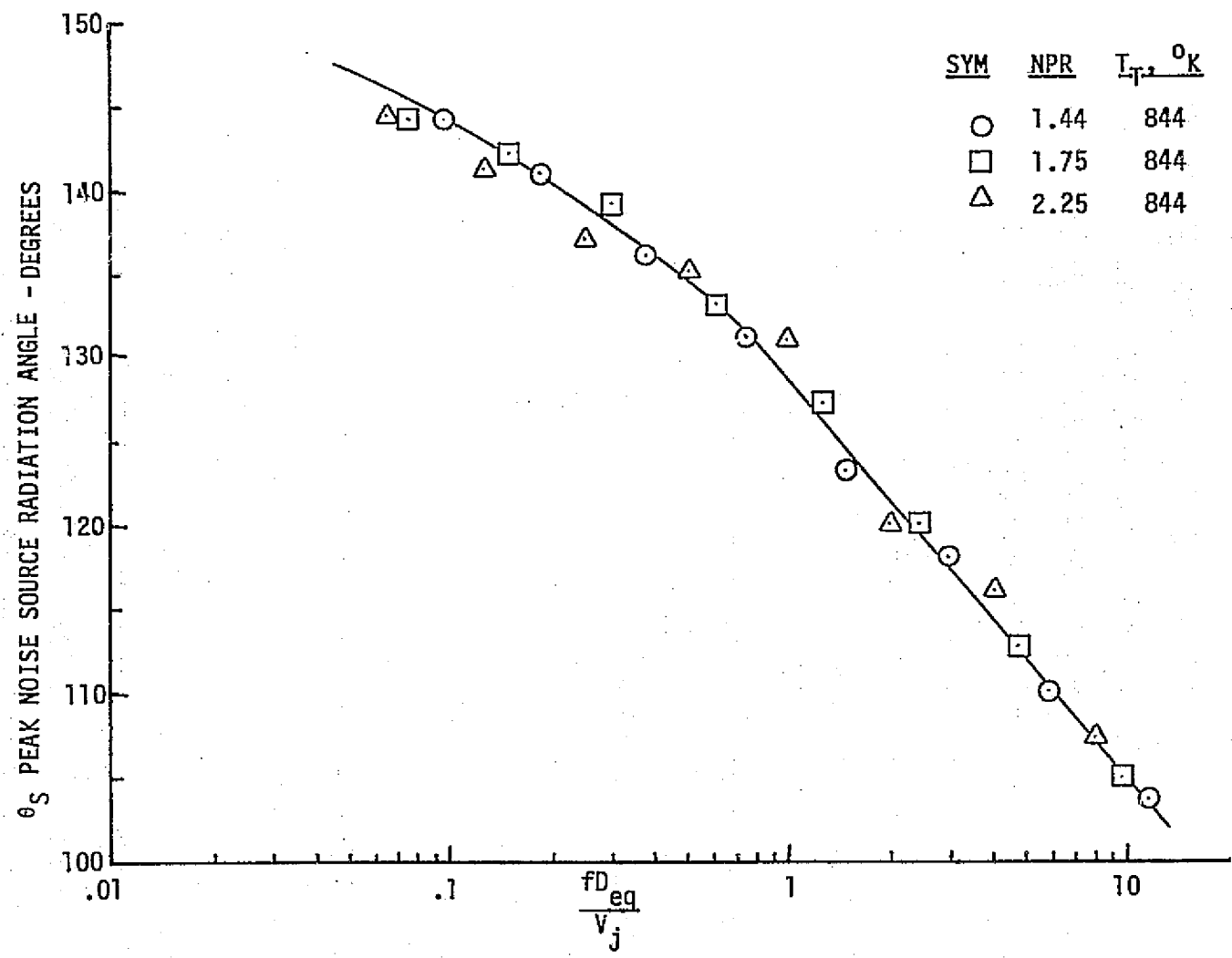


Figure 42.—Peak Noise Source Radiation Angles for the Annular Nozzle With Lined Ejector

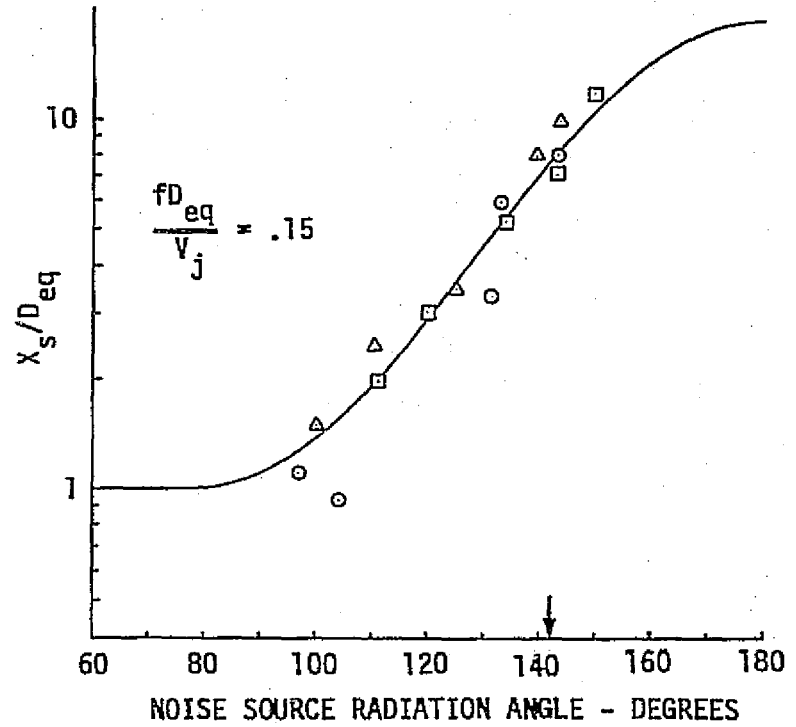
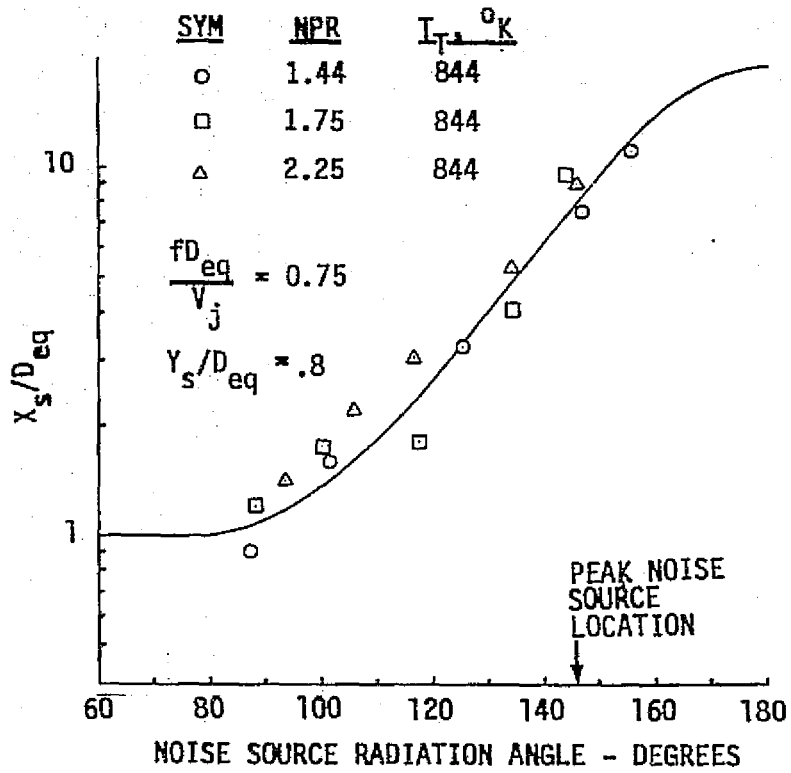


Figure 43.—Distributed Noise Source Locations for the Annular Nozzle With Lined Ejector

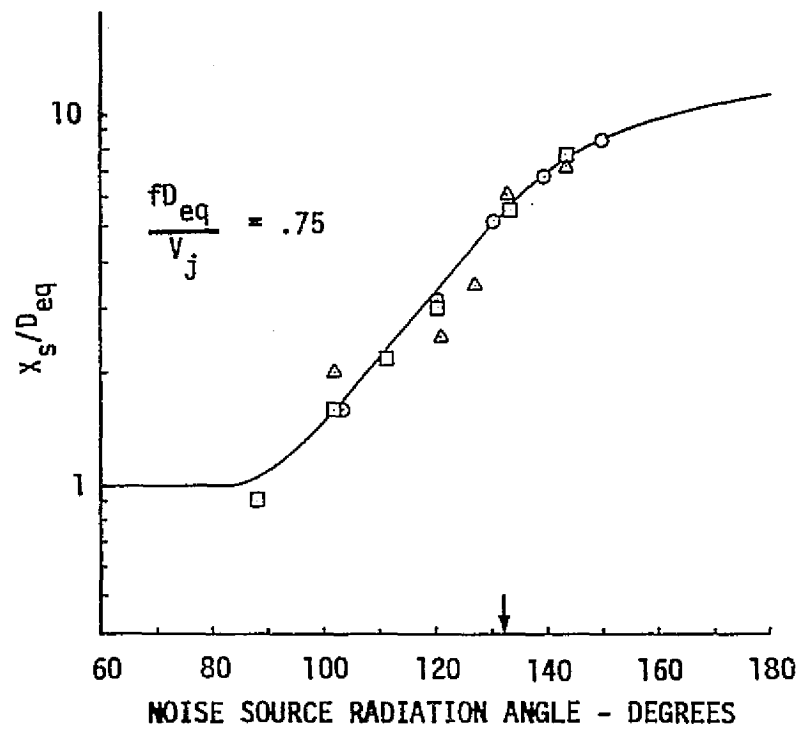
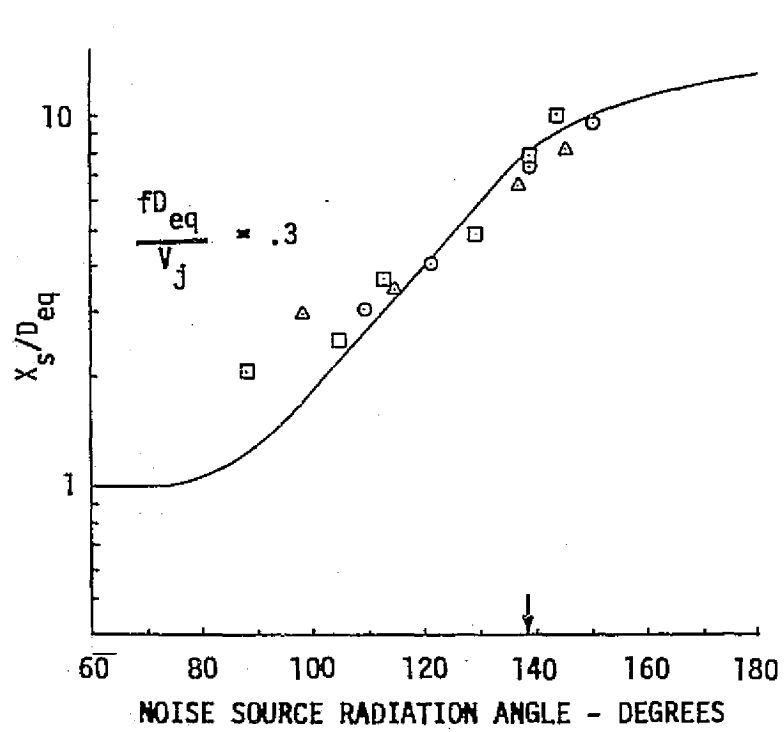


Figure 43.—(Continued)

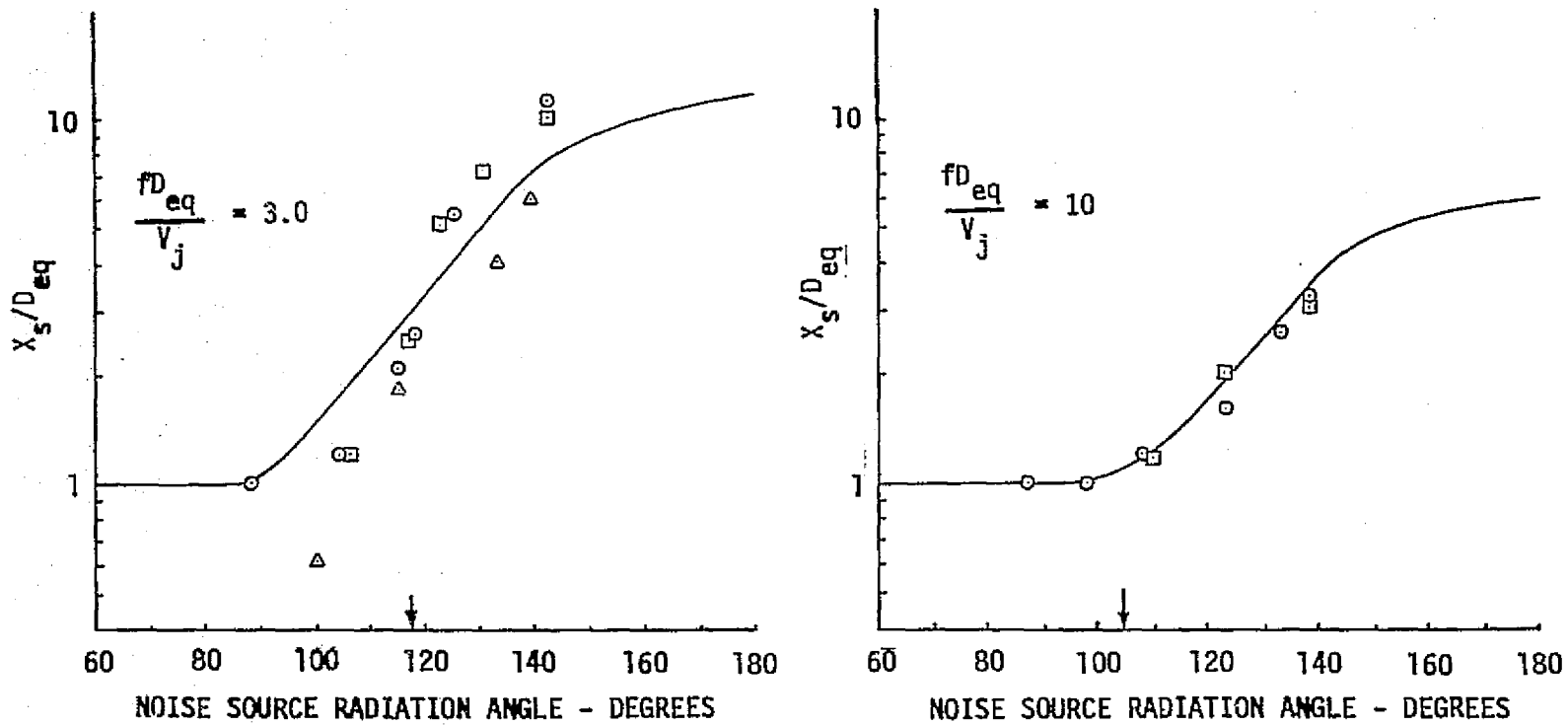


Figure 43.—(Concluded)

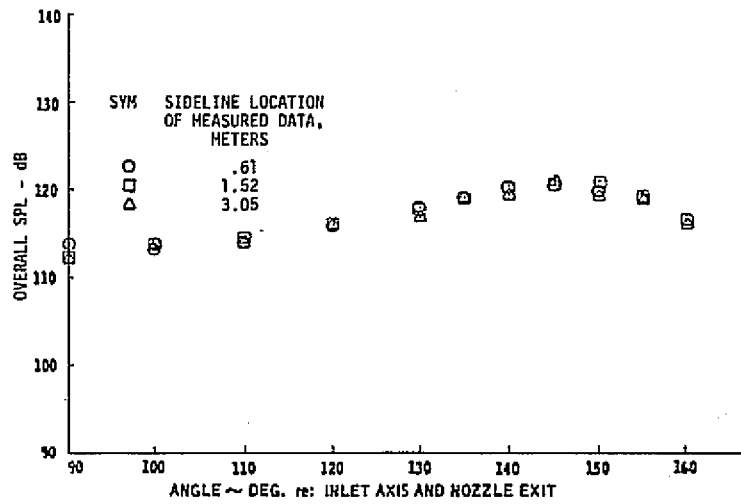


Figure 44.—OASPL and One-Third-Octave-Band SPL Directivity Data for the Annular Nozzle With the Lined Ejector Extrapolated to a 3.0-m Sideline—NPR = 1.44,  $T_T = 844$  K

ORIGINAL PAGE IS  
OF POOR QUALITY

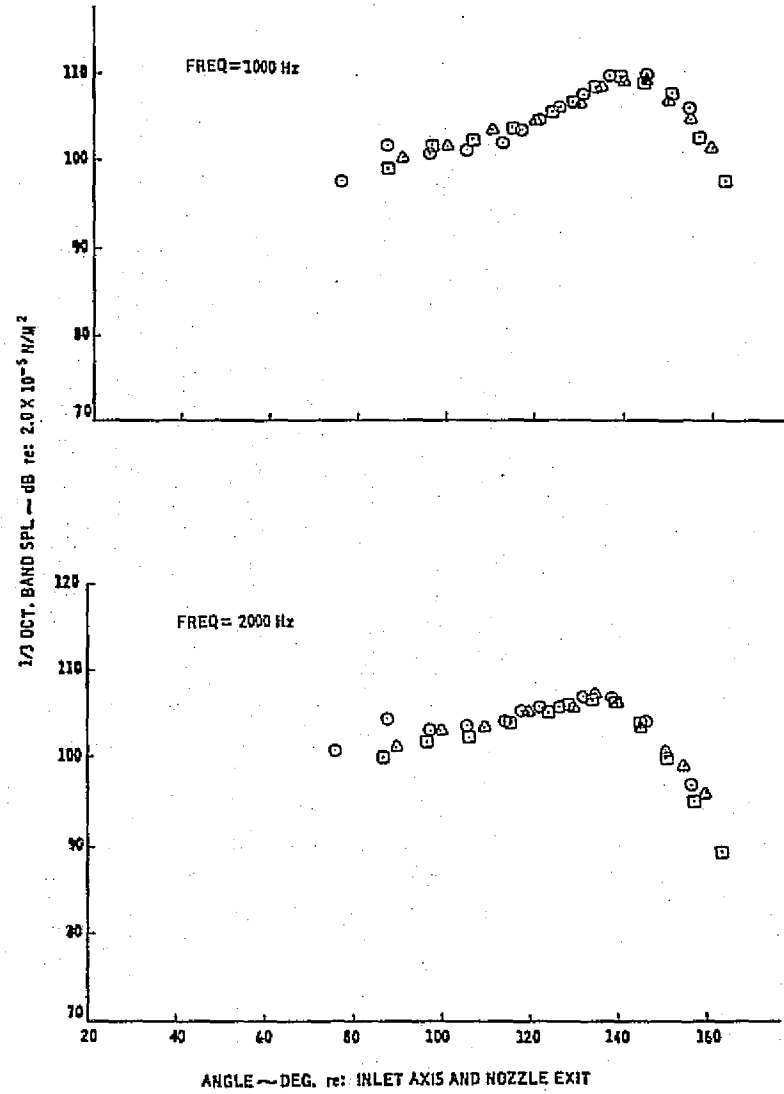
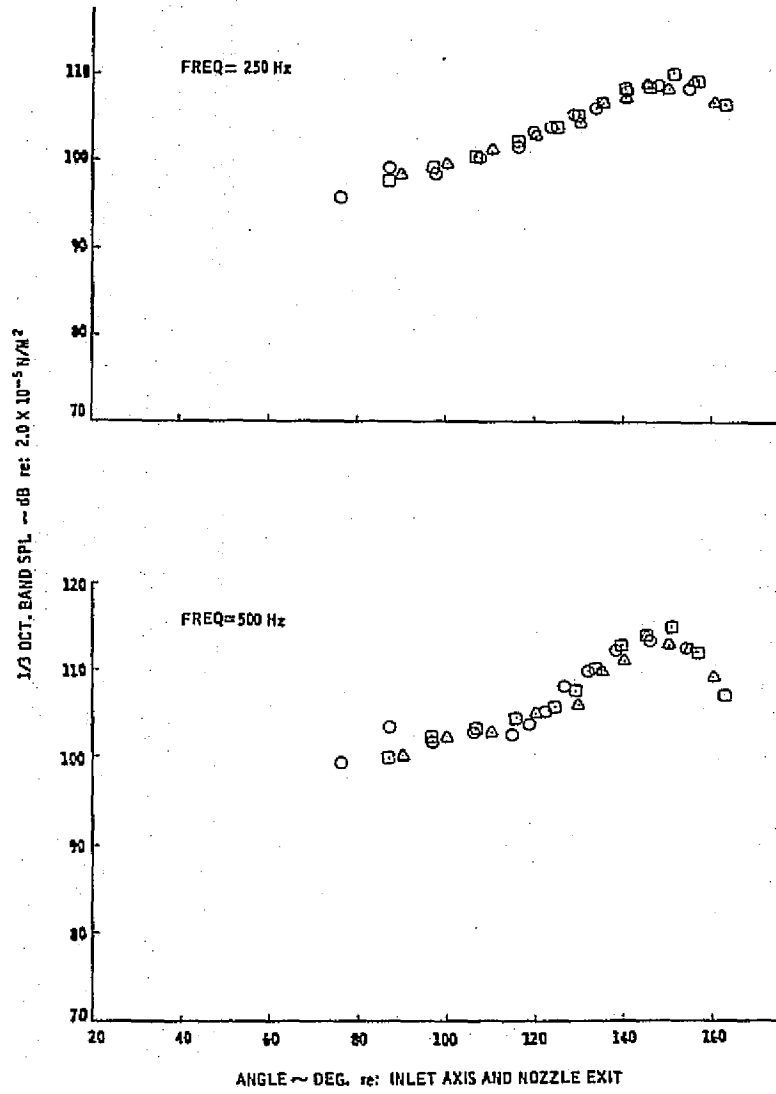


Figure 44.--(Continued)

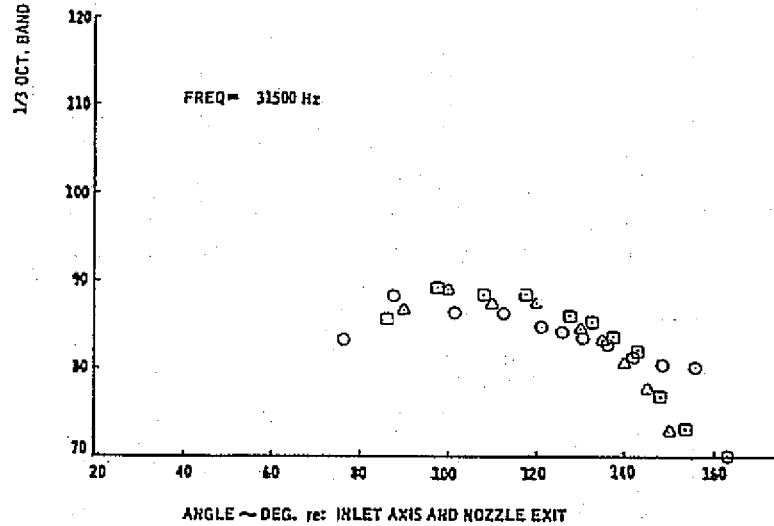
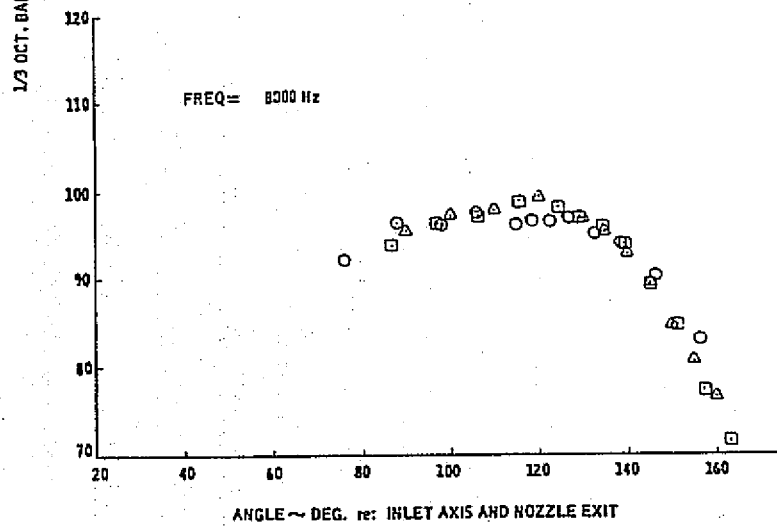
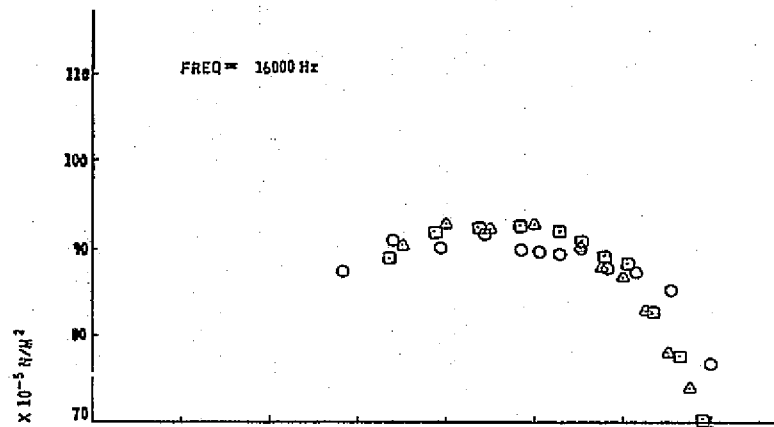
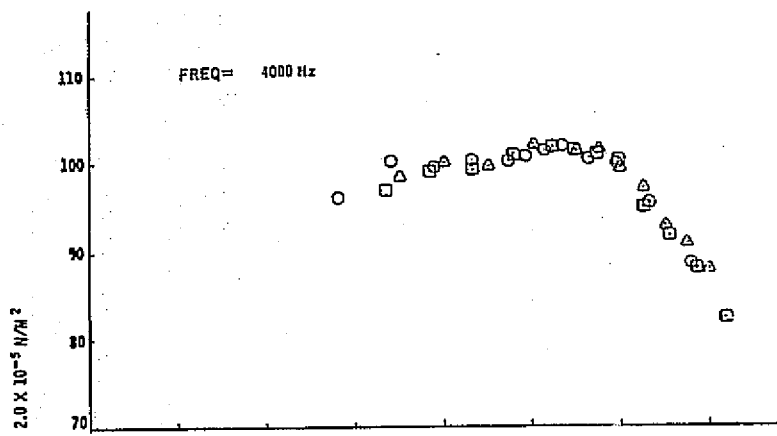


Figure 44.-(Concluded)

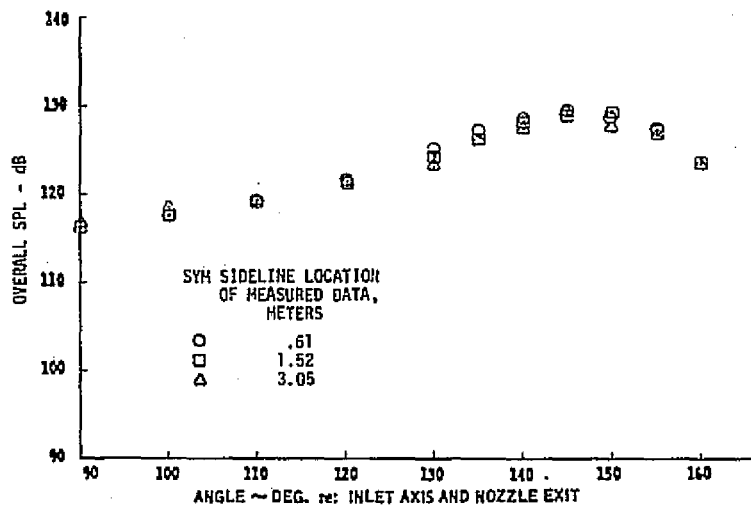
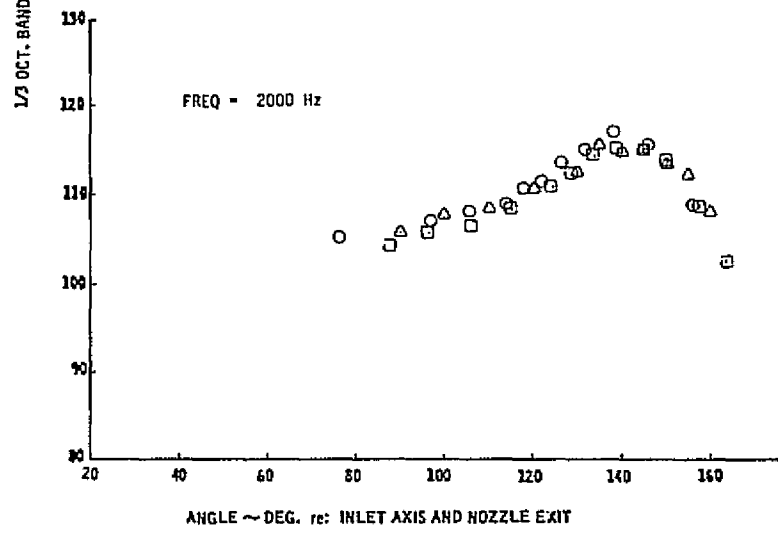
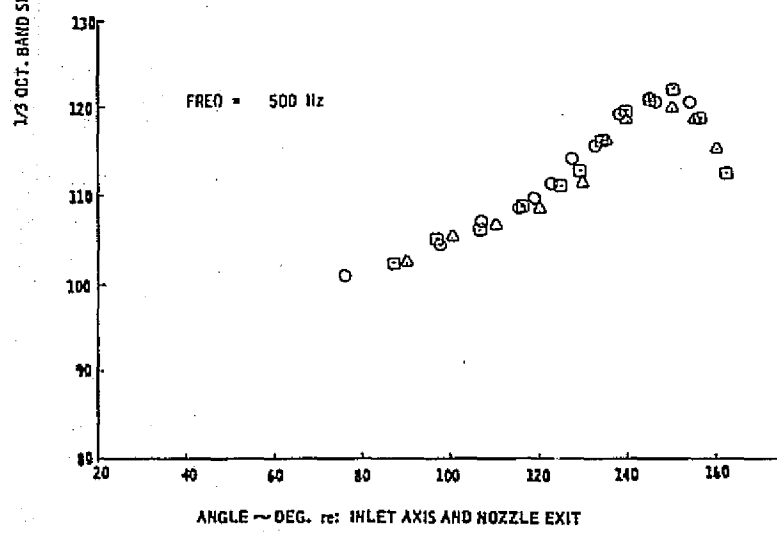
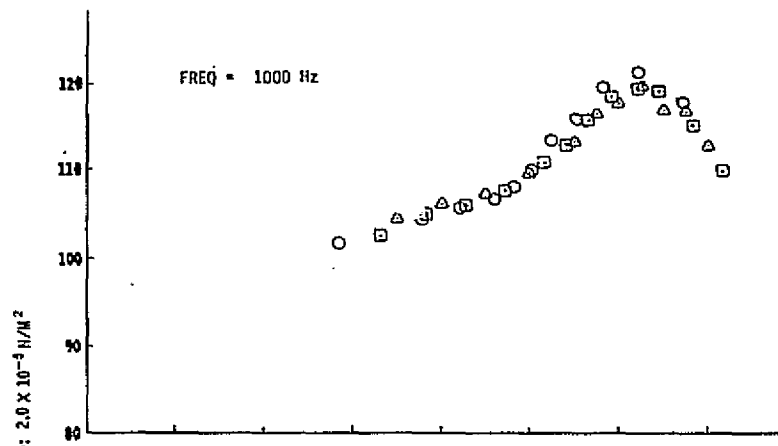
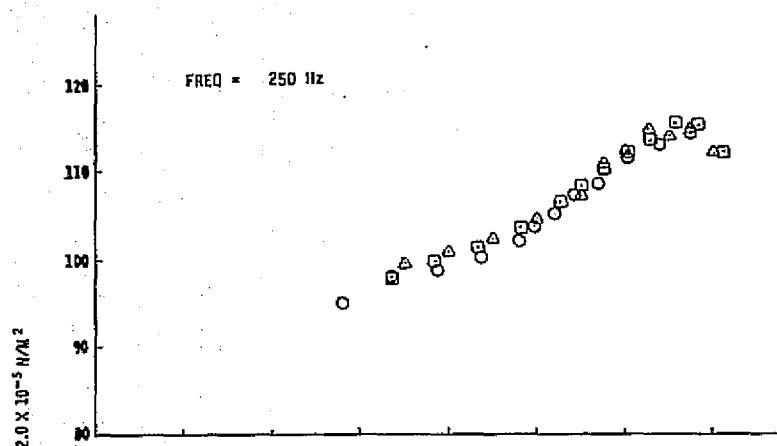


Figure 45.—OASPL and One-Third-Octave-Band SPL Directivity Data for the Annular Nozzle With Lined Ejector Extrapolated to a 3.0-m Sideline—NPR = 1.75,  $T_T = 844$  K



(Figure 45.--(Continued))

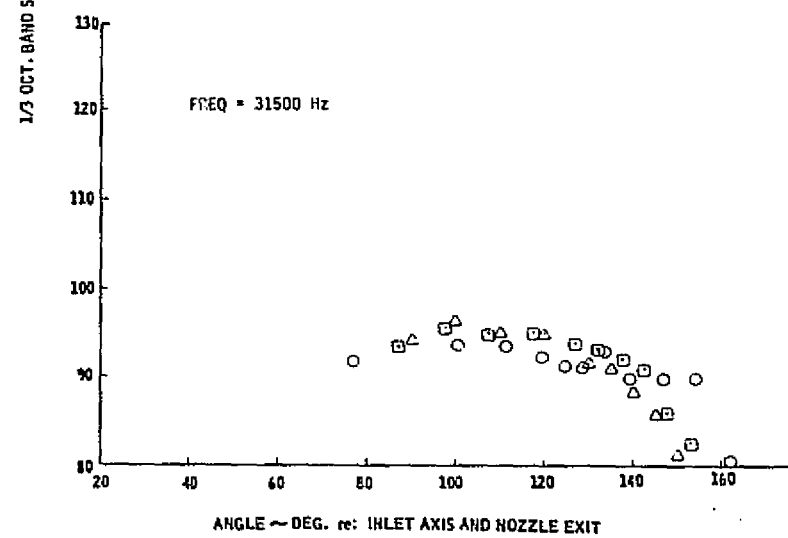
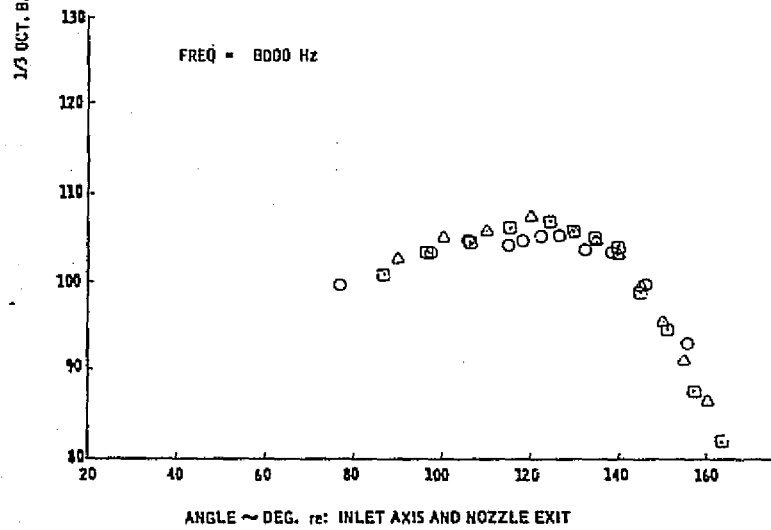
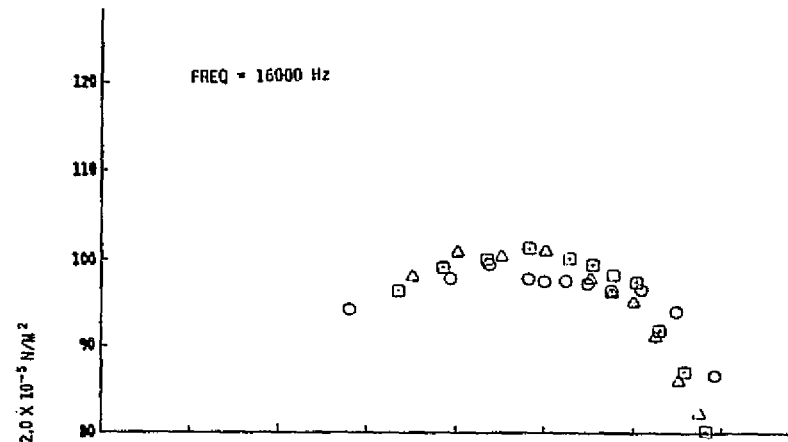
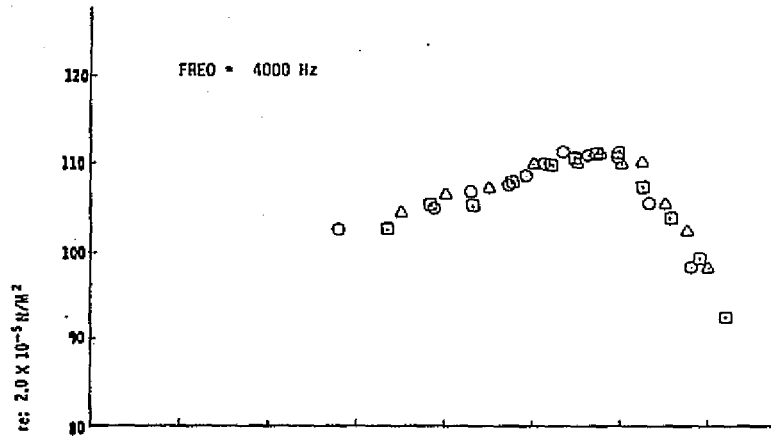


Figure 45.-(Concluded)

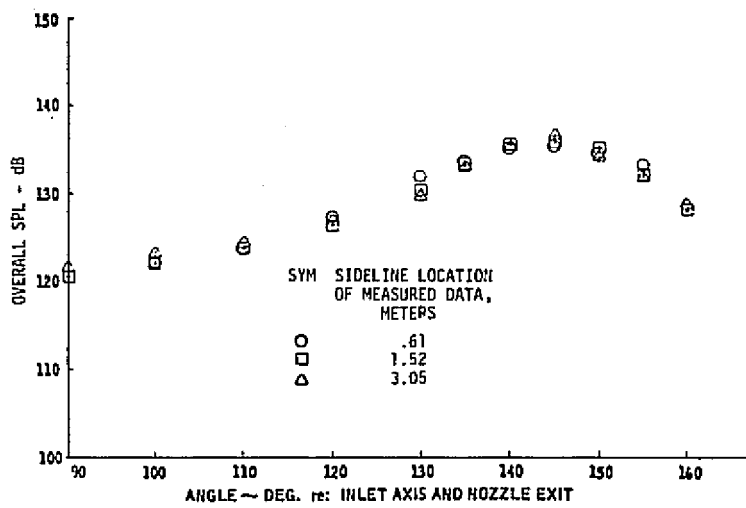


Figure 46.—OASPL and One-Third-Octave-Band SPL Directivity Data for the Annular Nozzle With Lined Ejector Extrapolated to  $\pm 3.0$ -Sideline—NPR = 2.25,  $T_T = 844$  K

ORIGINAL PAGE IS  
OF POOR QUALITY

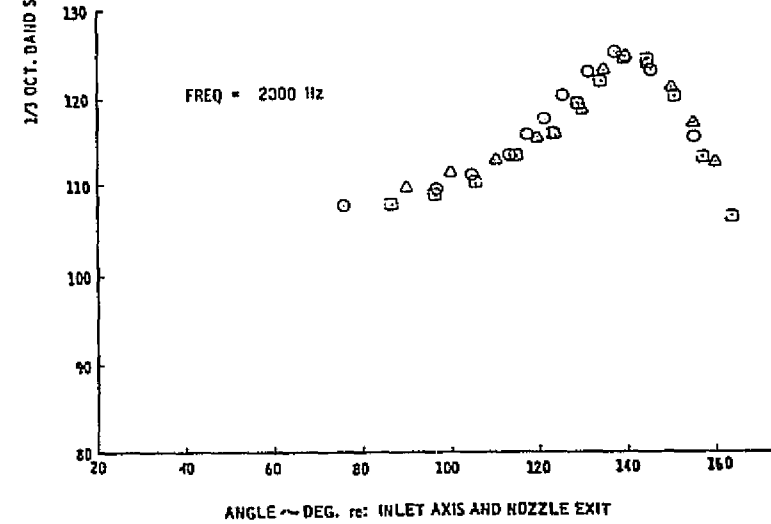
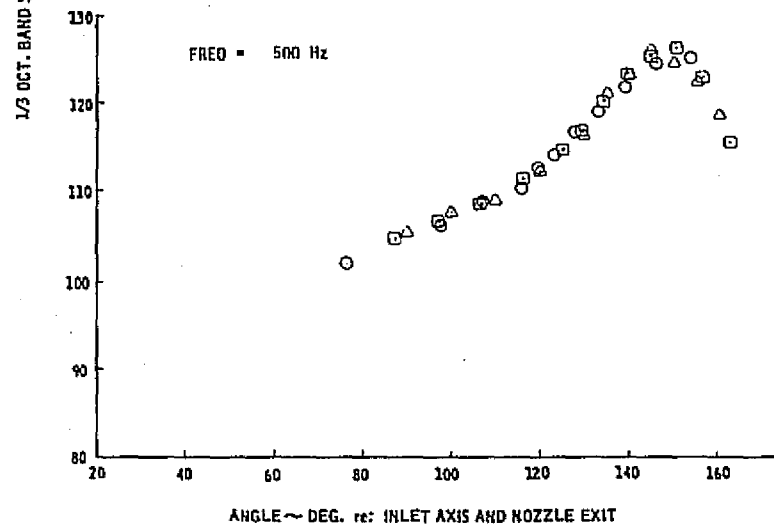
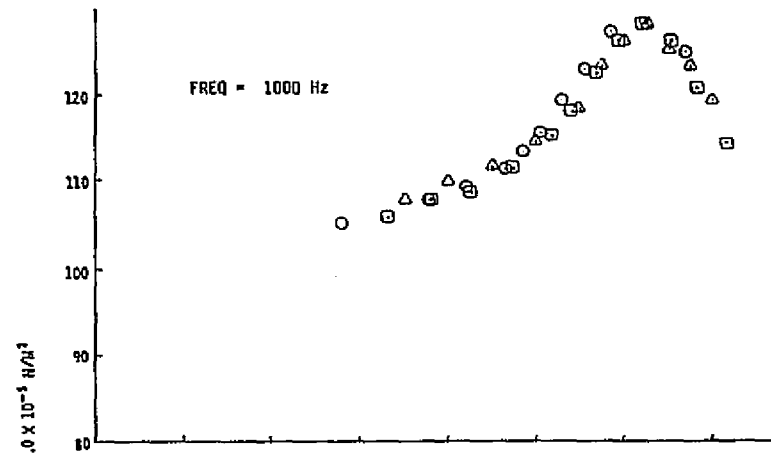
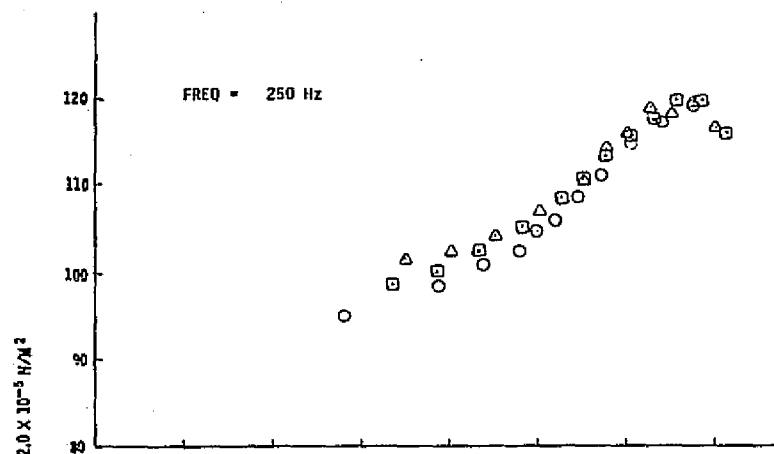


Figure 46.—(Continued)

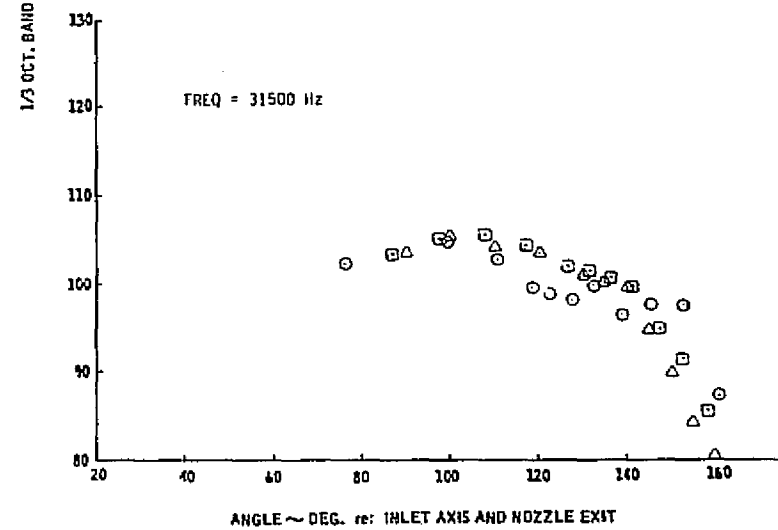
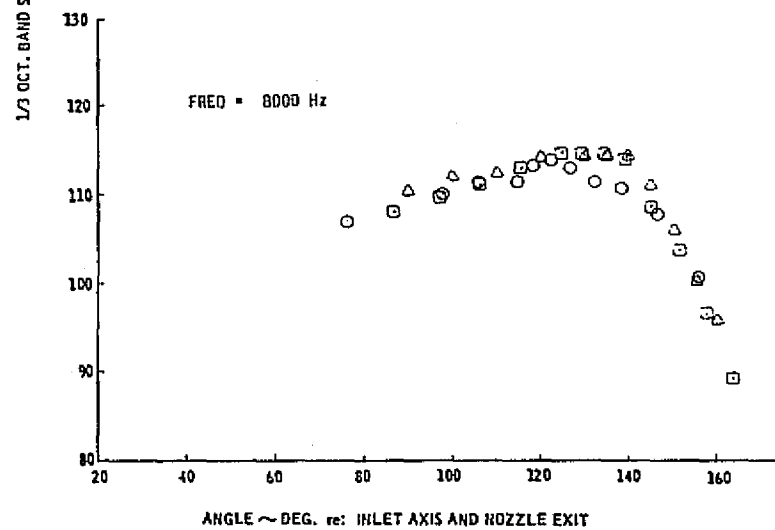
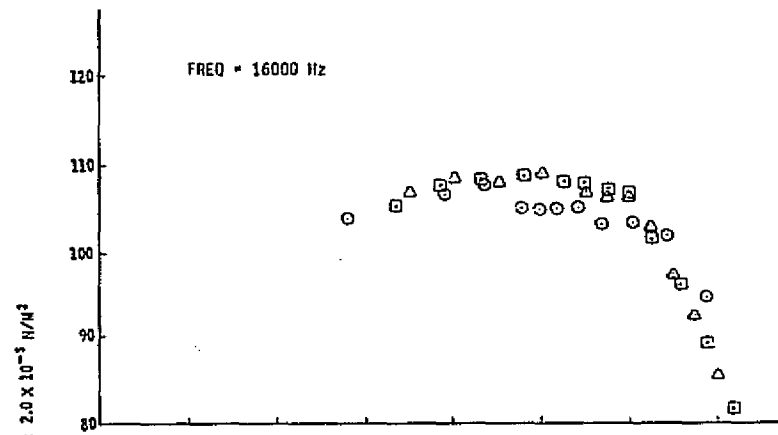
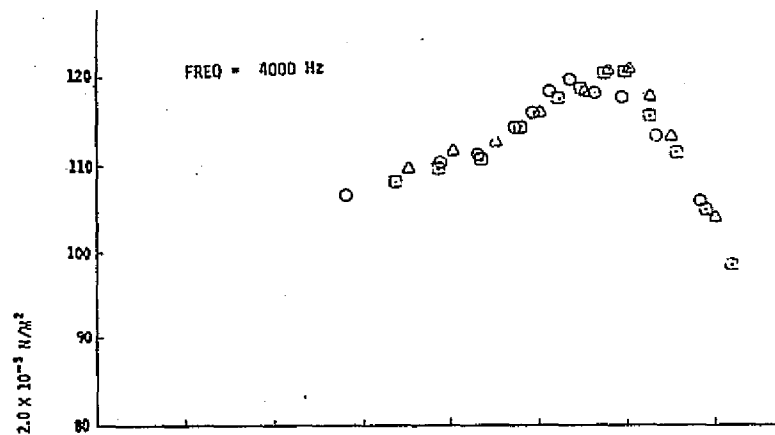


Figure 46.—(Concluded)

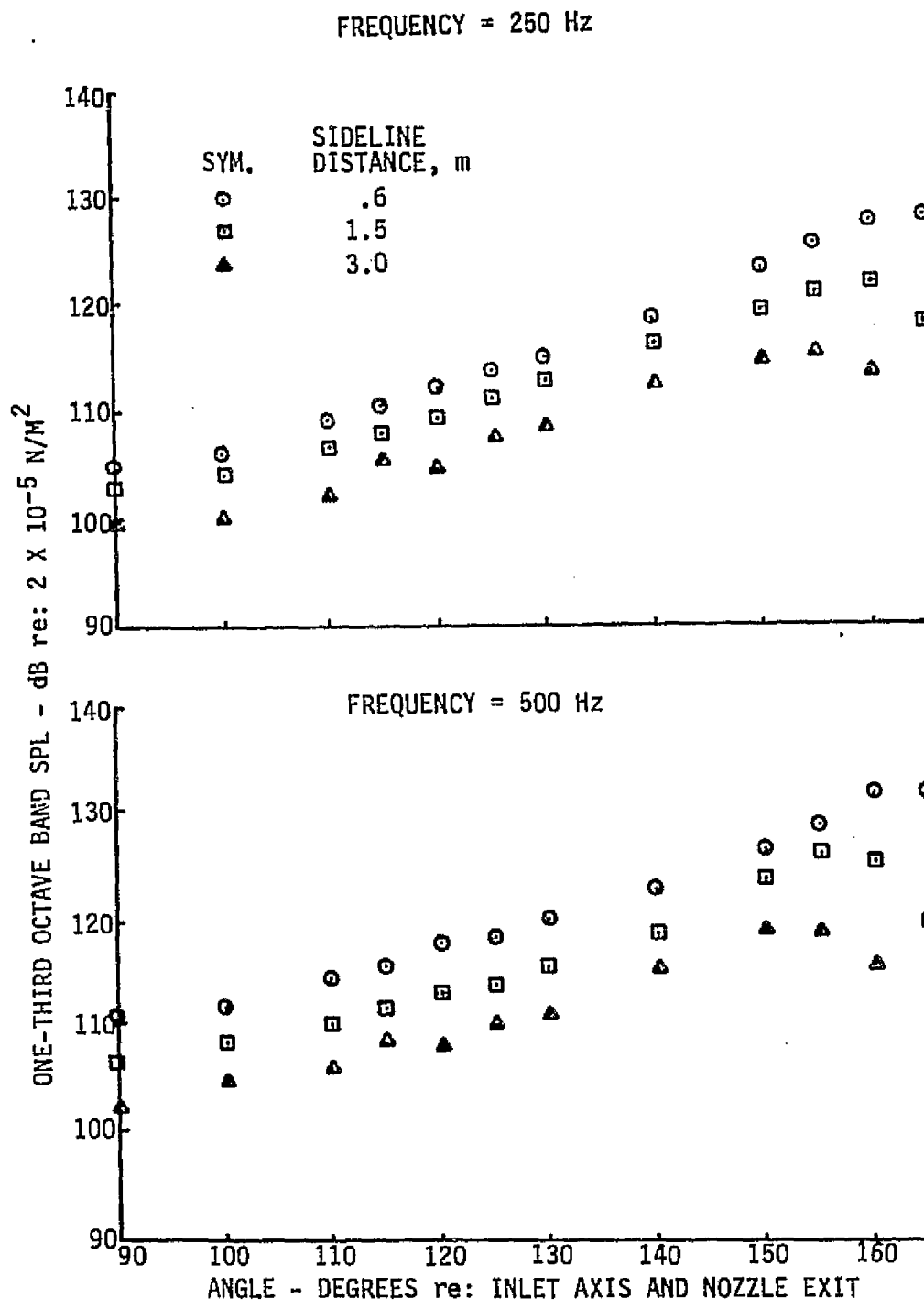


Figure 47.—One-Third-Octave-Band SPL Directivities for the 20-Lobe Nozzle With Lined Ejector—NPR = 2.25,  $T_T = 844 \text{ K}$

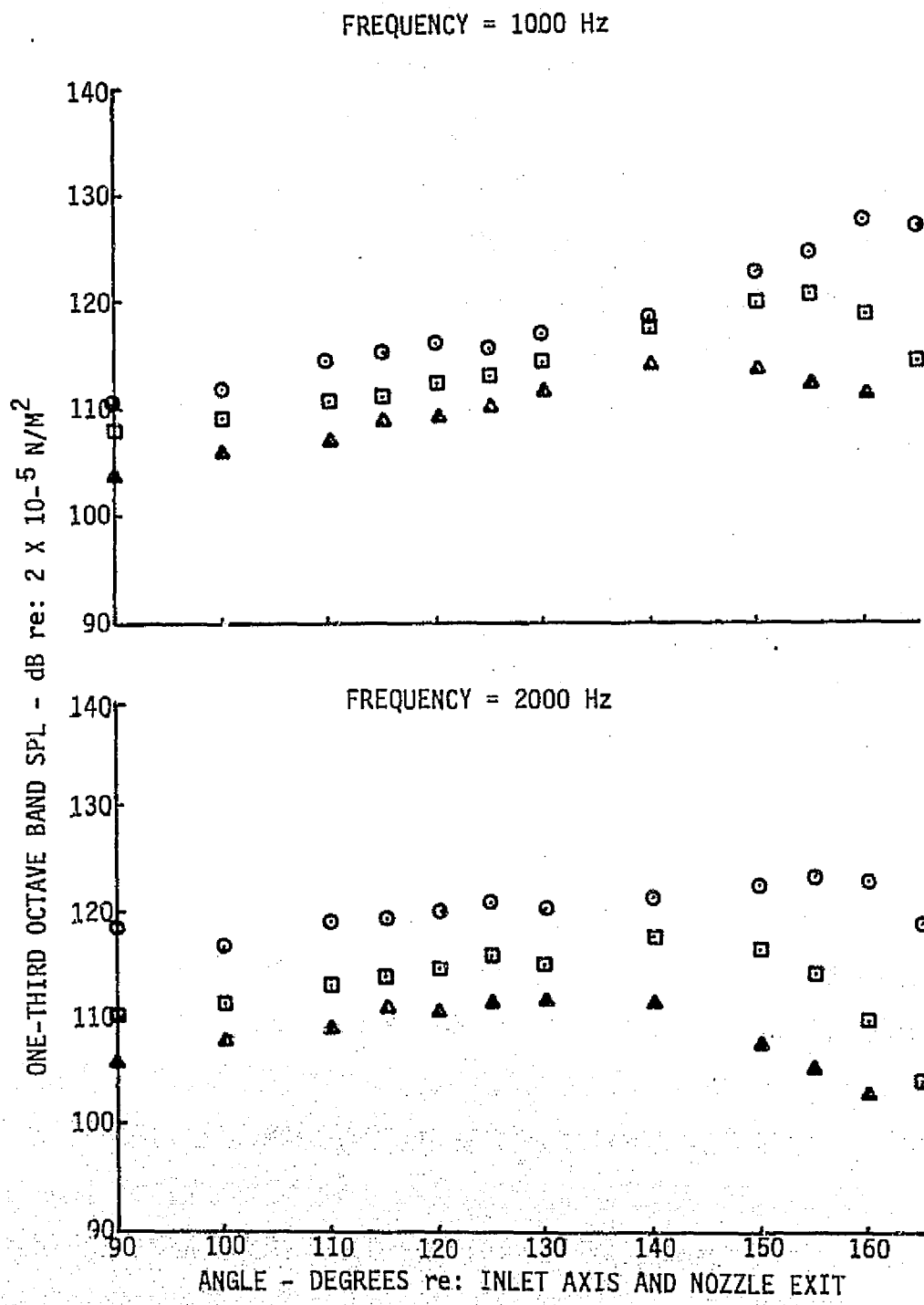
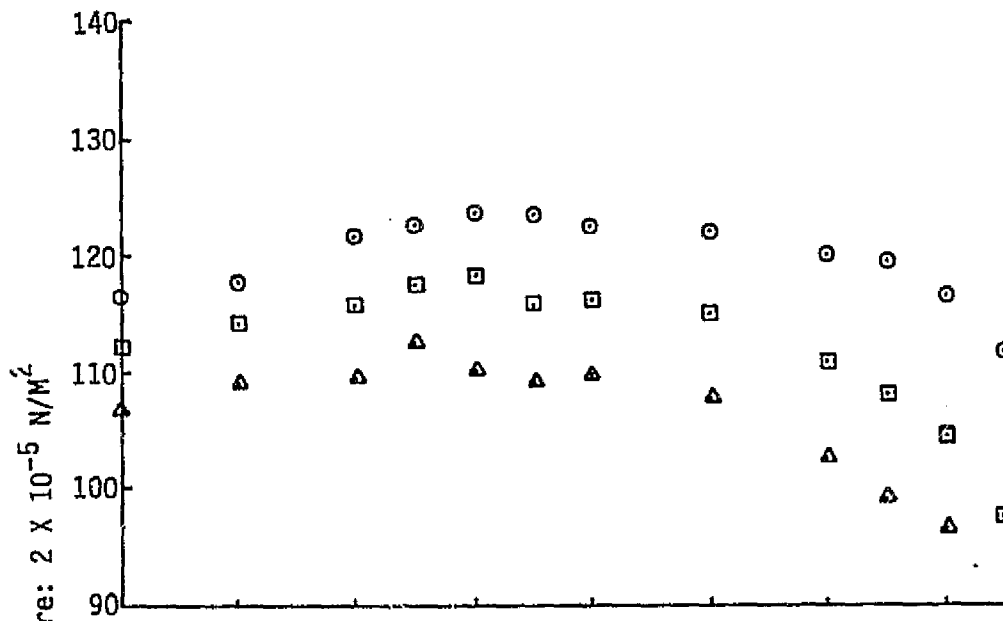


Figure 47.--(Continued)

FREQUENCY = 4000 Hz



FREQUENCY = 8000 Hz

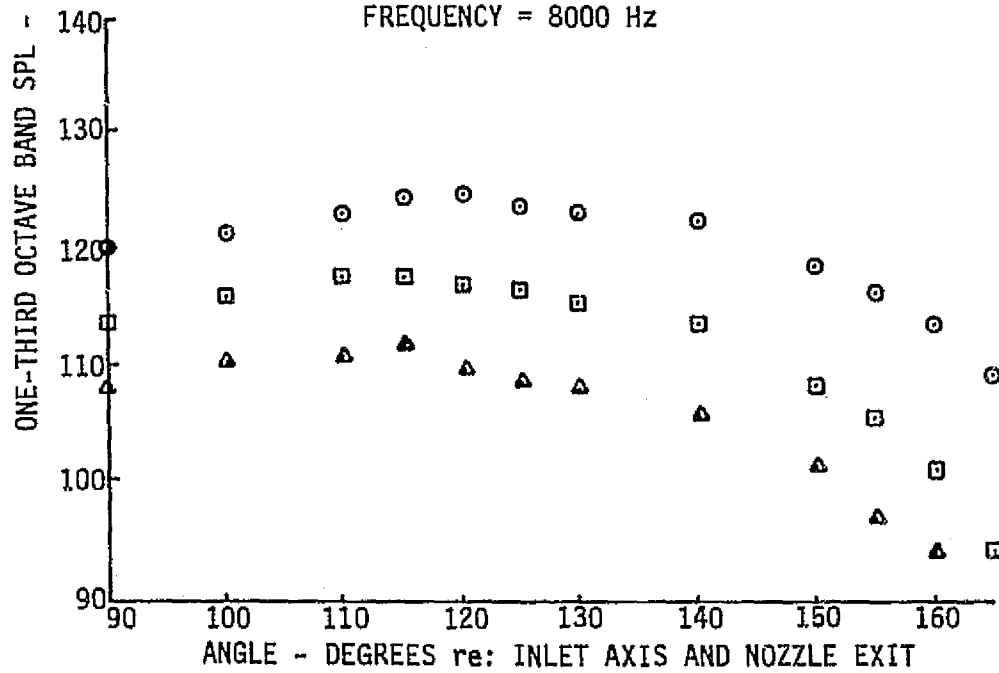
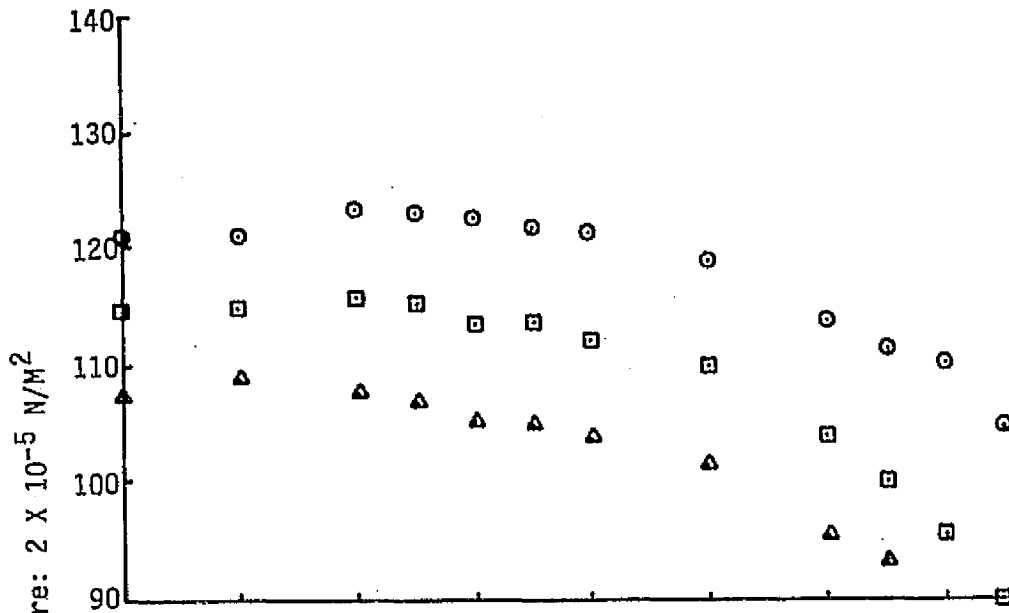


Figure 47.—(Continued)

FREQUENCY = 16000 Hz



FREQUENCY = 31500 Hz

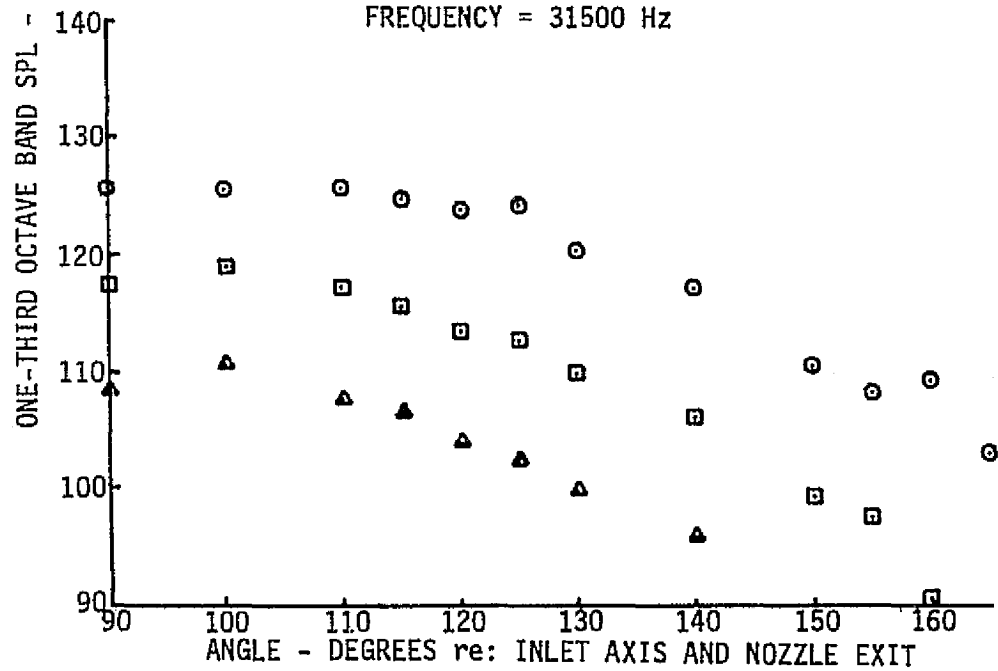


Figure 47.—(Concluded)

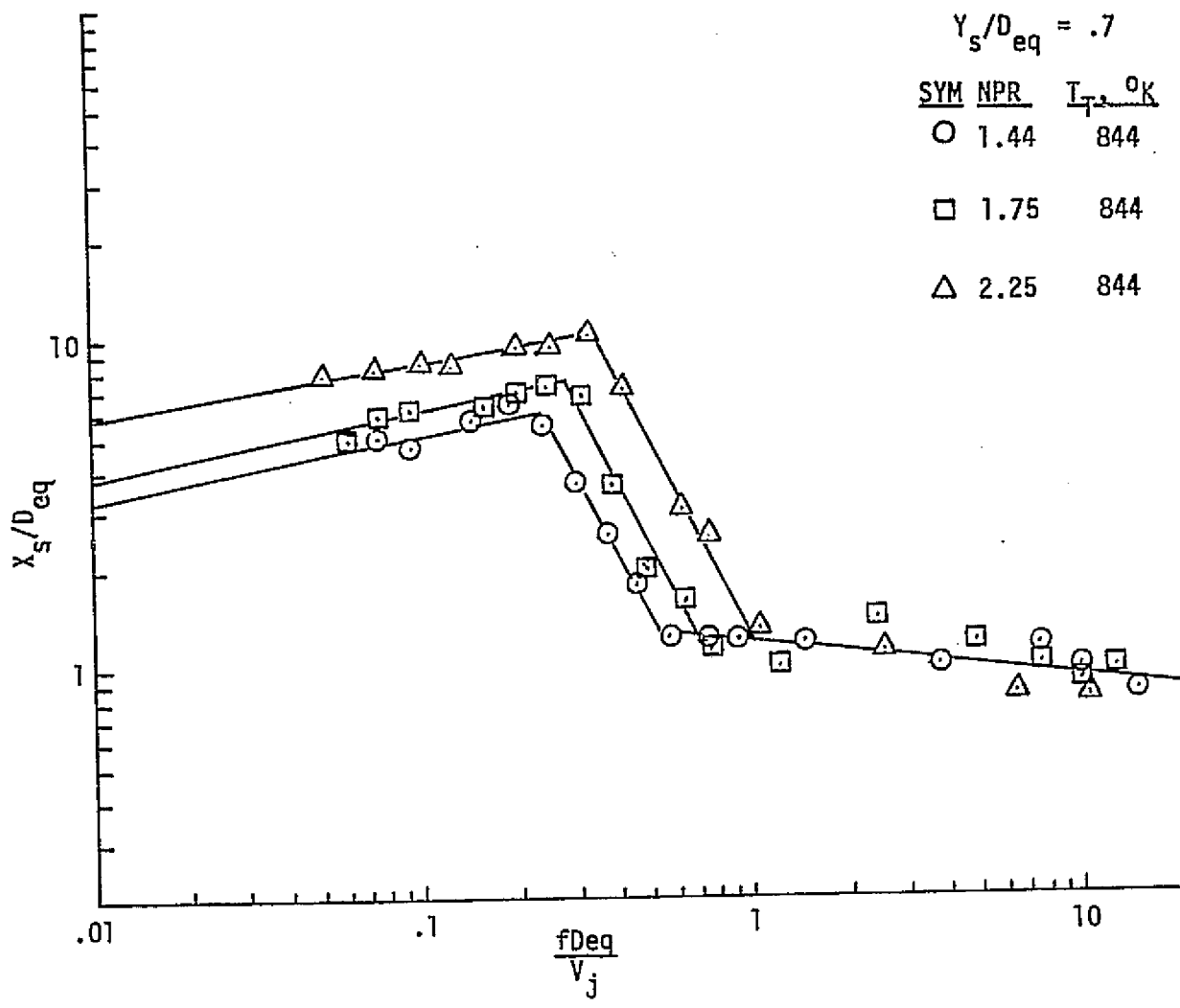


Figure 48.—Peak Noise Source Locations for the 20-Lobe Nozzle With Lined Ejector

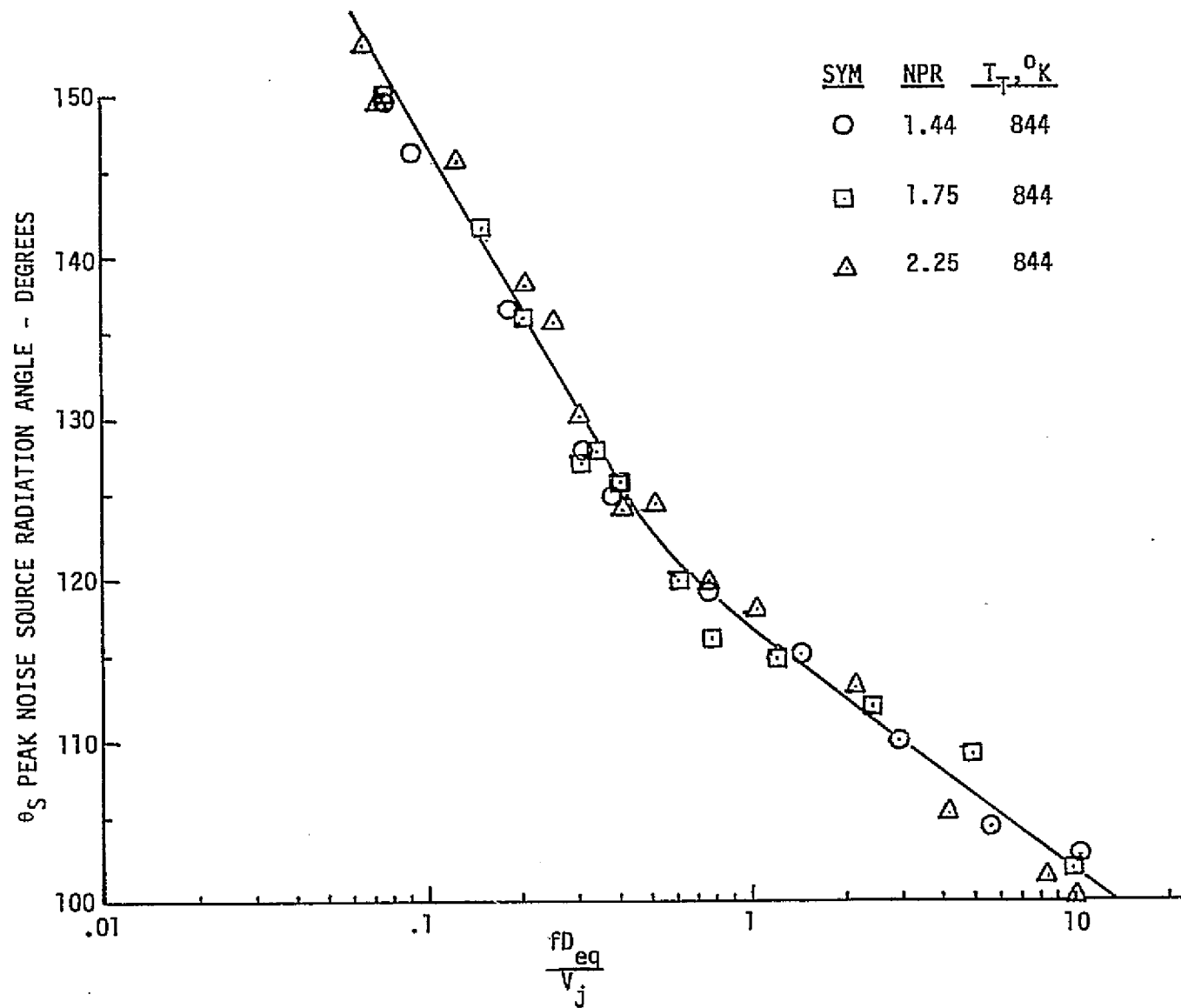


Figure 49.—Peak Noise Source Radiation Angles for the 20-Lobe Nozzle With Lined Ejector

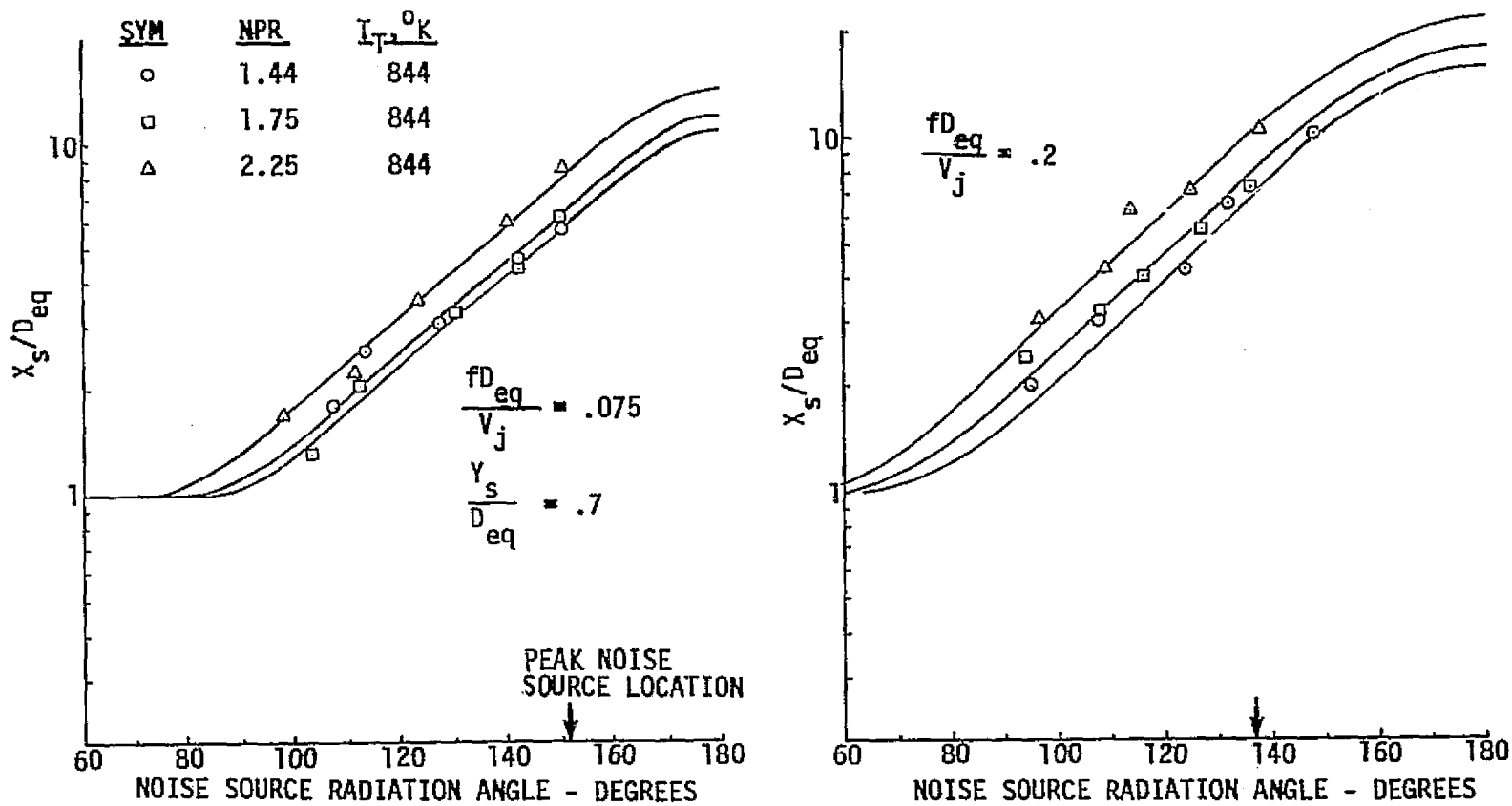


Figure 50.—Distributed Noise Source Locations for the 20-Lobe Nozzle With Lined Ejector

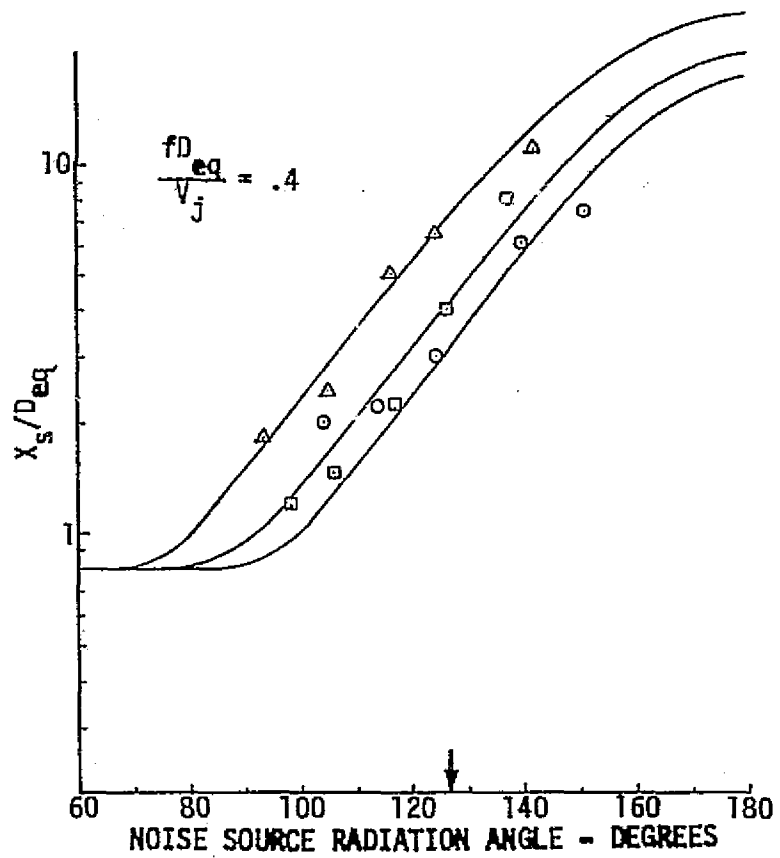
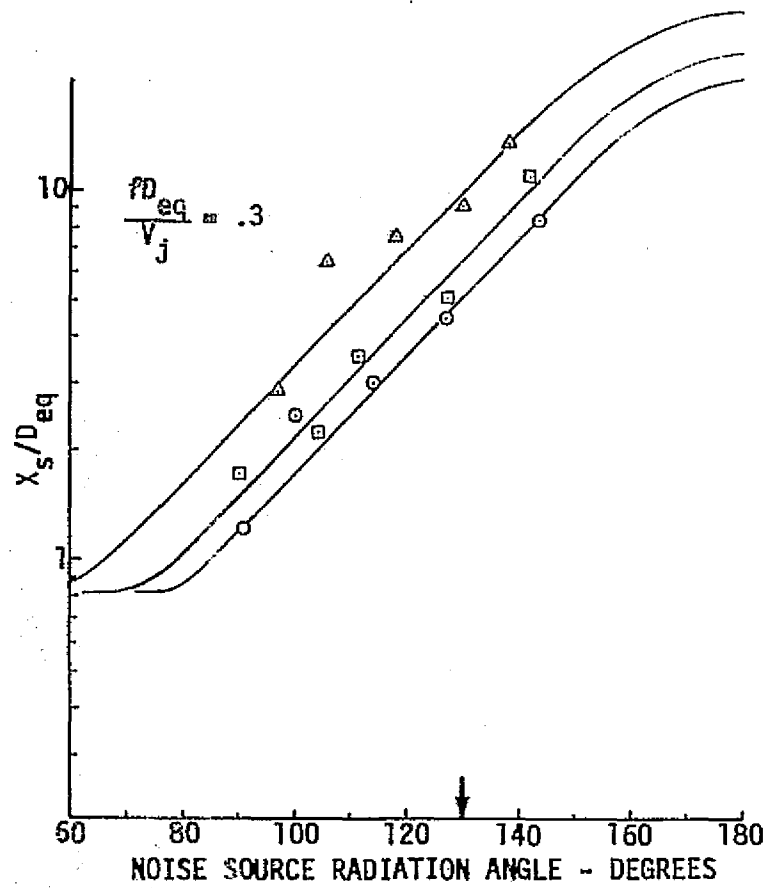


Figure 50.—(Continued)

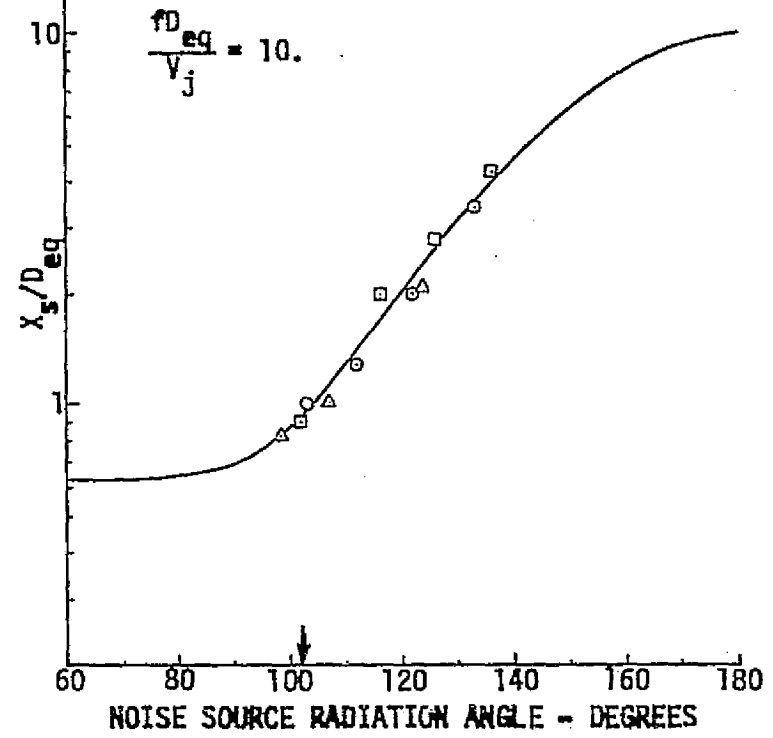
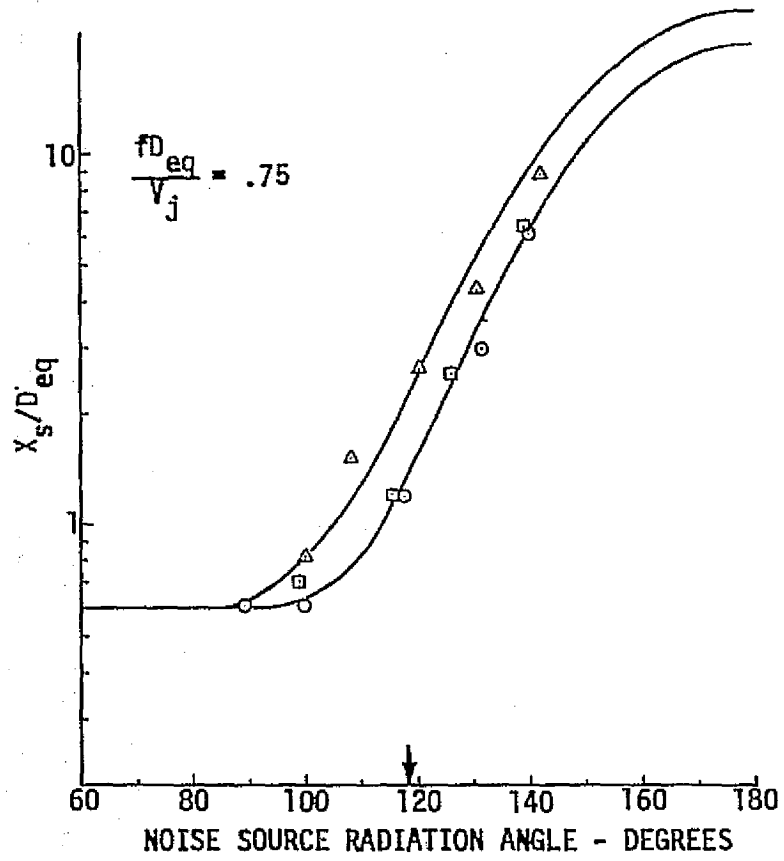


Figure 50.—(Concluded)

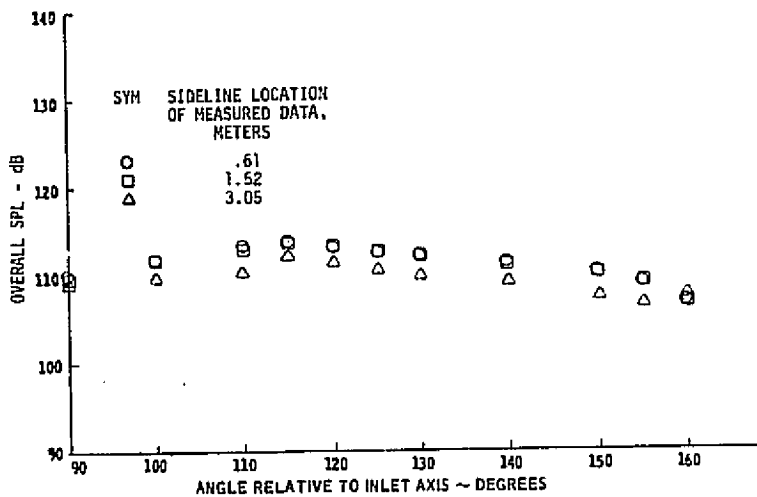


Figure 51.—OASPL and One-Third-Octave-Band SPL Directivity Data for the 20-Lobe Nozzle With Lined Ejector Extrapolated to a 3.0-m Sideline—NPR = 1.44,  $T_T = 844$  K

ORIGINAL PAGE IS  
OF POOR QUALITY

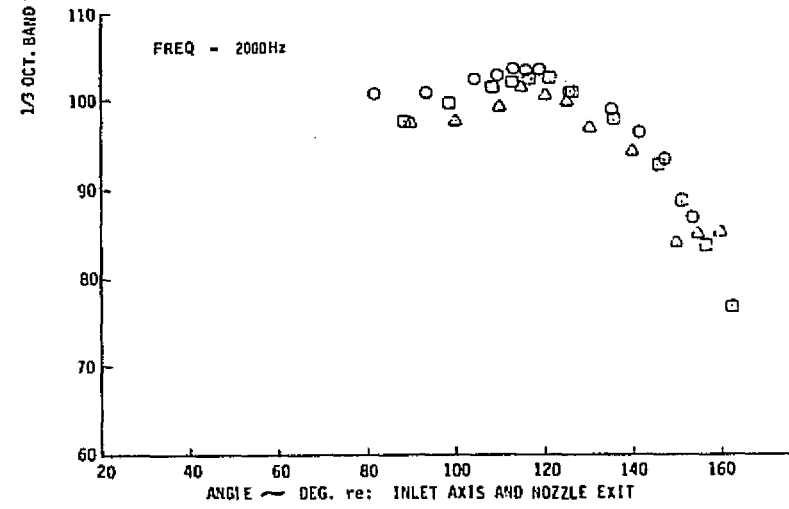
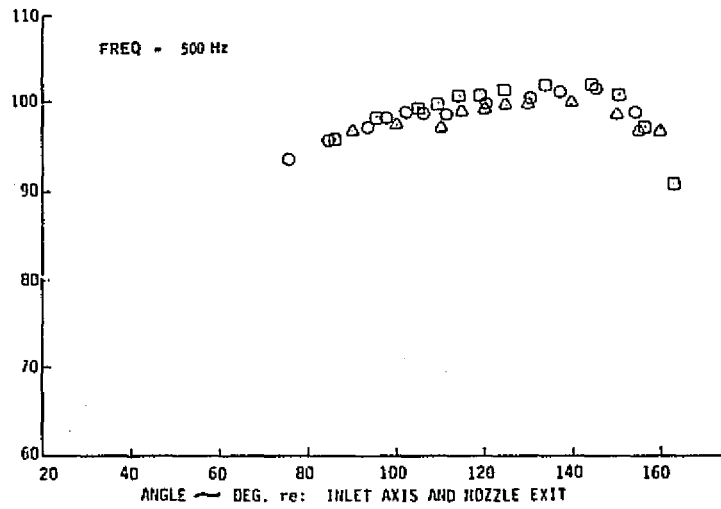
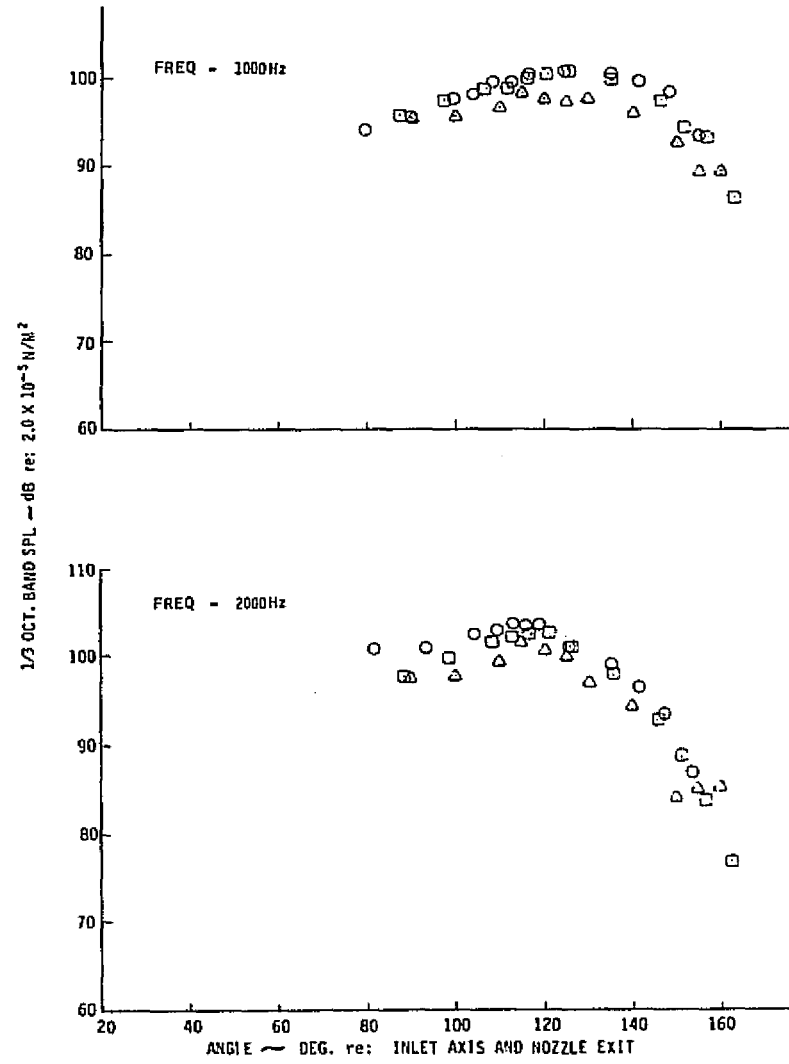
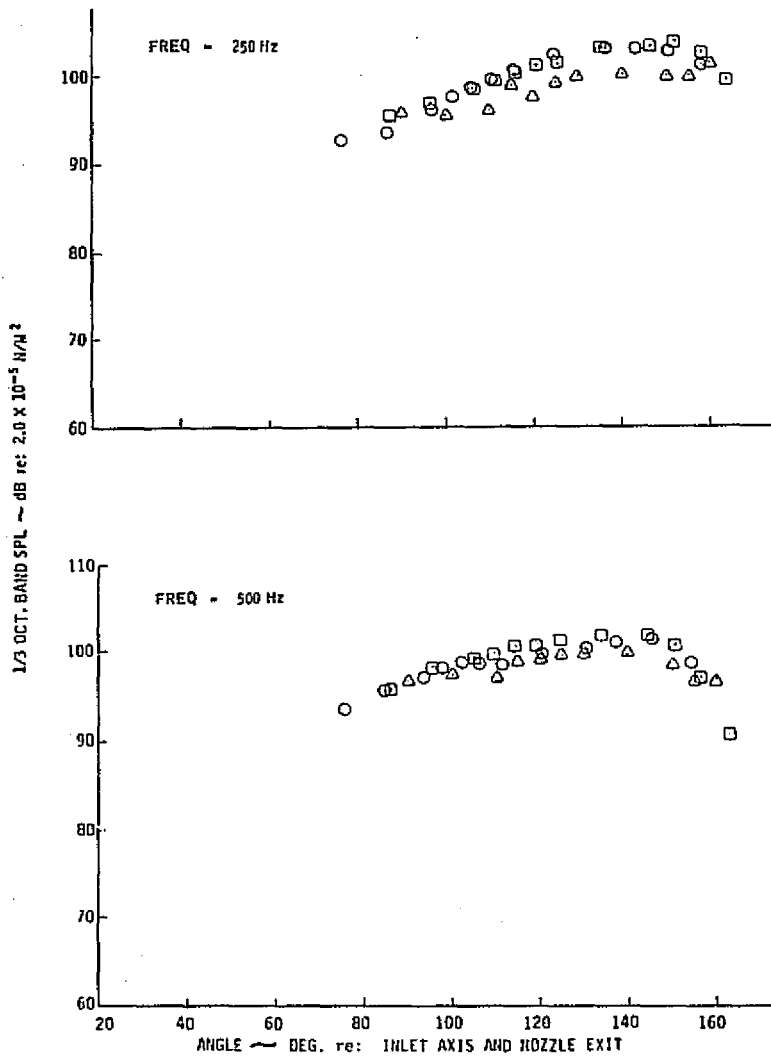


Figure 51.—(Continued)

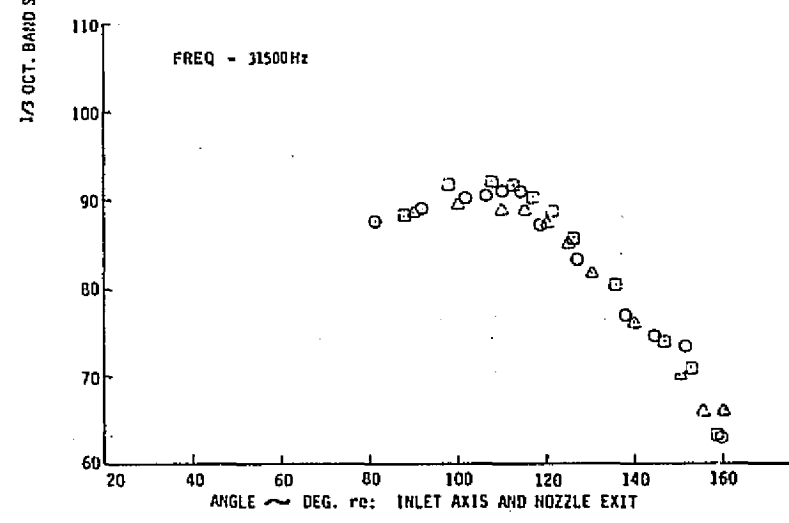
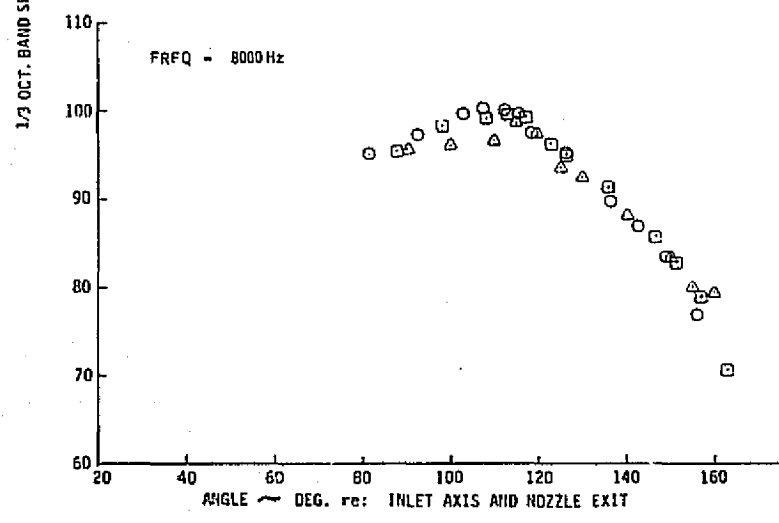
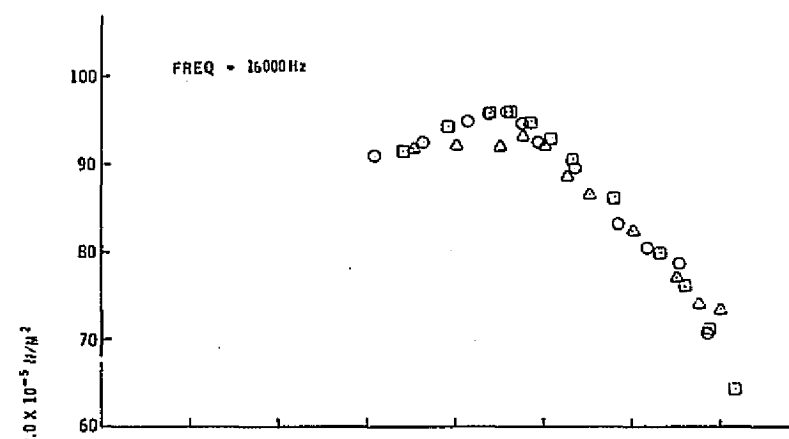
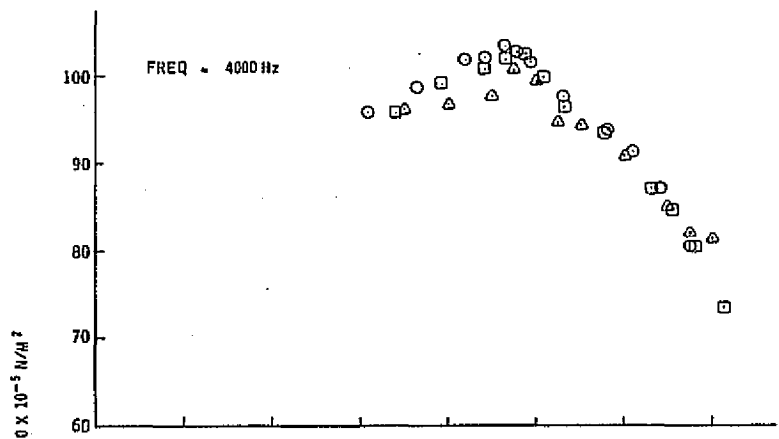


Figure 51.—(Concluded)

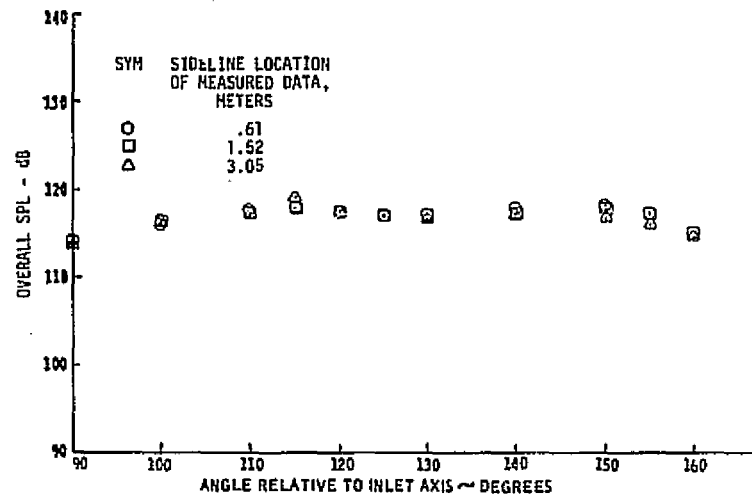


Figure 52.—OASPL and One-Third-Octave-Band SPL Directivity Data for the 20-Lobe Nozzle With Lined Ejector Extrapolated to a 3.0-m Sideline—NPR = 1.75,  $T_T = 844$  K

ORIGINAL PAGE IS  
OF POOR QUALITY

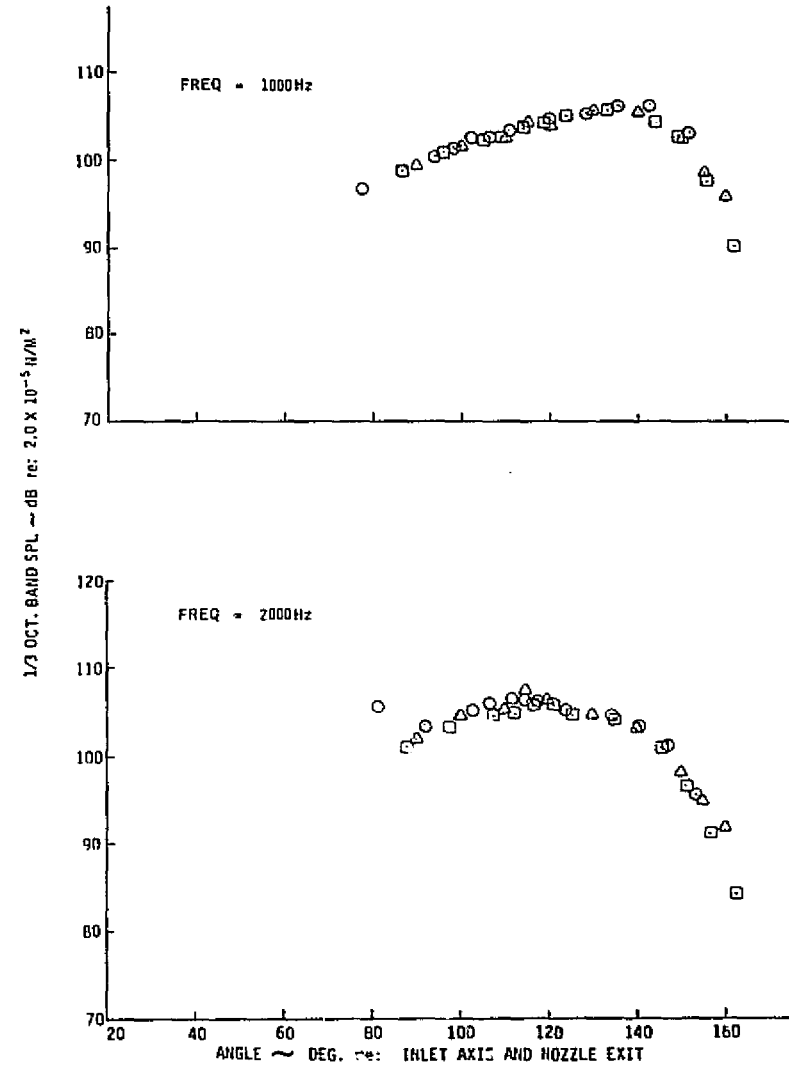
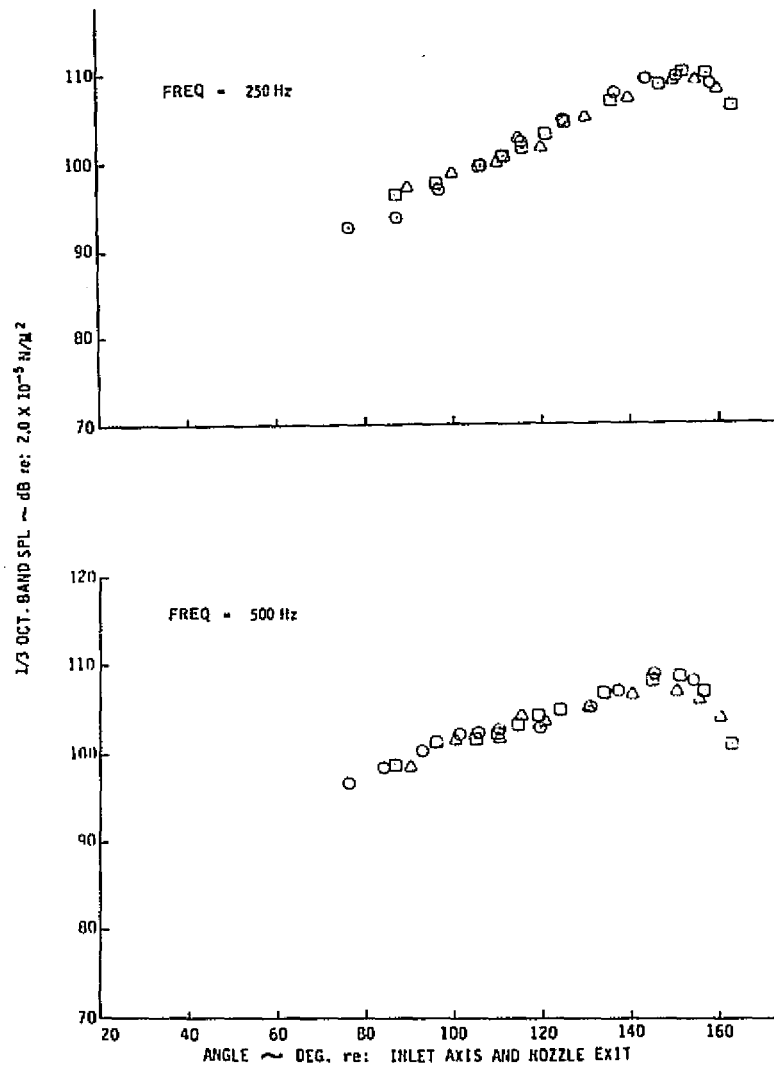


Figure 52.—(Continued)

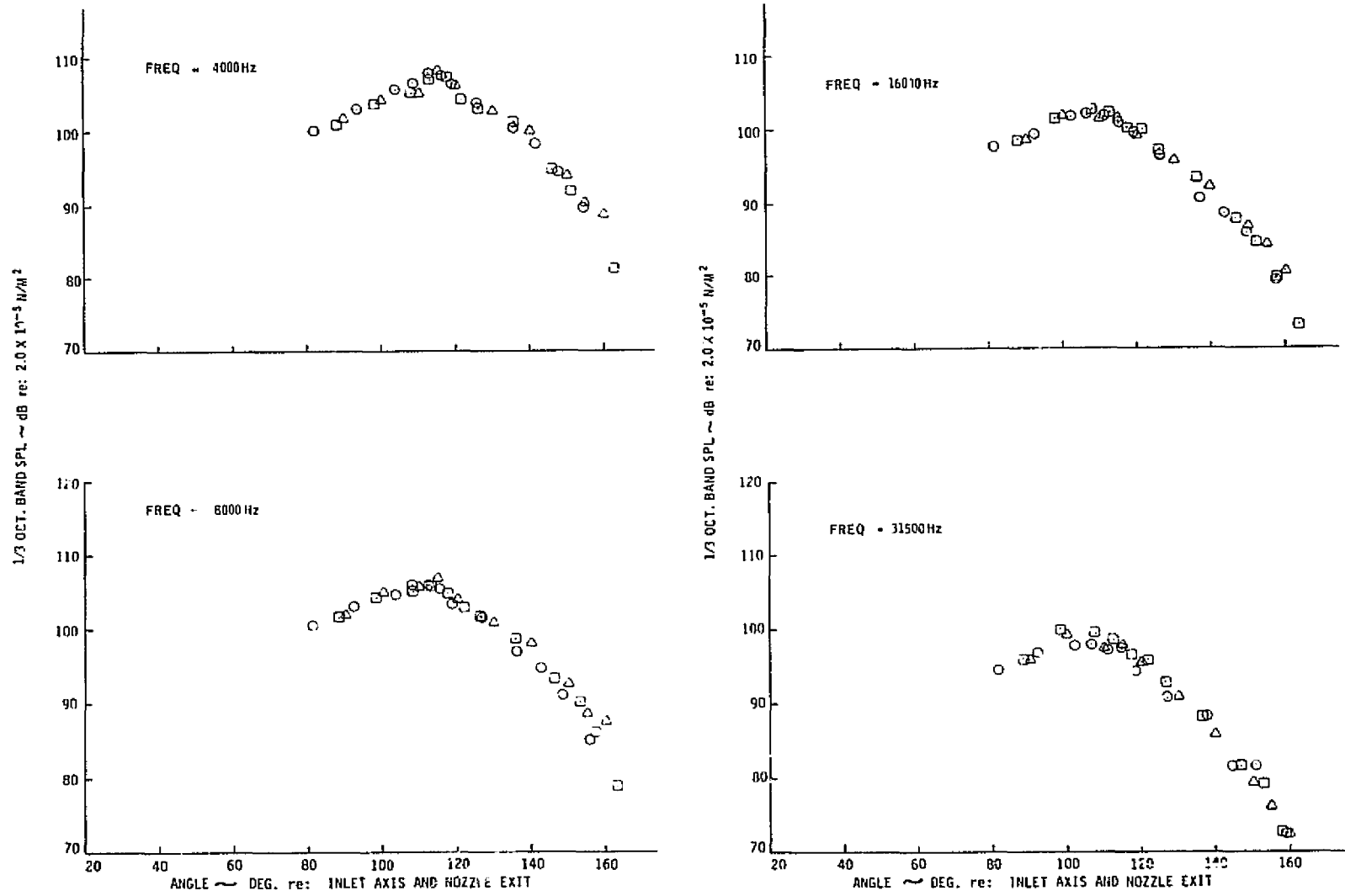


Figure 52.—(Concluded)

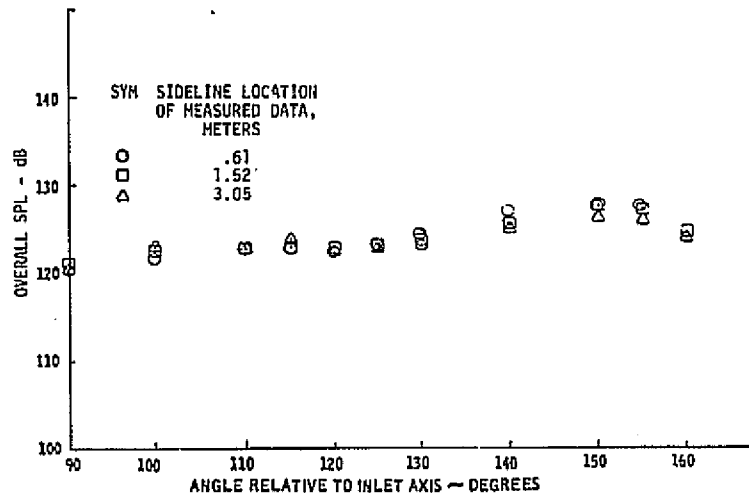


Figure 53.—OASPL and One-Third-Octave-Band SPL Directivity Data for the 20-Lobe Nozzle With Lined Ejector Extrapolated to a 3.0-m Sideline—NPR = 2.25,  $T_T = 844$  K

ORIGINAL PAGE IS  
OF POOR QUALITY

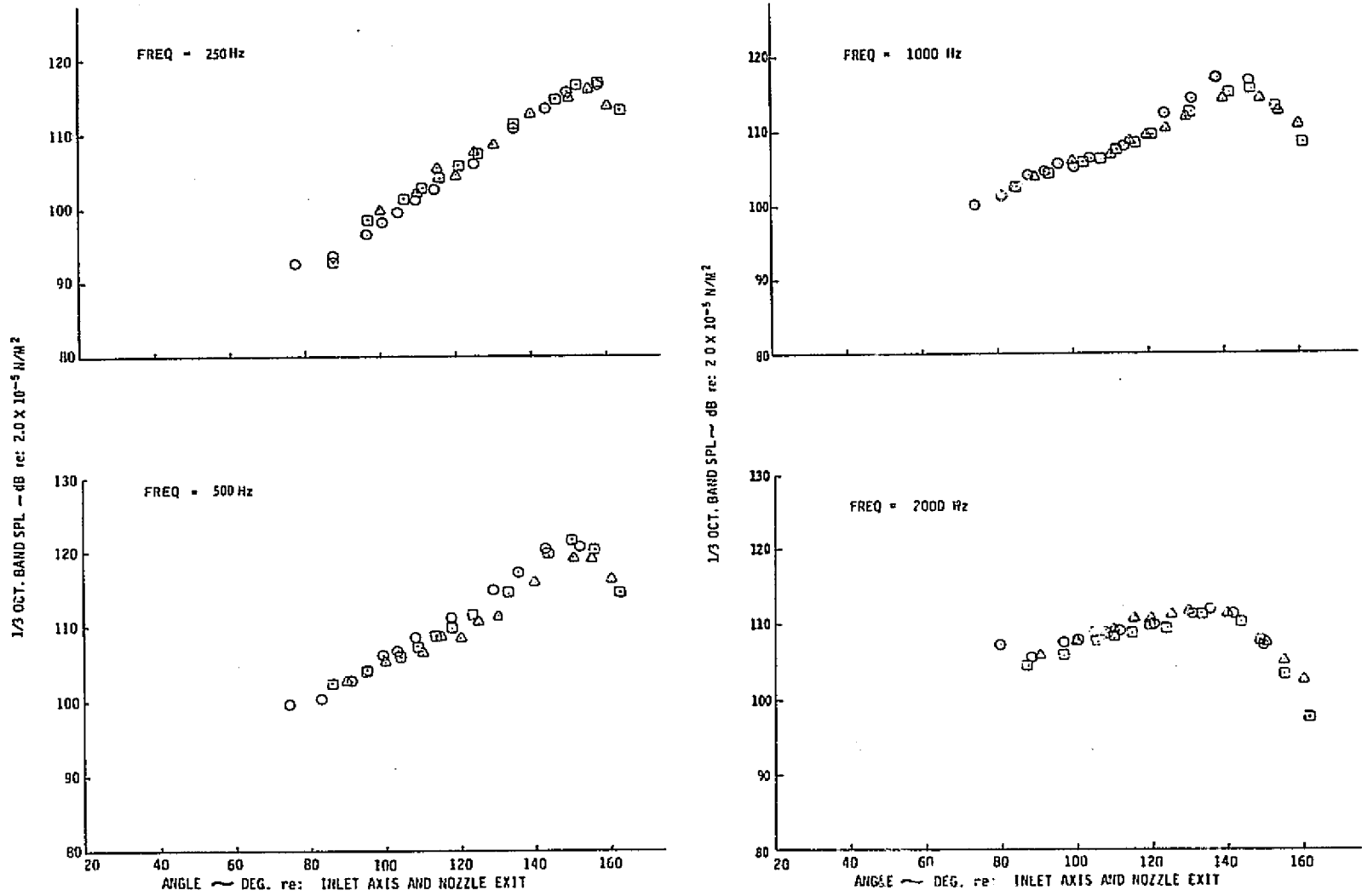


Figure 53.—(Continued)

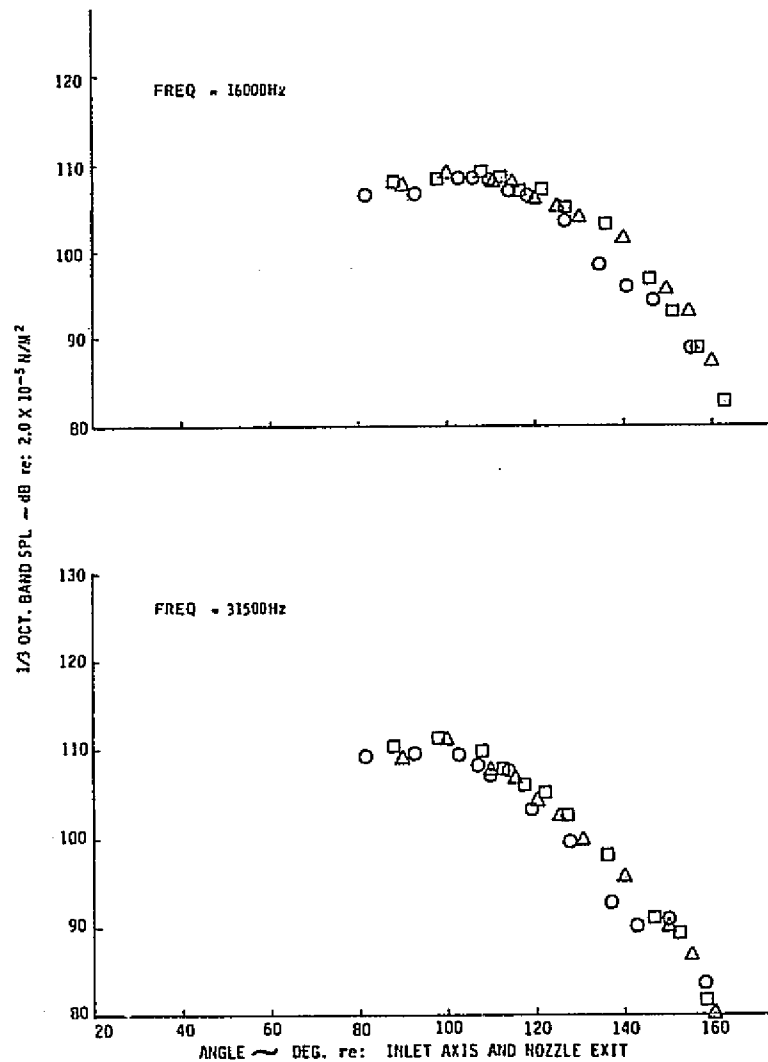
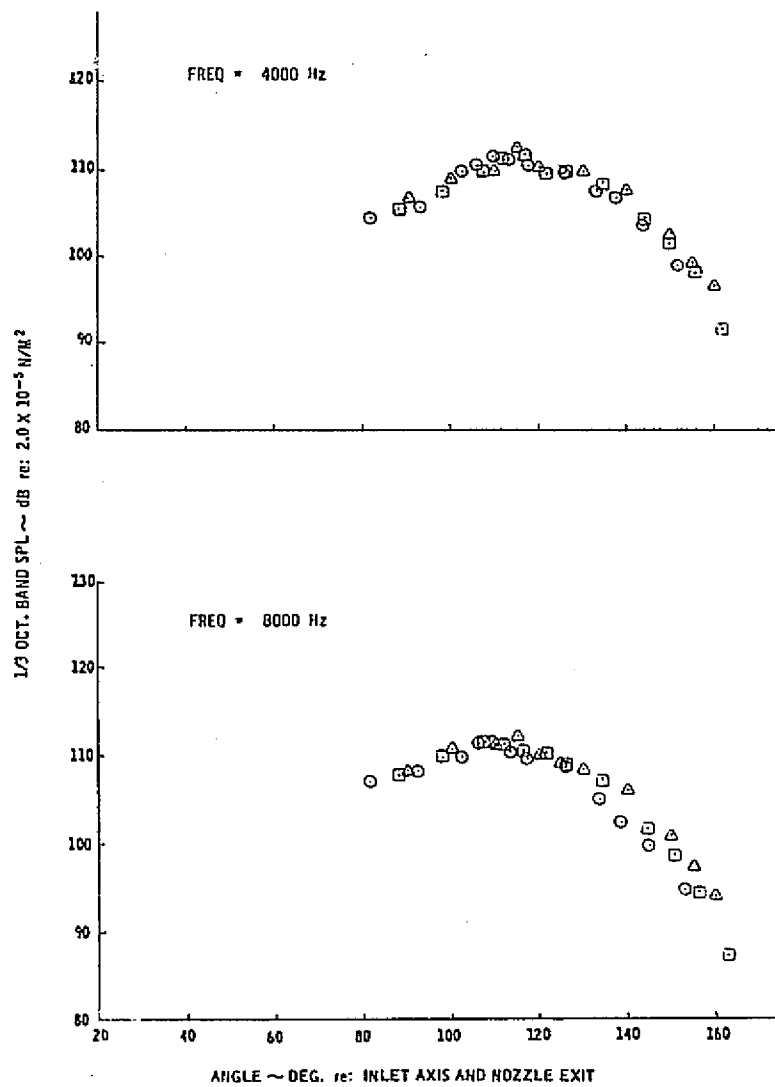


Figure 53.—(Concluded)

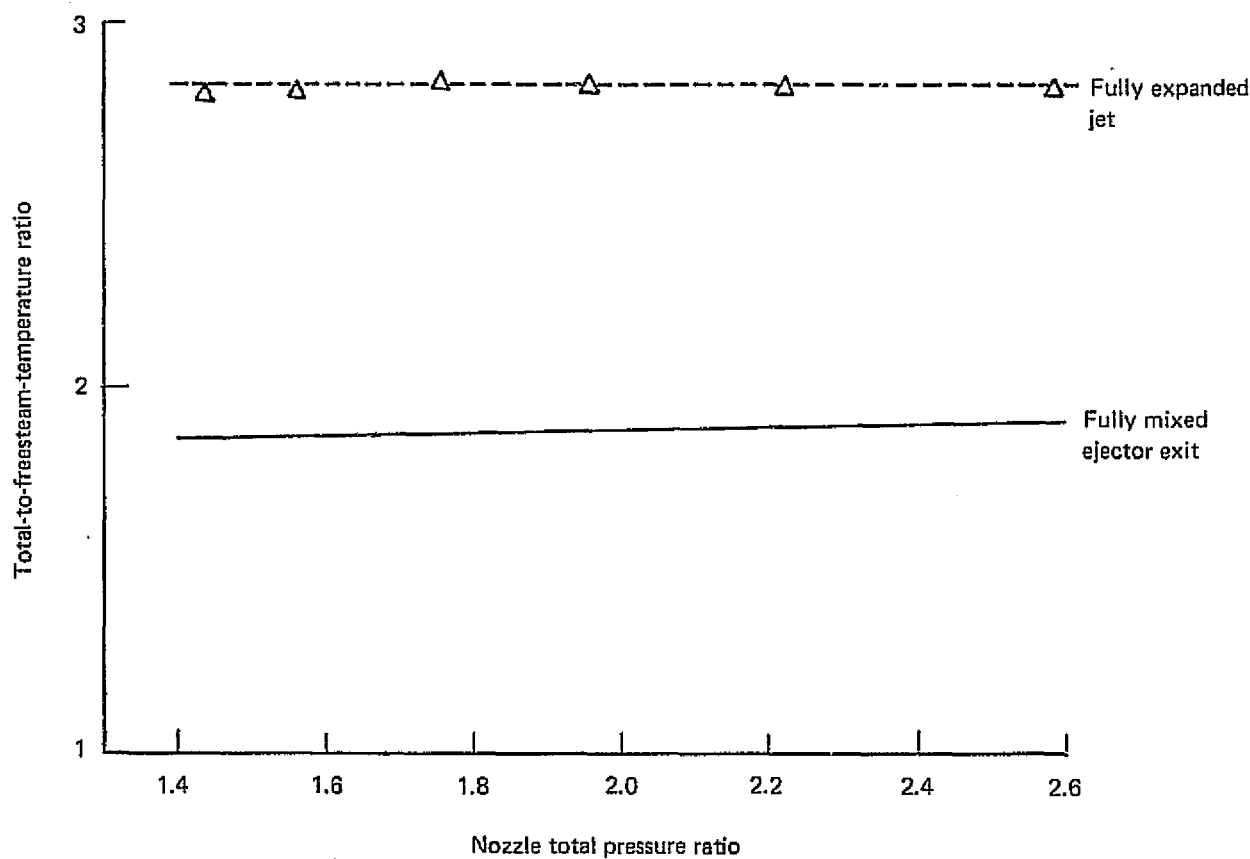
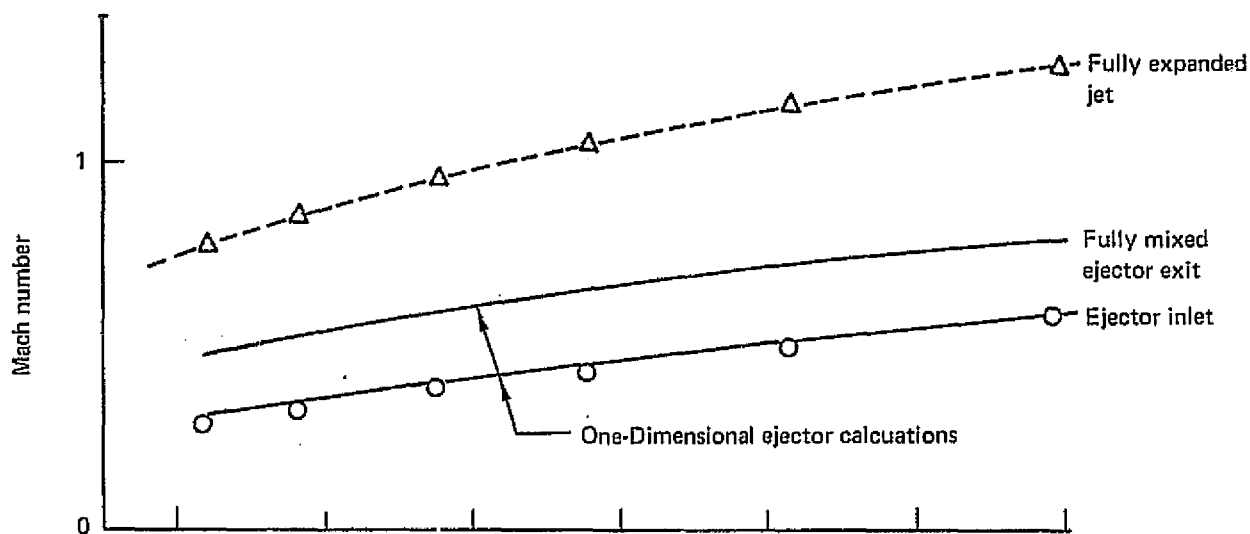


Figure 54.—Ejector Performance With 57-Tube Nozzle

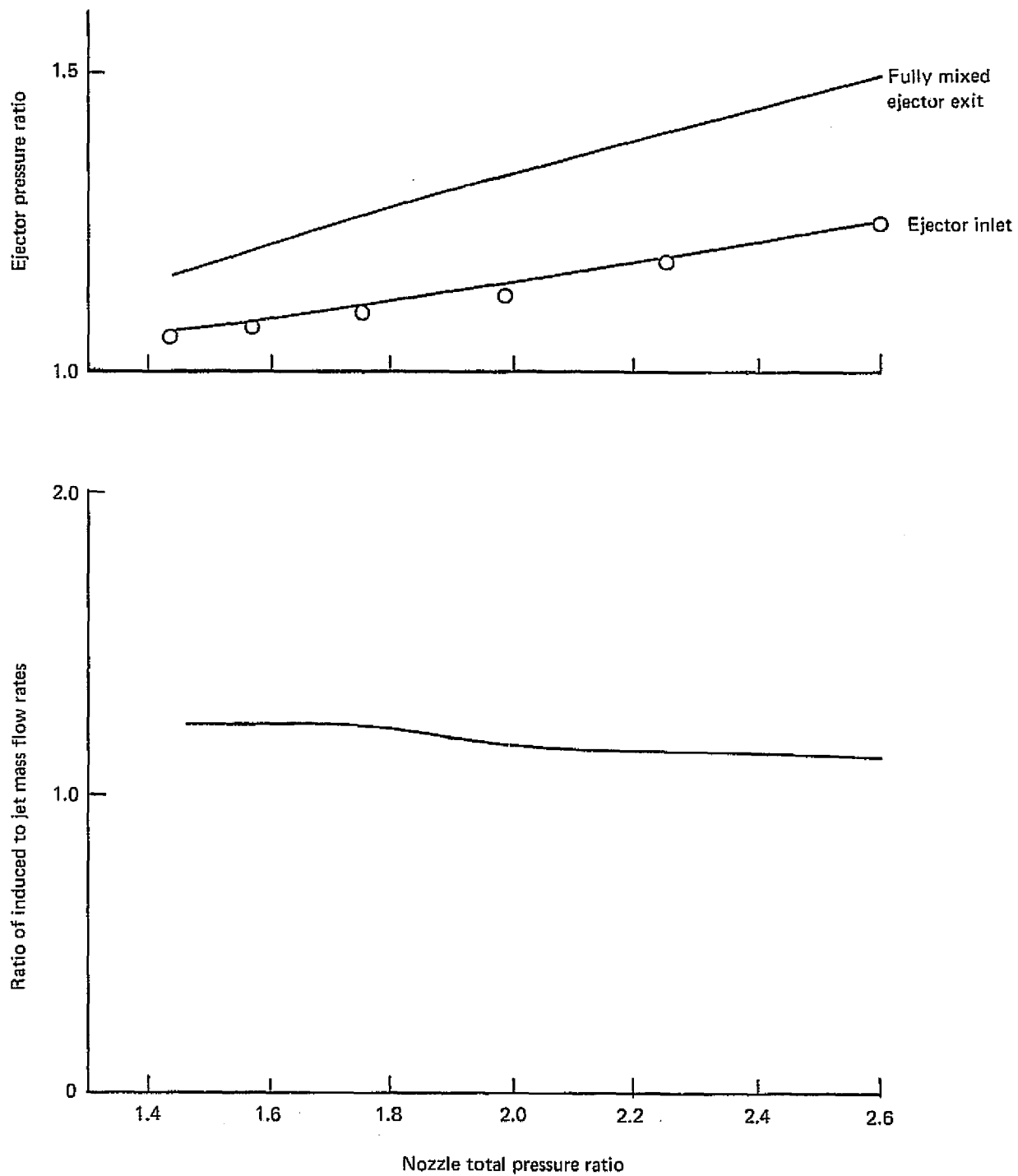


Figure 54.—(Concluded)

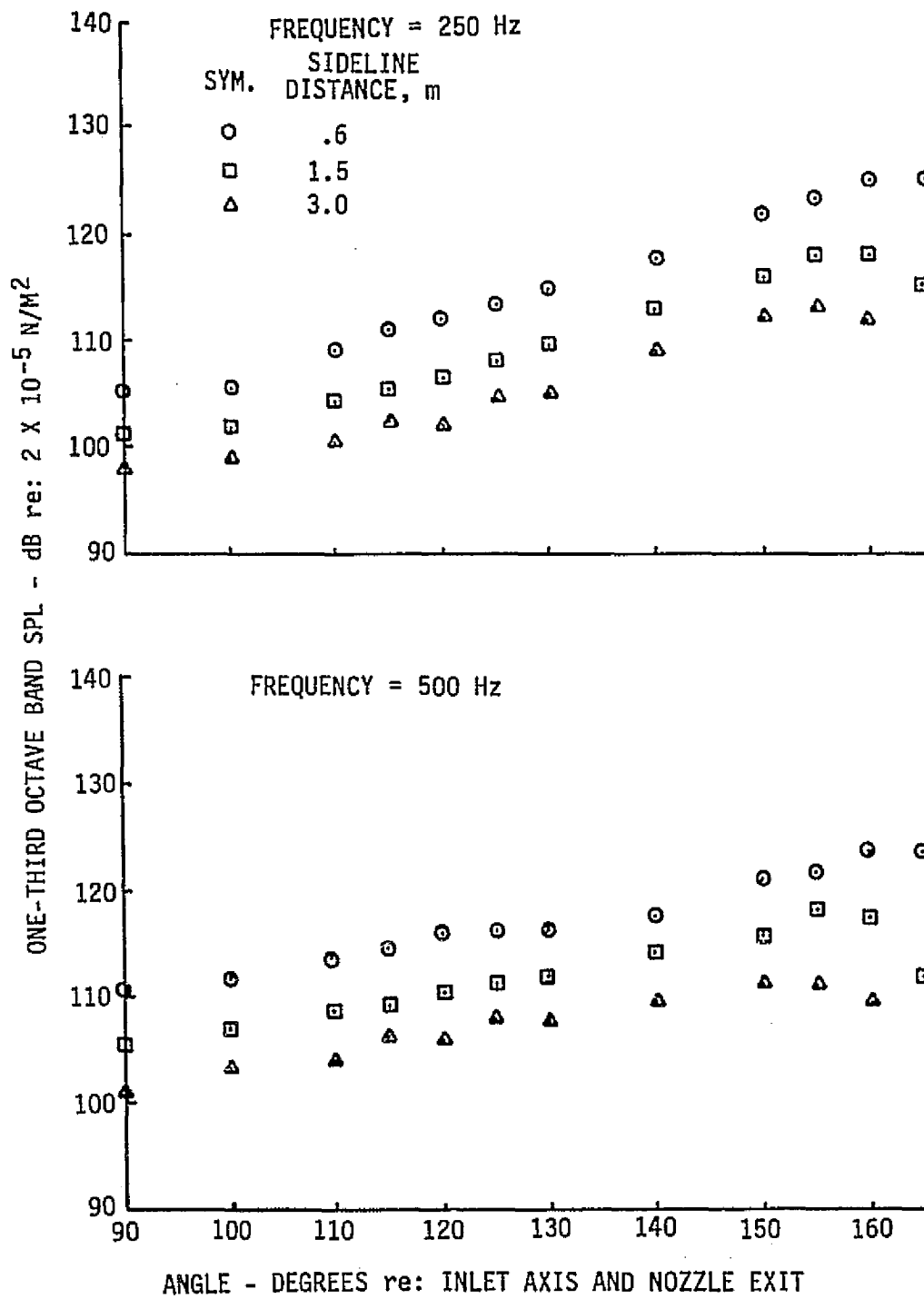


Figure 55.—One-Third-Octave-Band SPL Directivities for the 57-Tube Nozzle With Lined Ejector—NPR = 2.6,  $T_T = 844$  K

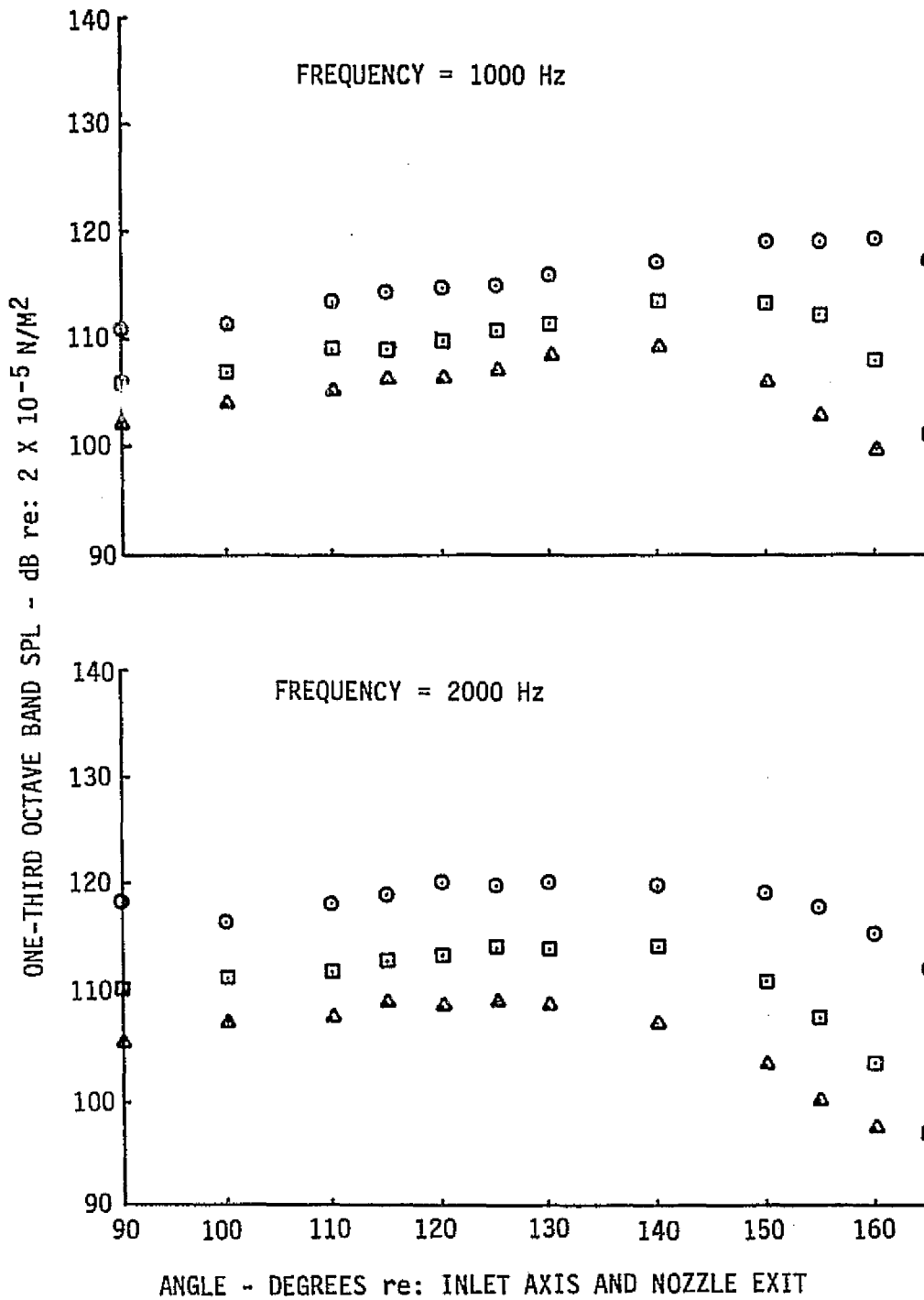


Figure 55.—(Continued)

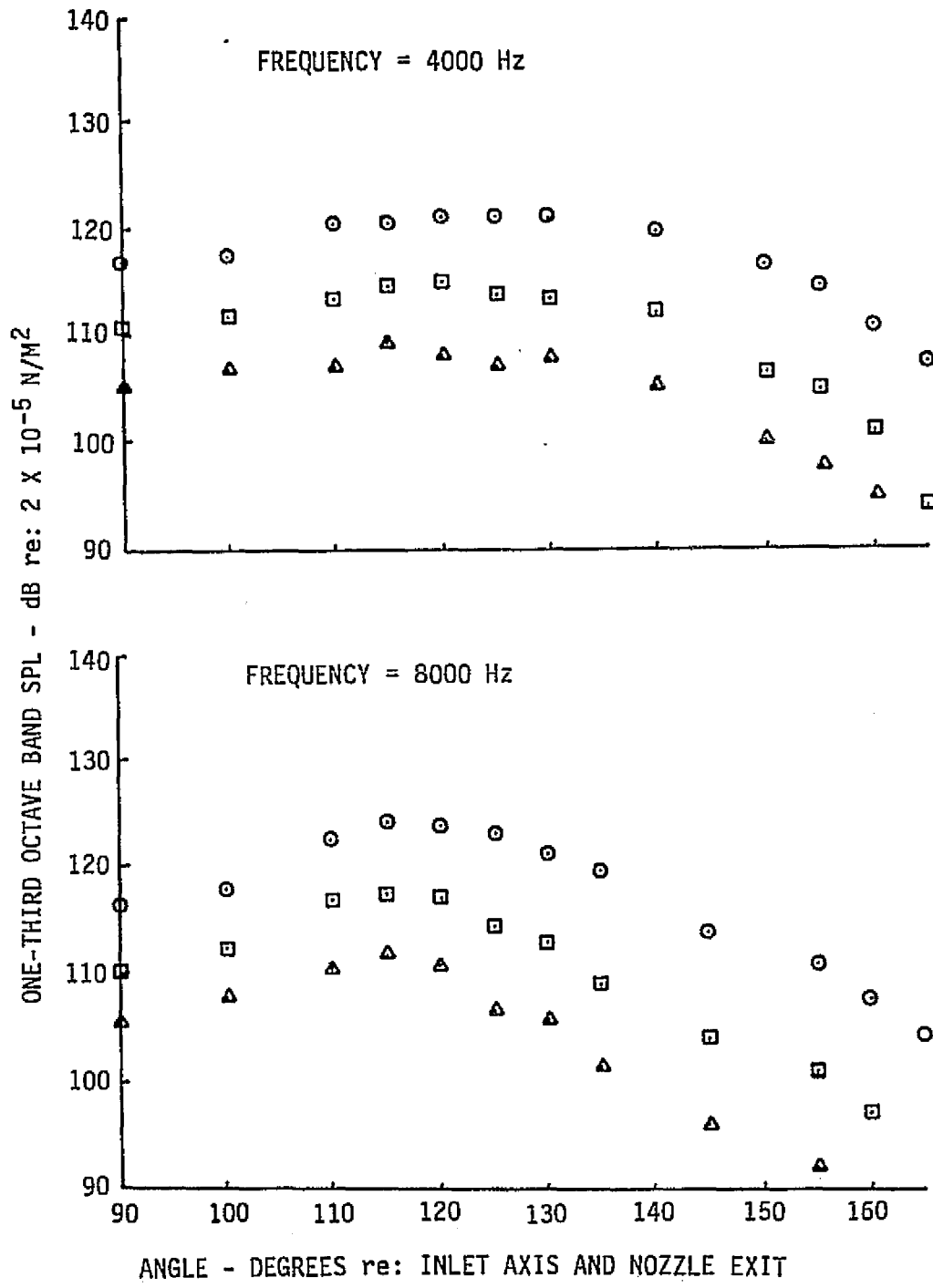


Figure 55.—(Continued)

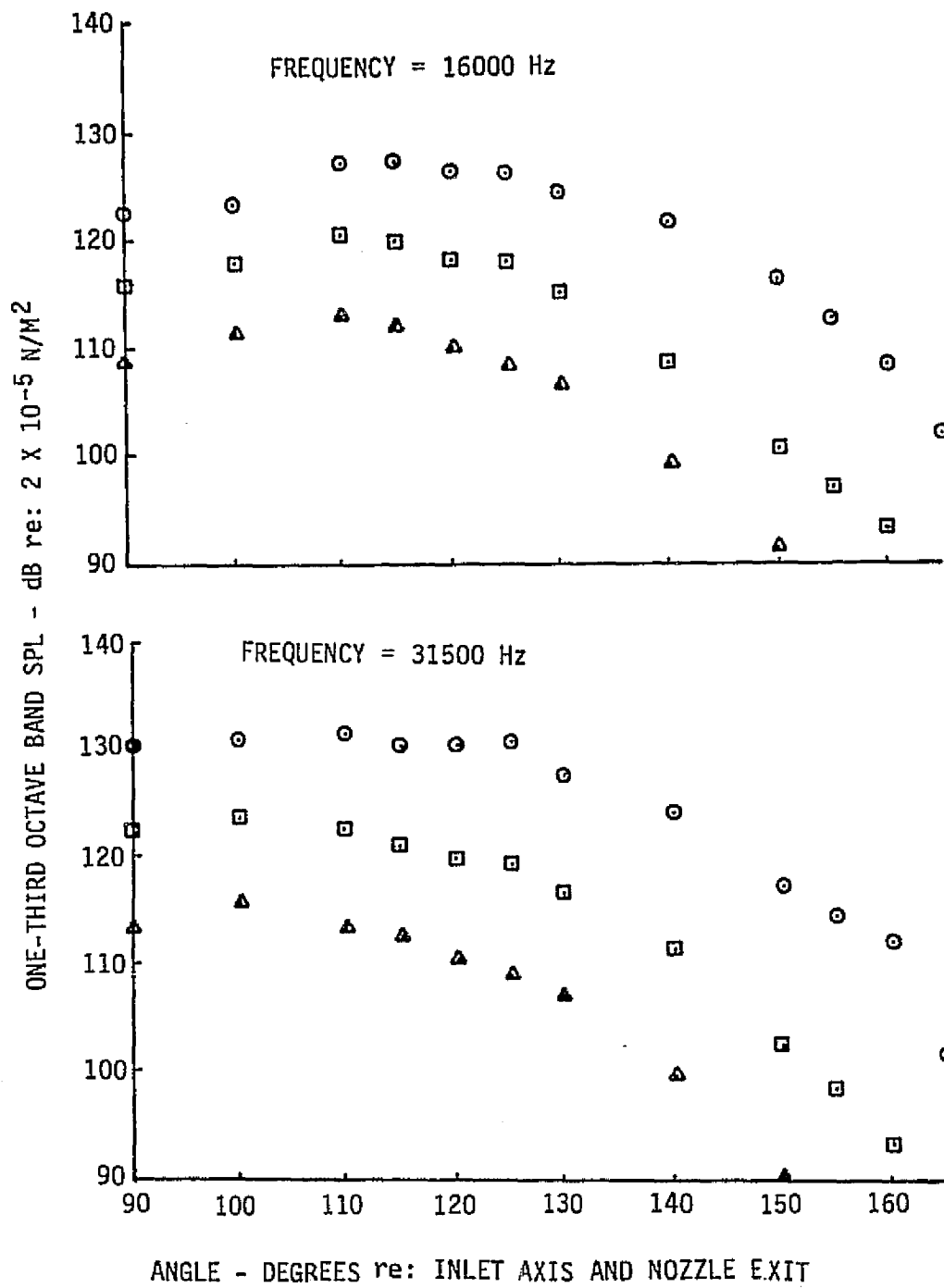


Figure 55.—(Concluded)

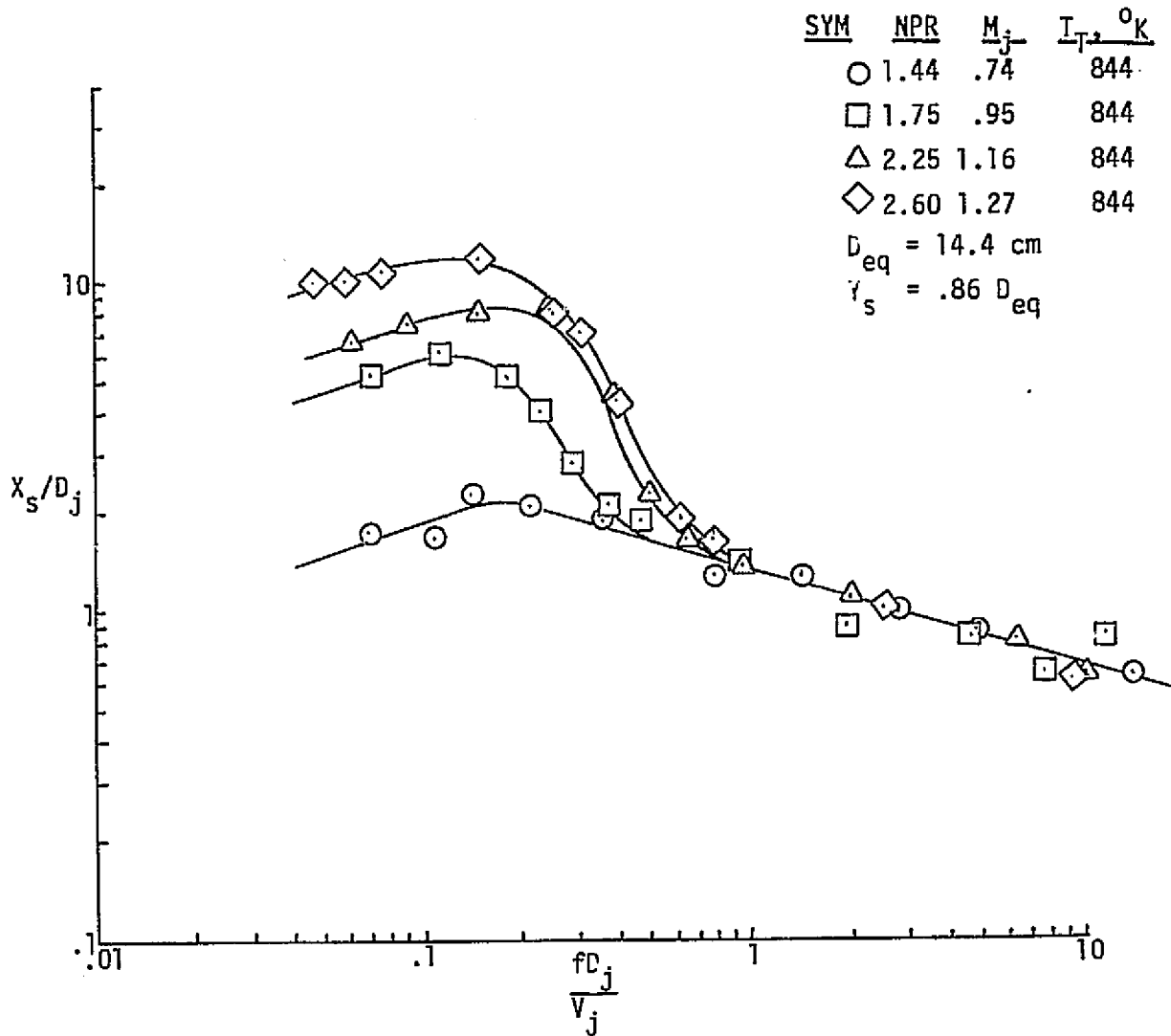


Figure 56.—Peak Noise Source Locations for a 57-Tube Composite Nozzle With Lined Ejector

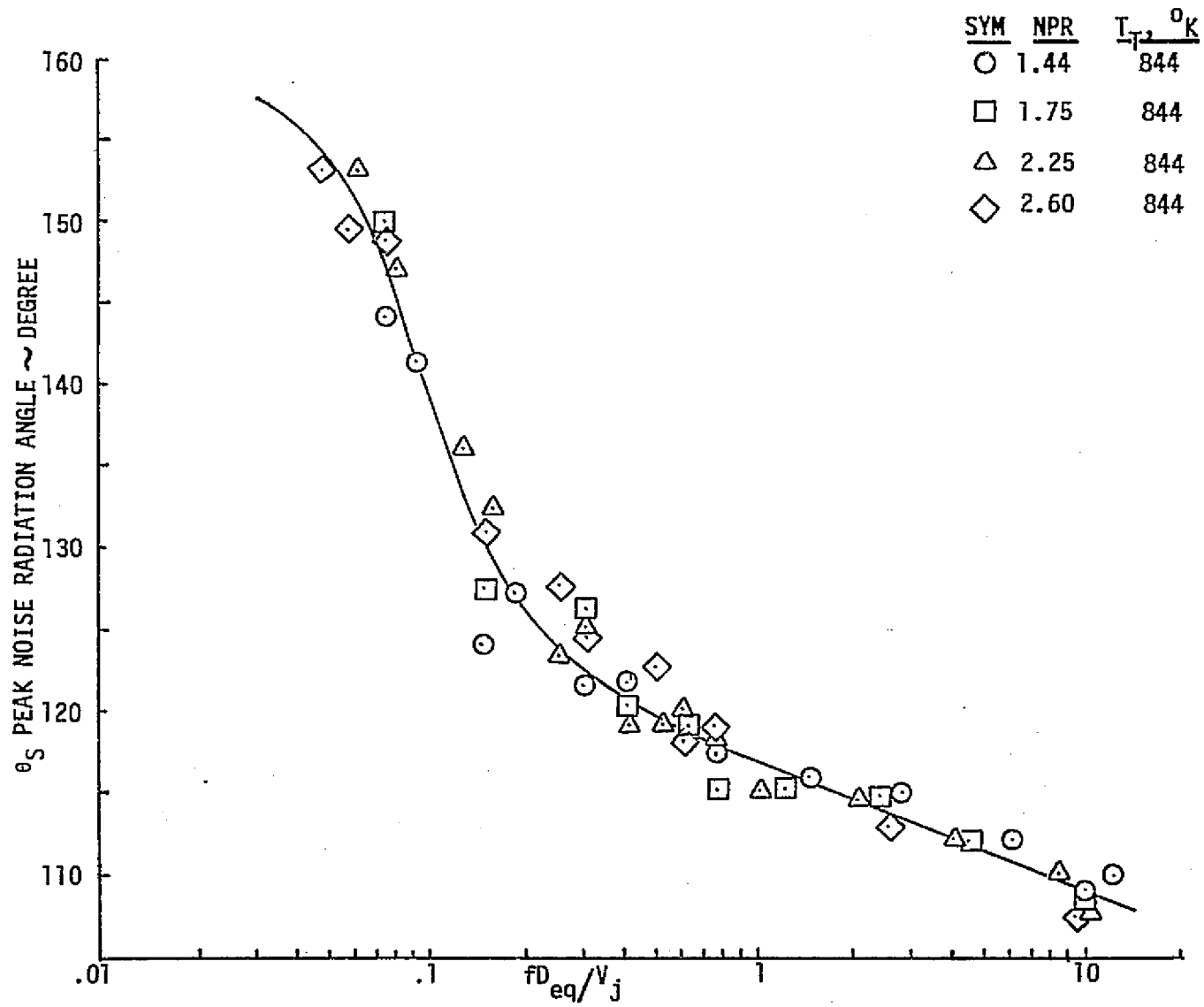


Figure 57.—Peak Noise Source Radiation Angles for a 57-Tube Composite Nozzle With Lined Ejector

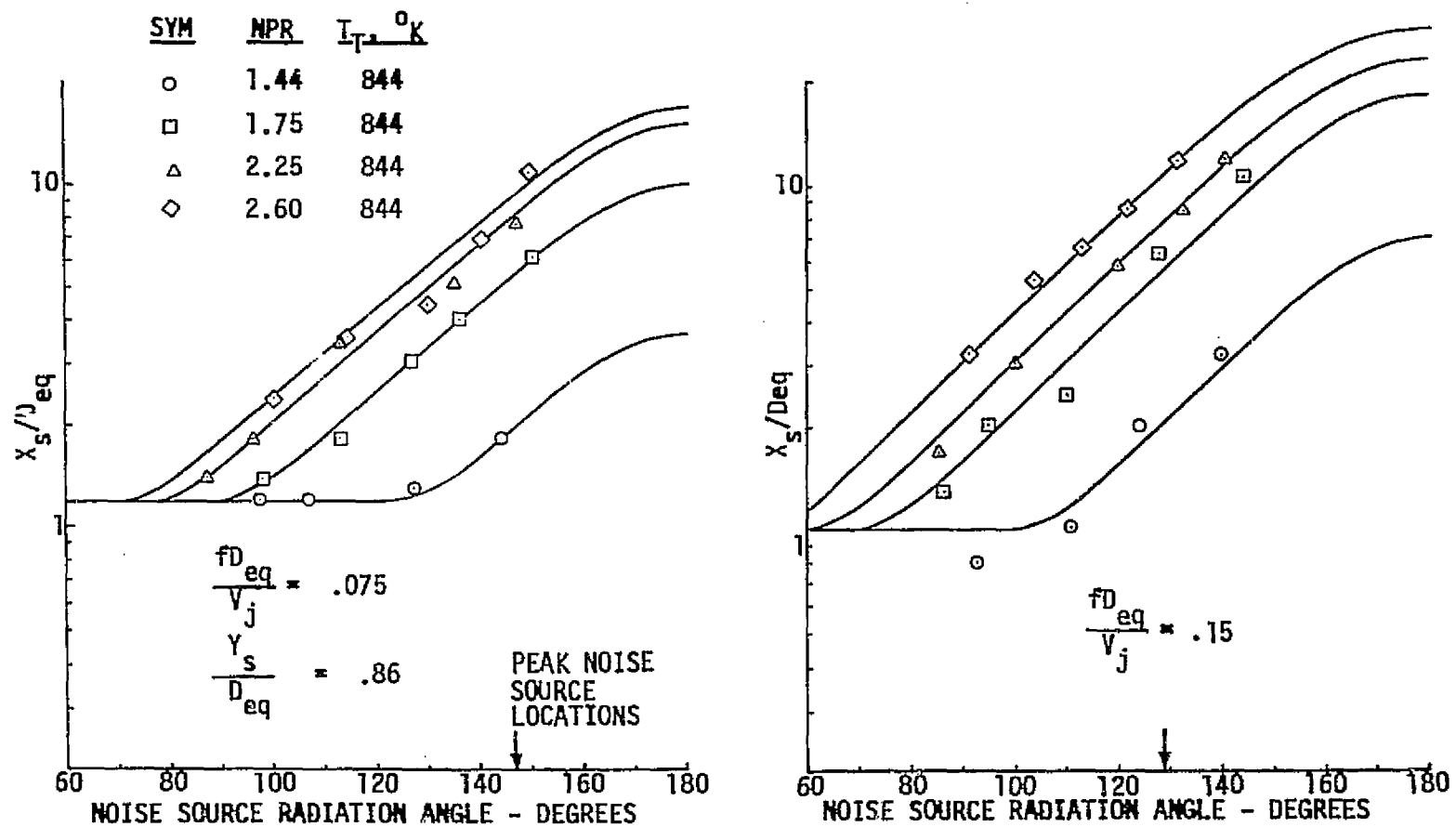


Figure 58.—Distributed Noise Source Locations for the 57-Tube Nozzle With Lined Ejector

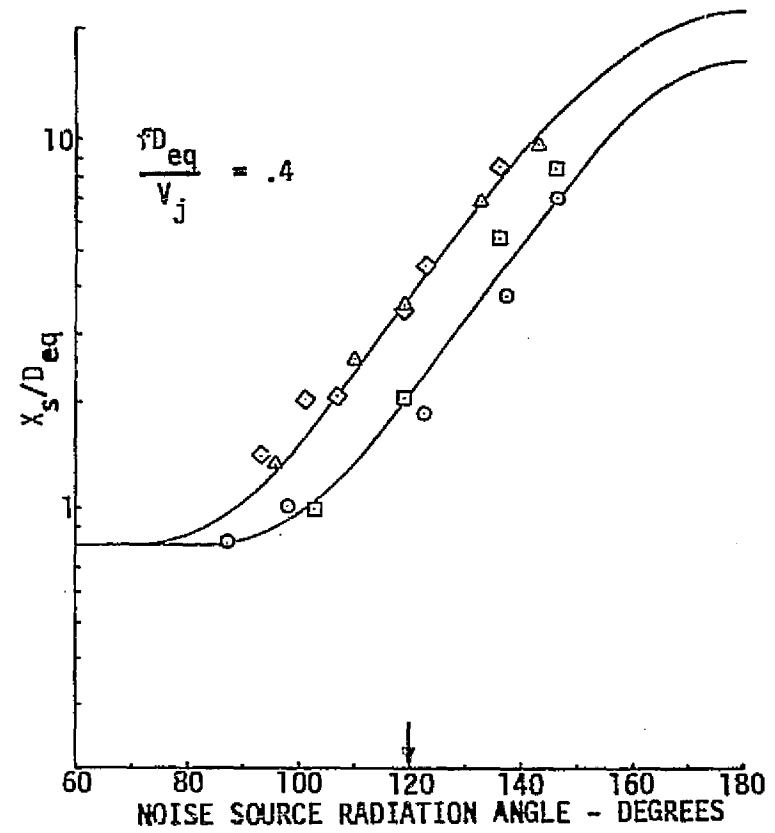
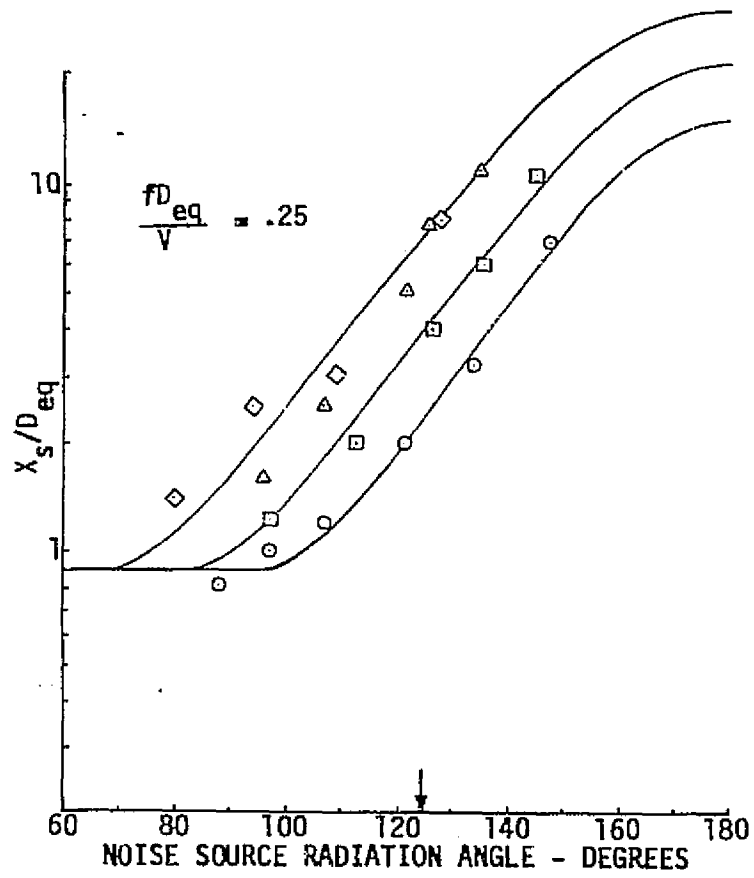


Figure 58.—(Continued)

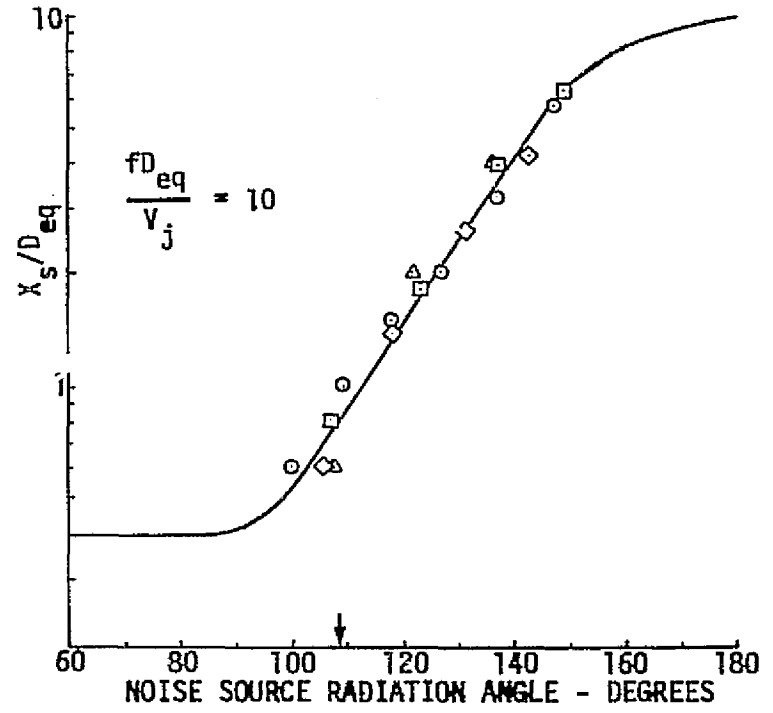
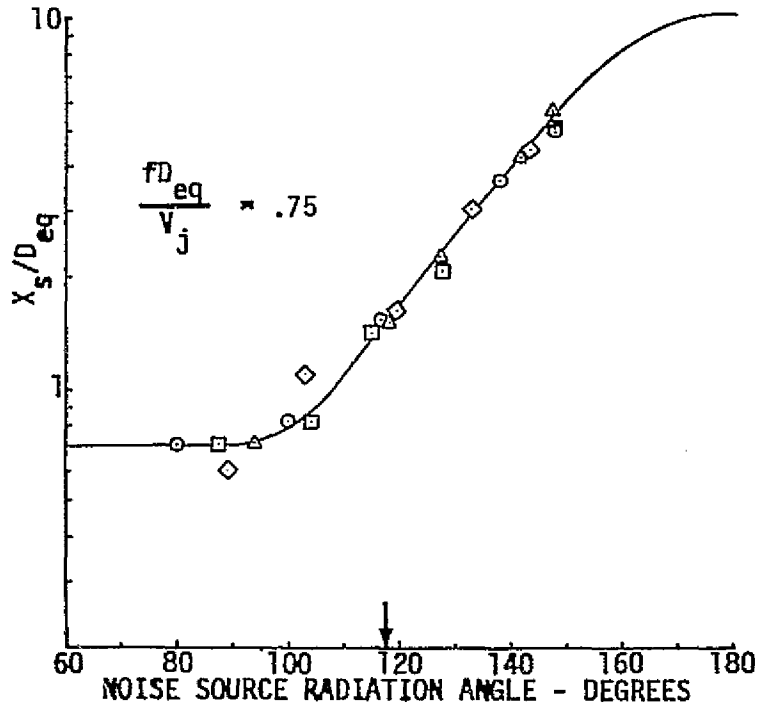


Figure 5B.—(Concluded)

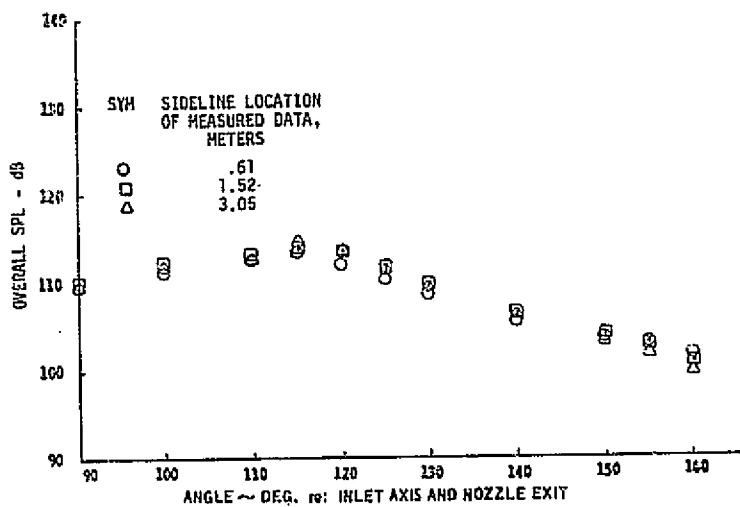


Figure 59.—OASPL and One-Third-Octave-Band SPL Data for the 57-Tube Nozzle With Lined Ejector Extrapolated to a 3.0-m Sideline—NPR = 1.44,  $T_T = 844$  K

ORIGINAL PAGE IS  
 OF POOR QUALITY

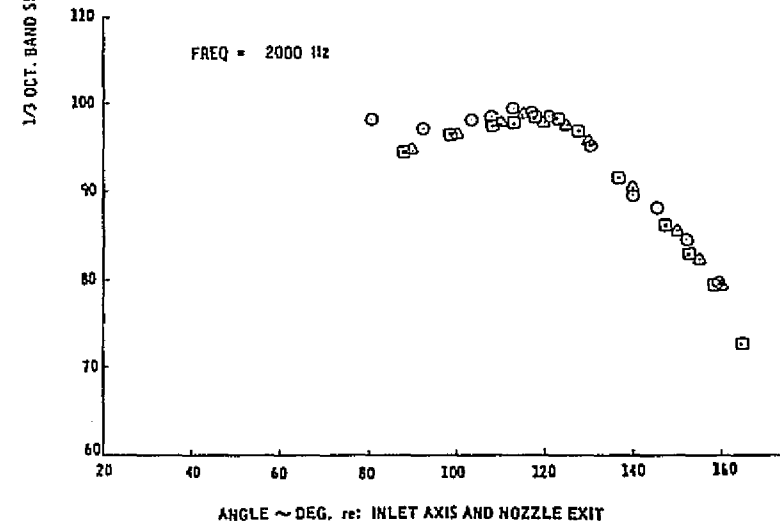
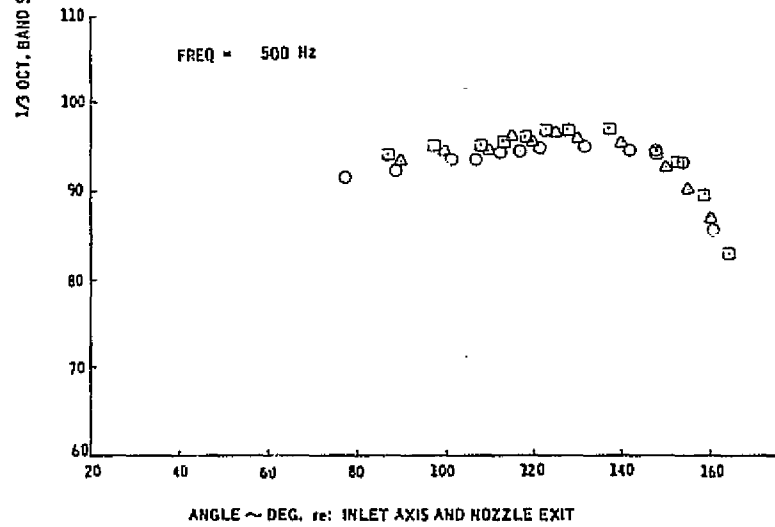
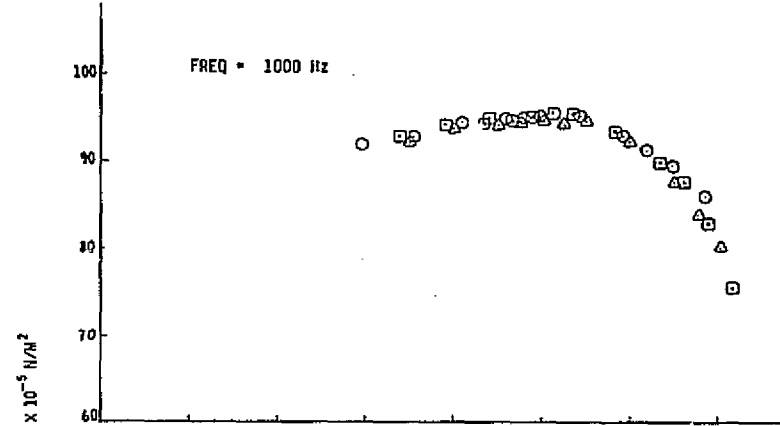
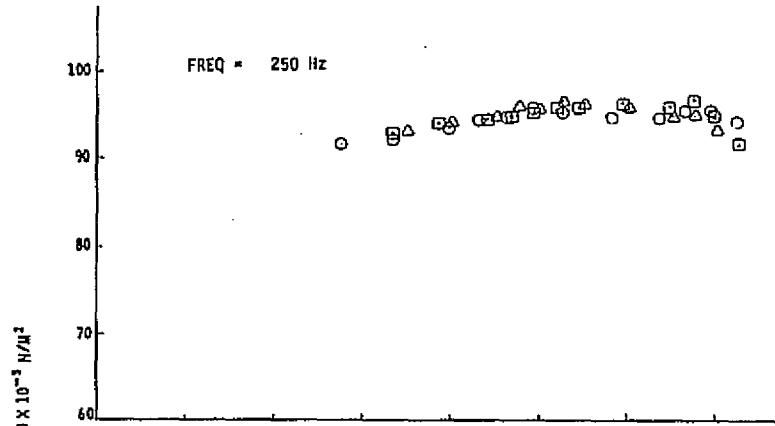


Figure 59.—(Continued)

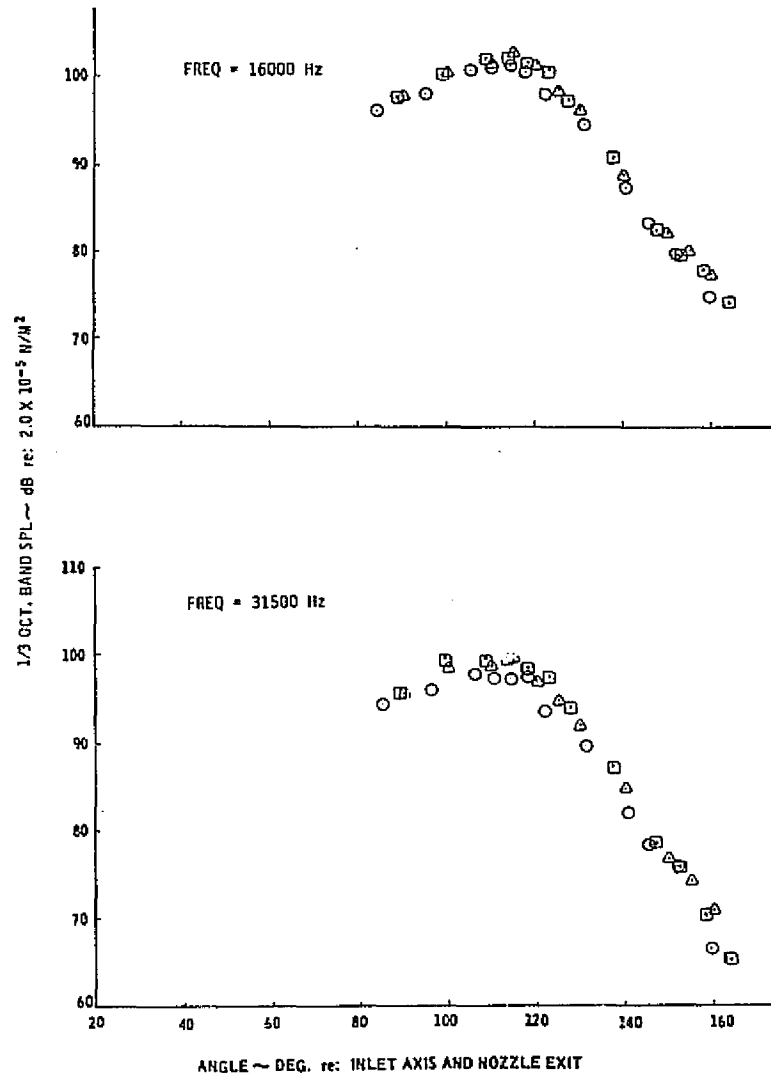
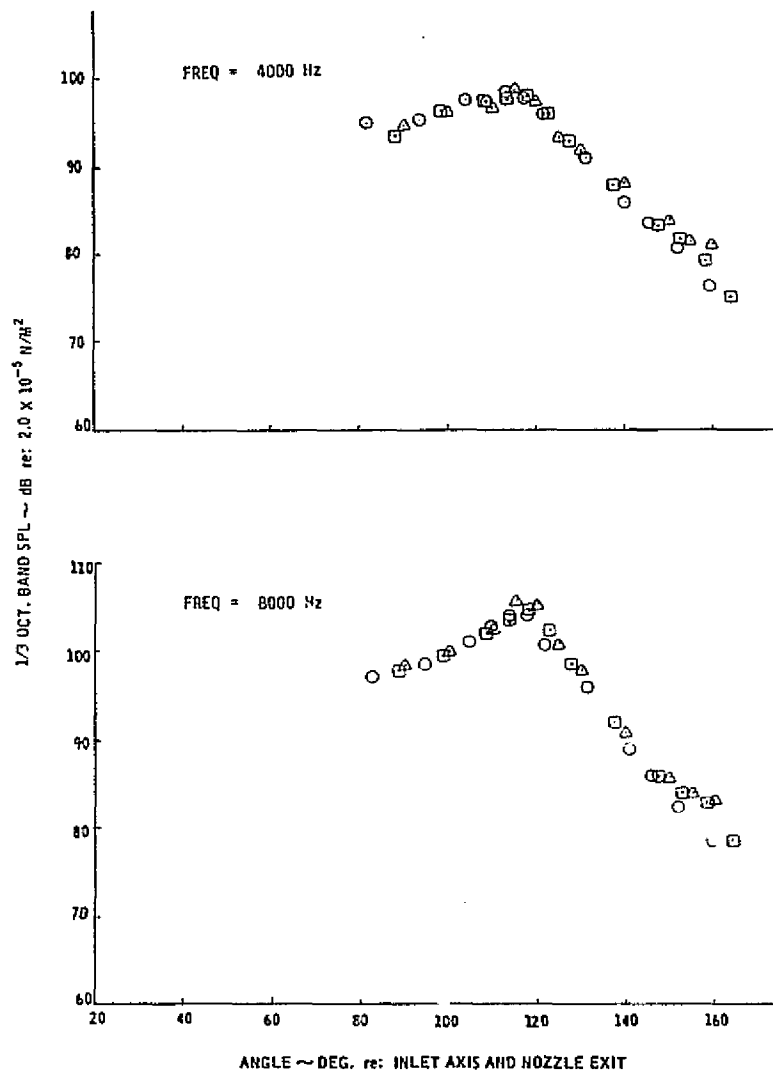


Figure 59.—(Concluded)

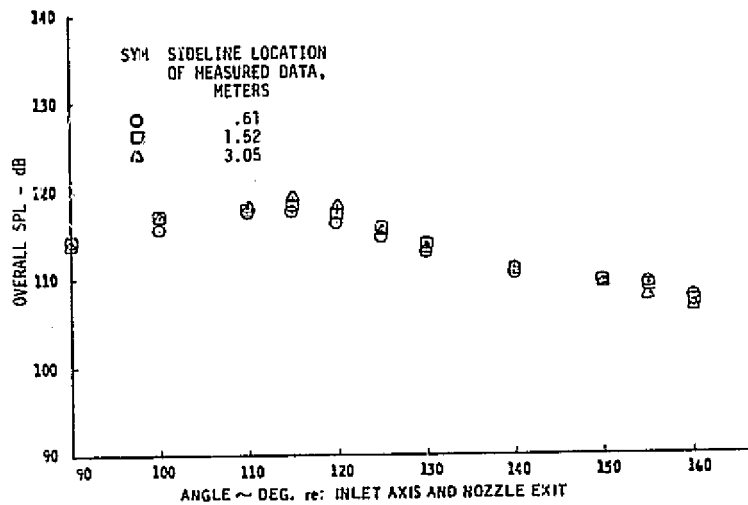


Figure 60.—OASPL and One-Third-Octave-Band SPL Data for the 57-Tube Nozzle With Lined Ejector Extrapolated to a 3.0-m Sideline—NPR = 1.75,  $T_T = 844$  K

ORIGINAL PAGE IS  
OF POOR QUALITY

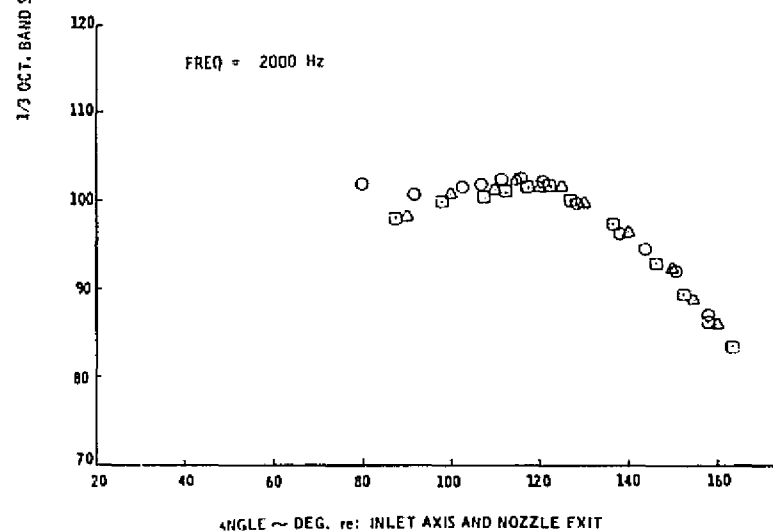
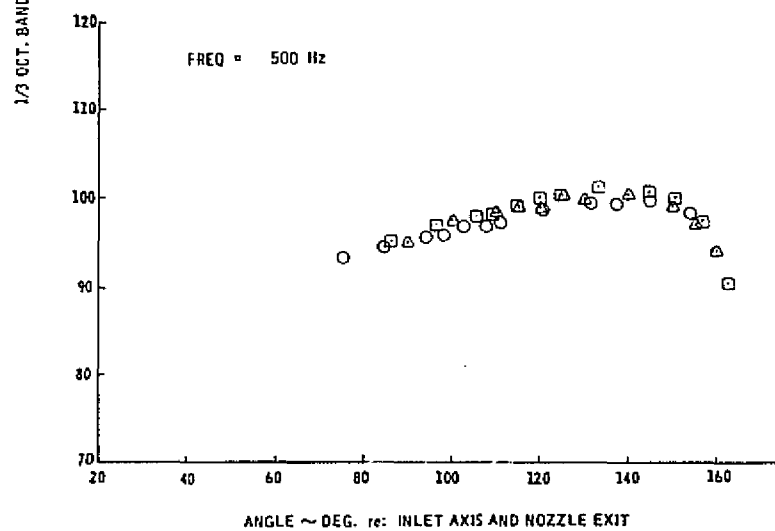
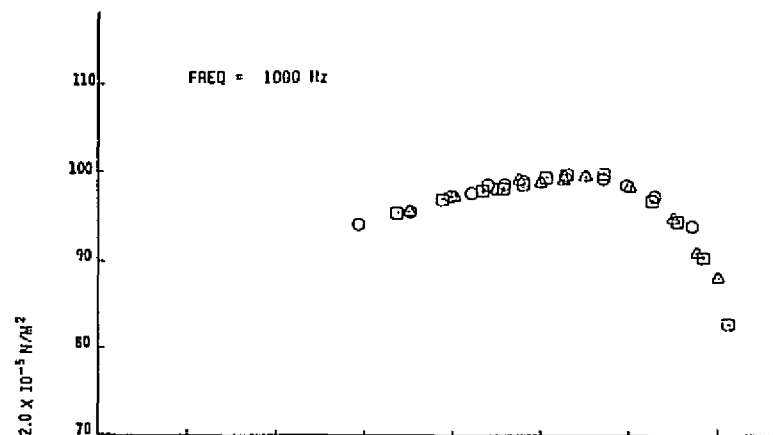
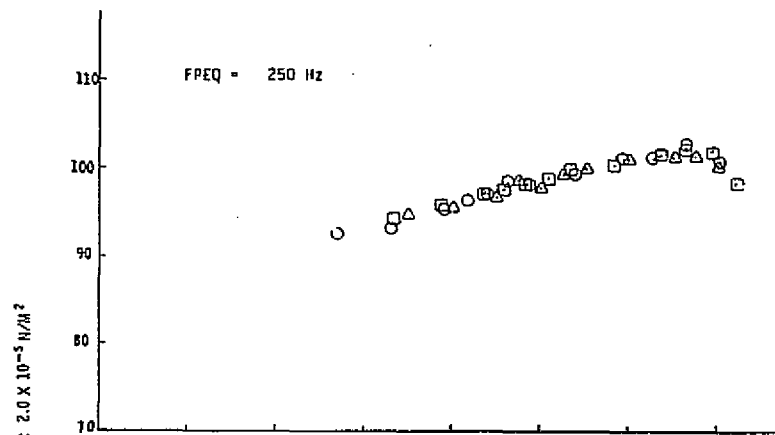


Figure 60.--(Continued)

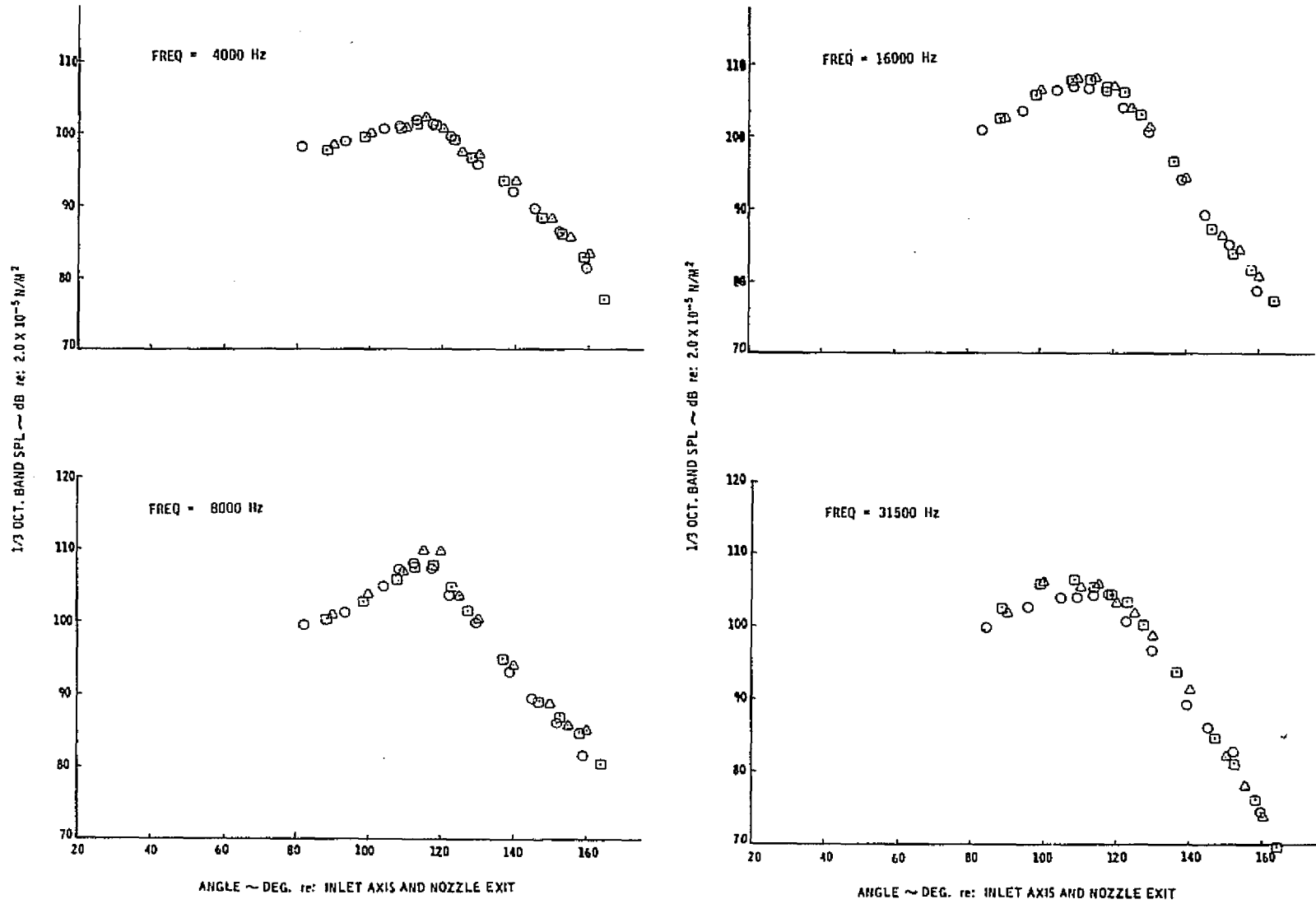


Figure 60.—(Concluded)

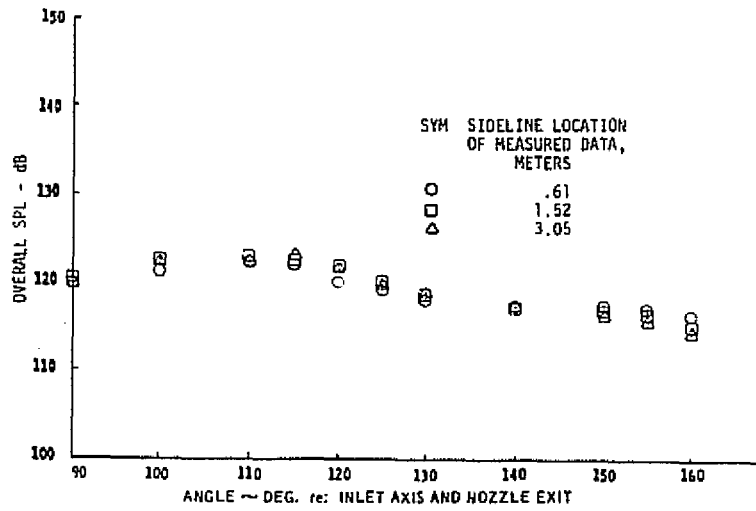


Figure 61.—OASPL and One-Third-Octave-Band SPL Data for the 57-Tube Nozzle With Lined Ejector Extrapolated to a 3.0-m Sideline—NPR = 2.25,  $T_T = 844$  K

ORIGINAL PAGE IS  
OF POOR QUALITY

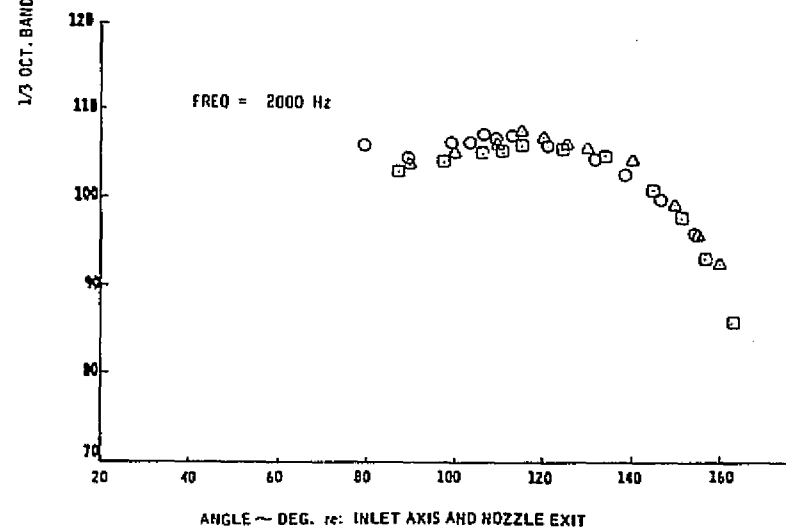
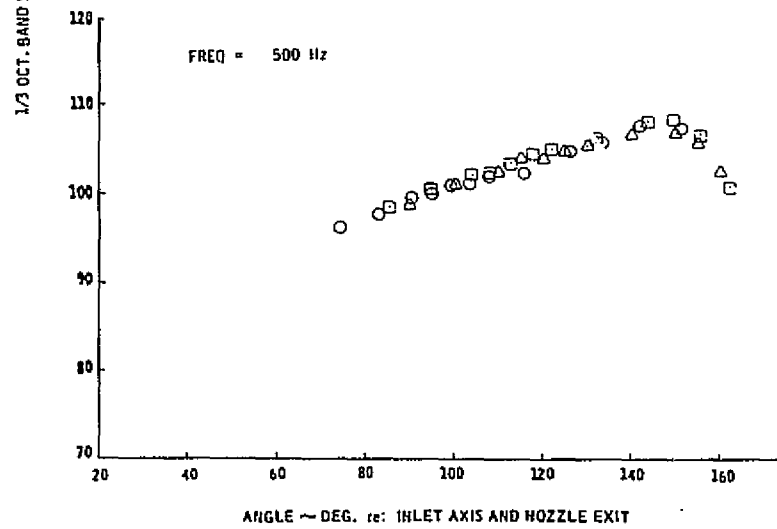
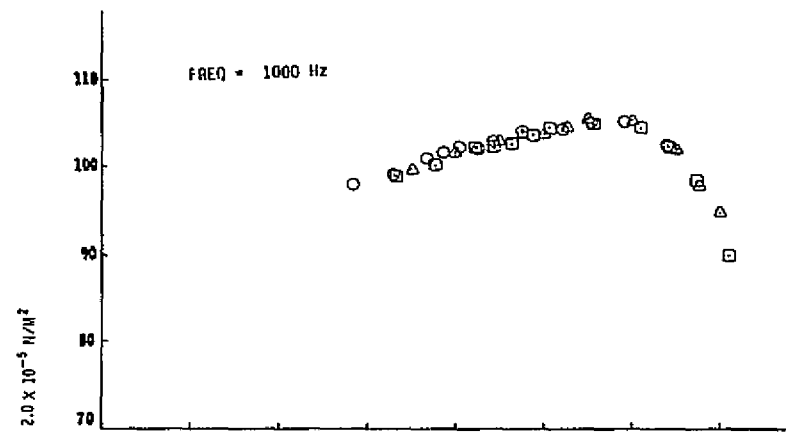
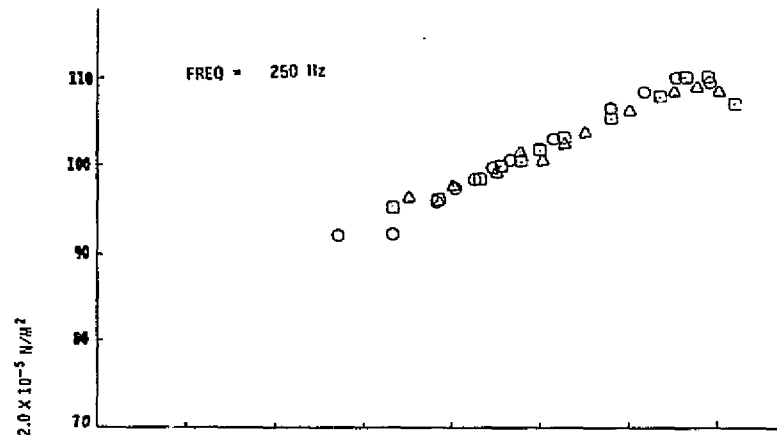
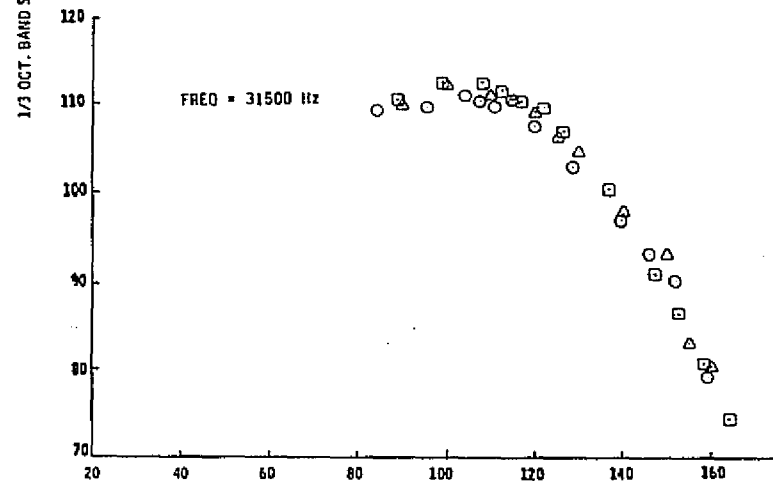
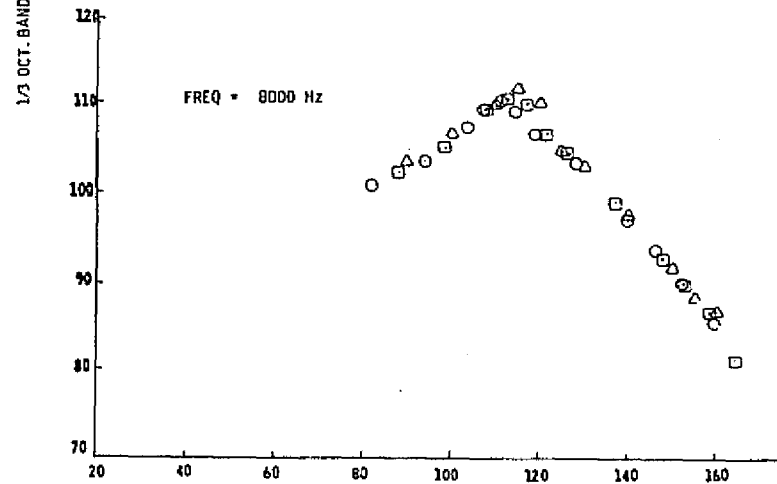
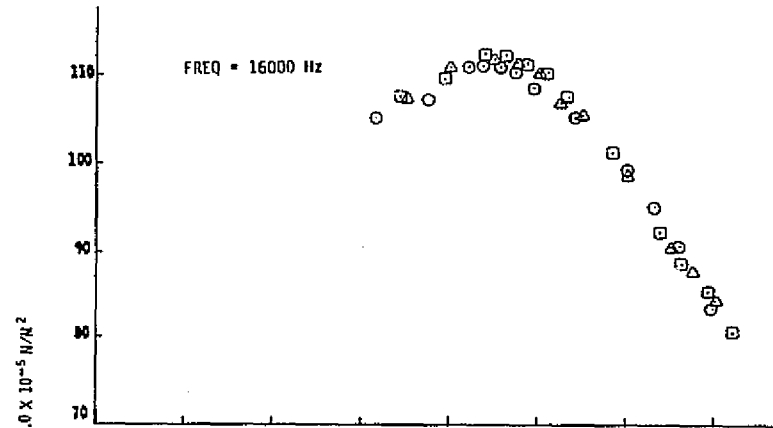
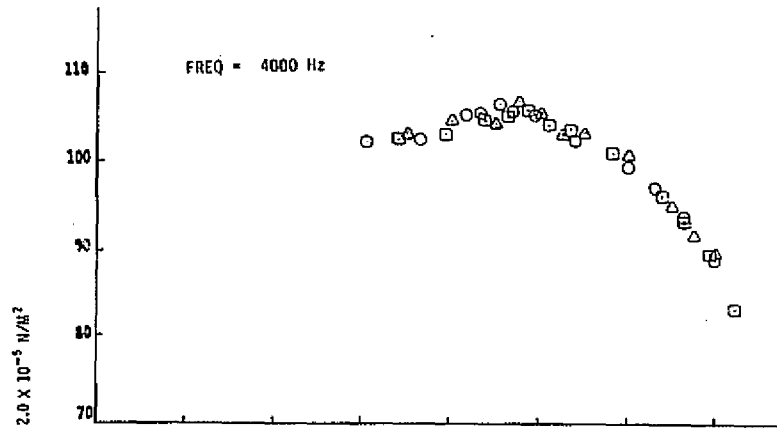


Figure 61.—(Continued)



ANGLE ~ DEG. re: INLET AXIS AND NOZZLE EXIT

ANGLE ~ DEG. re: INLET AXIS AND NOZZLE EXIT

Figure 61. (Concluded)

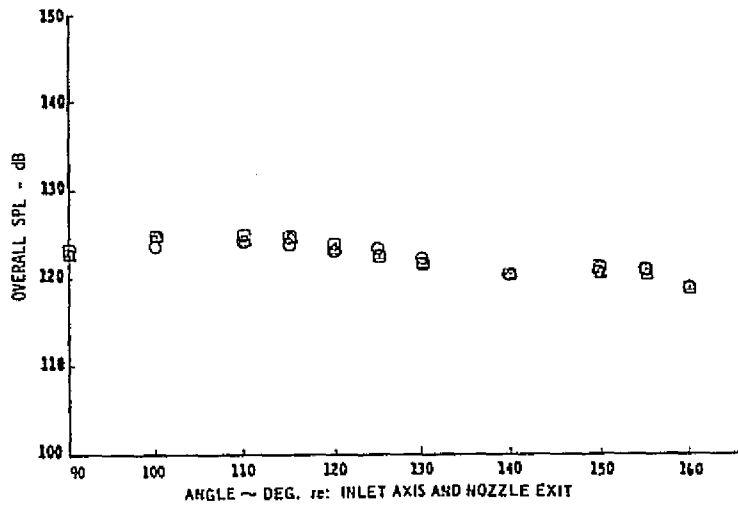


Figure 62.—OASPL and One-Third-Octave-Band SPL Data for the 57-Tube Nozzle With Lined Ejector Ejector Extrapolated to a 3.0-m Sideline—NPR = 2.60,  $T_T = 844$  K

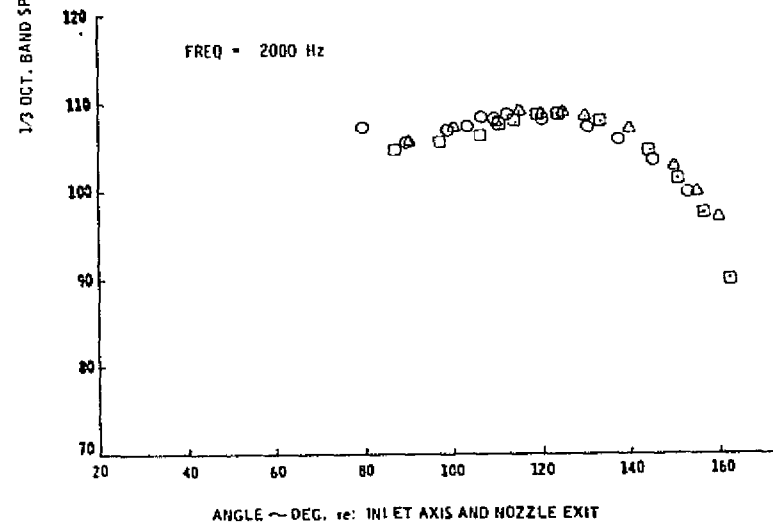
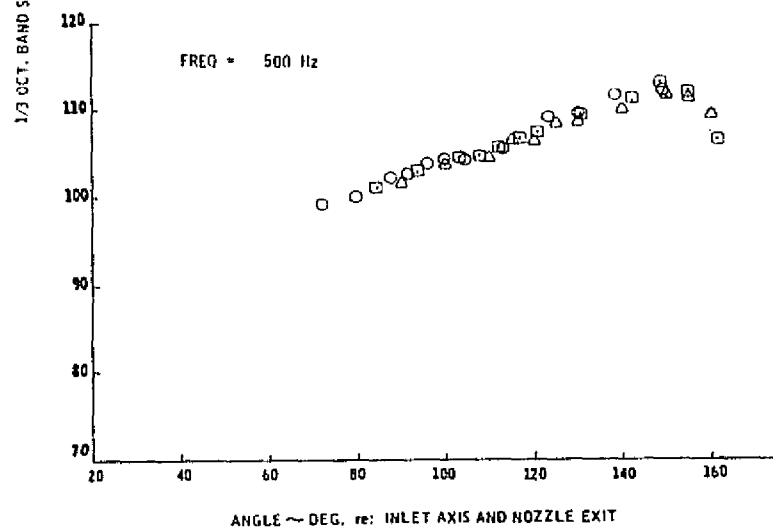
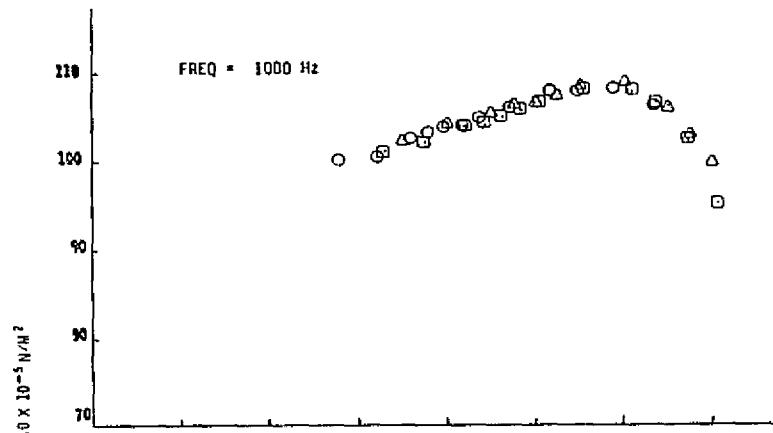
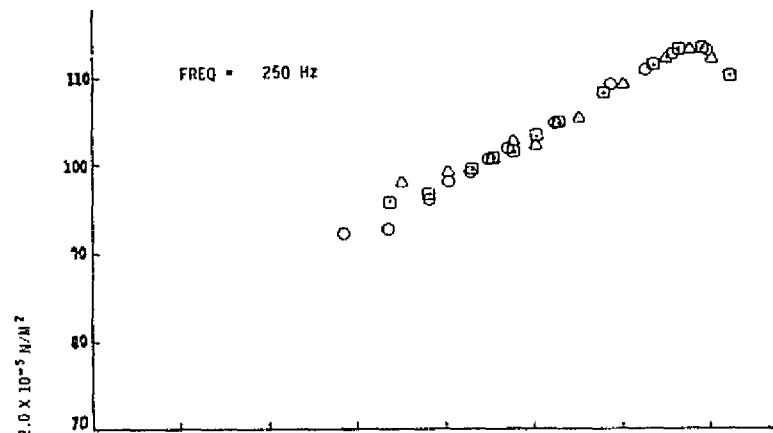


Figure 62.—(Continued)

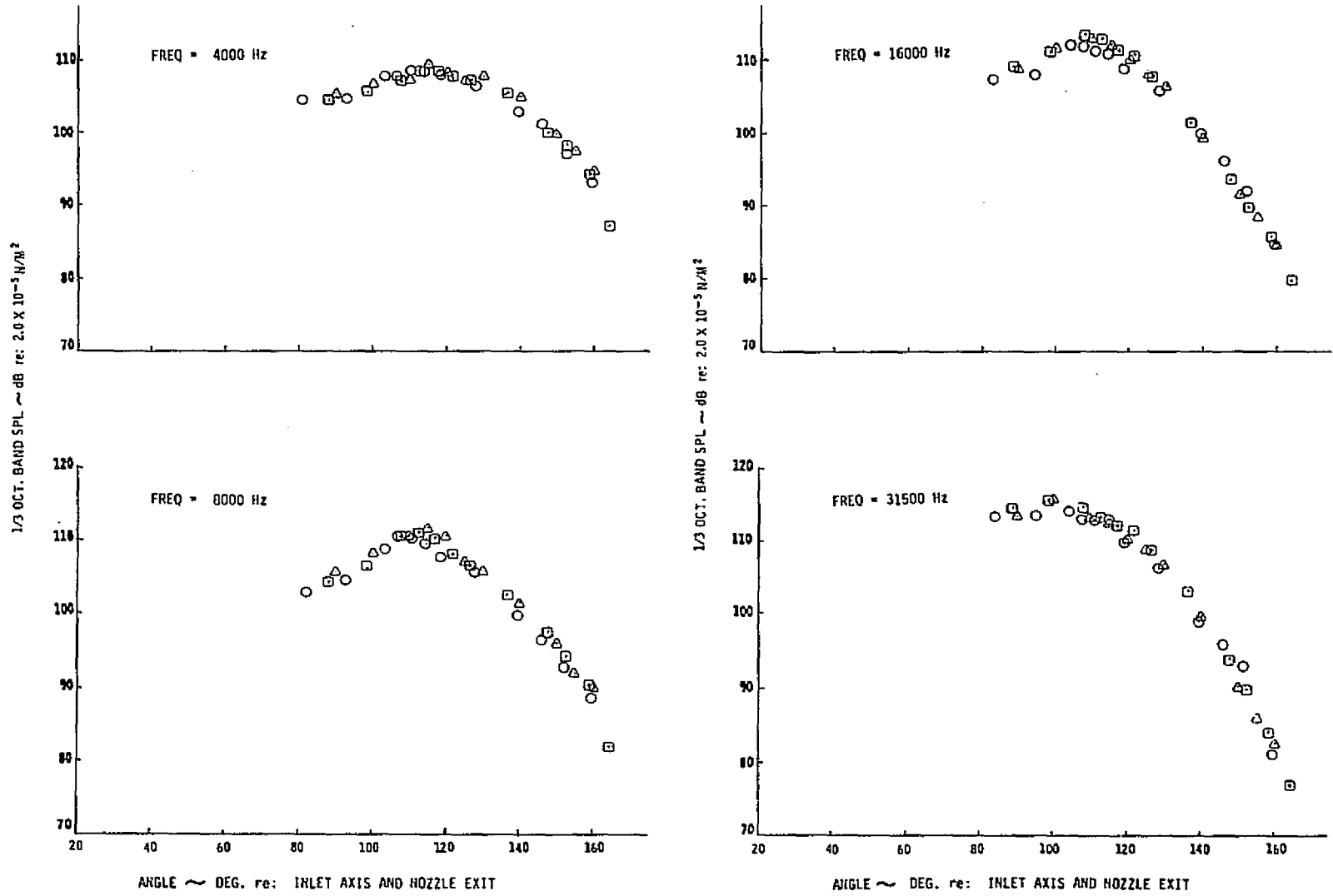


Figure 62.—(Concluded)

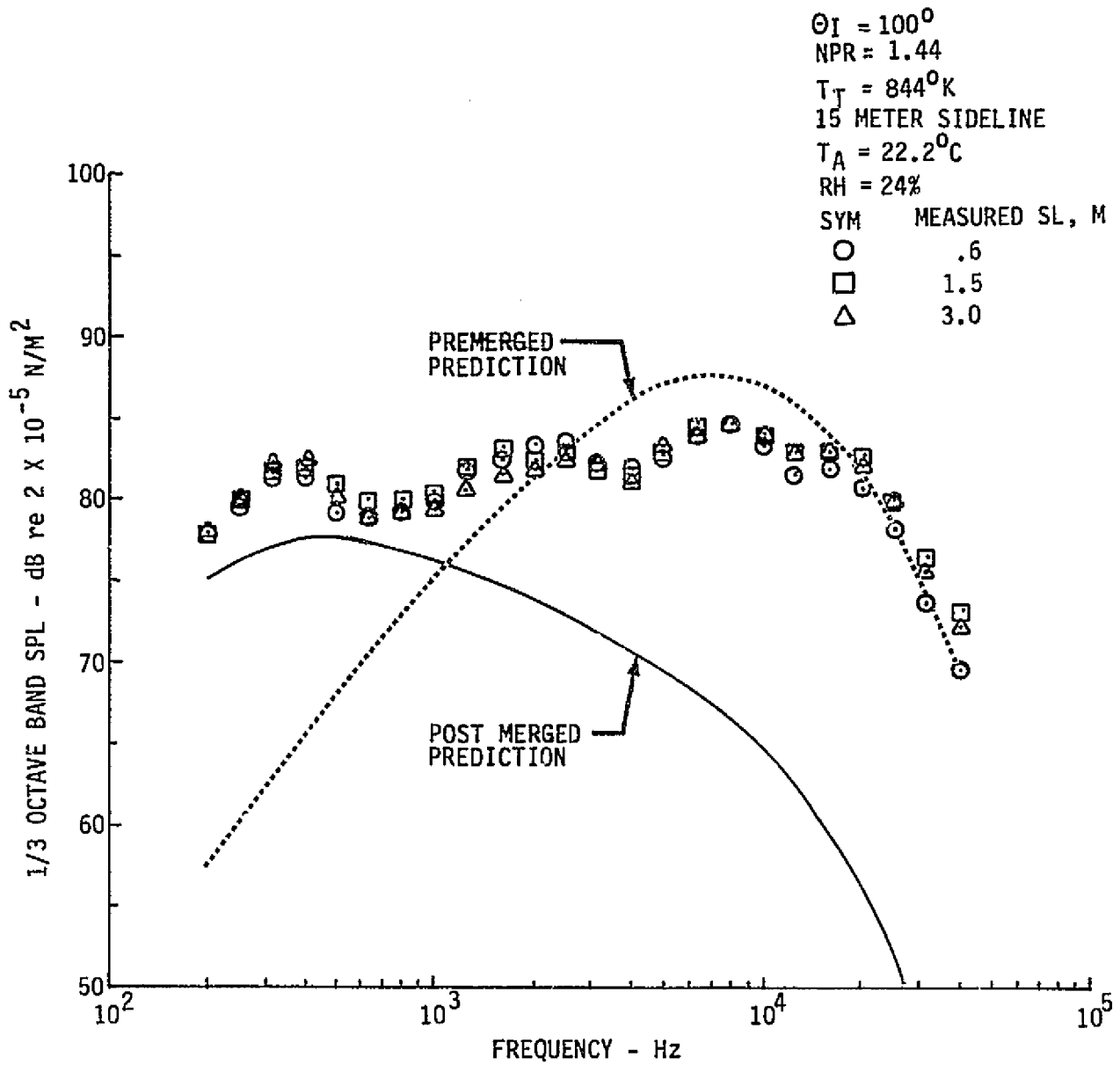


Figure 63.—Comparison of Data Extrapolated to a 15-m Sideline for the 57-Tube Nozzle and Lined Ejector With Clean, Far-Field Jet Noise Predictions

$\theta_I = 120^\circ$

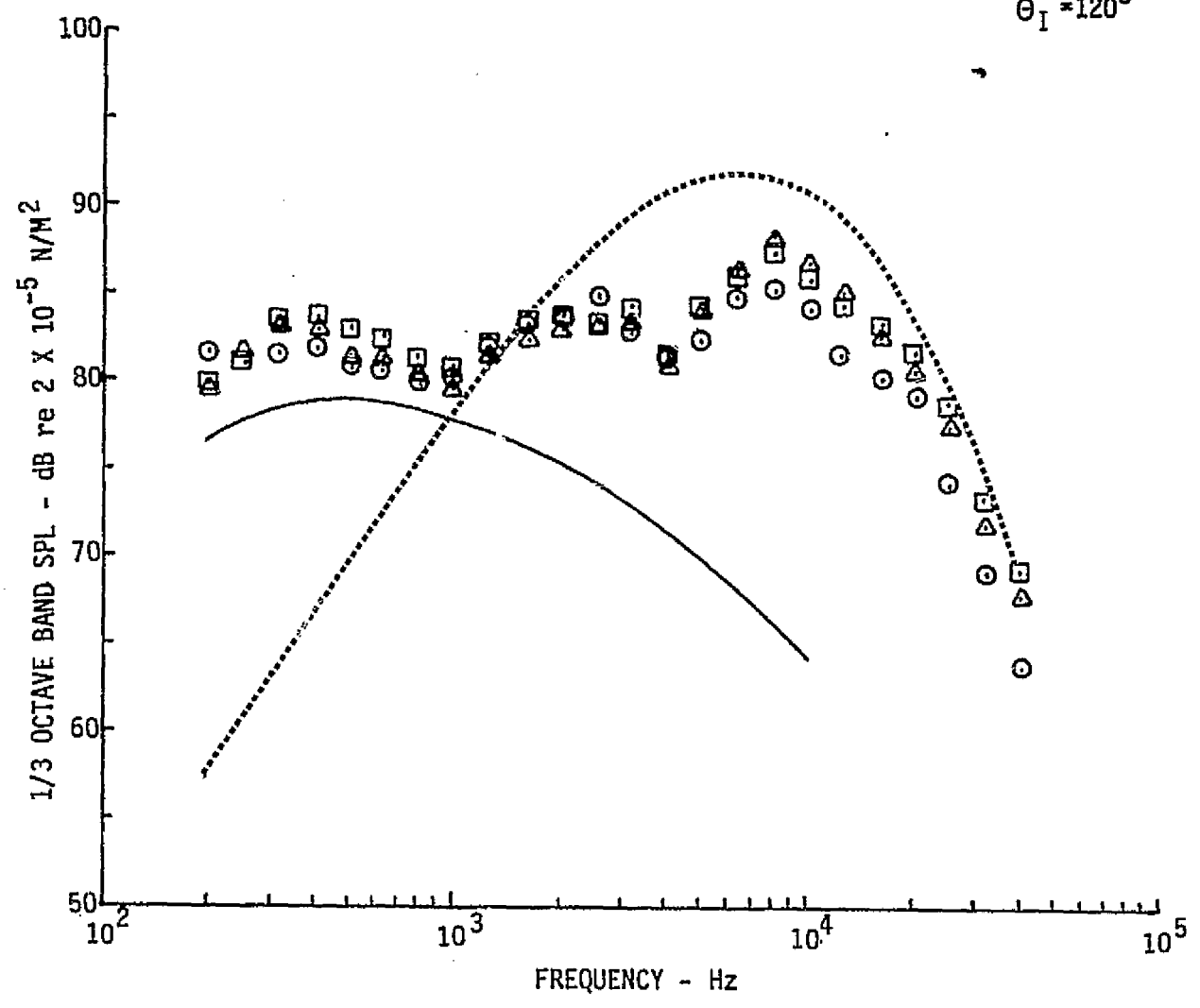


Figure 63.—(Continued)

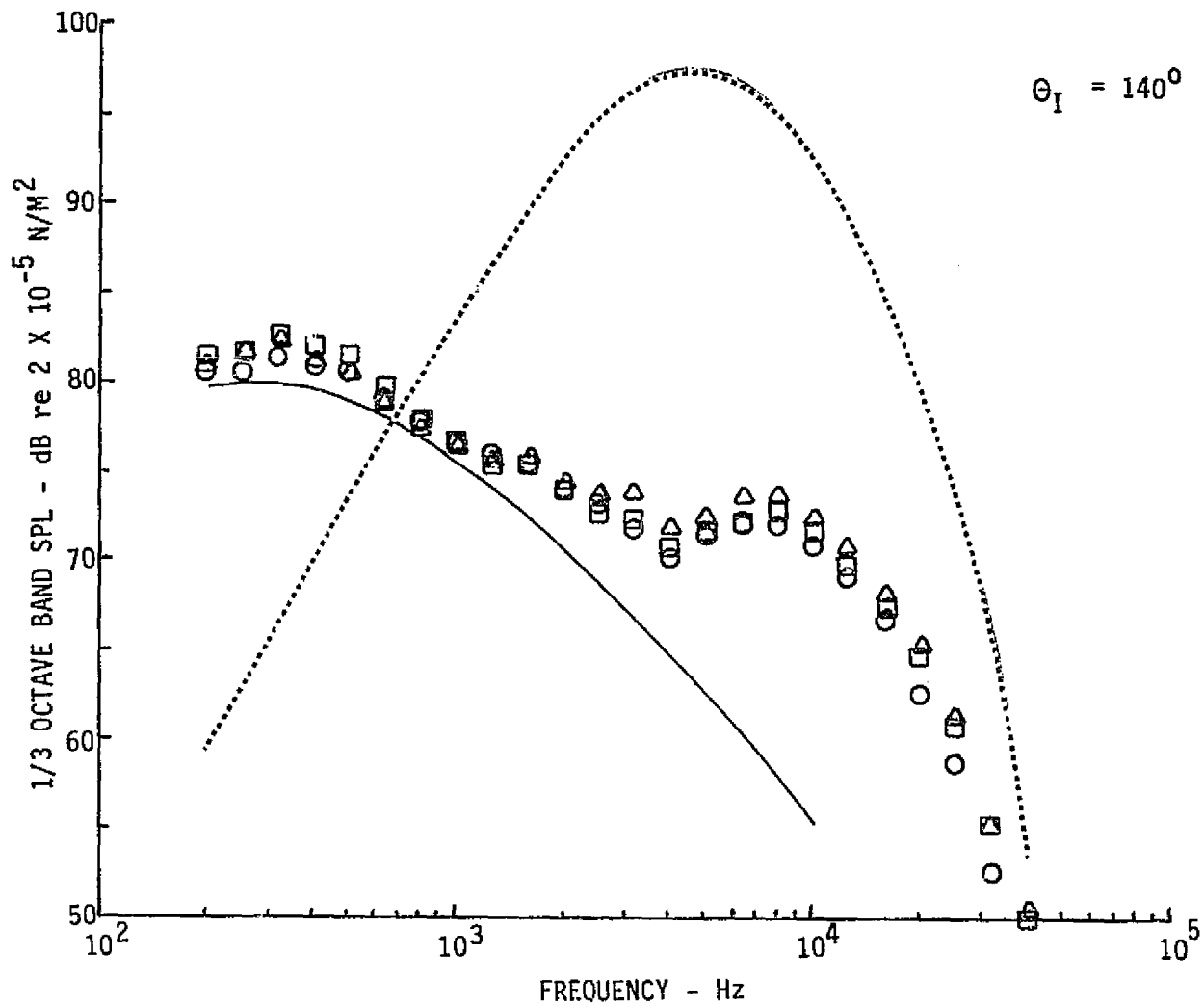


Figure 63.—(Continued)

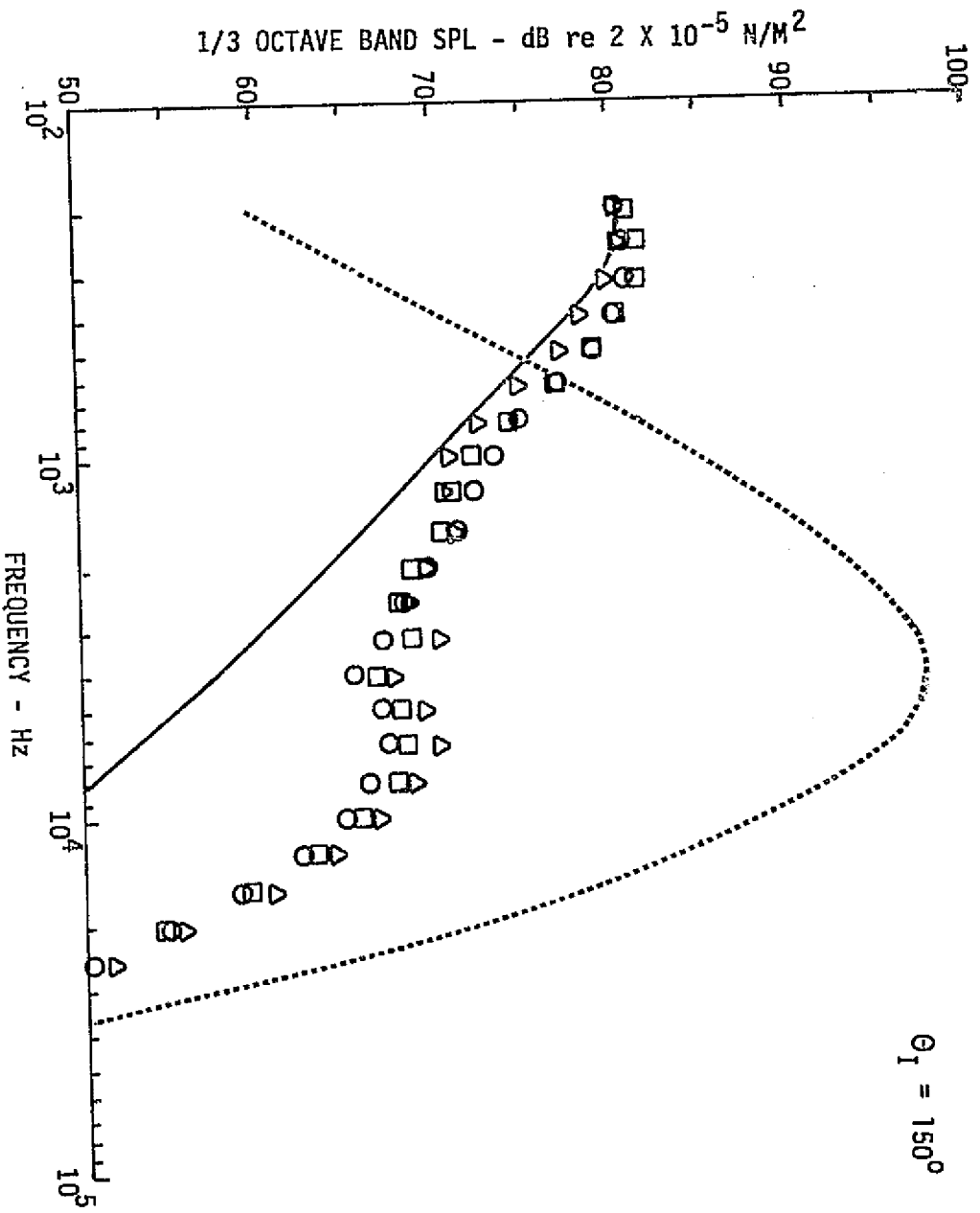


Figure 63.—(Continued)

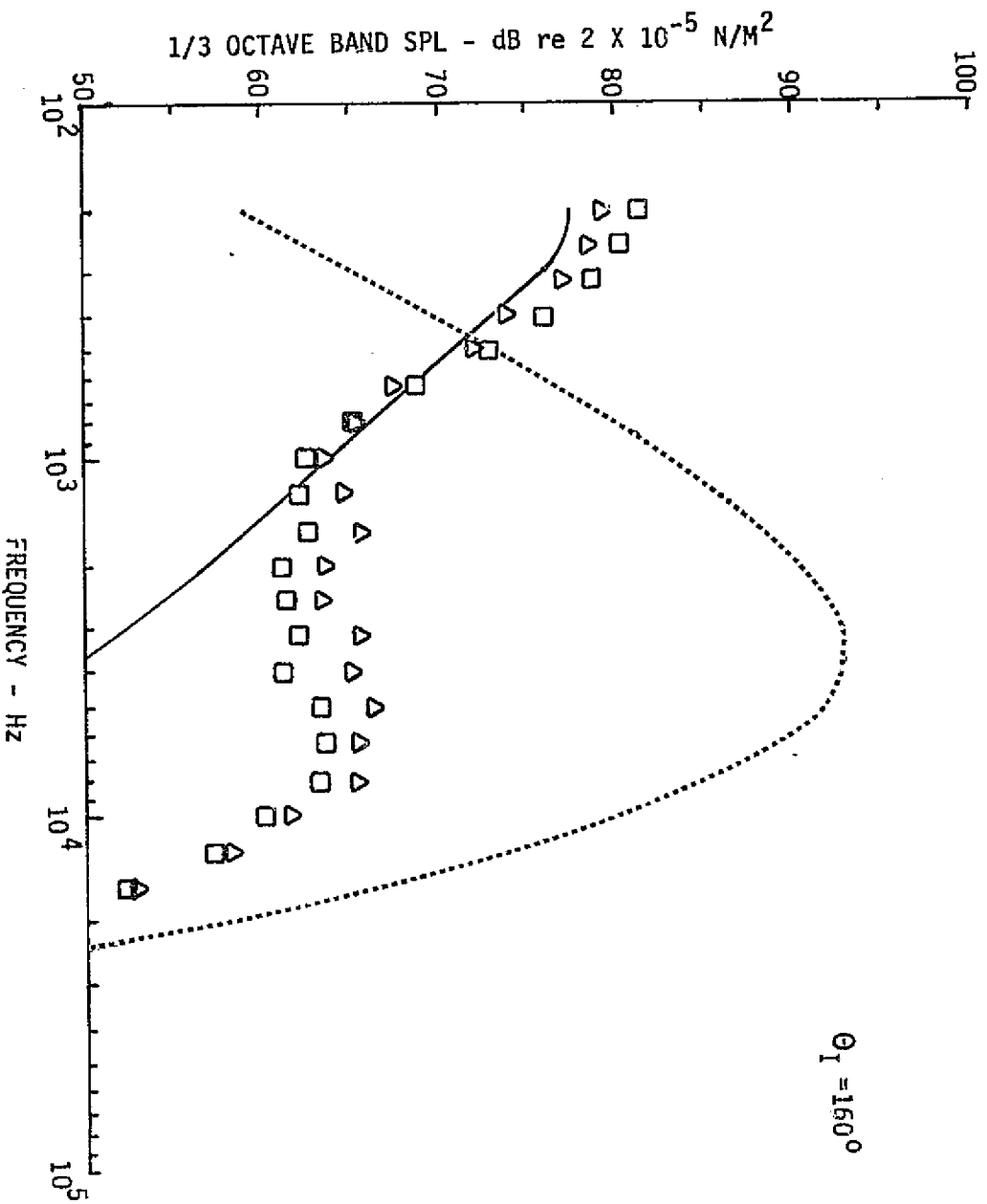


Figure 63.-(Concluded)